Title

Characterizing the Sources and Atmospheric Processing of Ambient Particulate Matter using Aerosol Mass Spectrometry

Author

Farley, Ryan Nilsson

Publication Date

2023

Peer reviewed|Thesis/dissertation

Characterizing the Sources and Atmospheric Processing of Ambient Particulate Matter using Aerosol Mass Spectrometry

By

RYAN FARLEY

DISSERTATION

Submitted in partial satisfaction of the requirements for the degree of

DOCTOR OF PHILOSOPHY

in

Agricultural and Environmental Chemistry

in the

OFFICE OF GRADUATE STUDIES

of the

UNIVERSITY OF CALIFORNIA

DAVIS

Approved:

Qi Zhang, Chair

Cort Anastasio

Christopher Cappa

Committee in Charge

2023

Abstract

Atmospheric particulate matter (PM) has important implications on air quality, global climate and human health. However, significant uncertainty remains in the chemical and physical transformations of PM during atmospheric transport. Ambient measurements are critical for understanding the sources and processing of the aerosols in order to inform models and public policy. In this work, high-resolution soot-particle aerosol mass spectrometry (SP-AMS) was used during three different field campaigns to obtain real-time measurements of aerosol composition and properties under a variety of different environments to better understand the atmospheric evolution of PM.

The first study was conducted at the Mt. Bachelor Observatory (MBO), a mountaintop site in the Pacific Northwest, in order to explore the aging of biomass burning (BB) emissions and their effects on the remote troposphere. Despite low aerosol concentrations, oxidized biomass burning organic aerosol (BBOA) exhibiting extremely low volatility was detected throughout the study. Five wildfire plume events that had undergone between 10 hours and 10 days of atmospheric transport were sampled and a statistically significant loss of OA mass relative to CO was seen, indicating the removal of OA during long range transport. The results from this field study were also integrated with observations from the Biomass Burning Observation Project (BBOP) campaign, which characterized fresh wildfire emissions to provide a detailed depiction of the evolution of biomass burning organic aerosol over its atmospheric lifetime.

The second study took place in Fresno, a highly polluted city in the San Joaquin Valley of California impacted by residential wood burning emissions. Here, the SP-AMS was operated in

a configuration to selectively measure only black carbon (BC) containing soot particles. A persistent, multiday fog event was used as a case study to examine the aqueous-phase processing of the soot aerosol within fog droplets. Fog processing resulted in a substantial increase in BC coating thickness due to the accumulation of ammonium nitrate and secondary OA formed in the aqueous phase. Reactions occurring in cloud and fog droplets were found to play a key role on the amount and composition of coating material present on black carbon aerosol.

Finally, a SP-AMS was operated during the Tracking Aerosol Convection Interactions Experiment (TRACER) in Houston, TX in order to explore the sources of soot particles and their effects on cloud properties. Both ensemble and single particle spectra were collected in order to directly characterize the black carbon mixing state. K-means clustering analysis of the single particle measurements revealed diverse and highly variable soot particle compositions with coating-to-mass ratios spanning between 0.1 and 100. The coating material was generally hygroscopic, including oxidized OA and sulfate, suggesting that these particles may act as effective CCN.

Contents

1. Introduction

Atmospheric particulate matter (PM) impacts global climate, degrades air quality and has negative implications on human health. PM has a wide array of both natural and anthropogenic sources, which include fossil fuel and biomass combustion, industrial emissions, wind-blown dust, sea spray and volcanic activity. Additionally, oxidation of volatile organic compounds (VOCs) and inorganic gases such as SO_2 and NO_x can result in the formation of secondary aerosol. PM is often subdivided based on particle size with common delimitations of mass of particles with diameters less than 1 µm (PM_1), 2.5 µm ($PM_{2.5}$) or 10 µm (PM_{10}). The chemical composition of PM is highly dependent on the source, and therefore is temporally and geographically heterogenous. The composition of particles can include thousands of different organic species, elemental carbon (soot), inorganic salts and crustal material. The environmental effects of aerosol are dependent on both the chemical composition and the physical properties such as particle size and morphology.

Atmospheric pollutants can undergo long range transport and impact locations hundreds or thousands of kilometers from the source. Examples of this include smoke from wildfires in the Pacific Northwest degrading air quality across North America (Jaffe et al., 2020) or Saharan Dust contributing to elevated PM in the southern U.S. (Bozlaker et al., 2013). During atmospheric transport, aerosol can undergo atmospheric aging processes such as condensation, coagulation and condensed phase reactions, which can result in both chemical and physical changes to the aerosol.

Aerosol alter the global climate system by interacting with solar radiation through a variety of different mechanisms. Particles are able to scatter or absorb incident radiation, known as the aerosol radiation interactions (IPCC, 2021; Seinfeld and Pandis, 2006). Scattering results in an overall net cooling effect, while absorption produces a warming effect. The sign and magnitude of the direct effect is dependent on particle properties (composition, size) and environmental conditions (surface albedo, altitude) (IPCC, 2021). The most significant absorbing components include black carbon (BC) and

mineral dust. Additionally, aerosol can act as cloud condensation nuclei (CCN) and ice nucleating particles (INPs) thereby altering cloud properties. These processes are termed aerosol cloud interactions (Twomey, 1974; Twomey et al., 1984). Elevated aerosol number concentration can increase cloud droplet number and decrease individual droplet size resulting in an increase of cloud albedo, impeding precipitation and increasing cloud lifetime (Christensen et al., 2020; Tao et al., 2012). These effects on cloud properties result in significant uncertainty in the overall magnitude of aerosol effects on climate and their impacts weather systems.

Atmospheric pollutants, including both particles and gas-phase species, have also been connected with a wide array of adverse human health effects (Pope et al., 1995). PM has been correlated with negative health outcomes including increased rates of asthma (Liu et al., 2019) and cardiovascular (Franklin et al., 2015), pulmonary (Pope III et al., 2002) and neurological diseases (Kilian and Kitazawa, 2018). Indeed, numerous studies have found elevated morbidity and mortality during pollution episodes from wildfire smoke (Heaney et al., 2022; Magzamen et al., 2021; Reid et al., 2016). Certain types of aerosol, including black carbon and particles associated with wildfires, have been found to be particularly detrimental to human health (Aguilera et al., 2021; Janssen et al., 2011)

1.1 Aerosol Quantification with Soot-Particle Aerosol Mass Spectrometer

The Aerodyne Soot Particle Aerosol Mass Spectrometer (SP-AMS) is a powerful instrumental tool that provides online measurements of size resolved aerosol composition at high time resolution (DeCarlo et al., 2006; Onasch et al., 2012). Field deployment of the SP-AMS offers a detailed characterization of aerosol composition and properties which can be used to identify different sources and chemical pathways in the atmosphere.

Ambient aerosols are first sampled through an aerodynamic lens system to focus particles less than 1 μm into a narrow particle beam. This inlet also served to concentrate the particles relative to the gas phase by several orders of magnitude. Following this, particles are accelerated by high vacuum

through the particle time of flight (PToF) chamber. The particle velocity is a function of vacuum aerodynamic diameter (D_{va}). A chopper wheel modulates the particle beam, with time zero defined when the particle passes the chopper wheel, and the end time recorded when ions are detected at the mass spectrometer. At the end of the PToF chamber, particles are vaporized using either a resistively heated thermal vaporizer or a high-intensity laser, or both. In the first case, particles impact a resistively heated thermal vaporizer, which is held at 600°C. At this temperature, non-refractory particulate matter (NR-PM) is vaporized near instantaneously. This includes most organics, and inorganic salts such as ammonium nitrate, sulfate and chloride. The soot particle aerosol mass spectrometer (SP-AMS) is modified to also include a laser vaporizer for the measurement of refractory material such as black carbon (rBC). A 1064 nm Yd:NG laser is operated perpendicular to the particle beam. Particles that absorb at this wavelength are heated to greater than 1000K, resulting in the vaporization of refractory material as well as non-refractory material that is internally mixed with rBC. The SP-AMS can be operated in three different vaporization configurations: laser off, laser on and thermal vaporizer on (dual vaporizer), or laser only. During laser off mode, the instrument is identical to the standard HR-ToF-AMS. When operated in dual vaporizer mode, all NR-PM_1 in addition to refractory material mixed with rBC is measured. Finally, in laser-only mode, only material that is internally mixed with rBC is measured.

Following vaporization, the resulting gas-phase molecules undergo 70 eV electron impact ionization, and the ion plume is directed into the time-of-flight mass spectrometer (ToF-MS). Ions are accelerated by a voltage difference, resulting in variable speed dependent on the mass to charge (m/Q) ratio of the ion. Following the time-of-flight chamber, ions are detected with a multichannel plate (MCP) detector. The ToF-AMS can be operated either in “V-mode” or “W-mode”, termed due to the path shape of the ions. W-mode utilizes an additional reflection, increasing the ion path length and the mass spectral resolution. However, lateral broadening of the ions decreases the instrument sensitivity

in W-mode. Typical sensitivity is *m/Δm* of 2100 and 4300 at *m/z* 200 for V-mode and W-mode respectively.

The concentration of aerosol species is linearly related to the signal recorded by the AMS and quantitative measurements can be achieved with the following formula (Jimenez, 2003)

$$C_S = \frac{1}{CE_s * RIE_s * IE_{NO3} * Q} \sum I_{s,i}$$

where C_s is the mass of species s, CE_s is the collection efficiency, RIE is the relative ionization efficiency compared to nitrate, IE_{NO3} is the ionization efficiency of nitrate, Q is the volumetric flow rate and $I_{s,I}$ is the ion signal of fragments associated with species s. CE_s is associated with particle losses due to transmission through the aerodynamic lens, overlap between the particle beam and vaporizer, and particle bounce off the vaporizer (Middlebrook et al., 2012). IE_{NO3} is experimentally determined using monodispersed ammonium nitrate by comparing the AMS signal with a co-located condensation particle counter (CPC). The relative ionization efficiency (RIE) of sulfate, nitrate, ammonium, chloride and rBC are also routinely measured using chemical standards. The aerosol composition is divided into different species by use of a fragmentation table (Allan et al., 2004).

1.2 Identification of Organic Aerosol Sources

Interpretation of AMS spectra is difficult to the enormous number of different compounds present in the atmosphere. Positive Matrix Factorization (PMF) is a bilinear model commonly applied to AMS data to identify sources and chemical processes occurring in the atmosphere (Paatero, 1999; Paatero and Tapper, 1994). Specifically, PMF assumes that each mass spectrum is a linear combination of different static profiles (mass spectra) that contribute varying amounts at different times (time series). The technique is similar to chemical mass balance (CMB), however it does not require *a priori* knowledge of the factor composition. The PMF model solves the equation **X** = **GF** + **E**, where **X** is the measured organic matrix, **G** and **F** are the computed matrices representing the factor profiles and time

series respectively, and **E** is a model residual matrix. A least squares technique is used where the value *Q* is minimized

$$Q = \sum_{i=0}^{m}\sum_{j=0}^{n}\left(e_{ij}/\sigma_{ij}\right)^2$$

where e_{ij} is the value in matrix **E** and σ_{ij} is the measurement uncertainty at point *ij*. The model can be solved with a number of different algorithms, including PMF2 and multilinear engine (ME2) (Canonaco et al., 2013; Ulbrich et al., 2009).

The number of factors that adequately describe the data is chosen by the user based on mass spectral features, time dependent variations and analysis of the residual. Different ambient measurements have resolved a wide range of different factor types having distinct mass spectral characteristics, highlighting the variation of aerosol composition in the atmosphere. Commonly resolved factors include primary sources such as hydrocarbon like organic aerosol (HOA) typically related to vehicle emissions, biomass burning organic aerosol (BBOA), cooking organic aerosol (COA) and coal combustion organic aerosol (CCOA). However, the identification of specific sources of SOA is more difficult and instead SOA is typically grouped based on their oxidation level or volatility.

1.3 Objectives and Aims

This thesis describes ambient measurements of aerosol chemical composition and physical properties focused on understanding PM sources and atmospheric evolution under a range of atmospheric environments. This was done through the detailed analysis of in-situ field measurements using a soot-particle aerosol mass spectrometer coupled with statistical techniques such as PMF and K-means clustering utilized to gain insights into the submicron aerosol composition and characterize the sources and processing pathways. Chapter 2 details the measurements of highly aged wildfire emissions at the Mt. Bachelor Observatory, a remote, mountaintop site in the Pacic Northwest. This chapter discusses the changes in biomass burning organic aerosol (BBOA) physical and chemical characteristics

with extensive aging through the analysis of five plume case studies. Chapter 3 integrates these highly processed wildfire measurements with results from the 2013 Biomass Burning Observation Project (BBOP), during which fresh wildfire plumes were characterized. A comprehensive analysis of the evolution of BBOA between the time of emission and multiple days of atmospheric transport is presented. Chapter 4 discusses the effect of cloud and fog processing on the properties of black carbon containing aerosol in Fresno, CA. A unique SOA chemical signature associated with aqueous phase processing within fog droplets was identified and it was found that fog processing played a crucial role in the composition and amount of black carbon coating material at this location. Finally, Chapter 5 provides a detailed characterization of the soot particle composition and properties in Houston, TX during the DOE sponsored Tacking Aerosol Convection Experiment (TRACER). The SP-AMS was alternated between ensemble and single particle measurements, providing a direct measurement of black carbon mixing state. This provided insight into the role of BC containing aerosol on cloud formation and properties.

Chapter 2 has been published in Environmental Science and Technology, chapter 4 has been accepted to Atmospheric Chemistry and Physics, and chapter 5 has been submitted to Atmospheric Chemistry and Physics.

References

Aguilera, R., Corringham, T., Gershunov, A. and Benmarhnia, T.: Wildfire smoke impacts respiratory health more than fine particles from other sources: observational evidence from Southern California, Nat. Commun., (2021), doi:10.1038/s41467-021-21708-0, 2021.

Allan, J. D., Delia, A. E., Coe, H., Bower, K. N., Alfarra, M. R., Jimenez, J. L., Middlebrook, A. M., Drewnick, F., Onasch, T. B., Canagaratna, M. R., Jayne, J. T. and Worsnop, D. R.: A generalised method for the extraction of chemically resolved mass spectra from Aerodyne aerosol mass spectrometer data, J. Aerosol Sci., 35(7), 909–922, doi:10.1016/j.jaerosci.2004.02.007, 2004.

Bozlaker, A., Prospero, J. M., Fraser, M. P. and Chellam, S.: Quantifying the contribution of long-range saharan dust transport on particulate matter concentrations in Houston, Texas, using detailed elemental analysis, Environ. Sci. Technol., 47(18), 10179–10187, doi:10.1021/es4015663, 2013.

Canonaco, F., Crippa, M., Slowik, J. G., Baltensperger, U. and Prévôt, A. S. H.: SoFi, an IGOR-based interface for the efficient use of the generalized multilinear engine (ME-2) for the source apportionment: ME-2 application to aerosol mass spectrometer data, Atmos. Meas. Tech., doi:10.5194/amt-6-3649-2013, 2013.

Christensen, M. W., Jones, W. K. and Stier, P.: Aerosols enhance cloud lifetime and brightness along the stratus-to-cumulus transition, Proc. Natl. Acad. Sci. U. S. A., 117(30), 17591–17598, doi:10.1073/pnas.1921231117, 2020.

DeCarlo, P. F., Kimmel, J. R., Trimborn, A., Northway, M. J., Jayne, J. T., Aiken, A. C., Gonin, M., Fuhrer, K., Horvath, T., Docherty, K. S., Worsnop, D. R. and Jimenez, J. L.: Field-deployable, high-resolution, time-of-flight aerosol mass spectrometer, Anal. Chem., doi:10.1021/ac061249n, 2006.

Franklin, B. A., Brook, R. and Arden Pope, C.: Air pollution and cardiovascular disease, Curr. Probl. Cardiol., 40(5), 207–238, doi:10.1016/j.cpcardiol.2015.01.003, 2015.

Heaney, A., Stowell, J. D., Liu, J. C., Basu, R., Marlier, M. and Kinney, P.: Impacts of Fine Particulate Matter From Wildfire Smoke on Respiratory and Cardiovascular Health in California, Geohealth, doi:10.1029/2021GH000578, 2022.

IPCC: Climate Change 2021: The Physical Science Basis. Contribution of Working Group I to the Sixth Assessment Report of the Intergovernmental Panel on Climate Change, edited by V. Masson-Delmotte, P. Zhai, A. Pirani, S. L. Connors, C. Pean, S. Berger, N. Caud, Y. Chen, L. Goldfarb, M. I. Gomis, M. Huang, K. Leitzell, E. Lonnoy, J. B. . Matthews, T. K. Maycock, T. Waterfield, O. Yelekci, R. Yu, and B. Zhou, Cambridge University Press, United Kingdom and New York, NY, USA., 2021.

Jaffe, D. A., O'Neill, S. M., Larkin, N. K., Holder, A. L., Peterson, D. L., Halofsky, J. E. and Rappold, A. G.: Wildfire and prescribed burning impacts on air quality in the United States, J. Air Waste Manage. Assoc., 0(0), doi:10.1080/10962247.2020.1749731, 2020.

Janssen, N. A. H., Hoek, G., Simic-lawson, M., Fischer, P., Bree, L. Van, Brink, H., Keuken, M., Atkinson, R. W., Anderson, H. R., Brunekreef, B. and Cassee, F. R.: Black Carbon as an Additional Indicator of the Adverse Health Effects of Airborne Particles Compared with PM 10 and PM 2 . 5, Environ. Health Perspect., 119(12), 1691–1699, 2011.

Jimenez, J. L.: Ambient aerosol sampling using the Aerodyne Aerosol Mass Spectrometer, J. Geophys. Res., doi:10.1029/2001jd001213, 2003.

Kilian, J. and Kitazawa, M.: The emerging risk of exposure to air pollution on cognitive decline and Alzheimer's disease – Evidence from epidemiological and animal studies, Biomed. J., 41(3), 141–162, doi:10.1016/j.bj.2018.06.001, 2018.

Liu, Y., Pan, J., Zhang, H., Shi, C., Li, G., Peng, Z., Ma, J., Zhou, Y. and Zhang, L.: Short-term exposure to ambient air pollution and asthma mortality, Am. J. Respir. Crit. Care Med., 200(1), 24–32, doi:10.1164/rccm.201810-1823OC, 2019.

Magzamen, S., Gan, R. W., Liu, J., Dell, K. O., Ford, B., Berg, K., Bol, K., Wilson, A., Fischer, E. V and Pierce, J. R.: Differential Cardiopulmonary Health Impacts of Local and Long-Range Transport of Wildfire Smoke GeoHealth, , 1–18, doi:10.1029/2020GH000330, 2021.

Middlebrook, A. M., Bahreini, R., Jimenez, J. L. and Canagaratna, M. R.: Evaluation of composition-dependent collection efficiencies for the Aerodyne aerosol mass spectrometer using field data, Aerosol Sci. Technol., doi:10.1080/02786826.2011.620041, 2012.

Onasch, T. B., Trimborn, A., Fortner, E. C., Jayne, J. T., Kok, G. L., Williams, L. R., Davidovits, P. and Worsnop, D. R.: Soot particle aerosol mass spectrometer: Development, validation, and initial application, Aerosol Sci. Technol., doi:10.1080/02786826.2012.663948, 2012.

Paatero, P.: The Multilinear Engine—A Table-Driven, Least Squares Program for Solving Multilinear Problems, Including the n-Way Parallel Factor Analysis Model, J. Comput. Graph. Stat., 8(4), 854–888, doi:10.1080/10618600.1999.10474853, 1999.

Paatero, P. and Tapper, U.: Positive matrix factorization: A non-negative factor model with optimal utilization of error estimates of data values, Environmetrics, doi:10.1002/env.3170050203, 1994.

Pope, C. A., Dockery, D. W. and Schwartz, J.: Review of epidemiological evidence of health effects of particulate air pollution, Inhal. Toxicol., 7(1), 1–18, doi:10.3109/08958379509014267, 1995.

Pope III, C. A., Burnett, R. T., Thun, M. J., Calle, E. E., Krewski, D. and Thurston, G. D.: Lung Cancer, Cardiopulmonary Mortality, and Long-term Exposure to Fine Particulate Air Pollution, J. Am. Med. Assoc., 287(9), 1132–1141 [online] Available from: http://jama.jamanetwork.com/article.aspx?doi=10.1001/jama.287.9.1132, 2002.

Reid, C. E., Brauer, M., Johnston, F. H., Jerrett, M., Balmes, J. R. and Elliott, C. T.: Critical review of health impacts of wildfire smoke exposure, Environ. Health Perspect., 124(9), 1334–1343, doi:10.1289/ehp.1409277, 2016.

Seinfeld, J. H. and Pandis, S. N.: Atmospheric Chemistry and Physics. From Air Pollution to Climate Change, Second Edition, Wiley Interscience., 2006.

Tao, W. K., Chen, J. P., Li, Z., Wang, C. and Zhang, C.: Impact of aerosols on convective clouds and precipitation, Rev. Geophys., 50(2), doi:10.1029/2011RG000369, 2012.

Twomey, S.: Pollution and the planetary albedo, Atmos. Environ., doi:10.1016/0004-6981(74)90004-3, 1974.

Twomey, S. A., Piepgrass, M. and Wolfe, T. L.: An assessment of the impact of pollution on global cloud albedo, Tellus, 36 B(5), 356–366, doi:10.1111/j.1600-0889.1984.tb00254.x, 1984.

Ulbrich, I. M., Canagaratna, M. R., Zhang, Q., Worsnop, D. R. and Jimenez, J. L.: Interpretation of organic components from Positive Matrix Factorization of aerosol mass spectrometric data, Atmos. Chem. Phys., doi:10.5194/acp-9-2891-2009, 2009.

2. Persistent Influence of Wildfire Emissions in the Western United States and Characteristics of Aged Biomass Burning Organic Aerosols Under Clean Air Conditions

This chapter has been published in the Atmospheric Chemistry and Physics: Farley, R., Bernays, N., Ja, D. A., Ketcherside, D., Hu, L., Zhou, S. and Collier, S.: Persistent Influence of Wildfire Emissions in the Western United States and Characteristics of Aged Biomass Burning Organic Aerosols under Clean Air Conditions, Environ. Sci. Technol., doi:10.1021/acs.est.1c07301, 2022.

2.1 Abstract

Wildfire-influenced air masses under regional background conditions were characterized at the Mt. Bachelor Observatory (~2800 m a.s.l.) in summer 2019 to provide a better understanding of the aging of biomass burning organic aerosols (BBOA) and their impacts on the remote troposphere in the western U.S. Submicron aerosol (PM_1) concentrations were low (average ±1σ = 2.2±1.9 μg sm^{-3}) but oxidized BBOA (average O/C = 0.84) were constantly detected throughout the study. The BBOA correlated well with black carbon, furfural and acetonitrile and comprised above 50% of PM_1 during plume events, when peak PM_1 concentration reached 18.0 μg sm^{-3}. Wildfire plumes with estimated transport times varying from ~10 hours to >10 days were identified. The plumes showed ΔOA/ΔCO values ranging from 0.038-0.122 ppb ppb^{-1} with a significant negative relation to plume age, indicating BBOA loss relative to CO during long-range transport. Additionally, increases of average O/C and aerosol sizes were seen in more aged plumes. The mass-based size mode was approximately 700 nm (D_{va}) in the most oxidized plume that likely originated in Siberia, suggesting aqueous-phase processing during transport. This work highlights the widespread impacts that wildfire emissions have on aerosol concentration and properties, and thus climate, in the western U.S.

2.2 Introduction

Biomass burning (BB) is a major source of atmospheric aerosols and significantly impacts global climate, public health and regional air quality (IPCC, 2013; Jaffe et al., 2020; Pope and Dockery, 2006). Depending on the physical properties and chemical composition of the aerosols, they can scatter or

absorb solar radiation, act as cloud condensation nuclei and alter cloud albedo (Brown et al., 2021; Quaas et al., 2009; Shrivastava et al., 2017; Twomey, 1974). BB is a large source of both primary organic aerosols (POA) and volatile organic compounds (VOCs) that can act as precursors for secondary organic aerosols (SOA) (Gilman et al., 2015; Hallquist et al., 2009; Jen et al., 2019). BB is also a large source of brown carbon (BrC), an aerosol component that is able to absorb sunlight in the visible wavelengths and positively influence global climate forcing (Adler et al., 2019; Andreae and Gelencsér, 2006; Bond and Bergstrom, 2006).

Wildfires are a highly variable and "uncontrollable" source of BB emissions that cause haze in both pristine areas and urban centers (Jaffe et al., 2008, 2020). In the western US, wildfires are becoming increasingly prevalent, and their emissions have been tied to elevated regional $PM_{2.5}$ concentrations and high pollution episodes that violated National Ambient Air Quality Standards (NAAQS) (Briggs et al., 2016; Jaffe et al., 2020; McClure and Jaffe, 2018b; Sedlacek et al., 2018; Westerling et al., 2006; Zhang et al., 2018a; Zhou et al., 2017). Additionally, studies are continuing to show that wildfire plumes are able to influence aerosol loading and atmospheric chemistry up to thousands of kilometers from the source (Baars et al., 2019; Hung et al., 2020; Schill et al., 2020; Teakles et al., 2017). Furthermore, OA that has undergone atmospheric processing has been found to be more detrimental to human health (Tuet et al., 2017; Wong et al., 2019). A deeper understanding of the chemical and optical properties of wildfire emissions and the evolution of BB aerosols in the atmosphere will help constrain atmospheric chemical transport models and global climate models (Barbero et al., 2015; Shrivastava et al., 2017; Spracklen et al., 2009; Zhang and Jaffe, 2017).

Biomass burning organic aerosols (BBOA) can have a wide range of volatility, with the volatility generally decreasing with increased atmospheric processing (Huffman et al., 2009; Jimenez et al., 2009; Zhou et al., 2017). The oxidation of VOCs and intermediate volatility organic compounds (IVOCs) emitted from BB has been seen to form low volatility products which can increase SOA production and

the atmospheric lifetime of the aerosols (Donahue et al., 2011; Lim et al., 2019; Palm et al., 2020). The exact properties of BBOA are highly dependent on burn conditions, fuel type and the magnitude of atmospheric processing (Coggon et al., 2016; Collier et al., 2016; Cubison et al., 2011; Gilman et al., 2015; Kleinman et al., 2020; Liu et al., 2014; May et al., 2014; Zhou et al., 2017). While many previous studies have investigated the composition of fresh fire emissions in laboratory and ambient conditions, as well as the transformation of BBOA in fire plumes over the course of the first hours of atmospheric aging (Cappa et al., 2020; Kleinman et al., 2020), only a few have investigated highly processed wildfire emissions at remote locations such as islands (Dzepina et al., 2015; Zuidema et al., 2018), high altitude locations (Du et al., 2015; Wang et al., 2017; Zhang et al., 2018b) and the remote troposphere (Schill et al., 2020; Schurman et al., 2015). These studies have found that long range transport of BB emissions can cause episodic increases of aerosol concentrations and that multiple days of aging may significantly influence ambient BB aerosol characteristics. However, it remains poorly understood how wildfire emissions and atmospheric aging processes affect the chemical composition and physical properties of background aerosols in pristine environments, and what impacts these have on climate.

In the present study, we provide an overview of the physical and chemical properties of aerosol particles and trace gases studied using a suite of real-time instruments at the Mt. Bachelor Observatory (MBO), a remote, high altitude site in the American Pacific Northwest (PNW) during the summer of 2019. MBO has been operated as an atmospheric chemistry observatory since 2004 (Zhang and Jaffe, 2017) and due to its remote location and minimal anthropogenic influence, is an ideal site for measurements of wildfire plumes ranging from locally emitted to long-range transport events from Alaska and Asia (Briggs et al., 2016; Reidmiller et al., 2009; Weiss-Penzias et al., 2006; Zhang and Jaffe, 2017; Zhou et al., 2017). During this study, hereafter named MBO19, we show that regionally transported BBOA is an important component of submicrometer aerosols (PM_1) even during periods of

relatively low fire activity and aerosol loading. In addition, we utilize the variety of BB plume sources to understand how aerosol properties change as a function of physical and photochemical age.

2.3 Methods

2.3.1 Sampling site

An intensive measurement campaign was conducted at the MBO, located at the summit of Mt. Bachelor (43.981°N 121.691°W, 2764 m a.s.l) from 1 August to 10 September 2019. Mt. Bachelor is an isolated volcanic peak approximately 31 km east of the city of Bend, Oregon (population 80,000). Few wildfires were active upwind of MBO during the sampling period, although there were fires throughout western North America (Fig. A1). In comparison, heavy wildfire plumes originating in Northern California and Southern Oregon were frequently sampled during the summer 2013 Biomass Burning Observation Period (BBOP) campaign at MBO (Fig. A1-2) (Collier et al., 2016; Zhang et al., 2018a; Zhou et al., 2017).

Boundary layer dynamics play an important role in the diurnal variation of aerosol composition at MBO. During daytime, upslope air can bring modified boundary layer (MBL) air masses to the sampling site, while at night the site is influenced by free tropospheric (FT) air masses (Zhang and Jaffe, 2017; Zhou et al., 2019). These different regimes can be differentiated based on ambient water vapor concentrations with values greater than 5.23 and 4.60 g/kg corresponding to MBL conditions during August and September, respectively (Zhang and Jaffe, 2017).

2.3.2 Real-time Measurements

Size resolved aerosol composition and volatility were studied at 2-minute time resolution using a Soot Particle Aerosol Mass Spectrometer (SP-AMS; Aerodyne Research, Inc.) downstream of a custom-built, automated thermodenuder (TD, Fig. A3). The SP-AMS and its use in studying wildfire smokes are described in detail elsewhere (Avery et al., 2020; Kleinman et al., 2020; Onasch et al., 2012). Briefly, the instrument operates by focusing aerosols through an aerodynamic lens with a size cutoff of 1 micron

aerodynamic diameter (PM_1). Particles are then sized prior to colliding with a 600°C resistively heated tungsten vaporizer. The resulting gaseous molecules are ionized by 70eV electron impact and are detected using a high resolution time-of-flight mass spectrometer (Canagaratna et al., 2007; DeCarlo et al., 2006). In this study, the SP-AMS was operated only in the lower mass resolution (m/□m = 2500) and higher sensitivity "V-Mode" for increased signal-to-noise (S/N) ratio, allowing the bulk ensemble mass spectra for non-refractory (NR) PM_1 to be calculated (DeCarlo et al., 2006). This includes the quantification of organics, the ammonium salts of sulfate, nitrate and chloride. The SP-AMS also allows for the simultaneous quantification of refractory black carbon (rBC) using an intracavity laser vaporizer (Avery et al., 2020; Onasch et al., 2012). A thermodenuder based on the design described in Fierz et al., (2007) was installed upstream of the SP-AMS to quantify aerosol volatility (Fierz et al., 2007). Additional information regarding SP-AMS operation and thermodenuder temperature settings is given in appendix A1.2 and Figure A3-5.

Information on additional real-time instrumentation deployed during this study is provided in SI section 1.2.3. Briefly, speciated VOC measurements were made every 1 minute with a Proton Transfer Reaction Time of Flight Mass Spectrometer (PTR-ToF-MS 4000, Ionicon Analytik, Austria), with the mass resolution up to m/Δm 4000(Müller et al., 2014). The PTR-ToF-MS background was checked every hour. During the campaign, it was calibrated every 2 days by the dynamic dilution and subsequent addition of 25 distinct VOCs including furfural and acetonitrile from gas standard mixtures(Permar et al., n.d.). A scanning mobility particle sizer (SMPS) consisted of a TSI 3082 electrostatic classifier with a TSI 3776 water-based condensation particle counter collected number distribution at a 5 minute time resolution between 14 and 615 nm. In addition, other data used in this study include CO (Picarro G2302 cavity ring-down spectroscopy) and submicrometer aerosol scattering coefficients (σ_{sp}) at wavelengths 450, 550, and 700 nm (TSI Model 3563 integrating nephelometer). CO and σ_{sp} data are reported in 5-min averages. The σ_{sp} values were corrected for drift and scattering truncation according to the scheme laid

out by Anderson and Ogren (1998) (Anderson and Ogren, 1998). Additional calibration details are provided in Briggs et al (2016) (Briggs et al., 2016). In this study, we focused on σ_{550nm}, which correlated well ($r^2 > 0.96$) with both σ_{700nm} and σ_{450nm}.

2.3.3 SP-AMS Data Analysis and Positive Matrix Factorization Analysis

SP-AMS results were analyzed with the SQUIRREL (v. 1.53A) and PIKA (v. 1.23A) software packages in Igor Pro (v. 8 Wavemetrics, Lake Oswego, OR). All mass concentrations were determined using the high resolution mass spectral (HRMS) data and are reported in STP conditions (273.15K, 101325Pa), notated with "μg sm^{-3}". Additional details regarding the SP-AMS ionization efficiency calibration and treatment of gas-phase interference are given in the SI Section 1.2.1. The SP-AMS limit of detection (LOD) was calculated as the three times the standard deviation during an extremely clean period when the average (±1σ) SMPS mass concentration was 0.013 (±0.017) μg sm^{-3}. The LOD was 139, 18, 18, 9, 25, 53 ng/m^3 for organics, nitrate, sulfate, chloride, ammonium and black carbon, respectively, for an averaging time of 2 minutes. These LOD values are higher than expected due to the decreased S/N caused by the installation of a radio frequency filter on the SP-AMS to reduce signal interference from nearby equipment including cell phone transmitters. The molar ratios of elements (O/C and H/C) for the bulk OA were calculated using the "Improved Ambient" method (Canagaratna et al., 2015b).

Positive matrix factorization (PMF) (Paatero and Tapper, 1994) was used to decompose the SP-AMS HRMS data using the PMF evaluation tool (PET) (Ulbrich et al., 2009) into a set of static factors and their time dependent contributions. The association of individual factors with specific emission sources or atmospheric processes was examined through analyses of the spectra, temporal variation patterns, and comparison with external tracers (Zhang et al., 2011). The time series of organic ions, major inorganic ions and TD data during both the laser on and laser off periods were included within the PMF analysis to decrease ambiguity in the solution space and provide insight into the volatility of each factor (Sun et al., 2012; Zhou et al., 2017). A detailed description of the preparation, analysis, and evaluation of

PMF solutions is given in appendix A1.3 and Figures A6-8. The final PMF solution consists of a low volatility oxygenated OA (LV-OOA), a semi-volatile oxygenated OA (SV-OOA) and a BBOA.

2.4 Results and Discussion

2.4.1 Aerosol Characteristics at MBO during Summer 2019

The concentrations of different aerosol components varied dynamically at MBO throughout the campaign (Figure A9). Generally, low PM_1 concentrations were seen during summer 2019, ranging from < 0.14 μg sm^{-3} to 18.0 μg sm^{-3} with an average (± 1σ) of 2.22 (± 1.86) μg sm^{-3}. Aerosol loading was on average dominated by organics (82.1%), followed by sulfate (11.3%), ammonium (4.1%), rBC (2.4%) and nitrate (2.0%) with chloride and potassium at or below LOD for most the campaign. The meteorology was typical for summer at a high-altitude site: the temperature ranged from -1.6°C to 20.7°C (average ± 1 of 12.0 ± 4.5°C) and RH varied from 7.4% to 100% (52 ± 23%). Although the weather was typically cool and dry, there were periods when MBO was in clouds and rain, which coincided with the lowest PM_1 concentrations.

MBO has been used extensively for trace gas and aerosol measurements since 2004, allowing for data comparisons with previous campaigns. Specifically, the results from 2019 are compared to the HR-AMS data collected at MBO during the BBOP in summer 2013, which is discussed in previous publications (Briggs et al., 2016; Collier et al., 2016; Zhang et al., 2018a; Zhou et al., 2017, 2019). Substantially higher PM_1 concentrations (up to 210 μg sm^{-3}) were sampled in 2013(Zhou et al., 2017) whereas the MBO19 measurements allow for detailed chemical characterization of discrete BB plumes that are significantly more aged and diluted than those sampled in 2013. The average PM_1 concentration during MBO19 is consistent with low loading periods observed during BBOP (NR-PM_1 = 2.8 ± 2.8 μg sm^{-3}), as well as other high-altitude, background sites around the world (3.8 ± 3.4 μg sm^{-3}) (Zhou et al., 2019).

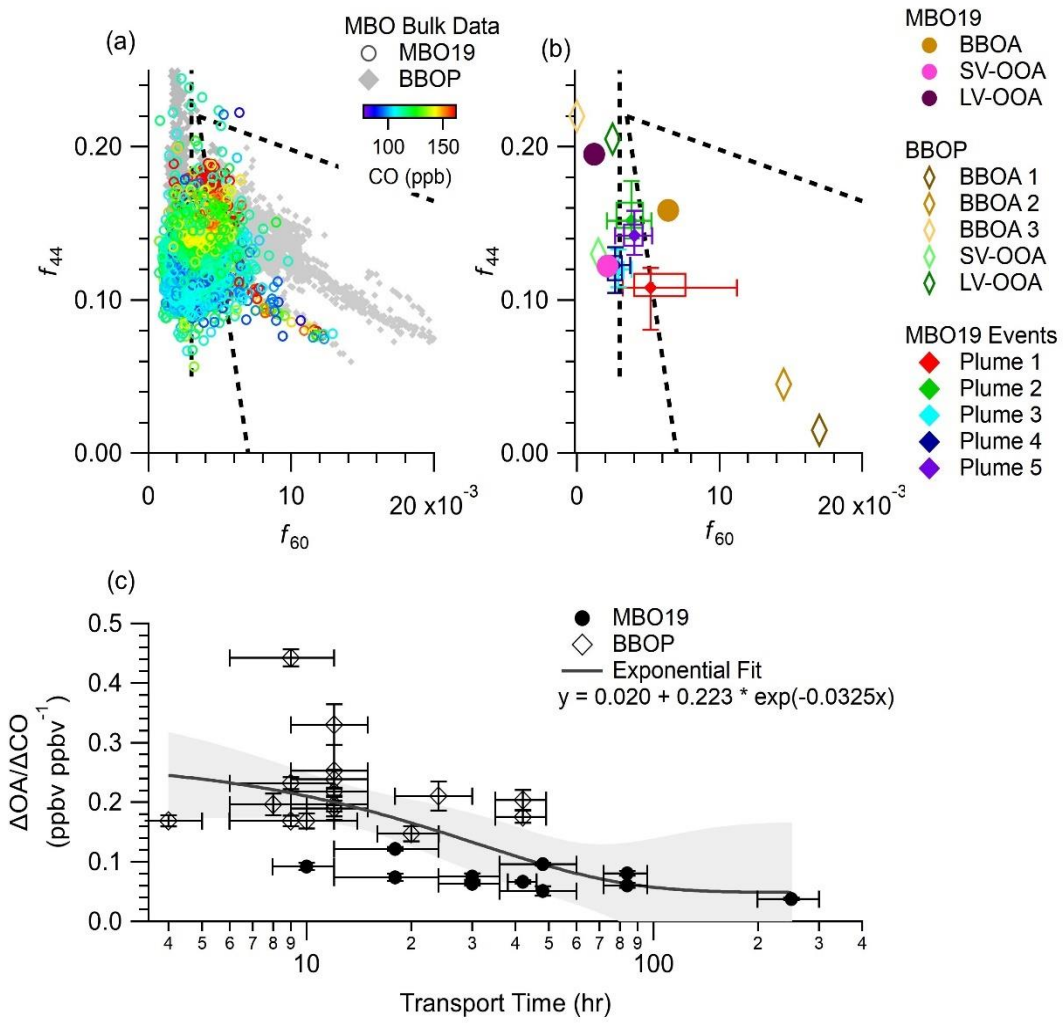

Figure 2.1: Overview of BBOA characteristics and the influences of atmospheric aging based on observations made during MBO19 and BBOP, respectively. Scatterplots of f_{44} and f_{60} for (a) bulk OA data and (b) OA factors resolved through PMF analysis of the SP-AMS data. (c) Changes in ΔOA/ΔCO with estimated transport times of wildfire plumes. The MBO19 data in (a) is colored by CO concentration. The dashed black lines in (a) and (b) represent the background f_{60} value of 0.3% and the boundaries set for ambient BBOA in Cubison et al (2011). Data points with OA < 1 μg sm^{-3} were removed to reduce noise. The f_{44} and f_{60} values in the five wildfire plume events identified during MBO19 are indicted by the colored boxes in (b), with the box bounds representing the 25th and 75th percentiles, and the error bars representing the 10th and 90th percentile. Points in (c) are the MBO19 wildfire plume events and BB plumes identified in Collier et al. (2016). The whiskers indicate the uncertainty in transport time and 1σ of the orthogonal distance regression between OA and CO. The solid line in (c) is the best fit of all the points with the gray area representing the 95th confidence interval. The fitting equation in provided in the legend of (c).

A commonly used HR-AMS tracer for BB is the signal at *m/z* 60 over total OA signal, known as f_{60}

(Cubison et al., 2011). In this study, over 95% of signal at *m/z* 60 is from the $C_2H_4O_2^+$ ion (*m/z* = 60.021), a fragment primarily generated from anhydrous sugars (e.g., levoglucosan) during cellulous combustion (Aiken et al., 2010; Alfarra et al., 2007; Schneider et al., 2006). For ambient OA, f_{60} < 0.3% generally represents no BB influence, while f_{60} > 1% represents prominent BB influence (Cubison et al., 2011). The campaign average of f_{60} was 0.29 ± 0.12% with events ranging up to 1.2% (Fig. 2.1 and Fig. A12). The periods with elevated f_{60} also showed an increase in CO concentrations (up to 180 ppbv; Fig. A9d), aerosol absorption and scattering (up to 6 Mm^{-1} and 70 Mm^{-1}, respectively at 530nm), and PM_1 (up to 18.0 µg sm^{-3}; Fig. A9c). Additionally, there were elevated concentrations of rBC, acetonitrile and furfural, all of which are BB tracers (Fig. A9g) (Coggon et al., 2016; Müller et al., 2016). The relative abundance of anhydrous sugars in BB aerosols, as represented by f_{60}, has been found to decrease during atmospheric transport due to evaporation or decay of BB POA and concurrent production of BB SOA (Cubison et al., 2011). Indeed, the f_{60} values during this campaign are generally lower than in fresh wildfire plumes and are consistent with other aged BB plumes sampled during BBOP and at other remote locations (Collier et al., 2016; Cubison et al., 2011; Forrister et al., 2015; Zhou et al., 2017). Figure 2.1a-b compare the aerosol composition from MBO19 and BBOP in the f_{44}-f_{60} space. f_{44}, defined analogously to f_{60}, is dominated by the CO_2^+ fragment, correlates with bulk aerosol O/C ratio, and represents the level of oxidation of OA (Ng et al., 2010). The f_{44}-f_{60} space is a common technique to investigate the effect of aging on the properties of BBOA with more aged/oxidized BBOA moving towards a lower f_{60} and a higher f_{44} (Cubison et al., 2011; Ortega et al., 2013). During MBO19, OA spanned a wide range of f_{60} and f_{44} values, indicating the influence of BB as well as the presence of additional, non-BB sources at the site (Fig 2.1a and A11). CO is a well-known tracer for BB emissions. Although photo-oxidation of biogenic VOCs can be a significant source of CO in remote regions as well, the strong correlations between CO and BB tracers such as benzene, acetonitrile and rBC suggest that the CO enhancements at MBO were largely due to BB influence. Figure 2.1a shows that elevated CO

concentrations correspond with high f_{60} values as well as high f_{44} values, suggesting that BB is an important source of highly oxidized aerosols. Furthermore, the OA data from the MBO19 and BBOP campaigns overlapped in the f_{60} - f_{44} space (Fig. 2.1a), suggesting similarities between the BBOA sources and atmospheric aging processes. However, BBOA in MBO19 was overall significantly more aged, In addition, Figure 2.1c shows a negative correlation between the enhancement ratio of OA relative to CO (ΔOA/ΔCO) in wildfire plumes and plume transport time, which highlights the impacts of atmospheric aging on BBOA characteristics (see detailed discussions in Section 3.4). Non-soil potassium salts (ns-K) have been identified as a tracer for BB in previous field studies (Aiken et al., 2010; Andreae, 1983; Ma et al., 2003; Park et al., 2007). SP-AMS is able to detect potassium through both surface ionization on the tungsten vaporizer (Drewnick et al., 2015) and laser vaporization of potassium salts internally mixed with rBC (Lee et al., 2016; Onasch et al., 2012). However, concentrations of K^+ were low and noisy throughout this campaign, which is consistent with previous studies finding minimal K^+ enhancements in wildfire plumes in this region of the PNW (Maudlin et al., 2015; Zhou et al., 2017). The reason for this lack of enhancement is unclear, however previous studies have found K^+ emission dependent on fuel type (Chen et al., 2007).

2.4.2 Organic Aerosol Sources at MBO and Biomass Burning Influences

In order to evaluate the influence of transported wildfire plumes on aerosol chemistry at MBO, PMF analysis was performed and resolved three meaningful factors. They include a BBOA (O/C = 0.84, 18% of OA), a semi-volatile oxygenated OA (SV-OOA) (O/C = 0.67, 76% of OA), and a low volatility oxygenated OA (LV-OOA) (O/C = 1.25, 6% of OA). The factor mass spectra and volatility thermal profiles are shown in Figure 2.2, and the time series and diurnal profiles are shown in Figures A9 and A10. The

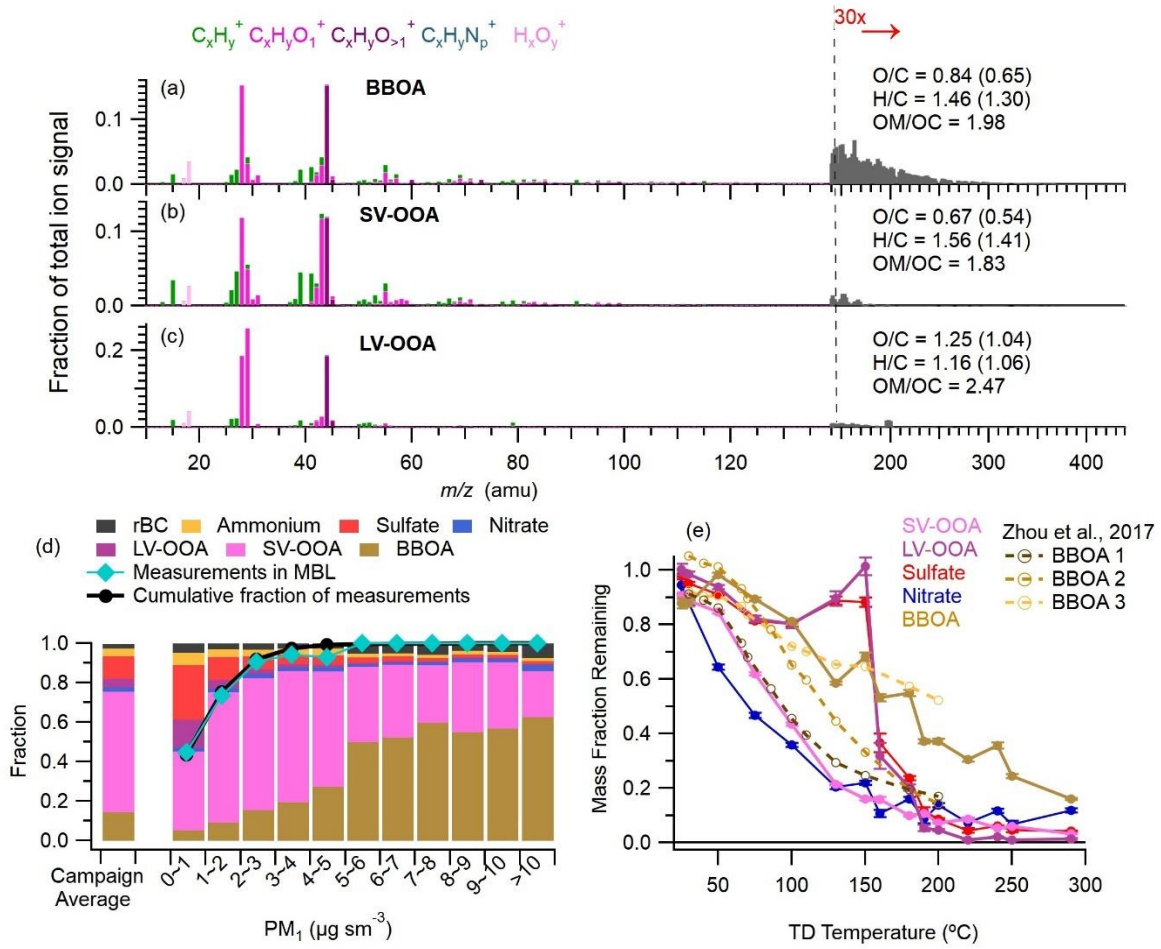

Figure 2.2: (a-c) Spectra of OA factors colored by ion family. HRMS ions are included for *m/z* <140, and UMR ions for m/z >140. "Improved Ambient" elemental ratios for each factor are denoted in the legend, with the "Aiken Ambient" value in parenthesis. (d) Fractional contribution of each species as a function of total PM_1 loading. (e) Volatility profiles of OA factors, sulfate and nitrate. Error bars show the standard deviation of the calculated slope. BBOA factors derived in Zhou et al., 2017 are also included for reference in (e).

time series of the BBOA factor correlated with rBC (r^2 = 0.52) and showed sporadic but large enhancements that are consistent with transported BB plumes (Fig. A9e). The factor was moderately oxidized with an O/C of 0.84 and an f_{60} value of 0.64%. The MBO19 BBOA is situated between the moderately oxidized BBOA-2 and the highly oxidized BBOA-3 resolved during BBOP in the f_{44}-f_{60} space (Fig 2.1b and A10). The volatility profile of the MBO19 BBOA also falls between those of BBOA-2 and BBOA-3 (Fig. 2.2e). These results highlight the fact that the oxidized BBOA observed at MBO contains

extremely low volatility species, e.g., 16% of the MBO19 BBOA mass was found to remain in the particle phase at TD temperature as high as 280°C.

The variation of BBOA concentration correlated poorly with ambient water vapor, signifying that there was wildfire influence on aerosol composition within both the MBL and the FT (Fig. 2.3). BB sources are almost exclusively located within the MBL, but large wildfires are able to inject aerosols into the FT, where the rate of deposition decreases and long range transport of aerosols is facilitated (Baars et al., 2019). This suggests that BBOA sampled within the FT is likely more heavily processed. In addition, since fires dominated by flaming combustion have larger plume injection heights and are more likely to penetrate the FT (Martin et al., 2010), plumes that have undergone long range transport may be more likely to have been emitted by fires with high modified combustion efficiency (MCE) characteristic of flaming combustion. The majority of the OA mass seen during MBO19 (76%) was contributed by the moderately oxidized SV-OOA factor (O/C = 0.67). There was a strong association of high concentrations of SV-OOA with higher water vapor values, occurring when MBO resided within the MBL (Fig. 2.3) and the diurnal trends of the SV-OOA concentration and water vapor are similar (Fig. A10b). Based on the correlation with gas-phase oxidation products such as methanol (r^2 = 0.82), methyl ethyl ketone (r^2 = 0.75) and formic acid (r^2 = 0.73), as well as significant contribution from $C_xH_y^+$ fragments in the HRMS (37% of the OA signal) and a high $C_2H_3O^+$ to CO_2^+ ratio of 0.99, this factor is likely primarily composed of biogenic SOA (Kiendler-Scharr et al., 2009; Setyan et al., 2012). The increased concentration of SV-OOA between 11:00 and 20:00 likely represents up-slope flow of BL-influenced air that was enriched with fresh SOA produced through daytime photochemical processes of regional biogenic VOCs. Finally, the LV-OOA factor was highly oxidized (O/C = 1.25) with significant contribution from CO_2^+ and CHO^+ ions in the HRMS (Fig. 2.2c). This factor represents a highly oxidized, regional background aerosol and accounts

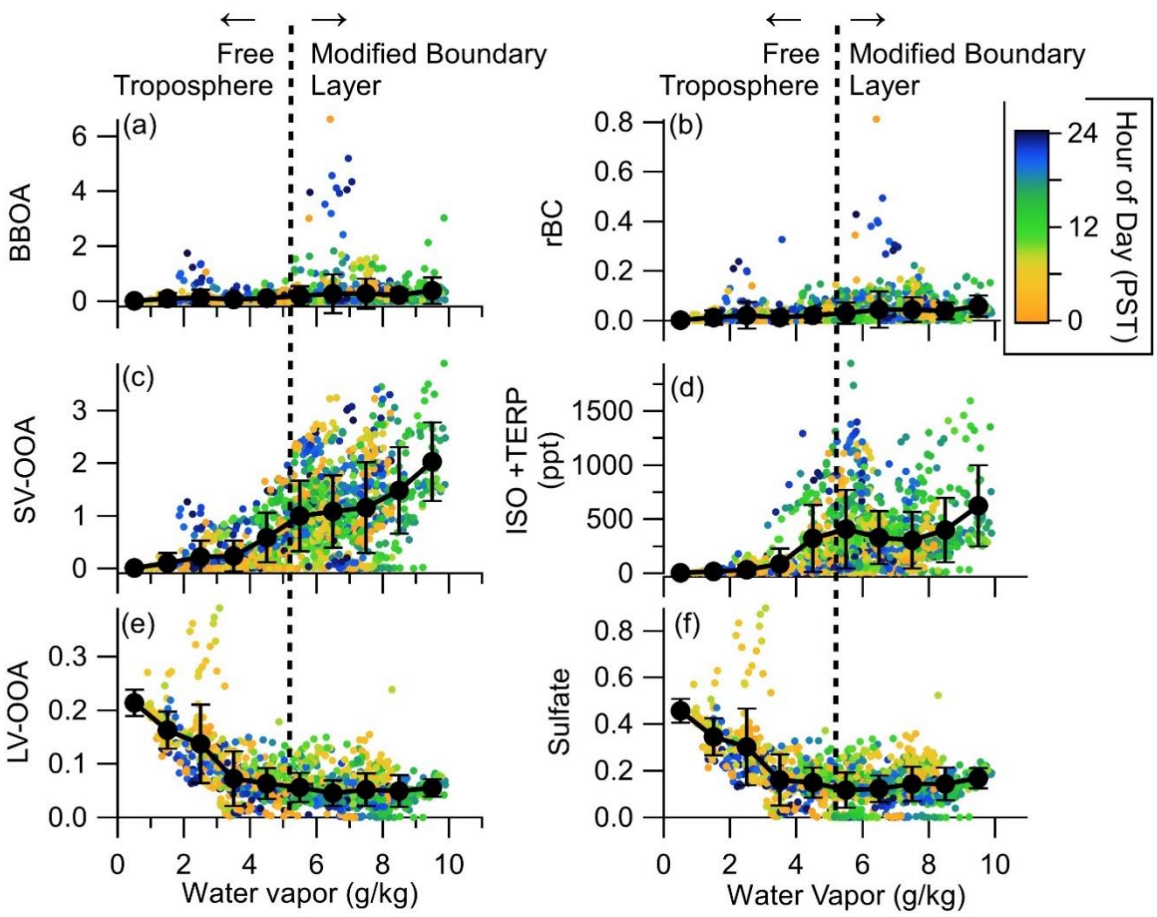

Figure 2.3: Concentration of species as a function of water vapor, colored by time of day. Solid black lines indicate the mean concentration within each water vapor mixing ratio bin, with errors bars indicating 1 standard deviation. The dashed line indicated the cut off between the free troposphere and the modified boundary layer(Zhang and Jaffe, 2017). ISO+TERP shows the sum of isoprene and monoterpenes.

for 6% of OA during MBO19. Additional details of the PMF solutions are described in SI 1.3.2.

The composition of PM_1 varied across the range of total PM_1 concentrations (Fig. 2.2d). At very low PM_1 loadings (< 1 μg m^{-3}), sulfate and LV-OOA together made up 41% of the PM_1 mass, with BBOA contributing only 5%, although there were periods with sulfate contributing up to 80% of total PM_1. Higher LV-OOA and sulfate concentrations were mostly seen at low water vapor values, primarily at night, when FT air masses were sampled (Fig. 2.3). This is an indication that sulfate aerosols and highly oxidized OA were enhanced in the regional FT, a finding that is consistent with previous observations at MBO (Zhou et al., 2019). As the PM_1 loading increased, the fractional contribution from BBOA increased

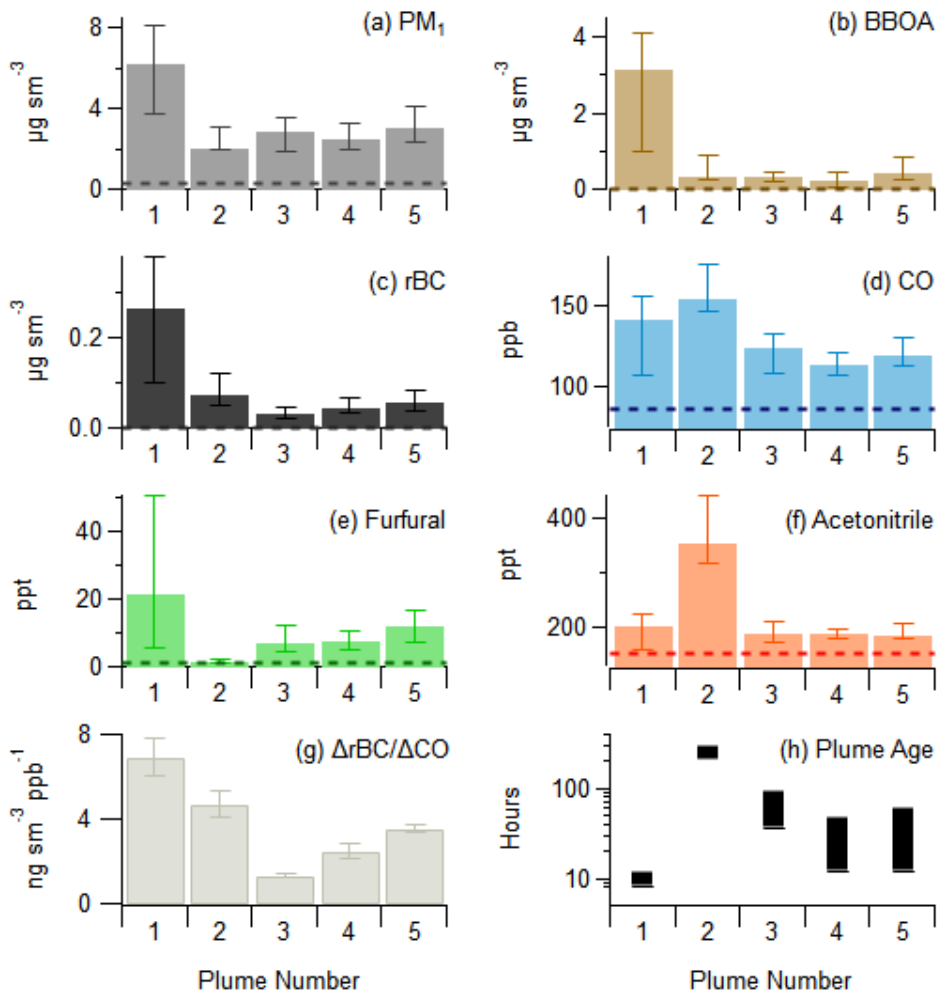

Plume Number	Duration (hr)	Probable Source Location	Approximate Distance to Source (km)
1	8	Milepost 97 fire 42.91, -123.27	180
2	14	Siberia	>4000
3	70	Northern California	250-350
4	19	Northern California	220-500
5	48	Northern California	150-540

Figure 2.4: (a-f) Median concentration of key particle and gas phase species. Dashed lines represent the background concentrations of each species during the campaign, calculated as the 10th percentile of the species throughout the campaign. (g) rBC concentration normalized to CO. (h) Plume age estimated from HYSPLIT back trajectory. Whiskers indicate the 25th and 75th percentile during each plume except for (g) where whiskers indicate 1σ of the orthogonal distance regression between the species. The transport time shown in (h) spans between the closest and furthest fire detection that the plume passed over. The table shows the duration of the plume event at MBO and likely sources of each plume event.

and contributions from sulfate and LV-OOA decreased. At $PM_1 > 5$ μg m^{-3}, BBOA accounted for 50-62% of PM_1 mass (Fig. 2.2d). These results highlight the important influences that wildfire emissions have on aerosols in the remote region of PNW, even under relatively clean air conditions.

2.4.3 Case Studies on Aged Wildfire Plumes at MBO

The location of MBO gives us a unique opportunity to sample BB influenced air masses that had undergone substantial atmospheric processing, and provides a glimpse into how atmospheric processing may influence the properties of aged BBOA. During this campaign, five distinct BB plume events (see shaded regions in Figure A9) were identified in a similar fashion as previous studies at MBO (Baylon et al., 2015). Specifically, plume events were defined as time periods satisfying the following conditions (1) CO > 110ppb and $\sigma_{550nm} > 20$ Mm^{-1} and (2) r^2 between CO and $PM_1 > 0.6$. Overall, the plume periods also showed increased PM_1 concentrations, dominated by OA, and elevated BBOA and rBC concentrations relative to the non-plume periods supporting their identification as biomass burning plumes (Fig. 2.4). The average HRMS of the bulk OA for each plume event is shown in Figure A16 and additional details are included in Figure A17.

Plume event 1 showed the highest PM_1 loadings with an average of 5.8±3.1 μg sm^{-3} and the BBOA factor making up 52% of the total mass (Fig. 2.4). HYSPLIT back trajectories show the sampled air mass passing over the Milepost 97 fire (42.913, -123.268) approximately 10 hours prior to reaching MBO (Fig. A18). This makes it a useful example for regionally emitted BBOA that has undergone relatively limited atmospheric processing. Indeed, this period appears to contain reasonably fresh BBOA with the f_{60} reaching 1.25% and $f_{>100mz}$ reaching 14.7%. The average HRMS during this period showed high contribution from the $C_xH_y^+$ family, lower f_{44} and O/C of 0.45 (Fig. A16). In contrast, plume event 2 showed significantly more oxidized aerosols (O/C = 0.69), a smaller f_{60} (0.50%), and a lower $f_{>100mz}$ (10.4%). It was characterized by extremely low water vapor mixing ratio (3.52±0.99 g/kg), and was the only plume that was sampled within the FT. Back trajectory analysis of this event indicates it was

transported from a series of large fires in Siberia (Fig. A19). Plume 2 also showed enhancement of sulfate and LV-OOA compared to the other plumes, which is consistent with highly aged aerosols transported within the FT (Fig. A17). Events 3-5 represent BB plumes originating from active wildfires in Northern California with transport times estimated at 12-96 hours (Fig. A19-21). Events 3 and 4 show f_{60} values of 0.30% and 0.25%, respectively, close to the background f_{60} values (0.3% ± 0.06%) seen for ambient OA (Cubison et al., 2011), likely due to mixing with fresh, biogenic SOA. Indeed, the OA of events 3 and 4 are significantly less oxidized than the BBOA-3 factor observed during BBOP, which also has f_{60} < 0.3% (O/C = 0.58 and 0.57, respectively, vs. O/C = 1.06 for BBOA-3). Despite these characteristics, events 3 and 4 show enhancements of all other BB tracer species, confirming the influence from BB emissions (Fig. 2.4). The OA within plume event 5 also showed characteristics of aged BBOA, with an O/C of 0.59 and an f_{60} of 0.39%.

The influence of plume processing on the concentration of gas-phase species is complex, and shows significant variation between events. While both CO and acetonitrile were enhanced considerably during all the plume periods, furfural was elevated only in less aged plumes (Fig. 2.4e-f). This is because CO and acetonitrile are fairly inert in the atmosphere with a lifetime longer than 1 month (de Gouw et al., 2003; Jiang et al., 2020), whereas furfural reacts quickly with hydroxyl and nitrate radicals in wildfire plumes, thus may show lower enhancement in aged emissions. Indeed, as displayed in Fig. 2.4e and 4h, the average enhancement of furfural concentration in individual events anticorrelates with plume age. The very low furfural concentration in plume 2 is consistent with the long-range transport and extensive atmospheric aging of the smoke originated from Siberia. Acetonitrile had the highest concentrations in event 2 and the smaller enhancements above the background within the other plume events may be due to either an elevated background concentration throughout the PNW due to the long lifetime, or differing combustion conditions and fuel types at the different fires (Chen et al., 2010; Roberts et al., 2020)

The enhancement of rBC relative to the enhancement of CO (ΔrBC/ΔCO) can be used as an indicator of the combustion efficiency of the BB source with increased ΔrBC/ΔCO occurring during flaming combustion (Kondo et al., 2011; May et al., 2014; Pan et al., 2017). During each plume event, rBC showed moderate correlations with CO (r^2 ranging from 0.25 to 0.58) and the ΔrBC/ΔCO values were consistent with previous measurements of fresh and transported BB emissions (Kondo et al., 2011; Selimovic et al., 2018). The highest ΔrBC/ΔCO were measured during plume events 1 and 2, suggesting that these fires had more influence from flaming conditions. However, it is also possible that ΔrBC/ΔCO decreased during transport by two different pathways. First, rBC may be removed via deposition during long range transport. This is most relevant to plume event 2 due to the possibility of wet deposition and cloud processing. Second, mixing of the BB plumes with CO produced from the oxidation of biogenic VOCs may enhance the background CO concentration. This could explain the lower values seen in plume events 3 and 4, which were most influenced by biogenic sources.

The size distributions during each plume events (Figure 2.5 and A23) can also provide insight into the processing history of the aerosols. Laboratory studies show that the mass weighted size distributions of fresh BB aerosols are typically small (D_{va} <100 nm) but quickly grow through condensation and coagulation over the course of aging (Grieshop et al., 2009; Zauscher et al., 2013). In addition, at urban locations with intense residential wood burning, the mass-based size distribution of BBOA was found to be broad, presenting a smaller mode peaking between 150 – 200 nm and a larger mode peaking between 400 - 500 nm (Ge et al., 2012b; Young et al., 2016). Plume events 1 and 5 both showed single modes, peaking at 400 nm and 500 nm, respectively, which is consistent with aged BBOA. This highlights the rapid growth of aerosols during the atmospheric transport of BB plumes. Event 2 also showed a single mode, but it peaks at 700nm, suggesting more pronounced aqueous-phase processing during transport. This is also consistent with previous studies at MBO that have found BB plumes transported from Siberia have a larger size mode (Laing et al., 2016). Interestingly, event 2 shows the

smallest number-based size mode at 90nm (Fig. 2.5a). It is likely that this mode represents free tropospheric sulfate aerosol formed through new particle formation, a process that has been previously recorded at MBO (Zhou et al., 2019). Plume events 3 and 4 showed broad size distributions, between 250-500nm, which can be explained by the mixing of BBOA with smaller biogenic SOA.

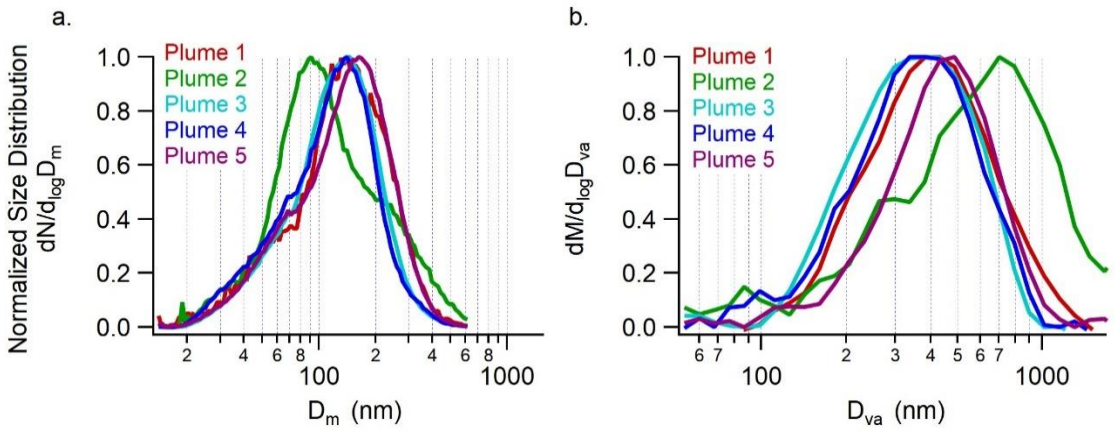

Figure 2.5: (a) Number-based size distribution of PM_1 measured by SMPS and (b) Mass-based size distribution of organic aerosols measured by SP-AMS. Distributions are averaged for the duration of each plume.

2.4.4 Evolution of Aerosol Properties in Aged Wildfire Plumes

The plume events identified during MBO19 allow for a quantitative analysis of the effect of prolonged aging on BB aerosol properties. Events 3-5 were further divided to optimize the correlations between OA and CO, as well as toluene and CO. For each event, the physical plume age was estimated from the HYSPLIT model and the photochemical age was determined based on the decay of toluene relative to CO (ΔToluene/ΔCO) or benzene (ΔToluene/ΔBenzene). The correlations between toluene and CO were strong during events 1, 3, and 4, with r^2 ranging from 0.79-0.95 (Fig. A24). There was no enhancement of toluene during event 2 and therefore an r^2 of 0. Although toluene signal was elevated during event 5, it had a negligible correlation with CO. The reason is unknown, but could be due to the mixing of fresh and aged plumes or influence from anthropogenic emissions, therefore, event 5 was excluded from further analysis. Generally, ΔToluene/ΔCO, ΔToluene/ΔBenzene and physical age were

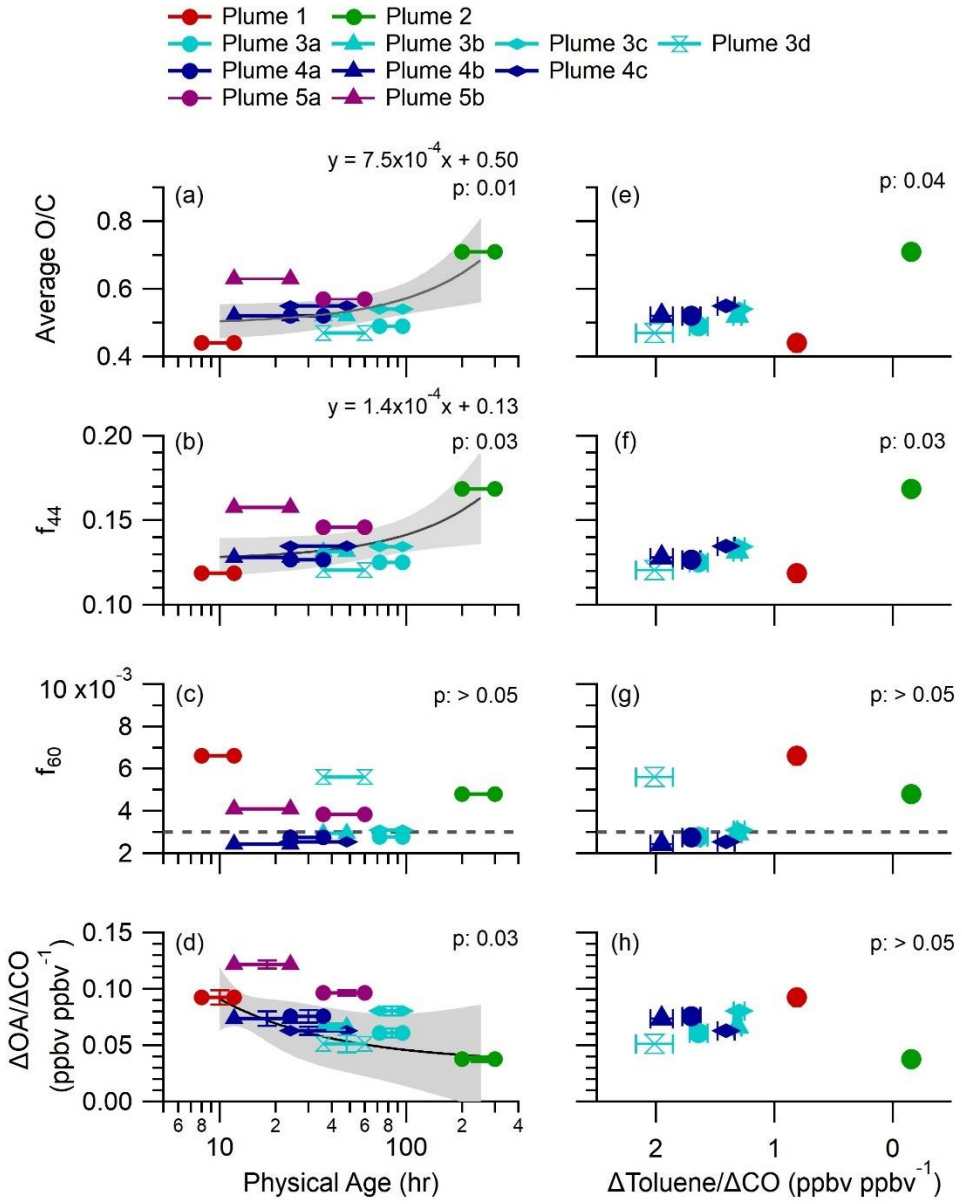

Figure 6: Relationships between aerosol properties and (a-d) physical age estimated from HYSPLIT back trajectories and (e-h) photochemical age calculated from ΔToluene/ΔCO. p-value determined from 2-tailed t-test. Note that Plume 5 is not included in (e-h) due to lack of correlation between toluene and CO. Whiskers represent the error of the linear regression. ΔOA/ΔCO is calculated as a dimensionless ratio (ppbv ppbv^{-1}). Fit lines for the MBO19 data shown in (a), (b), and (d) are represented by the gray solid lines, with the gray area representing the 95th confidence interval.

well correlated (Fig. A26), however, ΔToluene/ΔCO showed a more consistent trend than ΔToluene/ΔBenzene and is discussed below as a proxy for photochemical age. Additional details

regarding the ΔToluene/ΔCO calculation, the alternate use of ΔToluene/ΔBenzene as a photochemical age metric and comparison to literature values are described in section SI-1.4.

Figure 2.6 shows the change in aerosol properties as a function of both the physical age and ΔToluene/ΔCO. There is a positive relation ($p < 0.05$) between both bulk OA O/C and f_{44} and plume physical age, indicating oxidation processes occurring during transport (Figure 2.6a-b). A negative relation is seen between f_{60} and physical age as well, after plume sections with f_{60} values below the 0.3% background value are excluded. This decreasing trend of f_{60} is consistent with the loss of anhydrous sugars during transport, which is also shown in Fig. 2.1b. Here, the evolution of OA is seen within the f_{44}-f_{60} space as OA moves towards higher f_{44} values corresponding to increased plume processing (i.e., from event 1 to event 5 to event 2). Events 3 and 4 deviate from the trend line and are located more closely to the SV-OOA factor in the f_{44}-f_{60} space, likely due to influences by biogenic emissions (see discussions in Section 3.3).

Of particular interest is the change of the OA enhancement ratio relative to CO (ΔOA/ΔCO) with atmospheric aging (Fig. 2.1c). ΔOA/ΔCO will vary with either SOA production or OA losses through evaporation, deposition, and/or photodegradation reactions (Jolleys et al., 2012). Some field and laboratory studies have found substantial SOA production during aging of BB smoke (Ortega et al., 2013; Yokelson et al., 2009), while others have seen no enhancement (Garofalo et al., 2019; Zhou et al., 2017) or a decrease in OA mass (Akagi et al., 2012; Cubison et al., 2011). The ΔOA/ΔCO for each BB plume was determined as the orthogonal distance regression between the measured OA and CO for the duration of the plume (Figure 2.1c). All of the plumes identified during MBO19 show good correlations between OA and CO ($r^2 > 0.70$) with enhancement ratios varying from 0.038 to 0.122 ppb ppb^{-1}. Significantly higher ΔOA/ΔCO (0.219±0.067 ppb ppb^{-1}) calculated from Collier et al. (2016) were observed during BBOP for regionally transported, but less aged, wildfire plumes. The MBO values agree well with the ΔOA/ΔCO measured in wildfire plumes sampled during several aircraft campaigns compiled by Jolleys et al. (2012),

where the flight-average values ranged from 0.019±0.002 to 0.329±0.006 ppb ppb^{-1} and the values were systematically higher in fresher plumes than in aged plumes.

A large range of ΔOA/ΔCO values, varying from 0.092 ppb ppb^{-1} to 0.442 ppb ppb^{-1}, is seen at intermediate plume physical ages between 6 and 12 hours at MBO (Fig. 2.1c). This spread is likely due to differences in initial emission characteristics, such as the concentration of SOA precursors, burning condition, or fuel types(Collier et al., 2016; Jolleys et al., 2014). However, at above 12 hours, ΔOA/ΔCO shows a strong negative trend ($p < 0.05$) with physical age (Fig 2.6d). This suggests either the continued evaporation of volatile BB-POA, OA loss via deposition and heterogeneous oxidation or loss of BB-SOA via evaporation or fragmentation reactions. In addition, from this relationship, it appears that after 10-20 days of aging, ΔOA/ΔCO may begin to approach zero due to chemical destruction of BBOA. The extremely low ΔOA/ΔCO value seen in event 2 may also be affected by aerosol wet deposition during long range transport. It is worth noting that this analysis represents a small population of BB plumes and more measurements of ΔOA/ΔCO at transport ages > 1 day are needed to further probe this trend.

The ΔToluene/ΔCO was variable between the plumes, ranging from as high as 2 pptv $ppbv^{-1}$ during plume 3 to 0 pptv $ppbv^{-1}$ during plume 2, which is consistent with the loss of toluene through oxidation reactions (Fig 2.6). Overall, the trends seen between aerosol properties and ΔToluene/ΔCO agree well with the trends seen with physical age. However, due to the exclusion of plume 5 as discussed above, the relationships are less statistically robust. Furthermore, plume 1 appears to be an outlier; it displays a lower ΔToluene/ΔCO, indicating processing, despite a low O/C, short estimated physical age and other signs of fresh BB. It is possible that this plume had a lower toluene emission ratio due to differences of MCE or fuel type in the fire. Despite this, ΔToluene/ΔCO appears to be a promising metric for quantifying photochemical age in aged BB plumes.

2.5. Atmospheric Implications

Our atmospheric measurement study in the summer of 2019 at MBO, a remote, high elevation site with minimal anthropogenic influence, allowed a unique chance to study aged aerosols with influence from wildfires. The results are relevant to the tropospheric background in western North America during wildfire season, which often spans most of summer and fall. The atmospheric conditions during this study were typical for a pristine remote location as the PM_1 concentration was very low (2.22 ± 1.86 μg sm^{-3}) and was dominated by organic species (81%). However, biomass burning evidently affected this site, as seen through increased concentrations of CO, rBC, acetonitrile, furans, and SP-AMS tracer ions for anhydrous sugars. Five mild wildfire plume events were observed and their transport times were estimated to vary from ~ 10 hours to > 10 days. The OA in these aged wildfire plumes showed increasingly higher O/C ratio, larger size mode, and lower volatility with longer transport time and higher photochemical age. Additionally, a decrease of ΔOA/ΔCO as a function of transport time was seen, at a rate of approximately -0.022 ppb ppb^{-1} day^{-1}, suggesting a net loss of BBOA relative to CO during long range transport caused by processes such as evaporation, photolysis, and deposition. Near field measurements of BB plumes, however, often observed that ΔOA/ΔCO increased or remained constant during transport. These results yield important considerations for parameterizing the behavior of BBOA within global chemical transport and climate models over the course of multiple days, one of which is that it may not be appropriate to extrapolate changes in ΔOA/ΔCO based on near field measurements out to multiple days.

PMF analysis of the SP-AMS mass spectra resolved an aged BBOA factor and two OOA factors representing SOA originated in the boundary layer and the free troposphere, respectively. The BBOA factor had a higher O/C (= 0.84) and a lower f_{60} (= 0.61%) compared to fresh BBOA factors, but was consistent with the aged BBOA factors determined previously at MBO(Zhou et al., 2017). BBOA accounted for an average 18% of the OA mass during this study, however there is evidence that the

BBOA factor resolved by PMF in this study may have underestimated the contribution of BB to total OA, and should be treated as lower limit. As shown in Figure A15, there were time periods when the BBOA concentration approached 0 μg sm^{-3} but rBC, CO and furfural showed enhanced concentrations and strong correlations with total OA. Furthermore, the distribution of ion signals among the OA factors suggests that the SV-OOA factor was influenced by BB during low OA periods. For example, $C_2H_4O_2^+$ (*m/z* 60) and $C_3H_5O_2^+$ (*m/z* 73) are established BB tracers but nearly 60% of their signals are attributed to the SV-OOA factor (Fig. A14). Similar underestimations could occur during other field campaigns with low concentration periods where data is analyzed by PMF. Finally, the volatility profile of the BBOA also highlights that aged BB emissions may represent an important source of low and extremely low volatility organic compounds (LVOC and ELVOC) in remote areas. These results underscore the widespread influence of wildfires on aerosol properties and atmospheric chemistry in the western US during summertime, which may have important implications on regional and global climate.

References

Adler, G., Wagner, N. L., Lamb, K. D., Manfred, K. M., Schwarz, J. P., Franchin, A., Middlebrook, A. M., Washenfelder, R. A., Womack, C. C., Yokelson, R. J. and Murphy, D. M.: Evidence in biomass burning smoke for a light-absorbing aerosol with properties intermediate between brown and black carbon, Aerosol Sci. Technol., 53(9), 976–989, doi:10.1080/02786826.2019.1617832, 2019.

Aiken, A. C., De Foy, B., Wiedinmyer, C., Decarlo, P. F., Ulbrich, I. M., Wehrli, M. N., Szidat, S., Prevot, A. S. H., Noda, J., Wacker, L., Volkamer, R., Fortner, E., Wang, J., Laskin, A., Shutthanandan, V., Zheng, J., Zhang, R., Paredes-Miranda, G., Arnott, W. P., Molina, L. T., Sosa, G., Querol, X. and Jimenez, J. L.: Mexico city aerosol analysis during MILAGRO using high resolution aerosol mass spectrometry at the urban supersite (T0)-Part 2: Analysis of the biomass burning contribution and the non-fossil carbon fraction, Atmos. Chem. Phys., 10(12), 5315–5341, doi:10.5194/acp-10-5315-2010, 2010.

Akagi, S. K., Craven, J. S., Taylor, J. W., McMeeking, G. R., Yokelson, R. J., Burling, I. R., Urbanski, S. P., Wold, C. E., Seinfeld, J. H., Coe, H., Alvarado, M. J. and Weise, D. R.: Evolution of trace gases and particles emitted by a chaparral fire in California, Atmos. Chem. Phys., 12(3), 1397–1421, doi:10.5194/acp-12-1397-2012, 2012.

Alfarra, M. R., Prevot, A. S. H., Szidat, S., Sandradewi, J., Weimer, S., Lanz, V. A., Schreiber, D., Mohr, M. and Baltensperger, U.: Identification of the mass spectral signature of organic aerosols from wood burning emissions, Environ. Sci. Technol., doi:10.1021/es062289b, 2007.

Anderson, T. L. and Ogren, J. A.: Determining Aerosol Radiative Properties Using the TSI 3563 Integrating Nephelometer, Aerosol Sci. Technol., 29(1), 57–69, doi:10.1080/02786829808965551, 1998.

Andreae, M. O.: Soot carbon and excess fine potassium: Long-range transport of combustion-derived aerosols, Science (80-.)., 220(4602), 1148–1151, doi:10.1126/science.220.4602.1148, 1983.

Andreae, M. O. and Gelencsér, A.: Black carbon or brown carbon? the nature of light-absorbing carbonaceous aerosols, Atmos. Chem. Phys., doi:10.5194/acp-6-3131-2006, 2006.

Avery, A. M., Williams, L. R., Fortner, E. C., Robinson, W. A. and Onasch, T. B.: Particle detection using the dual-vaporizer configuration of the soot particle Aerosol Mass Spectrometer (SP-AMS), Aerosol Sci. Technol., 55(3), 254–267, doi:10.1080/02786826.2020.1844132, 2020.

Baars, H., Ansmann, A., Ohneiser, K., Haarig, M., Engelmann, R., Althausen, D., Hanssen, I., Gausa, M., Pietruczuk, A., Szkop, A., Stachlewska, I. S., Wang, D., Reichardt, J., Skupin, A., Mattis, I., Trickl, T., Vogelmann, H., Navas-Guzmán, F., Haefele, A., Acheson, K., Ruth, A. A., Tatarov, B., Müller, D., Hu, Q., Podvin, T., Goloub, P., Veselovskii, I., Pietras, C., Haeffelin, M., Fréville, P., Sicard, M., Comerón, A., García, A. J. F., Menéndez, F. M., Córdoba-Jabonero, C., Guerrero-Rascado, J. L., Alados-Arboledas, L., Bortoli, D., Costa, M. J., Dionisi, D., Liberti, G. L., Wang, X., Sannino, A., Papagiannopoulos, N., Boselli, A., Mona, L., D'Amico, G., Romano, S., Perrone, M. R., Belegante, L., Nicolae, D., Grigorov, I., Gialitaki, A., Amiridis, V., Soupiona, O., Papayannis, A., Mamouri, R. E., Nisantzi, A., Heese, B., Hofer, J., Schechner, Y. Y., Wandinger, U. and Pappalardo, G.: The unprecedented 2017-2018 stratospheric smoke event: Decay phase and aerosol properties observed with the EARLINET, Atmos. Chem. Phys., 19(23), 15183–15198, doi:10.5194/acp-19-15183-2019, 2019.

Barbero, R., Abatzoglou, J. T., Larkin, N. K., Kolden, C. A. and Stocks, B.: Climate change presents increased potential for very large fires in the contiguous United States, Int. J. Wildl. Fire, doi:10.1071/WF15083, 2015.

Baylon, P., Jaffe, D. A., Wigder, N. L., Gao, H. and Hee, J.: Ozone enhancement in western US wildfire plumes at the Mt. Bachelor Observatory: The role of NOx, Atmos. Environ., 109(x), 297–304, doi:10.1016/j.atmosenv.2014.09.013, 2015.

Bond, T. C. and Bergstrom, R. W.: Light absorption by carbonaceous particles: An investigative review, Aerosol Sci. Technol., 27–67, doi:10.1080/02786820500421521, 2006.

Briggs, N. L., Jaffe, D. A., Gao, H., Hee, J. R., Baylon, P. M., Zhang, Q., Zhou, S., Collier, S. C., Sampson, P. D. and Cary, R. A.: Particulate matter, ozone, and nitrogen species in aged wildfire plumes observed at the Mount Bachelor Observatory, Aerosol Air Qual. Res., doi:10.4209/aaqr.2016.03.0120, 2016.

Brown, H., Liu, X., Pokhrel, R., Murphy, S., Lu, Z., Saleh, R., Mielonen, T., Kokkola, H., Bergman, T., Myhre, G., Skeie, R. B., Watson-paris, D., Stier, P., Johnson, B., Bellouin, N., Schulz, M., Vakkari, V., Beukes, J. P., Zyl, P. G. Van, Liu, S. and Chand, D.: Biomass burning aerosols in most climate models are too absorbing, Nat. Commun., 1–15, doi:10.1038/s41467-020-20482-9, 2021.

Canagaratna, M. R., Jayne, J. T., Jimenez, J. L., Allan, J. D., Alfarra, M. R., Zhang, Q., Onasch, T. B., Drewnick, F., Coe, H., Middlebrook, A., Delia, A., Williams, L. R., Trimborn, A. M., Northway, M. J., DeCarlo, P. F., Kolb, C. E., Davidovits, P. and Worsnop, D. R.: Chemical and microphysical characterization of ambient aerosols with the aerodyne aerosol mass spectrometer, Mass Spectrom. Rev., 19(2), 173–181, doi:10.1002/mas.20115, 2007.

Canagaratna, M. R., Jimenez, J. L., Kroll, J. H., Chen, Q., Kessler, S. H., Massoli, P., Hildebrandt Ruiz, L.,

Fortner, E., Williams, L. R., Wilson, K. R., Surratt, J. D., Donahue, N. M., Jayne, J. T. and Worsnop, D. R.: Elemental ratio measurements of organic compounds using aerosol mass spectrometry: Characterization, improved calibration, and implications, Atmos. Chem. Phys., 15(1), doi:10.5194/acp-15-253-2015, 2015.

Cappa, C. D., Lim, C. Y., Hagan, D. H., Coggon, M., Koss, A., Sekimoto, K., de Gouw, J., Onasch, T. B., Warneke, C. and Kroll, J. H.: Biomass-burning-derived particles from a wide variety of fuels: Part 2: Effects of photochemical aging on particle optical and chemical properties, Atmos. Chem. Phys. Discuss, 2020.

Chen, L. A., Verburg, P., Shackelford, A., Zhu, D., Susfalk, R., Chow, J. C. and Watson, J. G.: Moisture effects on carbon and nitrogen emission from burning of wildland biomass, Atmos. Chem. Phys., (x), 6617–6625, doi:10.5194/acp-10-6617-2010, 2010.

Chen, L. W. A., Moosmüller, H., Arnott, W. P., Chow, J. C., Watson, J. G., Susott, R. A., Babbitt, R. E., Wold, C. E., Lincoln, E. N. and Wei, M. H.: Emissions from laboratory combustion of wildland fuels: Emission factors and source profiles, Environ. Sci. Technol., 41(12), 4317–4325, doi:10.1021/es062364i, 2007.

Coggon, M. M., Veres, P. R., Yuan, B., Koss, A., Warneke, C., Gilman, J. B., Lerner, B. M., Peischl, J., Aikin, K. C., Stockwell, C. E., Hatch, L. E., Ryerson, T. B., Roberts, J. M., Yokelson, R. J. and de Gouw, J. A.: Emissions of nitrogen-containing organic compounds from the burning of herbaceous and arboraceous biomass: Fuel composition dependence and the variability of commonly used nitrile tracers, Geophys. Res. Lett., 43(18), 9903–9912, doi:10.1002/2016GL070562, 2016.

Collier, S., Zhou, S., Onasch, T. B., Jaffe, D. A., Kleinman, L., Sedlacek, A. J., Briggs, N. L., Hee, J., Fortner, E., Shilling, J. E., Worsnop, D., Yokelson, R. J., Parworth, C., Ge, X., Xu, J., Butterfield, Z., Chand, D., Dubey, M. K., Pekour, M. S., Springston, S. and Zhang, Q.: Regional Influence of Aerosol Emissions from Wildfires Driven by Combustion Efficiency: Insights from the BBOP Campaign, Environ. Sci. Technol., doi:10.1021/acs.est.6b01617, 2016.

Cubison, M. J., Ortega, A. M., Hayes, P. L., Farmer, D. K., Day, D., Lechner, M. J., Brune, W. H., Apel, E., Diskin, G. S., Fisher, J. A., Fuelberg, H. E., Hecobian, A., Knapp, D. J., Mikoviny, T., Riemer, D., Sachse, G. W., Sessions, W., Weber, R. J., Weinheimer, A. J., Wisthaler, A. and Jimenez, J. L.: Effects of aging on organic aerosol from open biomass burning smoke in aircraft and laboratory studies, Atmos. Chem. Phys., doi:10.5194/acp-11-12049-2011, 2011.

DeCarlo, P. F., Kimmel, J. R., Trimborn, A., Northway, M. J., Jayne, J. T., Aiken, A. C., Gonin, M., Fuhrer, K., Horvath, T., Docherty, K. S., Worsnop, D. R. and Jimenez, J. L.: Field-deployable, high-resolution, time-of-flight aerosol mass spectrometer, Anal. Chem., doi:10.1021/ac061249n, 2006.

Donahue, N. M., Kroll, J. H., Pandis, S. N. and Robinson, A. L.: A two-dimensional volatility basis set – Part 2 : Diagnostics of organic-aerosol evolution, Atmos. Chem. Phys. Discuss, (January 2015), doi:10.5194/acpd-11-24883-2011, 2011.

Drewnick, F., Diesch, J. M., Faber, P. and Borrmann, S.: Aerosol mass spectrometry: Particle-vaporizer interactions and their consequences for the measurements, Atmos. Meas. Tech., 8(9), 3811–3830, doi:10.5194/amt-8-3811-2015, 2015.

Du, W., Sun, Y. L., Xu, Y. S., Jiang, Q., Wang, Q. Q., Yang, W., Wang, F., Bai, Z. P., Zhao, X. D. and Yang, Y. C.: Chemical characterization of submicron aerosol and particle growth events at a national background site (3295 m a . s . l .) on the Tibetan Plateau, Atmos. Chem. Phys., 10811–10824, doi:10.5194/acp-15-

10811-2015, 2015.

Dzepina, K., Mazzoleni, C., Fialho, P., China, S., Zhang, B., Owen, R. C., Helmig, D., Hueber, J., Kumar, S., Perlinger, J. A., Kramer, L. J., Dziobak, M. P., Ampadu, M. T., Olsen, S., Wuebbles, D. J. and Mazzoleni, L. R.: Molecular characterization of free tropospheric aerosol collected at the Pico Mountain Observatory: A case study with a long-range transported biomass burning plume, Atmos. Chem. Phys., 15(9), 5047–5068, doi:10.5194/acp-15-5047-2015, 2015.

Fierz, M., Vernooij, M. G. C. and Burtscher, H.: An improved low-flow thermodenuder, J. Aerosol Sci., doi:10.1016/j.jaerosci.2007.08.006, 2007.

Forrister, H., Liu, J., Scheuer, E., Dibb, J., Ziemba, L., Thornhill, K. L., Anderson, B., Diskin, G., Perring, A. E., Schwarz, J. P., Campuzano-Jost, P., Day, D. A., Palm, B. B., Jimenez, J. L., Nenes, A. and Weber, R. J.: Evolution of brown carbon in wildfire plumes, Geophys. Res. Lett., doi:10.1002/2015GL063897, 2015.

Garofalo, L. A., Pothier, M. A., Levin, E. J. T., Campos, T., Kreidenweis, S. M. and Farmer, D. K.: Emission and Evolution of Submicron Organic Aerosol in Smoke from Wildfires in the Western United States, ACS Earth Sp. Chem., 3(7), 1237–1247, doi:10.1021/acsearthspacechem.9b00125, 2019.

Ge, X., Setyan, A., Sun, Y. and Zhang, Q.: Primary and secondary organic aerosols in Fresno, California during wintertime: Results from high resolution aerosol mass spectrometry, J. Geophys. Res. Atmos., 117(18), 1–15, doi:10.1029/2012JD018026, 2012.

Gilman, J. B., Lerner, B. M., Kuster, W. C., Goldan, P. D., Warneke, C., Veres, P. R., Roberts, J. M., De Gouw, J. A., Burling, I. R. and Yokelson, R. J.: Biomass burning emissions and potential air quality impacts of volatile organic compounds and other trace gases from fuels common in the US, Atmos. Chem. Phys., doi:10.5194/acp-15-13915-2015, 2015.

de Gouw, J. A., Warneke, C., Parrish, D. D., Holloway, J. S., Trainer, M. and Fehsenfeld, F. C.: Emission sources and ocean uptake of acetonitrile (CH 3 CN) in the atmosphere, J. Geophys. Res., 108, 1–8, doi:10.1029/2002JD002897, 2003.

Grieshop, A. P., Logue, J. M., Donahue, N. M. and Robinson, A. L.: Laboratory investigation of photochemical oxidation of organic aerosol from wood fires 1: Measurement and simulation of organic aerosol evolution, Atmos. Chem. Phys., 9(4), 1263–1277, doi:10.5194/acp-9-1263-2009, 2009.

Hallquist, M., Wenger, J. C., Baltensperger, U., Rudich, Y., Simpson, D., Claeys, M., Dommen, J., Donahue, N. M., George, C., Goldstein, A. H., Hamilton, J. F., Herrmann, H., Hoffmann, T., Iinuma, Y., Jang, M., Jenkin, M. E., Jimenez, J. L., Kiendler-Scharr, A., Maenhaut, W., McFiggans, G., Mentel, T. F., Monod, A., Prévôt, A. S. H., Seinfeld, J. H., Surratt, J. D., Szmigielski, R. and Wildt, J.: The formation, properties and impact of secondary organic aerosol: Current and emerging issues, Atmos. Chem. Phys., doi:10.5194/acp-9-5155-2009, 2009.

Huffman, J. A., Docherty, K. S., Mohr, C., Cubison, M. J., Ulbrich, I. M., Ziemann, P. J., Onasch, T. B. and Jimenez, J. L.: Chemically-resolved volatility measurements of organic aerosol from different sources, Environ. Sci. Technol., doi:10.1021/es803539d, 2009.

Hung, W. T., Lu, C. H. (Sarah), Shrestha, B., Lin, H. C., Lin, C. A., Grogan, D., Hong, J., Ahmadov, R., James, E. and Joseph, E.: The impacts of transported wildfire smoke aerosols on surface air quality in New York State: A case study in summer 2018, Atmos. Environ., doi:10.1016/j.atmosenv.2020.117415, 2020.

IPCC: Summary for policymakers, in Climate Change 2014: Impacts, Adaptation, and Vulnerability. Part A: Global and Sectoral Aspects. Contribution of Working Group II to the Fifth Assessment Report of the

Intergovernmental Panel on Climate Change., 2013.

Jaffe, D., Hafner, W., Chand, D., Westerling, A. and Spracklen, D.: Interannual variations in PM2.5 due to wildfires in the Western United States, Environ. Sci. Technol., doi:10.1021/es702755v, 2008.

Jaffe, D. A., O'Neill, S. M., Larkin, N. K., Holder, A. L., Peterson, D. L., Halofsky, J. E. and Rappold, A. G.: Wildfire and prescribed burning impacts on air quality in the United States, J. Air Waste Manage. Assoc., 0(0), doi:10.1080/10962247.2020.1749731, 2020.

Jen, C. N., Hatch, L. E., Selimovic, V., Yokelson, R. J., Weber, R., Fernandez, A. E., Kreisberg, N. M., Barsanti, K. C. and Goldstein, A. H.: Speciated and total emission factors of particulate organics from burning western US wildland fuels and their dependence on combustion efficiency, Atmos. Chem. Phys., doi:10.5194/acp-19-1013-2019, 2019.

Jiang, J., Carter, W. P. L., Cocker, D. R. and Barsanti, K. C.: Development and Evaluation of a Detailed Mechanism for Gas-Phase Atmospheric Reactions of Furans, ACS Earth Sp. Chem., doi:10.1021/acsearthspacechem.0c00058, 2020.

Jimenez, J. L., Canagaratna, M. R., Donahue, N. M., Prevot, A. S. H., Zhang, Q., Kroll, J. H., DeCarlo, P. F., Allan, J. D., Coe, H., Ng, N. L., Aiken, A. C., Docherty, K. S., Ulbrich, I. M., Grieshop, A. P., Robinson, A. L., Duplissy, J., Smith, J. D., Wilson, K. R., Lanz, V. A., Hueglin, C., Sun, Y. L., Tian, J., Laaksonen, A., Raatikainen, T., Rautiainen, J., Vaattovaara, P., Ehn, M., Kulmala, M., Tomlinson, J. M., Collins, D. R., Cubison, M. J., Dunlea, E. J., Huffman, J. A., Onasch, T. B., Alfarra, M. R., Williams, P. I., Bower, K., Kondo, Y., Schneider, J., Drewnick, F., Borrmann, S., Weimer, S., Demerjian, K., Salcedo, D., Cottrell, L., Griffin, R., Takami, A., Miyoshi, T., Hatakeyama, S., Shimono, A., Sun, J. Y., Zhang, Y. M., Dzepina, K., Kimmel, J. R., Sueper, D., Jayne, J. T., Herndon, S. C., Trimborn, A. M., Williams, L. R., Wood, E. C., Middlebrook, A. M., Kolb, C. E., Baltensperger, U. and Worsnop, D. R.: Evolution of organic aerosols in the atmosphere, Science (80-.)., doi:10.1126/science.1180353, 2009.

Jolleys, M., Coe, H., McFiggans, G., McMeeking, G. R., Lee, T., Kreidenweis, S. M., Collett, J. L. and Sullivan, A.: Organic aerosol emission ratios from the laboratory combustion of biomass fuels, J. Geophys. Res. Atmos., 850–871, doi:10.1002/2014JD021589.Received, 2014.

Jolleys, M. D., Coe, H., McFiggans, G., Capes, G., Allan, J. D., Crosier, J., Williams, P. I., Allen, G., Bower, K. N., Jimenez, J. L., Russell, L. M., Grutter, M. and Baumgardner, D.: Characterizing the aging of biomass burning organic aerosol by use of mixing ratios: A meta-analysis of four regions, Environ. Sci. Technol., 46(24), 13093–13102, doi:10.1021/es302386v, 2012.

Kiendler-Scharr, A., Zhang, Q., Hohaus, T., Kleist, E., Mensah, A., Mentel, T. F., Spindler, C., Uerlings, R., Tillmann, R. and Wildt, J.: Aerosol mass spectrometric features of biogenic SOA: Observations from a plant chamber and in rural atmospheric environments, Environ. Sci. Technol., 43(21), 8166–8172, doi:10.1021/es901420b, 2009.

Kleinman, L., Sedlacek III, A., Adachi, K., Buseck, P., Collier, S., Dubey, M., Hodshire, A., Lewis, E., Onasch, T., Pierce, J., Shilling, J., Springston, S., Wang, J., Zhang, Q., Zhou, S. and Yokelson, R.: Rapid Evolution of Aerosol Particles and their Optical Properties Downwind of Wildfires in the Western U.S., Atmos. Chem. Phys., (April), 1–52, doi:10.5194/acp-2020-239, 2020.

Kondo, Y., Matsui, H., Moteki, N., Sahu, L., Takegawa, N., Kajino, M., Zhao, Y., Cubison, M. J., Jimenez, J. L., Vay, S., Diskin, G. S., Anderson, B., Wisthaler, A., Mikoviny, T., Fuelberg, H. E., Blake, D. R., Huey, G., Weinheimer, A. J., Knapp, D. J. and Brune, W. H.: Emissions of black carbon, organic, and inorganic aerosols from biomass burning in North America and Asia in 2008, J. Geophys. Res. Atmos., 116(8), 1–

25, doi:10.1029/2010JD015152, 2011.

Laing, J. R., Jaffe, D. A. and Hee, J. R.: Physical and optical properties of aged biomass burning aerosol from wildfires in Siberia and the Western USA at the Mt . Bachelor Observatory, Atmos. Chem. Phys., 15185–15197, doi:10.5194/acp-16-15185-2016, 2016.

Lee, A. K. Y., Willis, M. D., Healy, R. M., Wang, J. M., Jeong, C. H., Wenger, J. C., Evans, G. J. and Abbatt, J. P. D.: Single-particle characterization of biomass burning organic aerosol (BBOA): Evidence for non-uniform mixing of high molecular weight organics and potassium, Atmos. Chem. Phys., 16(9), 5561–5572, doi:10.5194/acp-16-5561-2016, 2016.

Lim, C. Y., Hagan, D. H., Coggon, M. M., Koss, A. R., Sekimoto, K., Gouw, J. De, Warneke, C., Cappa, C. D. and Kroll, J. H.: Secondary organic aerosol formation from the laboratory oxidation of biomass burning emissions, Atmos. Chem. Phys., 12797–12809, 2019.

Liu, Y., Goodrick, S. and Heilman, W.: Wildland fire emissions, carbon, and climate: Wildfire-climate interactions, For. Ecol. Manage., 317, 80–96, doi:10.1016/j.foreco.2013.02.020, 2014.

Ma, Y., Weber, R. J., Lee, Y. N., Orsini, D. A., Maxwell-Meier, K., Thornton, D. C., Bandy, A. R., Clarke, A. D., Blake, D. R., Sachse, G. W., Fuelberg, H. E., Kiley, C. M., Woo, J. H., Streets, D. G. and Carmichael, G. R.: Characteristics and influence of biosmoke on the fine-particle ionic composition measured in Asian outflow during the Transport and Chemical Evolution over the Pacific (TRACE-P) experiment, J. Geophys. Res. D Atmos., 108(21), doi:10.1029/2002jd003128, 2003.

Martin, M. V., Logan, J. A., Kahn, R. A., Leung, F., Nelson, D. L. and Diner, D. J.: and Physics Smoke injection heights from fires in North America : analysis of 5 years of satellite observations, , 1491–1510, 2010.

Maudlin, L. C., Wang, Z., Jonsson, H. H. and Sorooshian, A.: Impact of wildfires on size-resolved aerosol composition at a coastal California site, Atmos. Environ., 119, 59–68, doi:10.1016/j.atmosenv.2015.08.039, 2015.

May, A. A., McMeeking, G. R., Lee, T., Taylor, J. W., Craven, J. S., Burling, I. R., Sullivan, A. P., Akagi, S. K., Collett, J. L., Flynn, M. J., Coe, H., Urbanski, S. P., Seinfeld, J. H., Yokelson, R. J. and Kreidenweis, S. M.: Aerosol emissions from prescribed fires in the United States: A synthesis of laboratory and aircraft measurements, J. Geophys. Res. Atmos., 119(3), 7667–7683, doi:10.1002/2014JD021790.Received, 2014.

McClure, C. D. and Jaffe, D. A.: US particulate matter air quality improves except in wildfire-prone areas, Proc. Natl. Acad. Sci. U. S. A., 115(31), 7901–7906, doi:10.1073/pnas.1804353115, 2018.

Müller, M., Mikoviny, T., Feil, S., Haidacher, S., Hanel, G., Hartungen, E., Jordan, A., Märk, L., Mutschlechner, P., Schottkowsky, R., Sulzer, P., Crawford, J. H. and Wisthaler, A.: A compact PTR-ToF-MS instrument for airborne measurements of volatile organic compounds at high spatiotemporal resolution, Atmos. Meas. Tech., 7(11), 3763–3772, doi:10.5194/amt-7-3763-2014, 2014.

Müller, M., Anderson, B. E., Beyersdorf, A. J., Crawford, J. H., Diskin, G. S., Eichler, P., Fried, A., Keutsch, F. N., Mikoviny, T., Thornhill, K. L., Walega, J. G., Weinheimer, A. J., Yang, M., Yokelson, R. J. and Wisthaler, A.: In situ measurements and modeling of reactive trace gases in a small biomass burning plume, Atmos. Chem. Phys., 16(6), 3813–3824, doi:10.5194/acp-16-3813-2016, 2016.

Ng, N. L., Canagaratna, M. R., Zhang, Q., Jimenez, J. L., Tian, J., Ulbrich, I. M., Kroll, J. H., Docherty, K. S., Chhabra, P. S., Bahreini, R., Murphy, S. M., Seinfeld, J. H., Hildebrandt, L., Donahue, N. M., Decarlo, P. F.,

Lanz, V. A., Prévôt, A. S. H., Dinar, E., Rudich, Y. and Worsnop, D. R.: Organic aerosol components observed in Northern Hemispheric datasets from Aerosol Mass Spectrometry, Atmos. Chem. Phys., doi:10.5194/acp-10-4625-2010, 2010.

Onasch, T. B., Trimborn, A., Fortner, E. C., Jayne, J. T., Kok, G. L., Williams, L. R., Davidovits, P. and Worsnop, D. R.: Soot particle aerosol mass spectrometer: Development, validation, and initial application, Aerosol Sci. Technol., doi:10.1080/02786826.2012.663948, 2012.

Ortega, A. M., Day, D. A., Cubison, M. J., Brune, W. H., Bon, D., De Gouw, J. A. and Jimenez, J. L.: Secondary organic aerosol formation and primary organic aerosol oxidation from biomass-burning smoke in a flow reactor during FLAME-3, Atmos. Chem. Phys., doi:10.5194/acp-13-11551-2013, 2013.

Paatero, P. and Tapper, U.: Positive matrix factorization: A non-negative factor model with optimal utilization of error estimates of data values, Environmetrics, doi:10.1002/env.3170050203, 1994.

Palm, B. B., Peng, Q., Fredrickson, C. D., Lee, B. H., Garofalo, L. A. and Pothier, M. A.: Quantification of organic aerosol and brown carbon evolution in fresh wildfire plumes, Proc. Natl. Acad. Sci., doi:10.1073/pnas.2012218117, 2020.

Pan, X., Kanaya, Y., Taketani, F., Miyakawa, T., Inomata, S., Komazaki, Y., Tanimoto, H., Wang, Z., Uno, I. and Wang, Z.: Emission characteristics of refractory black carbon aerosols from fresh biomass burning: A perspective from laboratory experiments, Atmos. Chem. Phys., 17(21), 13001–13016, doi:10.5194/acp-17-13001-2017, 2017.

Park, R. J., Jacob, D. J. and Logan, J. A.: Fire and biofuel contributions to annual mean aerosol mass concentrations in the United States, Atmos. Environ., 41(35), 7389–7400, doi:10.1016/j.atmosenv.2007.05.061, 2007.

Permar, W., Wang, Q., Selimovic, V., Wielgasz, R. J., Yokelson, R. J., Hornbrook, R. S., Hills, A. J., Apel, E., Ku, I., Zhou, Y., Sive, B. C., Sullivan, A. P., Collett, J. L., Campos, T. L., Palm, B. B., Peng, Q., Thornton, J. A., Garofalo, L. A., Farmer, D. K., Kreidenweis, S. M., Levin, E. J. T., DeMott, P. J., Flocke, F. and Hu, L.: Emissions of trace organic gases from western U.S. wildfires based on WE- CAN aircraft measurements, J. Geophys. Res., n.d.

Pope, C. A. and Dockery, D. W.: Health effects of fine particulate air pollution: Lines that connect, J. Air Waste Manag. Assoc., doi:10.1080/10473289.2006.10464485, 2006.

Quaas, J., Ming, Y., Menon, S., Takemura, T., Wang, M., Penner, J. E., Gettelman, A., Lohmann, U., Bellouin, N., Boucher, O., Sayer, A. M., Thomas, G. E., McComiskey, A., Feingold, G., Hoose, C., Kristjnsson, J. E., Liu, X., Balkanski, Y., Donner, L. J., Ginoux, P. A., Stier, P., Grandey, B., Feichter, J., Sednev, I., Bauer, S. E., Koch, D., Grainger, R. G., Kirkevaring, A., Iversen, T., Seland, O., Easter, R., Ghan, S. J., Rasch, P. J., Morrison, H., Lamarque, J. F., Iacono, M. J., Kinne, S. and Schulz, M.: Aerosol indirect effects general circulation model intercomparison and evaluation with satellite data, Atmos. Chem. Phys., doi:10.5194/acp-9-8697-2009, 2009.

Reidmiller, D. R., Jaffe, D. A., Chandl, D., Strodel, S., Swartzendruber, P., Wolfe, G. M. and Thornton, J. A.: Interannual variability of long-range transport as seen at the Mt. Bachelor observatory, Atmos. Chem. Phys., 9(2), 557–572, doi:10.5194/acp-9-557-2009, 2009.

Roberts, J., Stockwell, C., Yokelson, R., de Gouw, J., Liu, Y., Selimovic, V., Koss, A., Sekimoto, K., Coggon, M., Yuan, B., Zarzana, K., Brown, S., Santin, C., Doerr, S. and Warneke, C.: The nitrogen budget of laboratory-simulated western U.S. wildfires during the FIREX 2016 FireLab study, Atmos. Chem. Phys.,

(2), 1–34, doi:10.5194/acp-2020-66, 2020.

Schill, G. P., Froyd, K. D., Bian, H., Kupc, A., Williamson, C., Brock, C. B., Ray, E., Hornbrook, R. S., Hills, A. J., Apel, E. C., Chin, M., Colarco, P. R. and Murphy, D. M.: Widespread biomass burning smoke throughout the remote troposphere, Nat. Geosci., Accepted(June), doi:10.1038/s41561-020-0586-1, 2020.

Schneider, J., Weimer, S., Drewnick, F., Borrmann, S., Helas, G., Gwaze, P., Schmid, O., Andreae, M. O. and Kirchner, U.: Mass spectrometric analysis and aerodynamic properties of various types of combustion-related aerosol particles, Int. J. Mass Spectrom., 258(1–3), 37–49, doi:10.1016/j.ijms.2006.07.008, 2006.

Schurman, M. I., Lee, T., Desyaterik, Y., Schichtel, B. A., Kreidenweis, S. M. and Collett, J. L.: Transport, biomass burning, and in-situ formation contribute to fine particle concentrations at a remote site near Grand Teton National Park, Atmos. Environ., 112, 257–268, doi:10.1016/j.atmosenv.2015.04.043, 2015.

Sedlacek, A. J., Buseck, P. R., Adachi, K., Onasch, T. B., Springston, S. R. and Kleinman, L.: Formation and evolution of tar balls from northwestern US wildfires, Atmos. Chem. Phys., 18(15), 11289–11301, doi:10.5194/acp-18-11289-2018, 2018.

Selimovic, V., Yokelson, R. J., McMeeking, G. R. and Coefield, S.: In-situ measurements of trace gases, PM, and aerosol optical properties during the 2017 NW US wildfire smoke event, Atmos. Chem. Phys. Discuss., 1–37, doi:10.5194/acp-2018-1063, 2018.

Setyan, A., Zhang, Q., Merkel, M., Knighton, W. B., Sun, Y., Song, C., Shilling, J. E., Onasch, T. B., Herndon, S. C., Worsnop, D. R., Fast, J. D., Zaveri, R. A., Berg, L. K., Wiedensohler, A., Flowers, B. A., Dubey, M. K. and Subramanian, R.: Characterization of submicron particles influenced by mixed biogenic and anthropogenic emissions using high-resolution aerosol mass spectrometry: Results from CARES, Atmos. Chem. Phys., 12(17), 8131–8156, doi:10.5194/acp-12-8131-2012, 2012.

Shrivastava, M., Cappa, C. D., Fan, J., Goldstein, A. H., Guenther, A. B., Jimenez, J. L., Kuang, C., Laskin, A., Martin, S. T., Ng, N. L., Petaja, T., Pierce, J. R., Rasch, P. J., Roldin, P., Seinfeld, J. H., Shilling, J., Smith, J. N., Thornton, J. A., Volkamer, R., Wang, J., Worsnop, D. R., Zaveri, R. A., Zelenyuk, A. and Zhang, Q.: Recent advances in understanding secondary organic aerosol: Implications for global climate forcing, Rev. Geophys., 55(2), doi:10.1002/2016RG000540, 2017.

Spracklen, D. V., Mickley, L. J., Logan, J. A., Hudman, R. C., Yevich, R., Flannigan, M. D. and Westerling, A. L.: Impacts of climate change from 2000 to 2050 on wildfire activity and carbonaceous aerosol concentrations in the western United States, J. Geophys. Res., doi:10.1029/2008jd010966, 2009.

Sun, Y. L., Zhang, Q., Schwab, J. J., Yang, T., Ng, N. L. and Demerjian, K. L.: Factor analysis of combined organic and inorganic aerosol mass spectra from high resolution aerosol mass spectrometer measurements, Atmos. Chem. Phys., doi:10.5194/acp-12-8537-2012, 2012.

Teakles, A. D., So, R., Ainslie, B., Nissen, R., Schiller, C., Vingarzan, R., McKendry, I., Marie Macdonald, A., Jaffe, A. D., Bertram, K. A., Strawbridge, B. K., Richard Leaitch, W., Hanna, S., Toom, D., Baik, J. and Huang, L.: Impacts of the July 2012 Siberian fire plume on air quality in the Pacific Northwest, Atmos. Chem. Phys., 17(4), 2593–2611, doi:10.5194/acp-17-2593-2017, 2017.

Tuet, W. Y., Chen, Y., Fok, S., Gao, D., Weber, R. J., Champion, J. A. and Ng, N. L.: Chemical and cellular oxidant production induced by naphthalene secondary organic aerosol (SOA): Effect of redox-active metals and photochemical aging, Sci. Rep., 7(1), 1–10, doi:10.1038/s41598-017-15071-8, 2017.

Twomey, S.: Pollution and the planetary albedo, Atmos. Environ., doi:10.1016/0004-6981(74)90004-3, 1974.

Ulbrich, I. M., Canagaratna, M. R., Zhang, Q., Worsnop, D. R. and Jimenez, J. L.: Interpretation of organic components from Positive Matrix Factorization of aerosol mass spectrometric data, Atmos. Chem. Phys., doi:10.5194/acp-9-2891-2009, 2009.

Wang, J., Zhang, Q., Chen, M., Collier, S., Zhou, S., Ge, X., Xu, J., Shi, J., Xie, C., Hu, J., Ge, S., Sun, Y. and Coe, H.: First Chemical Characterization of Refractory Black Carbon Aerosols and Associated Coatings over the Tibetan Plateau (4730 m a.s.l), Environ. Sci. Technol., 51(24), 14072–14082, doi:10.1021/acs.est.7b03973, 2017.

Weiss-Penzias, P., Jaffe, D. A., Swartzendruber, P., Dennison, J. B., Chand, D., Hafner, W. and Prestbo, E.: Observations of Asian air pollution in the free troposphere at Mount Bachelor Observatory during the spring of 2004, J. Geophys. Res. Atmos., doi:10.1029/2005JD006522, 2006.

Westerling, A. L., Hidalgo, H. G., Cayan, D. R. and Swetnam, T. W.: Warming and earlier spring increase Western U.S. forest wildfire activity, Science (80-.)., 313(5789), 940–943, doi:10.1126/science.1128834, 2006.

Wong, J. P. S., Tsagkaraki, M., Tsiodra, I., Mihalopoulos, N., Violaki, K., Kanakidou, M., Sciare, J., Nenes, A. and Weber, R. J.: Effects of Atmospheric Processing on the Oxidative Potential of Biomass Burning Organic Aerosols, Environ. Sci. Technol., 53(12), 6747–6756, doi:10.1021/acs.est.9b01034, 2019.

Yokelson, R. J., Crounse, J. D., DeCarlo, P. F., Karl, T., Urbanski, S., Atlas, E., Campos, T., Shinozuka, Y., Kapustin, V., Clarke, A. D., Weinheimer, A., Knapp, D. J., Montzka, D. D., Holloway, J., Weibring, P., Flocke, F., Zheng, W., Toohey, D., Wennberg, P. O., Wiedinmyer, C., Mauldin, L., Fried, A., Richter, D., Walega, J., Jimenez, J. L., Adachi, K., Buseck, P. R., Hall, S. R. and Shetter, R.: Emissions from biomass burning in the Yucatan, Atmos. Chem. Phys., 9(15), 5785–5812, doi:10.5194/acp-9-5785-2009, 2009.

Young, D. E., Kim, H., Parworth, C., Zhou, S., Zhang, X., Cappa, C. D., Seco, R., Kim, S. and Zhang, Q.: Influences of emission sources and meteorology on aerosol chemistry in a polluted urban environment: Results from DISCOVER-AQ California, Atmos. Chem. Phys., 16(8), 5427–5451, doi:10.5194/acp-16-5427-2016, 2016.

Zauscher, M. D., Wang, Y., Moore, M. J. K., Gaston, C. J. and Prather, K. A.: Air quality impact and physicochemical aging of biomass burning aerosols during the 2007 San Diego wildfires, Environ. Sci. Technol., 47(14), 7633–7643, doi:10.1021/es4004137, 2013.

Zhang, L. and Jaffe, D. A.: Trends and sources of ozone and sub-micron aerosols at the Mt. Bachelor Observatory (MBO) during 2004–2015, Atmos. Environ., doi:10.1016/j.atmosenv.2017.06.042, 2017.

Zhang, Q., Jimenez, J. L., Canagaratna, M. R., Ulbrich, I. M., Ng, N. L., Worsnop, D. R. and Sun, Y.: Understanding atmospheric organic aerosols via factor analysis of aerosol mass spectrometry: A review, Anal. Bioanal. Chem., doi:10.1007/s00216-011-5355-y, 2011.

Zhang, Q., Zhou, S., Collier, S., Jaffe, D., Onasch, T., Shilling, J., Kleinman, L. and Sedlacek, A.: Understanding composition, formation, and aging of organic aerosols in wildfire emissions via combined mountain top and airborne measurements, ACS Symp. Ser., 1299, 363–385, doi:10.1021/bk-2018-1299.ch018, 2018a.

Zhang, X., Xu, J., Kang, S., Liu, Y. and Zhang, Q.: Chemical characterization of long-range transport biomass burning emissions to the Himalayas : insights from high-resolution aerosol mass spectrometry,

Atmos. Chem. Phys., 4617–4638, 2018b.

Zhou, S., Collier, S., Jaffe, D. A., Briggs, N. L., Hee, J., Iii, A. J. S., Kleinman, L., Onasch, T. B. and Zhang, Q.: Regional influence of wildfires on aerosol chemistry in the western US and insights into atmospheric aging of biomass burning organic aerosol, Atmos. Chem. Phys., 17(3), doi:10.5194/acp-17-2477-2017, 2017.

Zhou, S., Collier, S., Jaffe, D. A. and Zhang, Q.: Free tropospheric aerosols at the Mt. Bachelor Observatory: More oxidized and higher sulfate content compared to boundary layer aerosols, Atmos. Chem. Phys., doi:10.5194/acp-19-1571-2019, 2019.

Zuidema, P., Sedlacek, A. J., Flynn, C., Springston, S., Delgadillo, R., Zhang, J., Aiken, A. C., Koontz, A. and Muradyan, P.: The Ascension Island Boundary Layer in the Remote Southeast Atlantic is Often Smoky, Geophys. Res. Lett., 45(9), 4456–4465, doi:10.1002/2017GL076926, 2018.

3. Chemical Evolution of Biomass Burning Aerosols Across Wildfire Plumes in the Western U.S.: From Near-Source to Regional Scales

3.1 Abstract

The current understanding of the atmospheric processing of biomass burning organic aerosol (BBOA) and its implications for tropospheric aerosol composition and physicochemical properties remains uncertain. To address this gap, this study investigates the transformation of BBOA from wildfire events in the U.S. Pacific Northwest. Using a high-resolution soot particle aerosol mass spectrometer (SP-AMS) aboard the DOE G-1 aircraft and a second SP-AMS stationed at the Mt. Bachelor Observatory (MBO; ~ 2800m a.s.l.), we analyze the dynamic changes observed in submicron particulate matter (PM_1) concentrations and chemical profiles within wildfire plumes that have undergone varying atmospheric aging durations. These plumes encompass observations ranging from near-field incidences that capture fresh emissions (< 1 hr) to plumes transported extensively across the western U.S. region, undergoing prolonged processing over multiple days. By strategically integrating data from both aerial and mountaintop measurements, we gain valuable insights into the evolutionary path of BBOA in wildfire smoke. While the BBOA oxidation evidently increases with aging, the normalized excess mixing ratio (NEMR) of OA to CO ratio remains relatively unchanged, due to a combination of the evaporation of semi-volatile species and oxidative aging. Secondary aerosol species originating from BB, such as phenolic SOA species and potassium nitrate and potassium sulfate, were also detected. By applying positive matrix factorization (PMF), we investigate the contributions of primary BBOA and secondary BBOA formed through atmospheric reactions involving volatile organic compounds. During each G1 research flight, distinct BBOA types representing various stages of atmospheric processing were identified. These findings shed light on the intricate mechanisms governing the evolution of BBOA characteristics and the formation of SOA within the dynamic environments of wildfire plumes, which could aid in refining atmospheric modeling of BBOA.

3.2 Introduction

The release of aerosols into the atmosphere from wildfires carries adverse consequences on human health, global climate forcing, and regional air quality (Holm et al., 2021; IPCC, 2021; Jaffe et al., 2020; Reid et al., 2016; Schill et al., 2020). These impacts are particularly important for the Western United States, a region that has observed a recent surge in the intensity and frequency of wildfire events. These events have given rise to recurrent and widespread severe air pollution episodes, notably during the summer and fall months (Jolly et al., 2015; McClure and Jaffe, 2018a; O'Dell et al., 2019; Westerling, 2016).

Biomass burning (BB) emits a complex mixture of primary organic aerosol (POA), inorganic species such as black carbon (BC), and volatile organic compounds (VOCs) which can react in the atmosphere to form secondary organic aerosol (SOA) (Andreae, 2019). Within BB plumes, organic aerosol (OA) constitutes a dominant fraction of submicron aerosol (PM_1), followed by BC and particulate chloride and nitrate (May et al., 2014). As they disperse through the atmosphere, BB plumes undergo a multitude of physical and chemical processes that lead to dynamic variations in both aerosol loading and compositional characteristics. For instance, oxidation reactions involving VOCs and $\cdot OH$, O_3 or $\cdot NO_3$ radicals in the gas phase can yield lower volatility species, which have the potential to condense and form SOA (Ahern et al., 2019; Coggon et al., 2019; Jorga et al., 2021). Additionally, heterogeneous and aqueous-phase reactions within BB plumes contribute to both accretion reactions, leading to the formation of SOA, and fragmentation reactions, resulting in the net loss of OA mass (Che et al., 2022; Jiang et al., 2021; Jimenez et al., 2009; Yu et al., 2016).

In addition to these chemical changes, compounds within BB plumes are in a state of equilibrium between the gas and particle phases, dependent on the species vapor pressure, organic aerosol concentration and particle phase state (Donahue et al., 2006). When dense BB plumes mix with clean background air, a greater portion of semi-volatile material partitions from the particle phase to the

gas phase due to dilution-induced evaporation. As suggested by Hodshire et al. (2021), this phenomenon might contribute to the changes observed in aerosol chemical properties within wildfire plumes. For instance, at the plume edge, where dilution effects are more pronounced compared to the central core, aerosols exhibit reduced signal intensity from anhydrous sugars (indicating primary BBOA), alongside an enhanced oxygen-to-carbon ratio (O:C). Furthermore, photochemistry is likely enhanced near the plume edges, due to increased light transmission, resulting in higher OH concentration (Palm et al., 2021).

The chemical and physical transformations occurring within BB plumes have significant impacts on the aerosol physiochemical characteristics. These changes include both the formation of brown carbon (BrC) species and photobleaching processes (Forrister et al., 2015; Palm et al., 2020). Moreover, the production of oxygenated species can significantly increase the overall hygroscopicity of aerosols within BB plumes, even though primary BBOA and BC are inherently hydrophobic (Lambe et al., 2011).

Normalizing OA to excess CO (ΔOA/ΔCO) to account for dilution offers a valuable approach to study the change of OA mass in BB plumes through atmospheric processes. An increase of ΔOA/ΔCO with plume age suggests the formation of SOA, while a decrease indicates the loss of organic matter due to evaporation, fragmentation reactions and deposition (Collier et al., 2016; Ortega et al., 2013). Previous laboratory studies have found increasing ΔOA/ΔCO when BB smoke is subjected to oxidative processing (Hodshire et al., 2019). However, field studies have shown varying results, with some measuring an increase (Yokelson et al., 2009) and others showing a decrease (Akagi et al., 2012; Cubison et al., 2011; Farley et al., 2022). Still others see no change in ΔOA/ΔCO with aging (Garofalo et al., 2019; Wu et al., 2021b; Zhou et al., 2017).

One hypothesis to account for the negligible change of ΔOA/ΔCO seen during some field studies is that the formation of SOA is offset by dilution-driven evaporation of semi-volatile POA (Cubison et al., 2011; Garofalo et al., 2019; Palm et al., 2020; Zhou et al., 2017). However, this scenario still results in

changes in the chemical composition of the OA, as semi-volatile and reduced species are replaced with lower volatility and more oxygenated compounds (Zhou et al., 2017). There are few studies that have explored dilution-induced change in BBOA composition, especially for aging periods greater than a few hours of physical age (Akherati et al., 2022; Kleinman et al., 2020).

Aerosol mass spectrometry (AMS) coupled with positive matrix factorization (PMF) analysis serves as a useful tool for studying the composition, sources, and transformations of ambient aerosols. BBOA factors are commonly resolved during PMF analysis of ambient measurements (Brito et al., 2014; Farley et al., 2022; Jimenez et al., 2009; Paglione et al., 2020; Young et al., 2016; Zhou et al., 2017) and several studies have successfully resolved multiple BBOA factors representing different stages of atmospheric processing of wildfire plumes. Additionally, the composition of aerosol and gas-phase species emitted during biomass burning exhibit variations across fuel types, resulting in differences in both POA and SOA originating from BB (Koss et al., 2018). Fortner et al. (2018) demonstrated that performing PMF analysis on laboratory burn data enables the successful identification of spectral features associated with different types of fuel.

Aircraft-based studies are valuable for studying the composition of wildfire plumes in near-field, often focusing on a few hours of physical aging (Kleinman et al., 2020; Permar et al., 2021; Sedlacek et al., 2022). A recent aircraft study conducted in West Africa sampled agricultural burning plumes after 0.5 hours to 12 hours of aging and revealed significant changes in OA composition which suggest rapid atmospheric processing (Wu et al., 2021b). In contrast, remote mountain top sites offer the capacity to sample transported plumes over a broader range of processing times with minimum interference from local emissions, including measurements of BB plumes that have undergone substantial atmospheric processing for as long as two weeks (Dzepina et al., 2015; Farley et al., 2022; Lee et al., 2022b; Zhang et al., 2018a).

In this study, we examine near-field SP-AMS measurements gathered aboard the DOE G1 aircraft, along with data gathered at the Mt. Bachelor Observatory (MBO; ~ 2800 m a.s.l.) during the 2013 Biomass Burning Observation Project (BBOP). Additionally, we incorporate observations of extensively aged wildfire plumes at MBO during the summer of 2019. This unique approach allows us to comprehensively characterize the evolution of wildfire plumes, ranging from those with less than 30 minutes processing time to those subjected to multiple days of physical transport. Our specific focus is on understanding the changes in BBOA composition and utilizing PMF analysis to unravel the chemical processes involved and examine the formation of SOA. Finally, we discuss the emergence of specific secondary compounds during the transport process.

3.3 Experimental and Data Analysis Methods

3.3.1 Campaign Description

The DOE G1 aircraft was based out of Pasco, WA during the Biomass Burning Observation Project (BBOP) from July-September of the 2013. Throughout this period, the aircraft sampled wildfire plumes across Washington, Oregon, and Idaho (Kleinman et al., 2020). Generally, the aircraft sampled plumes in a pseudo-lagrangian pattern, including transects upwind, directly over, and up to approximately 50km downwind of the emissions sources (Fig. 3.1). A suite of aerosol and trace gas measurement instruments were aboard and are detailed in Liu et al. (2017). The specific instrumentation used in this study is further discussed in detail here.

A High-Resolution Soot Particle Time-of-Flight Aerosol Mass Spectrometer (hereafter SP-AMS; Aerodyne Research) was used for the quantification of non-refractory PM_1 (including most organics, nitrate, sulfate, ammonium, and chloride) as well as refractory material internally mixed with refractory black carbon (rBC). Details of the instrument operation during this campaign are described in Collier et al. (2016) and an overview of the instrument principles are included in Onasch et al. (2012). The SP-AMS was run in dual vaporizer mode, with both an intracavity laser vaporizer and 600°C tungsten vaporizer

installed. Ambient aerosols are focused into the instrument by an aerodynamic lens and the particle beam intercepts a perpendicular Nd-YAG laser beam, resulting in the vaporization of any particles that contain internally mixed BC. Following this, remaining particles impact a tungsten thermal vaporizer, vaporizing non refractory material. The resulting gaseous species are ionized using 70eV electron impact ionization before extraction to the time-of-flight mass spectrometer operated in "Fast-MS" V-mode with 1 Hz time resolution (Kimmel et al., 2011). The instrument was alternated between 52 seconds of "open" and 8 seconds with particle beam blocked ("closed") to determine instrument background. Additionally, the instrument was operated with the laser vaporizer off for some of the plume transects. Both laser-on and laser-off data is considered unless noted otherwise.

CO was measured using Off-Axis Integrated Cavity Output Spectroscopy analyzer (Los Gatos Research, San Jose, CA). NO, NO_2 and NO_y were measured with a 3-channel chemiluminescence instrument (Air Quality Design, Golden, CO). Aerosol concentrations are reported at STP (273.15K, 1 atm). When time series data from different instrumentation were compared, the results were averaged to 10s time resolution to account for any time shift or varying instrument response time.

Out of the 18 research flights conducted during BBOP, this study focuses on a detailed analysis of three. Two of these flights (G1-0730b and G1-0821b) were chosen because they employed pseudo-lagrangian sampling to target fresh BBOA plumes, and exhibited exceptionally high OA loadings with excellent signal-to-noise ratios. Furthermore, both of these research flights sampled wildfire plumes originating from distinct source regions and showed no evidence of source mixing. The flight on the afternoon of July 30th (G1-0730b) sampled emissions from the Colockum Tarps fire in central WA while the August 21st flight (G1-0821b) sampled emissions from the Government Flats fire in Northern Oregon (Fig. 3.1). The third research flight analyzed was conducted on August 6th (G1-0806) and sampled locally and regionally transported plumes from the Douglas and Whisky complexes in Southern Oregon and the Salmon Complex in Northern California. This flight has the added advantage of occurring close to the

Mt. Bachelor Observatory (MBO) ground site, including a direct fly-by (Fig. 3.1). More details about these flights are included in Kleinman et al. (2020), Sedlacek et al. (2022) and Collier et al. (2016).

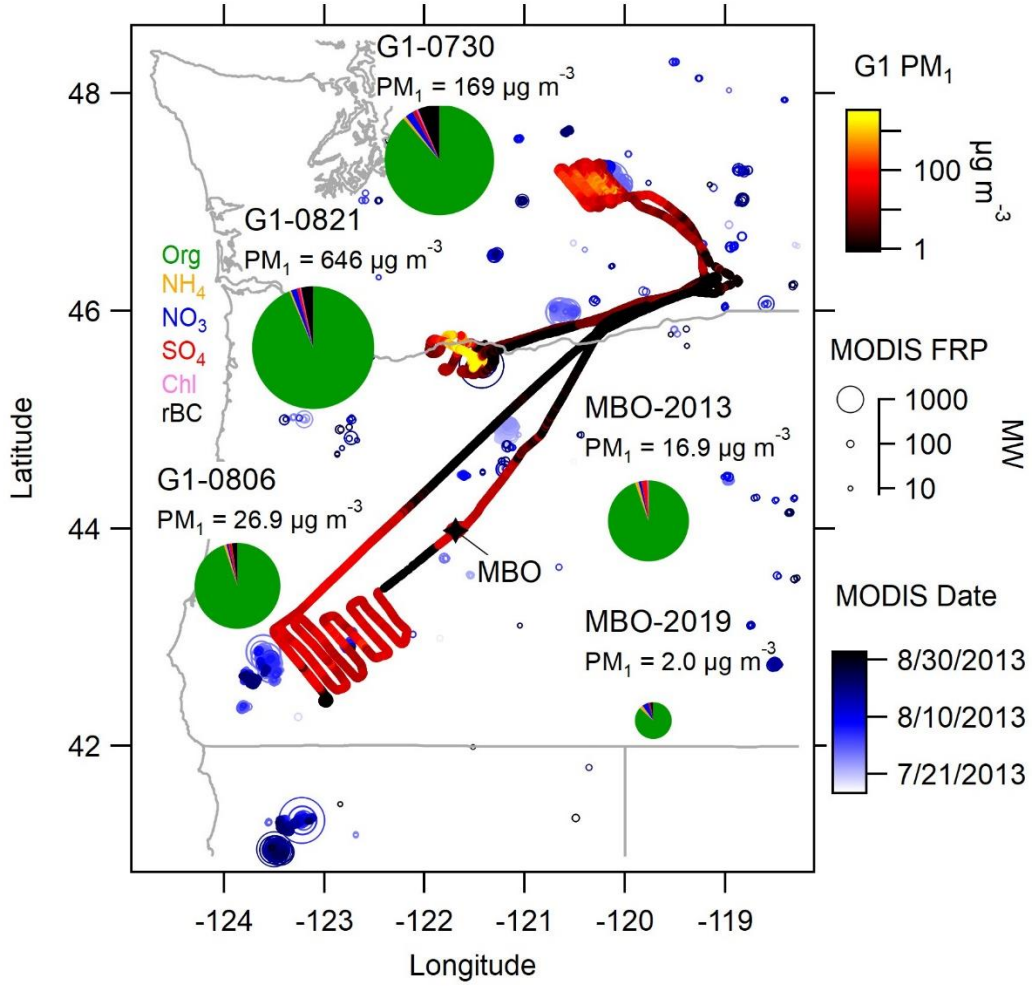

Figure 3.1: Map of the U.S. Pacific Northwest region featuring the flight paths of the G1 research flights used in this analysis, color-coded based on PM_1 concentration. Open circles indicate thermal anomalies detected by the MODIS satellite colored by date and sized by fire radiative power (FRP). Pie charts represent average PM_1 composition measure by SP-AMS, with chart size corresponding to the average $\log_{10}(PM_1)$.

The MBO is a mountaintop atmospheric monitoring site that has been operated since 2004 and been used extensively to characterize transported plumes from local, regional, and intercontinental wildfire events (Baylon et al., 2017; May et al., 2023; Zhang and Jaffe, 2017; Zhou et al., 2017). An SP-AMS was first deployed from Jul-Aug 2013 during the BBOP campaign without the laser vaporizer and was subsequently redeployed from Aug-Sept 2019. Additional details of these AMS deployments are described in previous publications (Collier et al., 2016; Farley et al., 2022; Zhou et al., 2017, 2019).

3.3.2 SP-AMS Data Analysis and Positive Matrix Factorization (PMF)

We expect that all OA during the plume events could be attributed to a set of BBOA factors that represent varying stages of atmospheric processing, or dominant fuel types with distinct emissions profiles. PMF analysis of the G1 SP-AMS data was applied separately to each research flight and was conducted using the ME-2 algorithm within SoFi Pro v9.4 based in Igor 9 (Canonaco et al., 2013). Analysis was performed separately on the three different research flights in order to capture natural variation in aerosol composition due to fuel type and modified combustion efficiency (MCE). For each dataset, one factor was constrained to the highly oxidized BBOA-3 factor identified in Zhou et al. (2017) using the *a*-value approach, while the other factors were allowed to vary freely. The 1 to 5 factor solutions for each research flight were analyzed based on the residual and temporal and spectral features (Zhang et al., 2011), and details are provided in section B1. A three-factor solution was chosen for G1-0821b and G1-0806, while a four-factor solution was chosen for G1-0730b. Subsequently, we categorized the PMF factors, based on their oxidation state and position within the f_{44}/f_{60} space, into fresh BBOA (F-BBOA), aged BBOA (A-BBOA), and highly aged BBOA (HA-BBOA).

The PMF solutions for the MBO ground site during BBOP and 2019 are described in Zhou et al. (2017) and Farley et al. (2022), respectively. During BBOP, three distinct BBOA factors were resolved, including a fresh BBOA (BBOA-1), a moderately aged BBOA (BBOA-2) and a highly aged BBOA (BBOA-3).

During MBO19, due to predominant influence from aged BBOA, only a single BBOA factor was resolved, which represents processed wildfire emissions.

3.3.3 Calculation of Normalized Excess Mixing Ratios (NEMR)

As the wildfire plumes were sampled at increasing distances, it is necessary to account for the dilution effect resulting from mixing with clean background air. To address this, the NEMR of species X relative to the CO concentration was calculated. For the G1-0730b and G1-0821b flights, this procedure was carried out on a point-by-point basis using the following equation

$$\frac{\Delta X}{\Delta CO} = \frac{X_i - X_{bckgd}}{CO_i - CO_{bckgd}} \quad (2)$$

where X_i and CO_i represent the concentrations of species X and CO at a given time point *i*. X_{bckgd} and CO_{bckgd} denote the background concentrations of X and CO, which were defined as the tenth percentile of the respective species measured at MBO during BBOP as this site is generally representative of the background conditions of the western U.S. (Weiss-Penzias et al., 2006; Zhou et al., 2019). Specifically, CO_{bckgd} and OA_{bckgd} were determined to be 0.08 ppm and 2.35 μg sm^{-3}, respectively. This method was used to account for rapid variations in plume composition sampled by the aircraft.

For BB plumes detected at MBO and during G1-0806, NEMRs were determined based on the orthogonal distance regression of species X against CO to better account for variations in background CO (Collier et al., 2016; Farley et al., 2022; Zhou et al., 2017). Plume events were characterized as periods with elevated concentrations of OA, CO and CO_2 accompanied by high correlations ($r^2 > 0.6$) between CO and PM_1 (Collier et al., 2016; Farley et al., 2022; Wigder et al., 2013). Detailed information about the plume events can be found in Collier et al. (2016) and Farley et al. (2022).

3.3.4 Estimation of Plume Age

The aerosol photochemical age was calculated based on the change in NO_x concentration relative to CO. NO_x and CO are both primary species emitted during combustion, however NO_x reacts

quickly with ·OH while CO is relatively inert in the atmosphere. Thus, photochemical age can be calculated using the following equation based on de Gouw et al. (2005) and Roberts et al. (1984)

$$t = \frac{1}{[OH]*k_{NO2+OH}} * [\ln(\frac{[NOx]}{[CO]})_{t=0} - \ln(\frac{[NOx]}{[CO]})_t] \quad (3.1)$$

where t is time in seconds, [·OH] is the ambient concentration of ·OH radical, and k_{NO2+OH} = 1.07x10^{-11} mlc cm^{-3} s^{-1} (Seinfeld and Pandis, 2006). The rate constant k_{CO+OH} is two orders of magnitude lower than k_{NO2+OH}, with a value of 1.5x10^{-13} mlc cm^{-3} s^{-1}. Therefore, it is not included in the calculation due to negligible impact on the final result. $(NO_x/CO)_{t=0}$ is the emission ratio of NO_x (ER_{NOx}) at the point of emission. Due to potential variations arising from fuel type or combustion conditions, the ER_{NOx} was defined separately for G1-0730b and G1-0821b, and was established as the highest 10-second average NO_x/CO ratio observed during the respective flight. Specifically, the values used were 9.52x10^{-3} and 17.8x10^{-3} during G1-0730b and G1-0821b, respectively, and show reasonable agreement with previous measurements of 9.2(±0.6)x10^{-3}, 8.0(±0.3)x10^{-3} and 9.1(±7)x10^{-3} (Akagi et al., 2012; Andreae, 2019; Simpson et al., 2011). Andreae (2019) reports higher values for temperate forests (24(±17)x10^{-3}) than boreal forests (9.1(±7)x10^{-3}) highlighting the importance of fuel type. The higher ER_{NOx} seen during G1-0821 may stem from differences in fuel type or modified combustion efficiency (MCE) during this wildfire (Burling et al., 2010). It is noteworthy that as ER_{NOx} was defined after a brief processing period, the photochemical age represents a lower limit and does not account for plume rise time. The calculation of photochemical age for the G1-0730b and G1-0821b flights was performed on a point-by-point basis following post-averaging of concentrations to 10 seconds intervals to remove potential time shifts resulting from the use of different sampling inlets.

For the G1-0806 flight and MBO measurements, we employed the approach described in Collier et al. (2016) to pinpoint individual plume events and subsequently determined a single NO_x/CO value for each plume event by calculating the slope through orthogonal distance regression over the duration of the event. Plume events with an $r^2 < 0.5$ between NO_x and CO were discarded from further analysis.

This included 1 of the 10 plumes during the G1-0806 flight, and 13 of the 18 plumes sampled at MBO during BBOP. The plumes with low correlation are likely due to either mixing of different sources or periods where NO_x has been fully depleted from the airmass. ER_{NOx} was set to $9.2x10^{-3}$ based on Simpson et al. (2011). The sensitivity of the calculated photochemical age was assessed, and similar results were seen when using the values reported in Simpson et al. (2011), Akagi et al. (2012), or those for boreal forests as presented by Andreae (2019), as expected given that the EF_{NOx} values in these studies are within 12% of each other. However, using the much higher temperate forest EF_{NOx} value from Andreae (2019) yielded photochemical ages about 50% higher (Fig. B1).

·OH concentration was not measured directly during this campaign, but previous studies have documented [·OH] in wildfire plumes ranging from $<1x10^6$ cm^{-3} to $1.7x10^7$ cm^{-3} (Akagi et al., 2012; Hobbs et al., 2003; Liao et al., 2021; Yokelson et al., 2009). For the purpose of this campaign, we assumed an

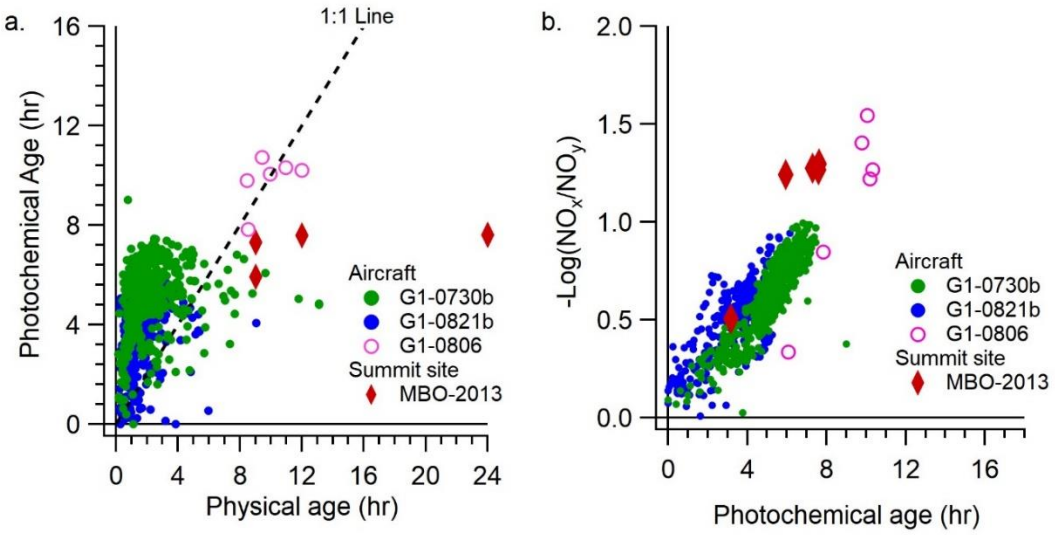

Figure 3.2: (a) Comparison between photochemical age derived from the ratio of NO_x/CO and the physical age calculated from aircraft distance and windspeed (G1 data) or HYSPLIT back trajectories (MBO). (b) comparison between the -Log(NOx/NO_y) and the photochemical age derived from NO_x/CO.

[·OH] of $1x10^7$ cm^{-3}, as this choice results in photochemical ages that roughly align with the physical transport times discussed below (Fig. 3.2). It is important to note that this assumed ·OH concentration

represents an average concentration over the duration of the plume transport. Yokelson et al., (2009) found a rapid decrease of [·OH] as BB plumes were diluted, suggesting that there may be considerable spatiotemporal variation in the [·OH].

The physical transport times for the G1-0730b and G1-0821b research flights were calculated by dividing the distance between the aircraft and the emission source by the windspeed measured by the aircraft at the time of sampling. The location of plume emission was determined by identifying thermal anomalies detected by MODIS aboard the Aqua and Terra satellites. For the smoke plumes captured during G1-0806 and during both MBO measurements periods, the physical transport time was estimated through a comparison of back trajectories obtained using the HYSPLIT model and the MODIS thermal anomalies. Further details regarding this approach can be found in Collier et al. (2016) and Farley et al. (2022).

As expected, plumes sampled during G1-0730b and G1-0821b show the lowest photochemical and physical ages, indicating the sampling of fresh emissions (Fig. 3.2a). Conversely, the plume events sampled during G1-0806 and at MBO during BBOP display more significant aging. The lack of a linear correlation between photochemical age and physical age can be attributed to spatial variations within the plume, such as emission sources, windspeed and ·OH concentration. Assuming [·OH] = $1x10^7$ cm^{-3} yields moderate agreements between photochemical age and physical age for plumes approximately 10 hours after emission. However, a higher photochemical age relative to physical age is observed for the G1-0730b and G1-0821b flights, suggesting that [·OH] in the freshest sections of the plume might be even higher. On the contrary, the opposite trend seen in the MBO13 plumes suggests that the average ·OH concentration in aged plumes is lower than $1x10^7$ cm^{-3}, consistent with other measurements of ·OH in the remote troposphere (Wolfe et al., 2019). At higher physical age values, the photochemical age appears to reach a plateau, possibly due to the near-complete removal of NO_x from the plume or lower ·OH concentrations as the plume is diluted downwind.

Another commonly used photochemical age metric involves tracking changes in the ratio of NO_x to total oxidized nitrogen (NO_y), usually expressed as $-\log(NO_x/NO_y)$ (Kleinman et al., 2020, 2008; Olszyna et al., 1994). The chemical conversion of NO_x into NO_y is a complex process involving multiple competing reactions and no single rate constant, so no attempt was made to convert $-\log(NO_x/NO_y)$ into a physical age. Nevertheless, a strong correlation is seen between $-\log(NO_x/NO_y)$ and photochemical age calculated using NO_x/CO, indicating that both approaches capture comparable chemical processes (Figure 3.2b).

At the MBO site, many of the BB plumes exhibited poor correlations between NO_x and CO with $r^2 < 0.5$. This pattern was observed in 13 out of the 18 plumes identified in 2013 and all 10 plumes in 2019, in which the NO_x concentrations were low as and the NO_x/CO slopes approached zero. These results highlight that both the NO_x/CO and NO_x/NO_y photochemical age metrics are best suited for fresher plumes when NO_x levels are elevated above the regional background. Attempting to calculate the photochemical age for plumes where NO_x has dropped to background levels would yield artificially low age estimates.

One source of uncertainty in converting NO_x/CO to photochemical age is the rapid formation of peroxyacetyl nitrate (PAN), which may account for as much as 40% of the loss of initial NO_x (Alvarado et al., 2010; Decker et al., 2021). Furthermore, the thermal decomposition of PAN in aged air masses may enhance NO_x concentrations, potentially resulting in an artificial decrease in estimated photochemical age. This is especially relevant at the MBO site where daytime temperatures regularly reached 20°C, corresponding with a PAN lifetime with respect to thermal decomposition of approximately 1 hour (Fischer et al., 2011; Talukdar et al., 1995).

3.3.5. **Quantification of Aerosol Volatility**

The volatility of aerosol particles was characterized at the MBO site during both the 2013 and 2019 studies using a digitally controlled thermodenuder (TD) system positioned upstream of the SP-AMS

(Farley et al., 2022; Zhou et al., 2017). The TD operation was automated via a custom program that cycled through 12 different temperatures ranging from 30 to 280°C, with 10-min intervals. An automatic 3-way ball valve facilitated the transition of the aerosol flow between the TD and the bypass sampling modes every 5 minutes. During the bypass mode, the temperature inside the TD was brought to thermal equilibrium with the next pre-set temperature before switching back to the TD mode. PMF analysis was conducted on the dataset comprising mass spectra acquired from both the TD and the bypass modes, thus allowed for the determination of the thermal profiles of individual OA factors.

Here, the aerosol volatility is quantified using the volatility basis set approach (Donahue et al., 2006). The VBS for each BBOA PMF factor was determined from the mass thermogram using the evaporation model described previously (Cappa, 2010; Cappa and Jimenez, 2010; Karnezi et al., 2014; Riipinen et al., 2010).

The mass flux of species *i* from the gas phase to the particle phase was calculated as

$$I_i = \frac{2\pi d_p M_i D_i \beta_{mi}}{RT_{TD}} \left(p_i - p_i^0\right) \quad (3.2)$$

where d_p is the particle diameter and R the ideal gas constant. D_i is the diffusion coefficient of *i* and assumed to be 5.8×10^{-6} m^2 s^{-1}. T_{TD} is the temperature within the thermodenuder, p_i^0 and p_i are the partial vapor pressures of *i* at the particle surface and far from the particle. As gas-phase species are removed by the thermodenuder, p_i^0 is assumed to be 0. M_i is the molecular weight of *i*, which was estimated to be 200 g mol^{-1} at $C^* = 1 \times 10^3$ and increase by 20 g mol^{-1} for every $\log_{10}C^*$ increment (Shiraiwa et al., 2014; Yu et al., 2016).

The mass flux was corrected for the transition regime by using β_{mi}

$$\beta_{mi} = \frac{1 + Kn_i}{1 + \left(\frac{4}{3\alpha_{mi}} + 0.377\right) Kn_i + \frac{4}{3\alpha_{mi}} Kn_i^2} \quad (3.3)$$

where Kn_i is the Knudsen number and α_{mi} is the mass accommodation coefficient, assumed to be 1 (May et al., 2013). The saturation vapor pressure of *i*, C_i^*, was estimated at 298K using the integrated Clausius-Clapeyron equation

$$C_i^*(T_{TD}) = C_i^*(298K)\exp\left[\frac{\Delta H_{vap,i}}{R}\left(\frac{1}{298} - \frac{1}{T_{TD}}\right)\right]\left(\frac{298}{T_{TD}}\right) \quad (3.4)$$

The enthalpy of vaporization was estimated from the parametrization from May et al. (2013)

$$\Delta H_{vap} = 85 - 4\log(C^*) \quad (3.5)$$

The mass flux was integrated over the residence time in the TD system (8.2 seconds) and multiplied by the total number of particles, assuming particle sphericity and an aerosol density of 1500 kg m^{-3}. For this analysis, a mono-dispersed particle population was assumed based on the average size distribution measured by the SP-AMS, with d_{va} of 500 nm for 2013 and 400 nm for 2019 (Farley et al., 2022; Zhou et al., 2017). Likewise, we utilized the average concentration of each PMF factor over the entire measurement period to constrain the total organic aerosol mass in each factor (C_{OA}). This was determined as 5 µg m^{-3}, 3 µg m^{-3}, 5 µg m^{-3} and 0.5 µg m^{-3} for BBOA-1, BBOA-2, BBOA-3 and the BBOA factor from 2019, respectively (Farley et al., 2022; Zhou et al., 2017).

The total organic aerosol mass (C_{OA}) was calculated as

$$C_{OA} = \sum_i C_{i,tot}\left(1 + \frac{C_i^*}{C_{OA}}\right)^{-1} \quad (3.6)$$

C_{OA} in each C^* bin was adjusted such that the reconstructed thermogram matched the measured thermogram and the total C_{OA}. From this, $C_{i,tot}$ was found using the following equation:

$$F_p = \left(1 + \frac{C_i^*}{C_{OA}}\right)^{-1} \quad (3.7)$$

where F_p is the fraction of mass in the condensed phase.

The OA evaporation rate was estimated following the method presented in Cappa and Jimenez (2010). Specifically, the total organic mass C_i was decreased by the dilution factor, and the new

equilibrium particle phase concentration was determined by iteratively solving equation 6 for C_{OA}. The percent of mass evaporated was then calculated as

$$E_{loss} = 100 * \left(1 - \frac{C_{OA}(DF)}{C_{OA}(0)/_{DF}}\right) \quad (3.8)$$

where C_{OA}(DF) is the OA concentration following evaporation, C_{OA}(0) is the original OA concentration, and DF is the dilution factor.

3.4 Results and Discussion

3.4.1 Overview of Variability of Organic Aerosol Chemistry within Wildfire Plumes

The measurements analyzed here encompass wildfire emissions that have undergone a wide range of atmospheric processing time, extending from less than one hour to multiple days of transport. The plumes sampled during the three research flights were characterized by high PM_1 loadings and CO concentrations (Fig. 3.1). As these flights were located within the remote free troposphere, PM originating from sources other than BB is expected to be negligible compared to the smoke plume. Both the G1-0821b and G1-0730b flights followed a pseudo-Lagrangian sampling approach, capturing fresh plumes that were likely less than 30 minutes post-emission during their closest transects. These transects exhibited the highest PM_1 and CO concentrations, reaching a maximum of 9,753 µg sm^{-3} and 16 ppmv, respectively, for G1-0821b, and 2,803 µg sm^{-3} and 5.1 ppmv, respectively, for G1-0730b. As the distance from the source increased, the plume gradually mixed with cleaner background air, and became increasingly dilute. The lower concentrations observed on the outer edges of each transect indicate that the plume structures were well-defined, and background concentrations of PM_1 remained low.

The G1-0806 research flight sampled wildfire emissions that were more dilute compared to the other two G1 flights, exhibiting significantly lower PM_1 concentrations peaking at 365 µg sm^{-3}. Considerably more spatial homogeneity was seen across individual transects during this flight,

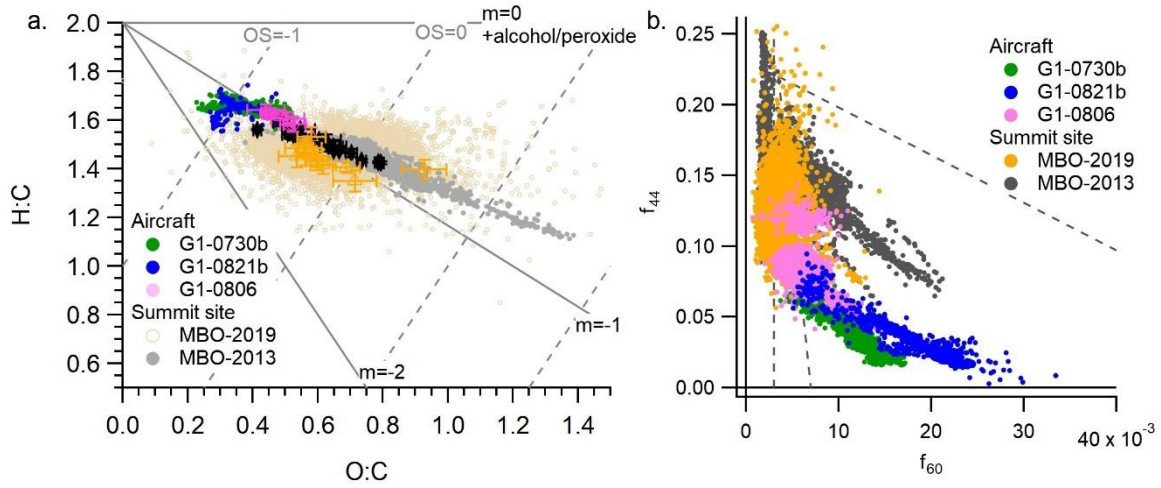

Figure 3.3: (a) Van Krevelen diagram plotting bulk H:C and O:C and (b) f_{44}/f_{60} triangle plot for BBOA in the wildfire plumes observed in this study.

suggesting a less well-defined plume that had mixed more extensively with the regional background air (Fig. 3.1). Based on comparison of back-trajectories with the location of MODIS-detected thermal anomalies, this flight likely sampled a mixture of local emissions and moderately processed emissions that mixed with the regional background. Throughout all three research flights, OA contributed the dominant fraction of PM_1, accounting for >89% of total mass (Fig. 3.1). Following this was rBC (2-6%), while chloride, sulfate, nitrate and ammonium each accounted for ≤2% of total PM_1.

The Mt. Bachelor summit site characterized BB plumes that had undergone significantly longer transport durations. During the 2013 campaign, a series of wildfires occurred about 200-350 km upwind of MBO in southern Oregon and northern California. In this analysis, only aerosol measurements at MBO with OA > 3μg m^{-3} and the mass fraction of BBOA factors > 40% (as based on source apportionment performed in Zhou et al. (2017)) were considered. This approach was adopted to mitigate the influence of periods dominated by non-BB sources such as biogenic SOA. A detailed analysis of the MBO 2013 results is documented in previous publications (Collier et al., 2016; Zhang et al., 2018a; Zhou et al., 2017, 2019). Overall, periods at MBO influenced by BB show similar aerosol

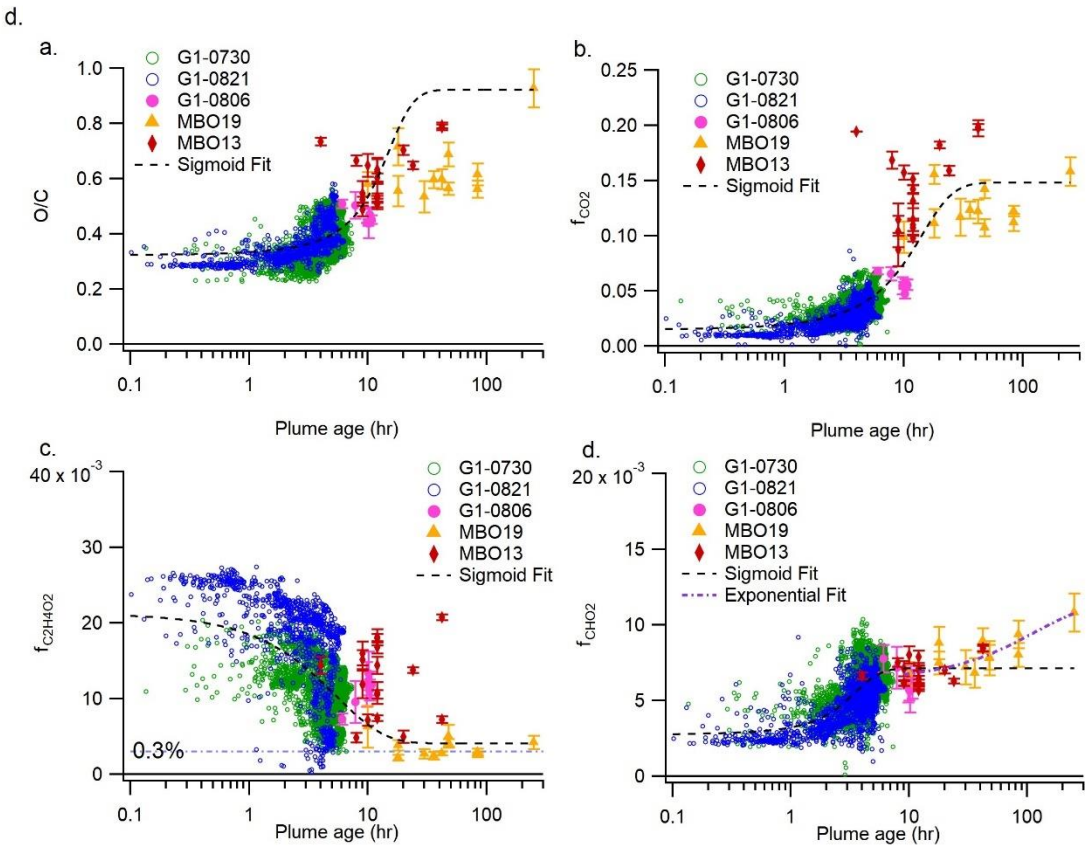

Figure 3.4: Change in (a) O/C, (b) f_{CO2}, (c) f_{C2H4O2} and (d) f_{CHO2} with plume age. Plume age is defined as the photochemical age for the G1 measurements and as the physical age for the MBO measurements. A sigmoid function is applied to fit all of the data points. In (d), an exponential fit for f_{CHO2} data points at more than 10 hours is also included.

characteristics to those observed during the G1 flights. NR-PM_1 was dominated by OA (94.9%) followed by SO_4 (2.3%), NH_4 (1.4%), NO_3 (1.2%) and chloride (<1%). Note that black carbon was not quantified at the MBO site in 2013. 18 BB plumes with clear emission sources are highlighted for detailed analysis, with physical transport times ranging from 4 to 42 hours (Collier et al., 2016). In 2019, wildfire emissions sampled at MBO were significantly more aged, with physical transport time of the BB plumes ranging from 10 to 250 hours (Farley et al., 2022). However, the overall aerosol composition was similar, with OA contributing 87% of PM_1 followed by NO_3 (5.6%), NH_4 (3.0%), rBC (2.7%) and sulfate (1.7%).

Back-trajectory analysis indicates that the BB-influenced airmass sampled during the G1-0806 flight was directly transported to MBO. This provided an interesting opportunity to analyze wildfire plumes from the same emission source but with a significantly increased transport time span and helps eliminate the effect of variations in fuel type and combustion efficiency.

Despite the differences in sampling location, the trends in aerosol evolution display similar patterns between the different measurement locations. The atmospheric processing of OA can be explored using the Van Krevelen diagram, plotting bulk O/C against H/C (Heald et al., 2010). The relationship between H/C and O/C, as depicted by the slope, can yield information regarding the dominant chemical reaction types within a specific chemical system, e.g., the formation and aging of SOA from a particular source. A slope of 0, -1, and -2 corresponds to the addition of alcohol/peroxide functional groups, carboxylic acid, and carbonyl groups, respectively. Previous ambient measurements in locations dominated by biogenic or anthropogenic emissions have typically shown slopes near -1 (Heald et al., 2010; Ng et al., 2011) while measurements of ambient BBOA have revealed slopes closer to zero (Brito et al., 2014; Gilardoni et al., 2016). However, experiments involving the aging of BB smoke in an oxidative flow reactor have indicated that the •OH oxidation of BBOA from most biomass fuels yields a slope close to −0.5, except for Ponderosa pine smoke, which exhibits a slope of nearly zero (Ortega et al., 2013). The mixing of aerosols from different sources can also result in variations in the overall O/C and H/C of OA that mimic the trends resulting from chemical transformations. However, this influence is expected to play a minor role on the observed changes in O/C and H/C for the wildfire plumes in this study, due to the predominance of BBOA in these measurements.

G1-0821b and G1-0730b demonstrate slopes of 0.05 and -0.15, respectively, suggesting that the formation of alcohol or peroxide functional groups played a significant role during the aging of freshly emitted wildfire plumes. This near-zero slope is especially apparent at O/C values < 0.4. As O/C values exceed 0.4, the slope gradually increases, as seen in the most oxidized aerosol during G1-0730b.

Conversely, G1-0806 and the MBO-13 plume events show negative slopes of -0.58 and -0.54, respectively. The trend observed during the MBO-19 plume events lacks a clear linear trend ($r^2 = 0.32$), indicating diverse processing pathways, or mixing with other sources of aerosol. Specifically, as MBO-19 had the lowest BBOA concentrations, the bulk aerosol properties may be influenced by biogenic SOA. This may also explain the slight offset between MBO-19 and MBO-13 seen in figure 3.3.

Taken together, these results indicate that while near-field processing primarily involves the formation of alcohol or peroxide moieties, the formation of carboxylic acids or carbonyl functional groups becomes increasingly prominent with extended aging. Additionally, there is a clear increase trend in the bulk OA O/C ratio with photochemical age (Fig. 3.4), similar to what is seen in other studies (Cappa et al., 2020; Cubison et al., 2011).

The three G1 flights were conducted during mid-afternoon in July-August when photochemical activity is expected to be strongest. As demonstrated by Zhou et al., (2017), daytime aging of wildfire plume resulted in significantly more oxidized BBOA. However, back trajectories performed during G1-0806 suggest that the plume transport time range from 0-15 physical hours. This implies that while most of the transport occurred during the daytime, the most aged emissions might have also experienced several hours of nighttime transport. Furthermore, the measurements at MBO continued for over 1 month, capturing BBOA transported both at night and during daytime. Although we do not have measurements of photolysis rates, visual observations of the plumes during the G1-0730b and G1-0821b flights indicate they were optically dense. Palm et al. (2021) has reported enhanced j_{HONO} and photolysis rates near the plume edges in comparison with the core (Palm et al., 2021). Likewise, as shown in Fig.

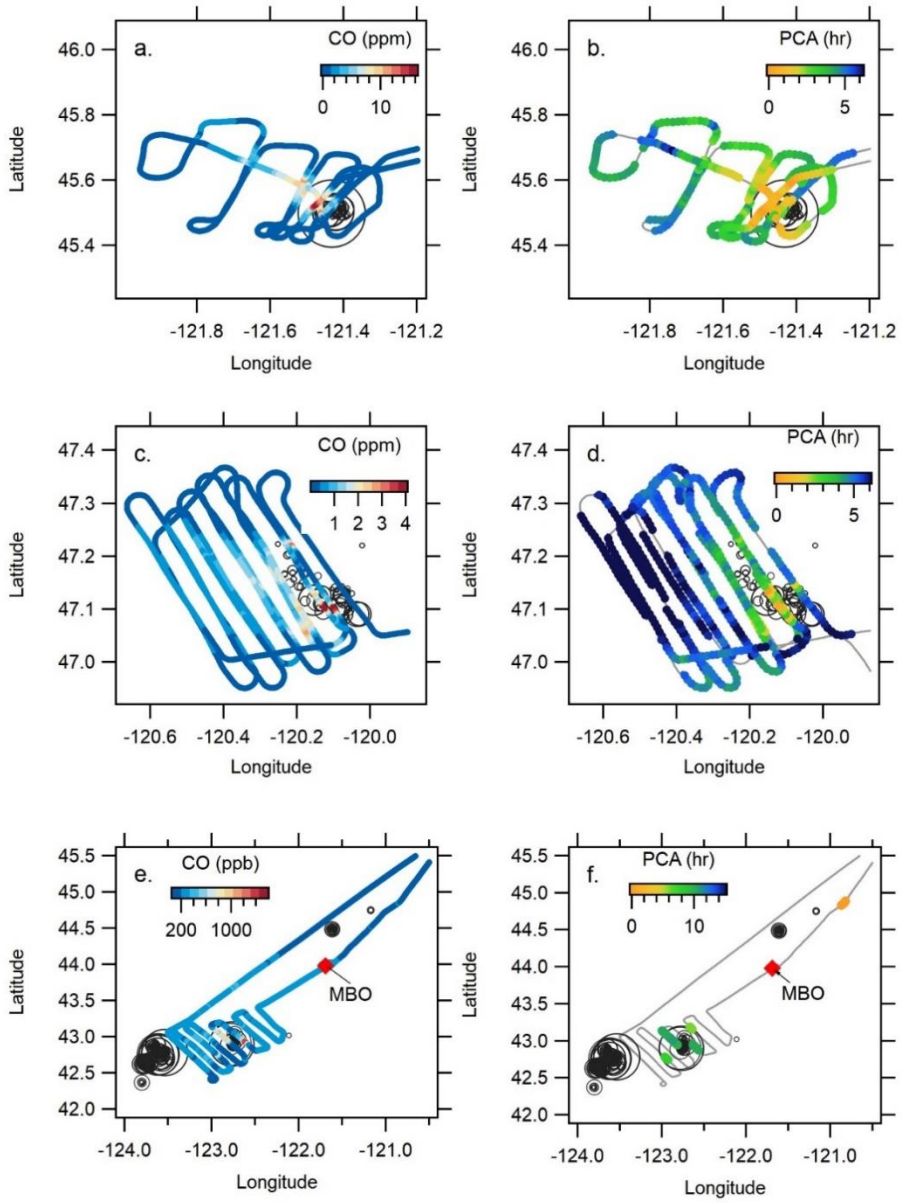

Figure 3.5: Flight track of G1-0821b colored by (a) CO and (b) photochemical age. Flight track of G1-0730b colored by (c) CO and (d) photochemical age. Flight track of G1-0806 colored by (e) CO and (f) photochemical age.

3.5, we see much higher photochemical ages on transect edges nearest the source when compared to the plume's core, suggesting that the photochemical age metric effectively captures this heterogeneity within the plume. Interestingly, as the plume undergoes dilution, this effect becomes increasingly

negligible, and eventually reverses, with the plume core showing higher photochemical ages relative to the edges. This is most likely a result of the spatial gradient of oxidants similar to what was reported in Palm et al. (2021).

The processing of BBOA can also be visualized using the f_{44}/f_{60} triangle plot introduced in Cubison et al. (2011). $f_{60,}$ the fraction of organic mass at *m/z* 60 (mostly $C_2H_4O_2^+$), is a tracer for anhydrous sugars including levoglucosan, while the analogous f_{44} (mostly CO_2^+) is a marker for carboxylic acids. Upon oxidation, f_{60} decreases while f_{44} increases in the AMS spectra of BBOA. As expected, all of the measurements considered here transition from the bottom right to the top left of the plot (Fig. 3.3b). Notably, for G1-0730b and G1-0821b, there is a clear increase of f_{CO2} and decrease in f_{C2H4O2} with photochemical age (Fig. 3.3). In periods of low photochemical age, we observe a decrease in f_{60} with only a minimal corresponding increase in f_{44}, whereas the trend becomes steeper after f_{60} drops below 0.1%. This trend is consistent with the loss of semi-volatile materials such as levoglucosan prior to the formation of carboxylic acids.

Potassium is often used as a tracer for BB in the ambient environment (Andreae, 1983; Li et al., 2003). Potassium salts are hydroscopic, and therefore their presence in aerosol can have important implications on CCN activity (Kristensen et al., 2021). Here, K^+ was measured, as well as a variety of potassium salts, including $K_3SO_4^+$, $K_2NO_3^+$, K_2Cl^+ and K_2OH^+. These salts likely represent the ionized adducts of K_2SO_4, KNO_3, KCl and KOH, respectivally. Previous studies have found negligible enhancement of K^+ at MBO (Farley et al., 2022; Zhou et al., 2017) and interestingly, no enhancement was seen during G1-0806 which sampled emissions from similar sources confirming that these sources were depleted in potassium. This can be explained by differences in fuel type, as fuels such as sage have been found to emit a higher mass fraction of K than montane species such as Douglas fir and Ponderosa pine (Chen et al., 2007; McMeeking et al., 2009).

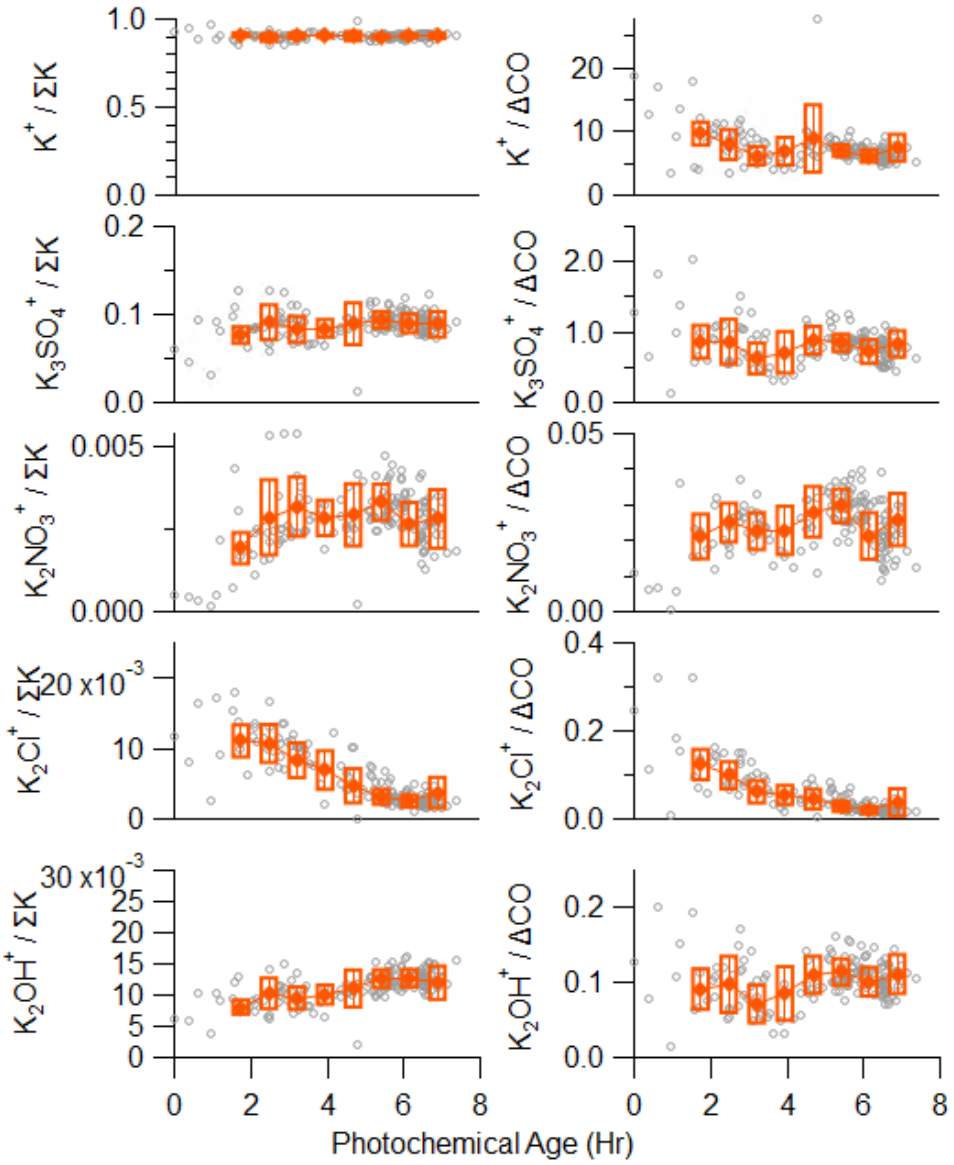

Figure 3.6: Change in fractional contribution potassium species to total potassium signal with photochemical age observed during the G1-0730b research flight.

High concentrations of K species were seen during both G1-0730b and G1-0821b sampling. Here we use G1-0730b as a case study to delve into the transformations of potassium salts. During this research flight, approximately 80-90% of the potassium was detected as K^+, however, non-negligible amounts of $K_3SO_4^+$, $K_2NO_3^+$, K_2Cl^+ and K_2OH^+ were also detected (Figure 3.6). While these compounds have been

detected with laser-ablation single particle mass spectrometry before (Pratt et al., 2010, 2011; Zauscher et al., 2013), their detection with SP-AMS has been infrequent (Farley et al., 2023).

Quantification of K-containing compounds is difficult with AMS measurements due to the potential of thermal ionization processes occurring on the tungsten vaporizer, or on the surface of rBC when the laser vaporizer is utilized. In this study, concentrations of K-containing species are reported in nitrate equivalents (i.e., RIE = 1). Additionally, we do not know the fragmentation pattern of K-containing compounds. We expect that K compounds are internally mixed with rBC, suggesting that laser vaporization is the dominant ionization process for the K^+ adducts. However, we do observe a shift in the $^{39}K^+$ peak by 0.007 amu, indicative of surface ionization occurring upon either the tungsten vaporizer or rBC particles as they are vaporized (Drewnick et al., 2015).

Most K is emitted as KCl and KOH during biomass combustion (Sorvajärvi et al., 2014). During atmospheric transport, these compounds can undergo acid replacement reactions with H_2SO_4 and HNO_3 to form K_2SO_4 and KNO_3, respectively. The presence of these species was found to increase with longer aging time, although these reactions are dependent on the availability of precursors (Li et al., 2003; Zauscher et al., 2013). There is also evidence to suggest that if sufficient $SO_{2(g)}$ is present during combustion, K_2SO_4 can be formed directly during the combustion process, especially at high temperatures (>1000°C) (Cao et al., 2019; Li et al., 2013). These conditions are more likely to be met during flaming combustion, may explain why previous studies have reported an exponential increase in particulate potassium concentration with MCE (Wang et al., 2020c).

During this campaign, K^+ exhibited the highest concentration, followed by $K_3SO_4^+$, K_2Cl^+, K_2OH^+, and $K_2NO_3^+$ (Figure 3.6). As expected, K_2Cl^+ shows a rapid decrease with photochemical age, with minimal enhancements at PCA > 5 hours, consistent with loss of KCl through rapid acid displacement. The decline of K_2Cl^+ concentration behaves as a pseudo-first-order reaction, with a rate constant of 0.37 hr^{-1}. This suggests that K_2Cl^+ could be a useful indicator of transport time in the near field, although its

sensitivity to H_2SO_4 and HNO_3 concentrations and aerosol pH remains unknown. $K_3SO_4^+$ was expected to be a secondary species, but no clear trend with photochemical age was observed. Instead, a strong dependence on sulfate was seen ($r^2 = 0.89$), indicating that formation of K_3SO_4 may be more strongly related to the sulfate concentration. It is likely that this compound has already formed by the time of the first transect or during the combustion process. Although concentrations of $K_2NO_3^+$ were low, they increased with age, consistent with secondary formation.

3.4.2. Age-Dependent NEMRs in Wildfire Plumes and Evidence of Chemical Transformation of BBOA

Figure 3.7 presents an overview of the changes in the normalized excess mass ratio of OA relative to CO (ΔOA/ΔCO) with plume age for the wildfire plumes observed in this study. During the G1-0730b and G1-0821b research flights, there is no statistically significant relationship between ΔOA/ΔCO and photochemical age, and much of the variability in ΔOA/ΔCO is associated with substantial changes in the OA concentration (Fig. 3.7). However, for plumes sampled during G1-0806 and at MBO, ΔOA/ΔCO exhibits a pronounced decreasing trend at a photochemical age greater than 12 hours. These findings indicate that within the first few hours of atmospheric aging, neither SOA production or OA evaporation dominates. However, at extended processing times (e.g., > 12 hours), the loss of aerosol mass due to

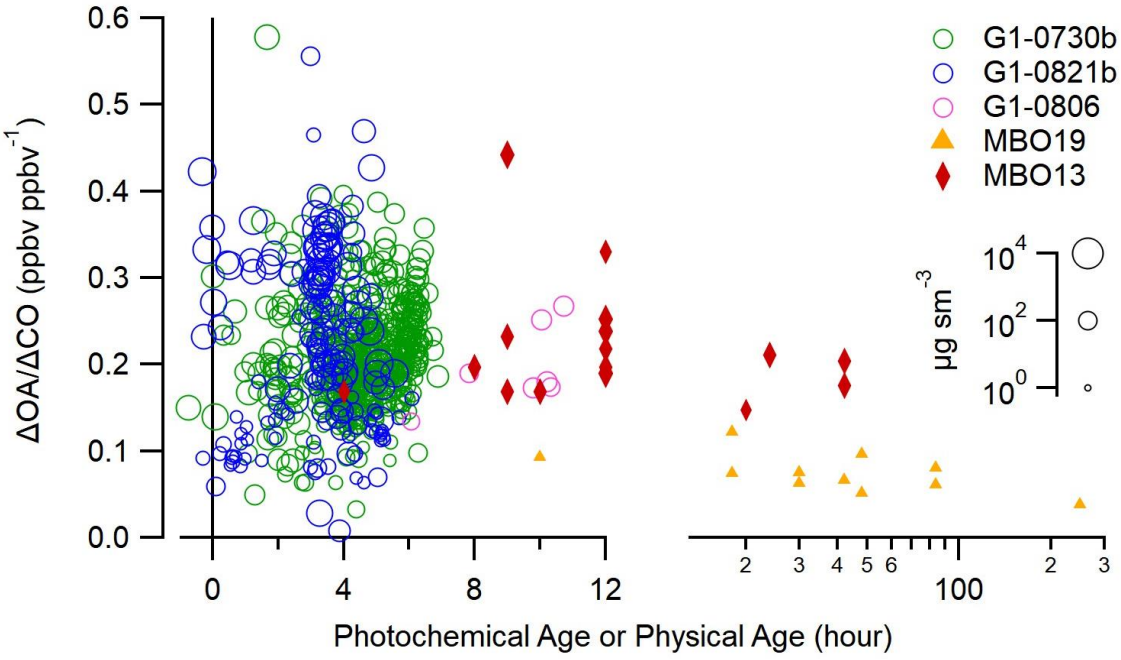

Figure 3.7: Change in ΔOA/ΔCO with plume age. Symbols are sized by the log transformed organic aerosol loading. x-axis transitions to log scale at 12 hours.

chemical fragmentation, evaporation, and/or deposition becomes more important in comparison to secondary aerosol formation.

Phenolic SOA, which includes nitrophenolic compounds and oligomers, is an important component of secondary BBOA and has an outsized impact on aerosol absorption and toxicity (Bonnefoy et al., 2010; Palm et al., 2020). Gas-phase phenolic compounds, such as phenol (C_6H_6O), guaical ($C_7H_8O_2$), catechol ($C_6H_6O_2$), and guaiacyl acetone ($C_{10}H_{12}O_3$), are emitted in large quantities from BB and can react in the gas or aqueous phase to form highly substituted compounds (Schauer et al., 2001; Simpson et al., 2005). These substituted phenols possess high Henry's Law constants and aqueous-phase processing pathways result in the efficient production of low volatility products (Ma et al., 2021; McFall et al., 2020; Smith et al., 2014, 2016). It is also thought that nitrophenol compounds are an important component of tarballs, which are extremely low volatility, light absorbing aerosols commonly found within wildfire plumes (Adachi et al., 2019). Laboratory studies have identified a number of HR-

AMS fragments that are indicative of phenol SOA (Jiang et al., 2021; Sun et al., 2010; Yu et al., 2014). Furthermore, these studies have also shown that over the course of several hours of photochemical aging, the composition of phenolic SOA undergoes transition from being dominated by large oligomeric compounds to smaller, oxygenated species, such as carboxylic acids (Jiang et al., 2023; Yu et al., 2016). The CHO_2^+ fragment serves as a mass spectral tracer ion for carboxylic acids, which were identified as important SOA products resulting from phenol photooxidation (Jiang et al., 2023). Figure 3.4c shows the f_{CHO2} as a function of photochemical age, and a clear increase is seen. Interestingly, the increase in this ion occurs earlier and at a faster rate than the increase in f_{CO2}, with an inflection point at 2.7 hours, in contrast to 8.5 hours.

Although the absolute concentration of nitrogen containing organics is generally low, they are an important component of brown carbon (BrC) and can have an outsized role on aerosol absorption (Palm et al., 2020). Organonitrates ($pRONO_2$) undergo fragmentation reactions during the ionization process within the AMS, resulting in the loss of the nitrate functional group. However the fraction of $pRONO_2$ to total particulate nitrate can be estimated by changes in the NO^+/NO_2^+ fragmentation ratio (Day et al., 2021; Farmer et al., 2010). Specifically, the "ratio-of-ratios" method was used:

$$f_{\mathrm{pRONO_2}} = \frac{(\mathrm{R_{Measured}} - \mathrm{R_{NH_4NO_3}})(1 + \mathrm{R_{pRONO_2}})}{(\mathrm{R_{pRONO_2}} - \mathrm{R_{NH_4NO_3}})(1 + \mathrm{R_{Measured}})}$$

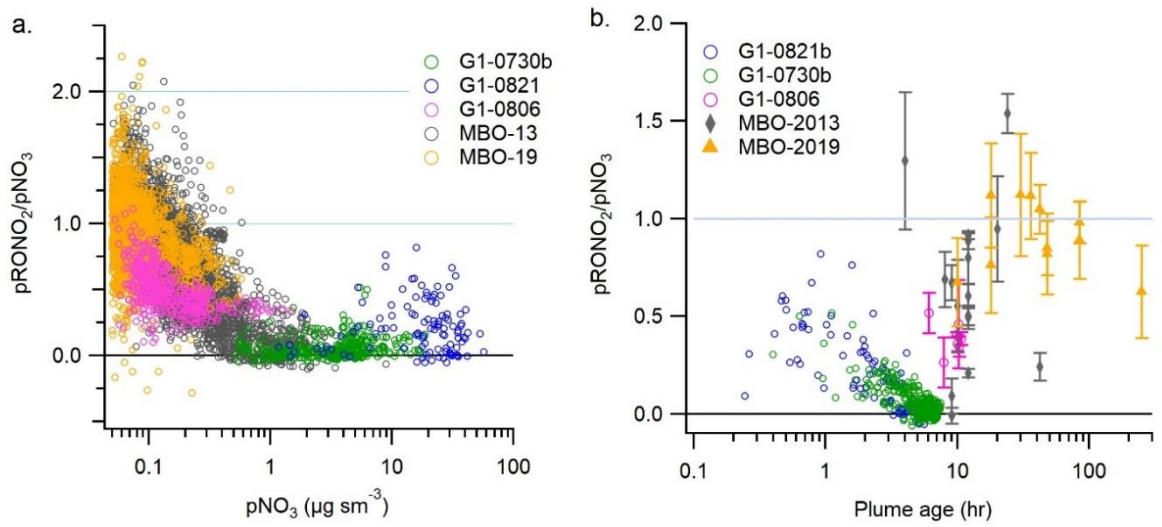

Figure 3.8: Fractional abundance of organonitrate to total particulate nitrate as a function of (a) total particulate nitrate and (b) plume age.

where f_{pRONO2} is the fraction of nitrate mass attributed to $pRONO_2$, $R_{measured}$, R_{pRONO2} and R_{NH4NO3} are the NO_2^+/NO^+ ratios in the ambient measurements, for pure ON and pure ammonium nitrate respectively (Day et al., 2021). An assumed R_{NH4NO3}/R_{pRONO2} value of 2.75 was assigned for pure $pRONO_2$.

The fraction of nitrate attributed to ON shows a decrease with increasing total nitrate concentration (Fig. 3.8a), a trend similar to findings from other studies (Day et al., 2021; Ge et al., 2021). At MBO, nearly all of the nitrate signal was associated with inorganic nitrate during periods with high total nitrate, which correspond with the BB periods. In contrast, both G1-0730b and G1-0821b exhibit an inverse relationship, with periods of higher f_{pRONO2} values observed at greater nitrate loadings. The f_{pRONO2} during these two flights appear to be related to photochemical age, with fresh emissions showing higher f_{pRONO2} (Fig 3.8b). For instance, at photochemical ages less than 1 hour, ON accounted for up to 80% of the particulate nitrate, but this percentage decreased to <10% after 5 hours. As the aging processes continue beyond 10 hours, the f_{pRONO2} increases and eventually approaches 1 for the most aged BB plumes.

3.4.3 Analysis of BBOA Transformation using Positive Matrix Factorization (PMF)

We employed PMF analysis to further probe the transformations of BBOA and gain a better understanding of the primary and secondary organic aerosol components in wildfire plumes. The spectral characteristics of all PMF factors are shown in Figure B2-4. The fresh BBOA factors (F-BBOA), representing primary BBOA, exhibit the highest signals at $C_2H_4O_2^+$ and $C_3H_5O_2^+$, which are indictive of levoglucosan and other anhydrosugars (Fig 3.9). Anhydrosugars are released during the pyrolysis of cellulose and their abundance in aerosols can vary based on the cellulose content of the fuel (Cubison et al., 2011). This variation is reflected in the spread of f_{C2H4O2} values in the fresh BBOA category. However, as these primary BBOA markers are lost through chemical degradation, the f_{C2H4O2} converge, and appear to be independent of the initial values.

Over the course of atmospheric processing observed during the G1-0730b and G1-0821b flights, the F-BBOA factors show a nearly monotonic decrease in fractional abundance with increasing photochemical age, gradually being replaced by the aged and highly aged BBOA factors (Fig. 3.10). This observation suggests that within the first few hours of aging primary BBOA material is lost via either evaporation or chemical reactions or secondary material is formed. In the plume transects with the lowest photochemical ages, the fresh BBOA factors accounted for approximately 80% of the OA mass (Fig. 3.10a). Over the first 10 hours of photochemical processing, this fraction decreased to approximately 20%. Most of the remaining mass is attributed to the aged BBOA factor (A-BBOA). However, between 3-18% of the total OA mass was attributed to the highly aged BBOA factor (HA-BBOA).

Figure 3.10b also highlights an example of near-field plume evolution during a cross-plume transect conducted during G1-0821b. In this instance, the aircraft flew directly from the furthest point away from the fire to the fire epicenter in about 5 minutes. This transect spans a range of photochemical ages from 0 to 6 hours, with OA loadings ranging between 10 and 10^4 μg m^{-3}.

Furthermore, the short time frame of the transect helps minimize uncertainties arising from changes in fire conditions during the measurement period. At the furthest point during this transect, the contribution from the F-BBOA factor is less than 5%, with A-BBOA contributing 78% and HA-BBOA contributing 17%. However, as the aircraft approached the emission source, the mass fraction of F-BBOA increased to 80%.

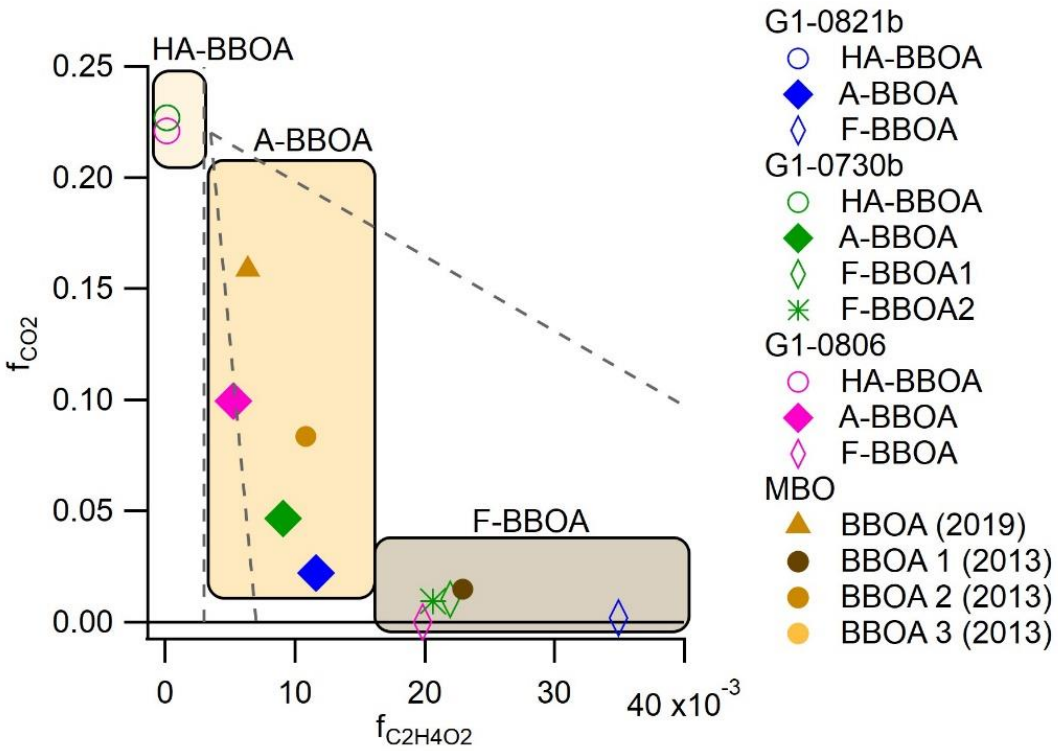

Figure 3.9: The distributions of the PMF factors within the fCO_2 (f_{44}) vs. the $fC_2H_4O_2$ (f_{60}) space. The factors are grouped into three types, as indicated by the shaded boxes.

Although PMF analysis was conducted separately for each of the G1 aircraft measurements and at the MBO summit site, a comparison of the spectral features provides further insights into the BBOA aging. All of the F- BBOA factors have similar O/C values ranging from 0.15 to 0.26. BBOA-1, the freshest factor identified at MBO, has a slightly higher O:C but comparable f_{60} value to the F- BBOA factors resolved from the G1 measurements. This consistency aligns with the understanding that even the freshest

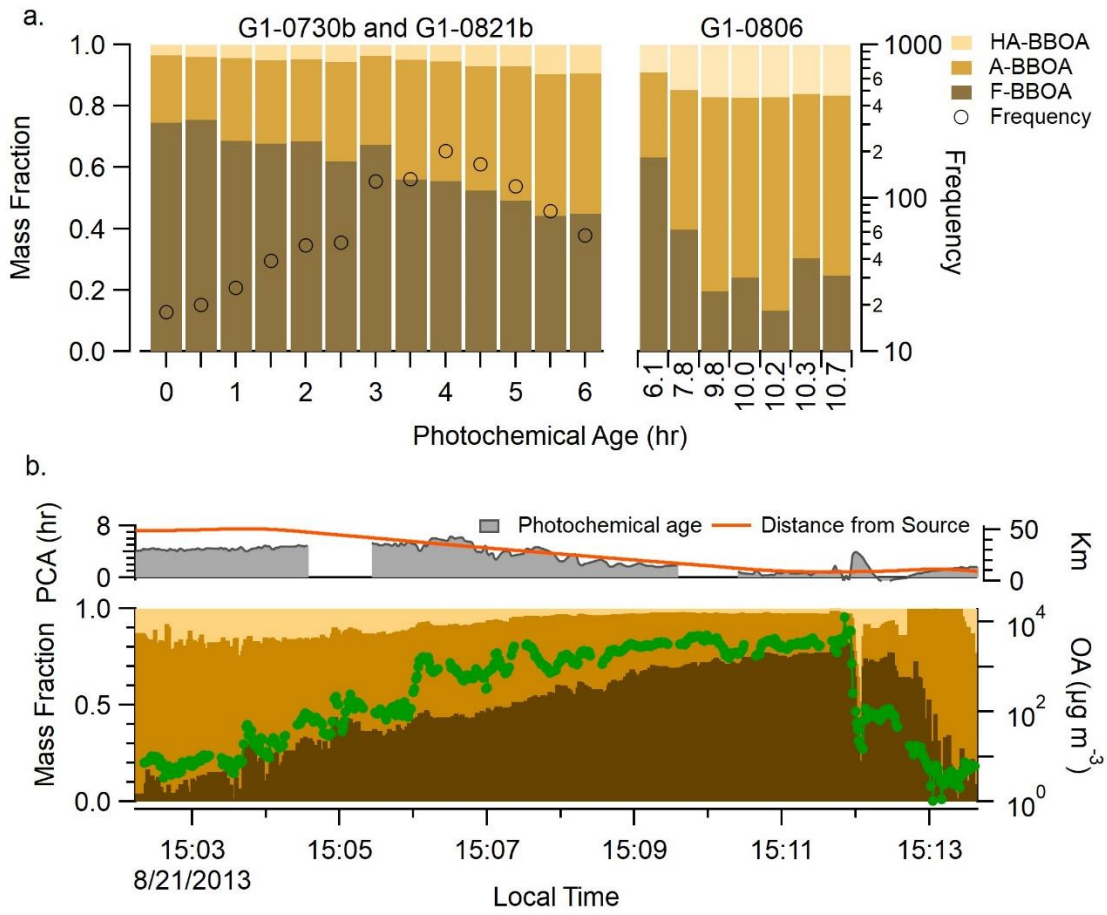

Figure 3.10: (a) Change in OA composition with photochemical age for the G1 research flights. Frequency corresponds to the number of data points within each age bin. (b) Change in OA composition during the along-plume transect during G1-0821.

plumes sampled at MBO had undergone at least 4 hours of processing, as well as significant dilution (Collier et al., 2016; Zhou et al., 2017).

The differences between the F-BBOA factors resolved during each of the research flights may be a result of fuel types with different emission profiles (Ahern et al., 2019; McClure et al., 2020). Two fresh BBOA factors were identified during the G1-0730b research flight, and although their spectra share similar f_{60} and f_{44} values, there are key differences. Notably, the fresh BBOA-1 factor exhibits enhanced signals in high *m/z* C_xH_y ions, such as $C_7H_7^+$ (*m/z* 91.05), $C_8H_9^+$ (*m/z* 105.05), $C_9H_7^+$ (*m/z* 115.06), and $C_{13}H_9^+$ (*m/z* 165.07), which may indicate the presence of polycyclic aromatic hydrocarbons (PAHs).

Additionally, these factors show different temporal patterns consistent with previous analysis that found considerable spatial variation of the chemical composition within this plume (Kleinman et al., 2020)

Furthermore, while both G1-0821b and G1-0730b showed strong correlations between OA and rBC, G1-0821b displayed a much higher ΔOA/ΔrBC in comparison to G1-0730b, with ratios of 30.19 and 14.91, respectively. As both of these fires had similar average MCE values, these differences are likely due to underlying fuel differences. The variations in fuel sources may also have implications for the BBOA composition. For instance, the high f_{60} identified in the fresh BBOA during G1-0821b is consistent with laboratory measurements of grass emissions (Cubison et al., 2011).

The identification of different fuel types was accomplished using high resolution (30m x 30m resolution) vegetation maps from the Landscape Fire and Resource Management Planning Tools (https://landfire.gov/) during the Government Flat fire (G1-0821b) and the Colockum Tarps fire (G1-0730b), as detailed in section S1.2. Overall, the Government Flat fire primarily consisted of open and closed canopy mixed conifer forests, while the Colockum Tarps fire had a high contribution from shrubland and herbaceous grassland. Although each individual fire covers a wide area, and emissions likely result from a mixture of different species, this suggests that the properties of BB POA can vary among wildfires in different ecosystems as has been noted previously (Cappa et al., 2020; Fortner et al., 2018; Jen et al., 2019). This distinction is noteworthy when performing source apportionment studies in areas impacted by wildfire smoke, especially when *a priori* spectral information is used, such as in ME-2 analysis (Canonaco et al., 2013). However, regardless of the initial POA signature, the BBOA for each flight ultimately converged towards a similar composition with processing, as represented by the aged BBOA factor.

3.4.4 Role of Dilution Induced Evaporation in Plume BBOA Processing

To determine the role of evaporation in the change in aerosol mass, the volatility of each BBOA factor identified at the MBO summit site was quantified from the mass thermograms (Fig. 3.11). Note

that no thermodenuder measurements were present aboard the G1 aircraft. As expected from the

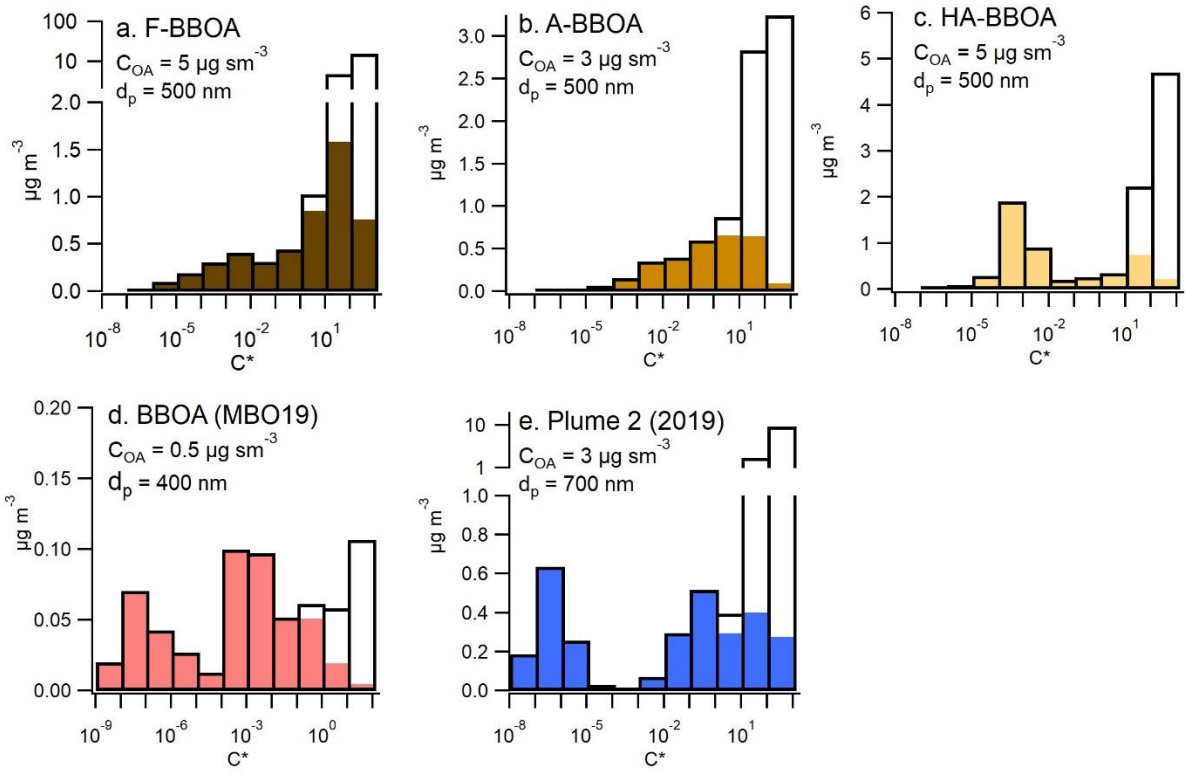

Figure 3.11: Volatility distribution corresponding to 298K of the BBOA factors identified in Zhou et al. (2017) and Farley et al. (2022). The colored bars correspond with the particle phase fraction, while the black boxes correspond with the total gas and particle phase concentration.

thermograms, F-BBOA shows the largest fraction of higher volatility material, peaking at C* of 10^1. As the aging of BBOA progresses, the C* distribution shifts towards lower volatility bins, peaking at 10^{-2} and 10^{-4} for A-BBOA and HA-BBOA, respectively. The BBOA identified in 2019 shows contribution at even lower C* values, consistent with extensive atmospheric processing. Finally, Figure 3.11e shows the OA volatility measured during a highly processed wildfire plume transported from Siberia. The C* distribution during this event also shows considerable OA mass at C* < 10^{-6}. The higher volatility material present during this period may be indicative of mixing with more volatile, non-BB aerosol during atmospheric transport.

The calculated amount of particle mass lost through evaporation at 298K with varying amounts of plume dilution is shown in in Figure 3.12b for each BBOA factor. As expected from the volatility distributions, BBOA-1 and

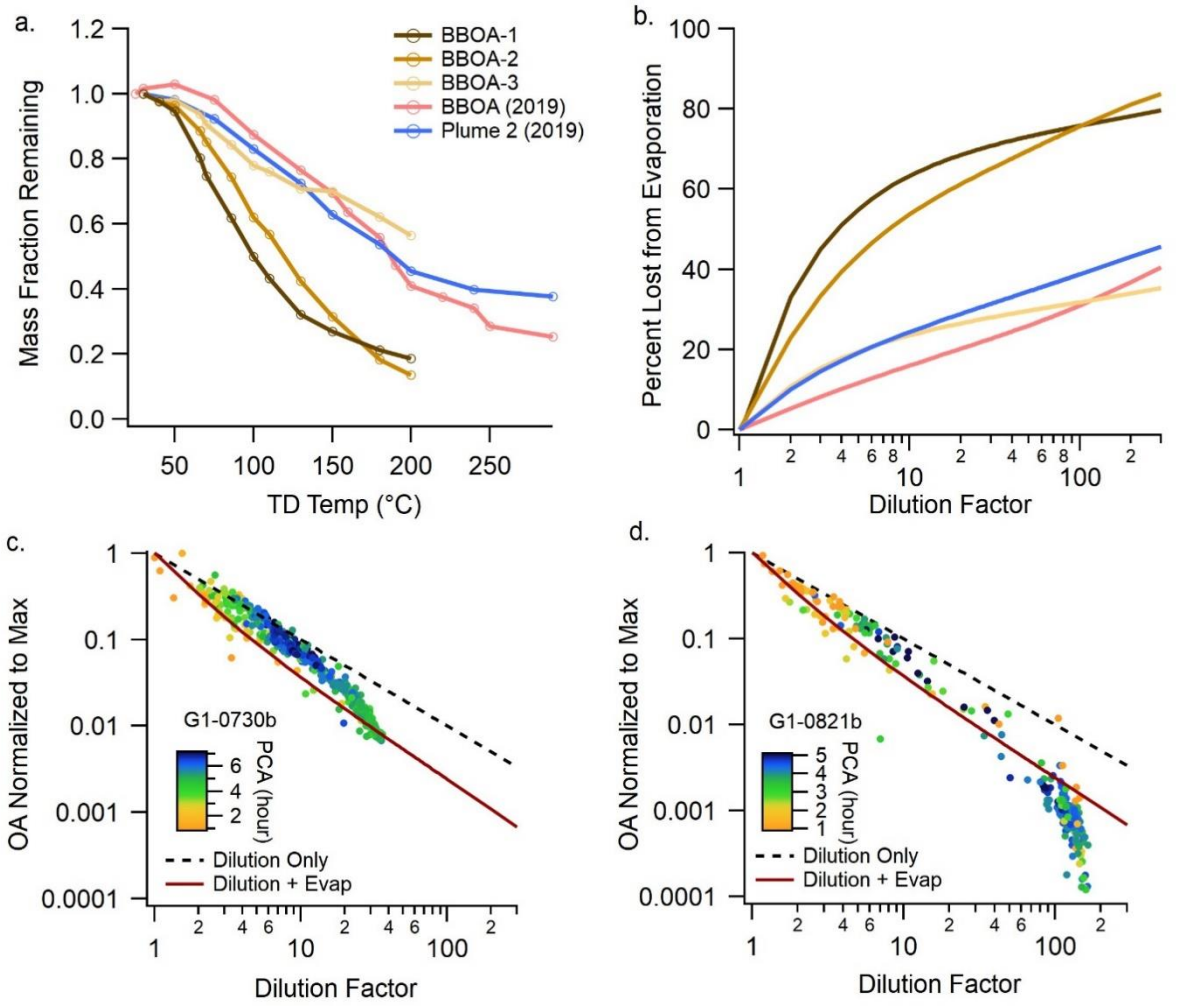

Figure 3.12: (a) mass thermogram for the BBOA factors. (b) Percent of OA mass lost through evaporation for each BBOA factor at increasing dilution factors. (c, d) Change in OA mass with increasing dilution factor during the (c) G1-0730b research flight and (d) G1-0821b research flight. The dashed line is the expected trend if only dilution is considered, while the red line accounts for evaporative loss.

BBOA-2 show up to 80% mass loss from evaporation, while BBOA-3, the 2019 BBOA factor and aged BBOA plume show lower evaporative losses.

During the G1-0730b and G1-0821b research flights, the dilution factor at time point *i* was estimated as $[CO_{max}]/[CO_i]$, where $[CO_{max}]$ is the highest CO concertation measured during the flight. The bulk aerosol volatility was assumed to be equal to that of BBOA-1 and Figure 3.12c and 11d shows the change in OA concentration at increasing dilution factor values. In general, the OA concentration is higher than expected if evaporation is accounted for, indicating the formation of substantial SOA material. Time points that are above the evaporation line generally correspond with higher photochemical ages ranging from 2 to 6 hours (Fig. 3.12c and 3.12d). For dilution factors exceeding 50, the OA mass exhibits a substantial deviation below the anticipated loss due to evaporation, indicting significant BBOA loss processes such as chemical degradation or deposition or substantial changes in the bulk aerosol volatility. The conversion of the measured mass thermogram to volatility distributions requires assumptions making a quantitative comparison difficult, however this analysis is consistent with the formation of SOA offsetting the evaporation of POA.

3.5 Atmospheric Implications

During the Biomass Burning Observation Project (BBOP) and the MBO-19 field campaign, we sampled wildfire plumes in the Pacific Northwest spanning a wide range of processing stages, from near-field plumes to plumes that had undergone regional and intercontinental transport. Photochemical age was calculated for fresh and intermediately aged plumes based on the decay of NO_x relative to CO. This metric offers a reliable estimate of physical transport time while revealing fine-scale variations within the plumes driven by spatiotemporal variations in oxidant concentrations. However, this metric is not applicable to heavily processed plumes in which NO_x concentrations have returned to background levels.

The wildfire plumes exhibited a clear increasing trend in oxidation markers, including bulk O/C, $f_{CO2,}$ and $f_{CHO2,}$ during the initial hours of photochemical processing. However, these values appeared to reach a plateau at extended aging. Through PMF analysis, we successfully identified distinct BBOA components that represented varying degrees of processing in each of the G1 research flights and the

MBO plumes. Notably, there was a rapid decrease in the mass fraction of fresh BBOA factors, replaced by more oxidized aerosol as the wildfire plumes aged. This transformation can be attributed to a combination of volatilization of the more volatile fresh BBOA and the formation of less volatile, more oxidized BBOAs. Furthermore, rapid formation of highly oxidized BBOA types with O/C of 1.06 was observed within the first few hours of photochemical processing.

References

Adachi, K., Sedlacek, A. J., Kleinman, L., Springston, S. R., Wang, J., Chand, D., Hubbe, J. M., Shilling, J. E., Onasch, T. B., Kinase, T., Sakata, K., Takahashi, Y. and Buseck, P. R.: Spherical tarball particles form through rapid chemical and physical changes of organic matter in biomass-burning smoke, Proc. Natl. Acad. Sci. U. S. A., 116(39), 19336–19341, doi:10.1073/pnas.1900129116, 2019.

Ahern, A. T., Robinson, E. S., Tkacik, D. S., Saleh, R., Hatch, L. E., Barsanti, K. C., Stockwell, C. E., Yokelson, R. J., Presto, A. A., Robinson, A. L., Sullivan, R. C. and Donahue, N. M.: Production of Secondary Organic Aerosol During Aging of Biomass Burning Smoke From Fresh Fuels and Its Relationship to VOC Precursors, J. Geophys. Res. Atmos., 124(6), 3583–3606, doi:10.1029/2018JD029068, 2019.

Akagi, S. K., Craven, J. S., Taylor, J. W., McMeeking, G. R., Yokelson, R. J., Burling, I. R., Urbanski, S. P., Wold, C. E., Seinfeld, J. H., Coe, H., Alvarado, M. J. and Weise, D. R.: Evolution of trace gases and particles emitted by a chaparral fire in California, Atmos. Chem. Phys., 12(3), 1397–1421, doi:10.5194/acp-12-1397-2012, 2012.

Akherati, A., He, Y., Garofalo, L. A., Hodshire, A. L., Farmer, D. K., Kreidenweis, S. M., Permar, W., Hu, L., Fischer, E. V., Jen, C. N., Goldstein, A. H., Levin, E. J. T., DeMott, P. J., Campos, T. L., Flocke, F., Reeves, J. M., Toohey, D. W., Pierce, J. R. and Jathar, S. H.: Dilution and photooxidation driven processes explain the evolution of organic aerosol in wildfire plumes, Environ. Sci. Atmos., doi:10.1039/d1ea00082a, 2022.

Alvarado, M. J., Logan, J. A., Mao, J., Apel, E., Riemer, D., Blake, D., Cohen, R. C., Min, K. E., Perring, A. E., Browne, E. C., Wooldridge, P. J., Diskin, G. S., Sachse, G. W., Fuelberg, H., Sessions, W. R., Harrigan, D. L., Huey, G., Liao, J., Case-Hanks, A., Jimenez, J. L., Cubison, M. J., Vay, S. A., Weinheimer, A. J., Knapp, D. J., Montzka, D. D., Flocke, F. M., Pollack, I. B., Wennberg, P. O., Kurten, A., Crounse, J., St. Clair, J. M., Wisthaler, A., Mikoviny, T., Yantosca, R. M., Carouge, C. C. and Le Sager, P.: Nitrogen oxides and PAN in plumes from boreal fires during ARCTAS-B and their impact on ozone: An integrated analysis of aircraft and satellite observations, Atmos. Chem. Phys., 10(20), 9739–9760, doi:10.5194/acp-10-9739-2010, 2010.

Andreae, M. O.: Soot carbon and excess fine potassium: Long-range transport of combustion-derived aerosols, Science (80-.)., 220(4602), 1148–1151, doi:10.1126/science.220.4602.1148, 1983.

Andreae, M. O.: Emission of trace gases and aerosols from biomass burning - An updated assessment, Atmos. Chem. Phys., doi:10.5194/acp-19-8523-2019, 2019.

Baylon, P., Jaffe, D. A., de Gouw, J. and Warneke, C.: Influence of long-range transport of Siberian biomass burning at the Mt. Bachelor Observatory during the spring of 2015, Aerosol Air Qual. Res.,

17(11), 2751–2761, doi:10.4209/aaqr.2017.06.0213, 2017.

Bonnefoy, A., Chiron, S. and Botta, A.: Environmental Nitration Processes Enhance the Mutagenic Potency of Aromatic Compounds, Environ. Toxicol., 165(April), 16, doi:10.1002/tox, 2010.

Brito, J., Rizzo, L. V., Morgan, W. T., Coe, H., Johnson, B., Haywood, J., Longo, K., Freitas, S., Andreae, M. O. and Artaxo, P.: Ground-based aerosol characterization during the South American Biomass Burning Analysis (SAMBBA) field experiment, Atmos. Chem. Phys., 14(22), 12069–12083, doi:10.5194/acp-14-12069-2014, 2014.

Burling, I. R., Yokelson, R. J., Griffith, D. W. T., Johnson, T. J., Veres, P., Roberts, J. M., Warneke, C., Urbanski, S. P., Reardon, J., Weise, D. R., Hao, W. M. and de Gouw, J. A.: Laboratory measurements of trace gas emissions from biomass burning of fuel types from the southeastern and southwestern United States, Atmos. Chem. Phys., 11115–11130, doi:10.5194/acp-10-11115-2010, 2010.

Canonaco, F., Crippa, M., Slowik, J. G., Baltensperger, U. and Prévôt, A. S. H.: SoFi, an IGOR-based interface for the efficient use of the generalized multilinear engine (ME-2) for the source apportionment: ME-2 application to aerosol mass spectrometer data, Atmos. Meas. Tech., doi:10.5194/amt-6-3649-2013, 2013.

Cao, W., Martí-Rosselló, T., Li, J. and Lue, L.: Prediction of potassium compounds released from biomass during combustion, Appl. Energy, 250(May), 1696–1705, doi:10.1016/j.apenergy.2019.05.106, 2019.

Cappa, C. D.: A model of aerosol evaporation kinetics in a thermodenuder, Atmos. Meas. Tech., 579–592, doi:10.5194/amt-3-579-2010, 2010.

Cappa, C. D. and Jimenez, J. L.: Quantitative estimates of the volatility of ambient organic aerosol, Atmos. Chem. Phys., 5409–5424, doi:10.5194/acp-10-5409-2010, 2010.

Cappa, C. D., Lim, C. Y., Hagan, D. H., Coggon, M., Koss, A., Sekimoto, K., de Gouw, J., Onasch, T. B., Warneke, C. and Kroll, J. H.: Biomass-burning-derived particles from a wide variety of fuels: Part 2: Effects of photochemical aging on particle optical and chemical properties, Atmos. Chem. Phys. Discuss, 2020.

Che, H., Segal-Rozenhaimer, M., Zhang, L., Dang, C., Zuidema, P., Dobracki, A., Sedlacek, A. J., Coe, H., Wu, H., Taylor, J., Zhang, X., Redemann, J. and Haywood, J.: Cloud processing and weeklong ageing affect biomass burning aerosol properties over the south-eastern Atlantic, Commun. Earth Environ., 1–9, doi:10.1038/s43247-022-00517-3, 2022.

Chen, L. W. A., Moosmüller, H., Arnott, W. P., Chow, J. C., Watson, J. G., Susott, R. A., Babbitt, R. E., Wold, C. E., Lincoln, E. N. and Wei, M. H.: Emissions from laboratory combustion of wildland fuels: Emission factors and source profiles, Environ. Sci. Technol., 41(12), 4317–4325, doi:10.1021/es062364i, 2007.

Coggon, M. M., Lim, C. Y., Koss, A. R., Sekimoto, K., Yuan, B., Gilman, J. B., Hagan, D. H., Selimovic, V., Zarzana, K. J., Brown, S. S., M Roberts, J., Müller, M., Yokelson, R., Wisthaler, A., Krechmer, J. E., Jimenez, J. L., Cappa, C., Kroll, J. H., De Gouw, J. and Warneke, C.: OH chemistry of non-methane organic gases (NMOGs) emitted from laboratory and ambient biomass burning smoke: Evaluating the influence of furans and oxygenated aromatics on ozone and secondary NMOG formation, Atmos. Chem. Phys., 19(23), 14875–14899, doi:10.5194/acp-19-14875-2019, 2019.

Collier, S., Zhou, S., Onasch, T. B., Jaffe, D. A., Kleinman, L., Sedlacek, A. J., Briggs, N. L., Hee, J., Fortner, E., Shilling, J. E., Worsnop, D., Yokelson, R. J., Parworth, C., Ge, X., Xu, J., Butterfield, Z., Chand, D.,

Dubey, M. K., Pekour, M. S., Springston, S. and Zhang, Q.: Regional Influence of Aerosol Emissions from Wildfires Driven by Combustion Efficiency: Insights from the BBOP Campaign, Environ. Sci. Technol., doi:10.1021/acs.est.6b01617, 2016.

Cubison, M. J., Ortega, A. M., Hayes, P. L., Farmer, D. K., Day, D., Lechner, M. J., Brune, W. H., Apel, E., Diskin, G. S., Fisher, J. A., Fuelberg, H. E., Hecobian, A., Knapp, D. J., Mikoviny, T., Riemer, D., Sachse, G. W., Sessions, W., Weber, R. J., Weinheimer, A. J., Wisthaler, A. and Jimenez, J. L.: Effects of aging on organic aerosol from open biomass burning smoke in aircraft and laboratory studies, Atmos. Chem. Phys., doi:10.5194/acp-11-12049-2011, 2011.

Day, D. A., Campuzano-Jost, P., Nault, B. A., Palm, B. B., Hu, W., Guo, H., Wooldridge, P. J., Cohen, R. C., Docherty, K. S., Huffman, J. A., De Sá, S. S., Martin, S. T. and Jiménez, J. L.: A Systematic Re-evaluation of Methods for Quantification of Bulk Particle-phase Organic Nitrates Using Real-time Aerosol Mass Spectrometry, Atmos. Meas. Tech., 3(2), 6, 2021.

Decker, Z. C. J., Robinson, M. A., Barsanti, K. C., Bourgeois, I., Coggon, M. M., Digangi, J. P., Diskin, G. S., Flocke, F. M., Franchin, A., Fredrickson, C. D., Gkatzelis, G. I., Hall, S. R., Halliday, H., Holmes, C. D., Huey, L. G., Lee, Y. R., Lindaas, J., Middlebrook, A. M., Montzka, D. D., Moore, R., Neuman, J. A., Nowak, J. B., Palm, B. B., Peischl, J., Piel, F., Rickly, P. S., Rollins, A. W., Ryerson, T. B., Schwantes, R. H., Sekimoto, K., Thornhill, L., Thornton, J. A., Tyndall, G. S., Ullmann, K., Van Rooy, P., Veres, P. R., Warneke, C., Washenfelder, R. A., Weinheimer, A. J., Wiggins, E., Winstead, E., Wisthaler, A., Womack, C. and Brown, S. S.: Nighttime and daytime dark oxidation chemistry in wildfire plumes: An observation and model analysis of FIREX-AQ aircraft data, Atmos. Chem. Phys., 21(21), 16293–16317, doi:10.5194/acp-21-16293-2021, 2021.

Donahue, N. M., Robinson, A. L., Stanier, C. O. and Pandis, S. N.: Coupled partitioning, dilution, and chemical aging of semivolatile organics, Environ. Sci. Technol., doi:10.1021/es052297c, 2006.

Drewnick, F., Diesch, J. M., Faber, P. and Borrmann, S.: Aerosol mass spectrometry: Particle-vaporizer interactions and their consequences for the measurements, Atmos. Meas. Tech., 8(9), 3811–3830, doi:10.5194/amt-8-3811-2015, 2015.

Dzepina, K., Mazzoleni, C., Fialho, P., China, S., Zhang, B., Owen, R. C., Helmig, D., Hueber, J., Kumar, S., Perlinger, J. A., Kramer, L. J., Dziobak, M. P., Ampadu, M. T., Olsen, S., Wuebbles, D. J. and Mazzoleni, L. R.: Molecular characterization of free tropospheric aerosol collected at the Pico Mountain Observatory: A case study with a long-range transported biomass burning plume, Atmos. Chem. Phys., 15(9), 5047–5068, doi:10.5194/acp-15-5047-2015, 2015.

Farley, R., Bernays, N., Ja, D. A., Ketcherside, D., Hu, L., Zhou, S. and Collier, S.: Persistent Influence of Wildfire Emissions in the Western United States and Characteristics of Aged Biomass Burning Organic Aerosols under Clean Air Conditions, Environ. Sci. Technol., doi:10.1021/acs.est.1c07301, 2022.

Farley, R. N., Collier, S., Cappa, C. D., Williams, L. R., Onasch, T. B., Russell, M., Kim, H. and Zhang, Q.: Source Apportionment of Soot Particles and Aqueous-Phase Processing of Black Carbon Coatings in an Urban Environment, Atmos. Chem. Phys. Discuss, (August), 1–34, 2023.

Farmer, D. K., Matsunaga, A., Docherty, K. S., Surratt, J. D., Seinfeld, J. H., Ziemann, P. J. and Jimenez, J. L.: Response of an aerosol mass spectrometer to organonitrates and organosulfates and implications for atmospheric chemistry, Proc. Natl. Acad. Sci. U. S. A., 107(15), 6670–6675, doi:10.1073/pnas.0912340107, 2010.

Fischer, E. V., Jaffe, D. A. and Weatherhead, E. C.: Free tropospheric peroxyacetyl nitrate (PAN) and

ozone at Mount Bachelor: Potential causes of variability and timescale for trend detection, Atmos. Chem. Phys., 11(12), 5641–5654, doi:10.5194/acp-11-5641-2011, 2011.

Forrister, H., Liu, J., Scheuer, E., Dibb, J., Ziemba, L., Thornhill, K. L., Anderson, B., Diskin, G., Perring, A. E., Schwarz, J. P., Campuzano-Jost, P., Day, D. A., Palm, B. B., Jimenez, J. L., Nenes, A. and Weber, R. J.: Evolution of brown carbon in wildfire plumes, Geophys. Res. Lett., doi:10.1002/2015GL063897, 2015.

Fortner, E., Onasch, T., Canagaratna, M., Williams, L. R., Lee, T., Jayne, J. and Worsnop, D.: Examining the chemical composition of black carbon particles from biomass burning with SP-AMS, J. Aerosol Sci., 120(November 2017), 12–21, doi:10.1016/j.jaerosci.2018.03.001, 2018.

Garofalo, L. A., Pothier, M. A., Levin, E. J. T., Campos, T., Kreidenweis, S. M. and Farmer, D. K.: Emission and Evolution of Submicron Organic Aerosol in Smoke from Wildfires in the Western United States, ACS Earth Sp. Chem., 3(7), 1237–1247, doi:10.1021/acsearthspacechem.9b00125, 2019.

Ge, D., Nie, W., Sun, P., Liu, Y., Wang, T., Wang, J., Wang, J., Wang, L., Zhu, C., Wang, R., Liu, T., Chi, X. and Ding, A.: Characterization of particulate organic nitrates in the Yangtze River Delta, East China, using the time-of-flight aerosol chemical speciation monitor, Atmos. Environ., 272(September 2021), 118927, doi:10.1016/j.atmosenv.2021.118927, 2021.

Gilardoni, S., Massoli, P., Paglione, M., Giulianelli, L., Carbone, C., Rinaldi, M., Decesari, S., Sandrini, S., Costabile, F., Gobbi, G. P., Pietrogrande, M. C., Visentin, M., Scotto, F., Fuzzi, S. and Facchini, M. C.: Direct observation of aqueous secondary organic aerosol from biomass-burning emissions, Proc. Natl. Acad. Sci., doi:10.1073/pnas.1602212113, 2016.

de Gouw, J. A., Middlebrook, A. M., Warneke, C., Goldan, P. D., Kuster, W. C., Roberts, J. M., Fehsenfeld, F. C., Worsnop, D. R., Canagaratna, M. R., Pszenny, A. A. P., Keene, W. C., Marchewka, M., Bertman, S. B. and Bates, T. S.: Budget of organic carbon in a polluted atmosphere: Results from the New England Air Quality Study in 2002, J. Geophys. Res. D Atmos., 110(16), 1–22, doi:10.1029/2004JD005623, 2005.

Heald, C. L., Kroll, J. H., Jimenez, J. L., Docherty, K. S., Decarlo, P. F., Aiken, A. C., Chen, Q., Martin, S. T., Farmer, D. K. and Artaxo, P.: A simplified description of the evolution of organic aerosol composition in the atmosphere, Geophys. Res. Lett., doi:10.1029/2010GL042737, 2010.

Hobbs, P. V., Sinha, P., Yokelson, R. J., Christian, T. J., Blake, D. R., Gao, S., Kirchstetter, T. W., Novakov, T. and Pilewskie, P.: Evolution of gases and particles from a savanna fire in South Africa, J. Geophys. Res. Atmos., 108(13), doi:10.1029/2002jd002352, 2003.

Hodshire, A. L., Akherati, A., Alvarado, M. J., Brown-Steiner, B., Jathar, S. H., Jimenez, J. L., Kreidenweis, S. M., Lonsdale, C. R., Onasch, T. B., Ortega, A. M. and Pierce, J. R.: Aging Effects on Biomass Burning Aerosol Mass and Composition: A Critical Review of Field and Laboratory Studies, Environ. Sci. Technol., 53(17), 10007–10022, doi:10.1021/acs.est.9b02588, 2019.

Hodshire, A. L., Ramnarine, E., Akherati, A., Alvarado, M. L., Farmer, D. K., Jathar, H., Kreidenweis, S. M., Lonsdale, C. R., Onasch, T. B. and Springston, S. R.: Dilution impacts on smoke aging : evidence in Biomass Burning Observation Project (BBOP) data, , 6839–6855, 2021.

Holm, S. M., Miller, M. D. and Balmes, J. R.: Health effects of wildfire smoke in children and public health tools: a narrative review, J. Expo. Sci. Environ. Epidemiol., 31(1), 1–20, doi:10.1038/s41370-020-00267-4, 2021.

IPCC: Climate Change 2021: The Physical Science Basis. Contribution of Working Group I to the Sixth Assessment Report of the Intergovernmental Panel on Climate Change, edited by V. Masson-Delmotte,

P. Zhai, A. Pirani, S. L. Connors, C. Pean, S. Berger, N. Caud, Y. Chen, L. Goldfarb, M. I. Gomis, M. Huang, K. Leitzell, E. Lonnoy, J. B. . Matthews, T. K. Maycock, T. Waterfield, O. Yelekci, R. Yu, and B. Zhou, Cambridge University Press, United Kingdom and New York, NY, USA., 2021.

Jaffe, D. A., O'Neill, S. M., Larkin, N. K., Holder, A. L., Peterson, D. L., Halofsky, J. E. and Rappold, A. G.: Wildfire and prescribed burning impacts on air quality in the United States, J. Air Waste Manage. Assoc., 0(0), doi:10.1080/10962247.2020.1749731, 2020.

Jen, C. N., Hatch, L. E., Selimovic, V., Yokelson, R. J., Weber, R., Fernandez, A. E., Kreisberg, N. M., Barsanti, K. C. and Goldstein, A. H.: Speciated and total emission factors of particulate organics from burning western US wildland fuels and their dependence on combustion efficiency, Atmos. Chem. Phys., doi:10.5194/acp-19-1013-2019, 2019.

Jiang, W., Misovich, M. V., Hettiyadura, A. P. S., Laskin, A., McFall, A. S., Anastasio, C. and Zhang, Q.: Photosensitized Reactions of a Phenolic Carbonyl from Wood Combustion in the Aqueous Phase - Chemical Evolution and Light Absorption Properties of AqSOA, Environ. Sci. Technol., 55(8), 5199–5211, doi:10.1021/acs.est.0c07581, 2021.

Jiang, W., Niedek, C., Anastasio, C. and Zhang, Q.: Photoaging of Phenolic Secondary Organic Aerosol in the Aqueous Phase : Evolution of Chemical and Optical Properties and Effects of Oxidants, , (March), 1–25, 2023.

Jimenez, J. L., Canagaratna, M. R., Donahue, N. M., Prevot, A. S. H., Zhang, Q., Kroll, J. H., DeCarlo, P. F., Allan, J. D., Coe, H., Ng, N. L., Aiken, A. C., Docherty, K. S., Ulbrich, I. M., Grieshop, A. P., Robinson, A. L., Duplissy, J., Smith, J. D., Wilson, K. R., Lanz, V. A., Hueglin, C., Sun, Y. L., Tian, J., Laaksonen, A., Raatikainen, T., Rautiainen, J., Vaattovaara, P., Ehn, M., Kulmala, M., Tomlinson, J. M., Collins, D. R., Cubison, M. J., Dunlea, E. J., Huffman, J. A., Onasch, T. B., Alfarra, M. R., Williams, P. I., Bower, K., Kondo, Y., Schneider, J., Drewnick, F., Borrmann, S., Weimer, S., Demerjian, K., Salcedo, D., Cottrell, L., Griffin, R., Takami, A., Miyoshi, T., Hatakeyama, S., Shimono, A., Sun, J. Y., Zhang, Y. M., Dzepina, K., Kimmel, J. R., Sueper, D., Jayne, J. T., Herndon, S. C., Trimborn, A. M., Williams, L. R., Wood, E. C., Middlebrook, A. M., Kolb, C. E., Baltensperger, U. and Worsnop, D. R.: Evolution of organic aerosols in the atmosphere, Science (80-.)., doi:10.1126/science.1180353, 2009.

Jolly, W. M., Cochrane, M. A., Freeborn, P. H., Holden, Z. A., Brown, T. J., Williamson, G. J. and Bowman, D. M. J. S.: Climate-induced variations in global wildfire danger from 1979 to 2013, Nat. Commun., 6(May), 1–11, doi:10.1038/ncomms8537, 2015.

Jorga, S. D., Florou, K., Kaltsonoudis, C., Kodros, J. K., Vasilakopoulou, C., Cirtog, M., Fouqueau, A., Picquet-Varrault, B., Nenes, A. and Pandis, S. N.: Nighttime chemistry of biomass burning emissions in urban areas: A dual mobile chamber study, Atmos. Chem. Phys., 21(19), 15337–15349, doi:10.5194/acp-21-15337-2021, 2021.

Karnezi, E., Riipinen, I. and Pandis, S. N.: Measuring the atmospheric organic aerosol volatility distribution: A theoretical analysis, Atmos. Meas. Tech., 7(9), 2953–2965, doi:10.5194/amt-7-2953-2014, 2014.

Kimmel, J. R., Farmer, D. K., Cubison, M. J., Sueper, D., Tanner, C., Nemitz, E., Worsnop, D. R., Gonin, M. and Jimenez, J. L.: Real-time aerosol mass spectrometry with millisecond resolution, Int. J. Mass Spectrom., 303(1), 15–26, doi:10.1016/j.ijms.2010.12.004, 2011.

Kleinman, L., Sedlacek III, A., Adachi, K., Buseck, P., Collier, S., Dubey, M., Hodshire, A., Lewis, E., Onasch, T., Pierce, J., Shilling, J., Springston, S., Wang, J., Zhang, Q., Zhou, S. and Yokelson, R.: Rapid Evolution of

Aerosol Particles and their Optical Properties Downwind of Wildfires in the Western U.S., Atmos. Chem. Phys., (April), 1–52, doi:10.5194/acp-2020-239, 2020.

Kleinman, L. I., Springston, S. R., Daum, P. H., Lee, Y. N., Nunnermacker, L. J., Senum, G. I., Wang, J., Weinstein-Lloyd, J., Alexander, M. L., Hubbe, J., Ortega, J., Canagaratna, M. R. and Jayne, J.: The time evolution of aerosol composition over the Mexico City plateau, Atmos. Chem. Phys., 8(6), 1559–1575, doi:10.5194/acp-8-1559-2008, 2008.

Koss, A. R., Sekimoto, K., Gilman, J. B., Selimovic, V., Coggon, M. M., Zarzana, K. J., Yuan, B., Lerner, B. M., Brown, S. S., Jimenez, J. L., Krechmer, J., Roberts, J. M., Warneke, C., Yokelson, R. J. and De Gouw, J.: Non-methane organic gas emissions from biomass burning: Identification, quantification, and emission factors from PTR-ToF during the FIREX 2016 laboratory experiment, Atmos. Chem. Phys., 18(5), 3299–3319, doi:10.5194/acp-18-3299-2018, 2018.

Kristensen, T. B., Falk, J., Lindgren, R., Andersen, C., Malmborg, V. B., Eriksson, A. C., Korhonen, K., Carvalho, R. L., Boman, C., Pagels, J. and Svenningsson, B.: Properties and emission factors of cloud condensation nuclei from biomass cookstoves - Observations of a strong dependency on potassium content in the fuel, Atmos. Chem. Phys., 21(10), 8023–8044, doi:10.5194/acp-21-8023-2021, 2021.

Lambe, A. T., Onasch, T. B., Massoli, P., Croasdale, D. R., Wright, J. P., Ahern, A. T., Williams, L. R., Worsnop, D. R., Brune, W. H. and Davidovits, P.: Laboratory studies of the chemical composition and cloud condensation nuclei (CCN) activity of secondary organic aerosol (SOA) and oxidized primary organic aerosol (OPOA), Atmos. Chem. Phys., doi:10.5194/acp-11-8913-2011, 2011.

Lee, J. Y., Peterson, P. K., Vear, L. R., Cook, R. D., Sullivan, A. P., Smith, E., Hawkins, L. N., Olson, N. E., Hems, R., Snyder, P. K. and Pratt, K. A.: Wildfire Smoke Influence on Cloud Water Chemical Composition at Whiteface Mountain , New York Journal of Geophysical Research : Atmospheres, , 1–20, doi:10.1029/2022JD037177, 2022.

Li, B., Sun, Z., Li, Z., Aldén, M., Jakobsen, J. G., Hansen, S. and Glarborg, P.: Post-flame gas-phase sulfation of potassium chloride, Combust. Flame, 160(5), 959–969, doi:10.1016/j.combustflame.2013.01.010, 2013.

Li, J., Pósfai, M., Hobbs, P. V. and Buseck, P. R.: Individual aerosol particles from biomass burning in southern Africa: 2. Compositions and aging of inorganic particles, J. Geophys. Res. D Atmos., 108(13), 1–12, doi:10.1029/2002jd002310, 2003.

Liao, J., Wolfe, G., Hannun, R., St. Clair, J., Hanisco, T., Gilman, J., Lamplugh, A., Selimovic, V., Diskin, G., Nowak, J., Halliday, H., DiGangi, J., Hall, S., Ullmann, K., Holmes, C., Fite, C., Agastra, A., Ryerson, T., Peischl, J., Bourgeois, I., Warneke, C., Coggon, M., Gkatzelis, G., Sekimoto, K., Fried, A., Richter, D., Weibring, P., Apel, E., Hornbrook, R., Brown, S., Womack, C., Robinson, M., Washenfelder, R., Veres, P. and Neuman, J. A.: Formaldehyde evolution in U.S. wildfire plumes during FIREX-AQ, Atmos. Chem. Phys. Discuss., (May), 1–38, doi:10.5194/acp-2021-389, 2021.

Liu, X., Huey, L. G., Yokelson, R. J., Selimovic, V., Simpson, I. J., Müller, M., Jimenez, J. L., Campuzano-Jost, P., Beyersdorf, A. J., Blake, D. R., Butterfield, Z., Choi, Y., Crounse, J. D., Day, D. A., Diskin, G. S., Dubey, M. K., Fortner, E., Hanisco, T. F., Hu, W., King, L. E., Kleinman, L., Meinardi, S., Mikoviny, T., Onasch, T. B., Palm, B. B., Peischl, J., Pollack, I. B., Ryerson, T. B., Sachse, G. W., Sedlacek, A. J., Shilling, J. E., Springston, S., St. Clair, J. M., Tanner, D. J., Teng, A. P., Wennberg, P. O., Wisthaler, A. and Wolfe, G. M.: Airborne measurements of western U.S. wildfire emissions: Comparison with prescribed burning and air quality implications, J. Geophys. Res., 122(11), 6108–6129, doi:10.1002/2016JD026315, 2017.

Ma, L., Guzman, C., Niedek, C., Tran, T., Zhang, Q. and Anastasio, C.: Kinetics and Mass Yields of Aqueous Secondary Organic Aerosol from Highly Substituted Phenols Reacting with a Triplet Excited State, Environ. Sci. Technol., doi:10.1021/acs.est.1c00575, 2021.

May, A. A., Levin, E. J. T., Hennigan, C. J., Riipinen, I., Lee, T., Collett, J. L., Jimenez, J. L., Kreidenweis, S. M. and Robinson, A. L.: Gas-particle partitioning of primary organic aerosol emissions: 3. Biomass burning, J. Geophys. Res. Atmos., 118(19), 11,327-11,338, doi:10.1002/jgrd.50828, 2013.

May, A. A., McMeeking, G. R., Lee, T., Taylor, J. W., Craven, J. S., Burling, I. R., Sullivan, A. P., Akagi, S. K., Collett, J. L., Flynn, M. J., Coe, H., Urbanski, S. P., Seinfeld, J. H., Yokelson, R. J. and Kreidenweis, S. M.: Aerosol emissions from prescribed fires in the United States: A synthesis of laboratory and aircraft measurements, J. Geophys. Res. Atmos., 119(3), 7667–7683, doi:10.1002/2014JD021790.Received, 2014.

May, N. W., Bernays, N., Farley, R., Zhang, Q. and Jaffe, D. A.: Intensive aerosol properties of boreal and regional biomass burning aerosol at Mt. Bachelor Observatory: larger and black carbon (BC)-dominant particles transported from Siberian wildfires, Atmos. Chem. Phys., 23, 2747–2764, doi:https://doi.org/10.5194/acp-23-2747-2023, 2023.

McClure, C. D. and Jaffe, D. A.: Investigation of high ozone events due to wildfire smoke in an urban area, Atmos. Environ., doi:10.1016/j.atmosenv.2018.09.021, 2018.

McClure, C. D., Lim, C. Y., Hagan, D. H., Kroll, J. H. and Cappa, C. D.: Biomass-burning-derived particles from a wide variety of fuels - Part 1: Properties of primary particles, Atmos. Chem. Phys., 20(3), 1531–1547, doi:10.5194/acp-20-1531-2020, 2020.

McFall, A. S., Johnson, A. W. and Anastasio, C.: Air-Water Partitioning of Biomass-Burning Phenols and the Effects of Temperature and Salinity, Environ. Sci. Technol., 54(7), 3823–3830, doi:10.1021/acs.est.9b06443, 2020.

McMeeking, G. R., Kreidenweis, S. M., Baker, S., Carrico, C. M., Chow, J. C., Collett, J. L., Hao, W. M., Holden, A. S., Kirchstetter, T. W., Malm, W. C., Moosmüller, H., Sullivan, A. P. and Cyle E., W.: Emissions of trace gases and aerosols during the open combustion of biomass in the laboratory, J. Geophys. Res. Atmos., 114(19), 1–20, doi:10.1029/2009JD011836, 2009.

Ng, N. L., Canagaratna, M. R., Jimenez, J. L., Chhabra, P. S., Seinfeld, J. H. and Worsnop, D. R.: Changes in organic aerosol composition with aging inferred from aerosol mass spectra, Atmos. Chem. Phys., 11(13), 6465–6474, doi:10.5194/acp-11-6465-2011, 2011.

O'Dell, K., Ford, B., Fischer, E. V. and Pierce, J. R.: Contribution of Wildland-Fire Smoke to US PM 2.5 and Its Influence on Recent Trends, Environ. Sci. Technol., doi:10.1021/acs.est.8b05430, 2019.

Olszyna, K. J., Bailey, E. M., Simonaitis, R. and Meagher, J. F.: O3 and NOy relationships at a rural site, J. Geophys. Res., 99(D7), doi:10.1029/94jd00739, 1994.

Onasch, T. B., Trimborn, A., Fortner, E. C., Jayne, J. T., Kok, G. L., Williams, L. R., Davidovits, P. and Worsnop, D. R.: Soot particle aerosol mass spectrometer: Development, validation, and initial application, Aerosol Sci. Technol., doi:10.1080/02786826.2012.663948, 2012.

Ortega, A. M., Day, D. A., Cubison, M. J., Brune, W. H., Bon, D., De Gouw, J. A. and Jimenez, J. L.: Secondary organic aerosol formation and primary organic aerosol oxidation from biomass-burning smoke in a flow reactor during FLAME-3, Atmos. Chem. Phys., doi:10.5194/acp-13-11551-2013, 2013.

Paglione, M., Gilardoni, S., Rinaldi, M., Decesari, S., Zanca, N., Sandrini, S., Giulianelli, L., Bacco, D., Ferrari, S., Poluzzi, V., Scotto, F., Trentini, A., Poulain, L., Herrmann, H., Wiedensohler, A., Canonaco, F., Prévôt, A. S. H., Massoli, P., Carbone, C., Facchini, M. C. and Fuzzi, S.: The impact of biomass burning and aqueous-phase processing on air quality: A multi-year source apportionment study in the Po Valley, Italy, Atmos. Chem. Phys., 20(3), 1233–1254, doi:10.5194/acp-20-1233-2020, 2020.

Palm, B. B., Peng, Q., Fredrickson, C. D., Lee, B. H., Garofalo, L. A. and Pothier, M. A.: Quantification of organic aerosol and brown carbon evolution in fresh wildfire plumes, Proc. Natl. Acad. Sci., doi:10.1073/pnas.2012218117, 2020.

Palm, B. B., Peng, Q., Hall, S. R., Ullmann, K., Campos, T. L., Weinheimer, A., Montzka, D., Tyndall, G., Permar, W., Hu, L., Flocke, F., Fischer, E. V, Thornton, J. A., Sciences, A., Observations, A. C., Science, A. and Collins, F.: Spatially resolved photochemistry impacts emissions estimates in fresh wildfire plumes, Geophys. Res. Lett., doi:10.1029/2021GL095443, 2021.

Permar, W., Wang, Q., Selimovic, V., Wielgasz, C., Yokelson, R. J., Hornbrook, R. S., Hills, A. J., Apel, E. C., Ku, I. T., Zhou, Y., Sive, B. C., Sullivan, A. P., Collett, J. L., Campos, T. L., Palm, B. B., Peng, Q., Thornton, J. A., Garofalo, L. A., Farmer, D. K., Kreidenweis, S. M., Levin, E. J. T., DeMott, P. J., Flocke, F., Fischer, E. V. and Hu, L.: Emissions of Trace Organic Gases From Western U.S. Wildfires Based on WE-CAN Aircraft Measurements, J. Geophys. Res. Atmos., 126(11), 1–29, doi:10.1029/2020JD033838, 2021.

Pratt, K. A., Heymsfield, A. J., Twohy, C. H., Murphy, S. M., DeMott, P. J., Hudson, J. G., Subramanian, R., Wang, Z., Seinfeld, J. H. and Prather, K. A.: In situ chemical characterization of aged biomass-burning aerosols impacting cold wave clouds, J. Atmos. Sci., 67(8), 2451–2468, doi:10.1175/2010JAS3330.1, 2010.

Pratt, K. A., Murphy, S. M., Subramanian, R., Demott, P. J., Kok, G. L., Campos, T., Rogers, D. C., Prenni, A. J., Heymsfield, A. J., Seinfeld, J. H. and Prather, K. A.: Flight-based chemical characterization of biomass burning aerosols within two prescribed burn smoke plumes, Atmos. Chem. Phys., 11(24), 12549–12565, doi:10.5194/acp-11-12549-2011, 2011.

Reid, C. E., Brauer, M., Johnston, F. H., Jerrett, M., Balmes, J. R. and Elliott, C. T.: Critical review of health impacts of wildfire smoke exposure, Environ. Health Perspect., 124(9), 1334–1343, doi:10.1289/ehp.1409277, 2016.

Riipinen, I., Pierce, J. R., Donahue, N. M. and Pandis, S. N.: Equilibration time scales of organic aerosol inside thermodenuders: Evaporation kinetics versus thermodynamics, Atmos. Environ., 44(5), 597–607, doi:10.1016/j.atmosenv.2009.11.022, 2010.

Roberts, J. M., Fehsenfeld, F. C., Liu, S. C., Bollinger, M. J., Hahn, C., Albritton, D. L. and Sievers, R. E.: Measurements of aromatic hydrocarbon ratios and NOx concentrations in the rural troposphere: Observation of air mass photochemical aging and NOx removal, Atmos. Environ., 18(11), 2421–2432, doi:10.1016/0004-6981(84)90012-X, 1984.

Schauer, J. J., Kleeman, M. J., Cass, G. R. and Simoneit, B. R. T.: Measurement of emissions from air pollution sources. 3. C1-C29 organic compounds from fireplace combustion of wood, Environ. Sci. Technol., 35(9), 1716–1728, doi:10.1021/es001331e, 2001.

Schill, G. P., Froyd, K. D., Bian, H., Kupc, A., Williamson, C., Brock, C. B., Ray, E., Hornbrook, R. S., Hills, A. J., Apel, E. C., Chin, M., Colarco, P. R. and Murphy, D. M.: Widespread biomass burning smoke throughout the remote troposphere, Nat. Geosci., Accepted(June), doi:10.1038/s41561-020-0586-1, 2020.

Sedlacek, A. J., Lewis, E. R., Onasch, T. B., Zuidema, P., Redemann, J., Jaffe, D. and Kleinman, L. I.: Using the Black Carbon Particle Mixing State to Characterize the Lifecycle of Biomass Burning Aerosols, , doi:10.1021/acs.est.2c03851, 2022.

Seinfeld, J. H. and Pandis, S. N.: Atmospheric Chemistry and Physics. From Air Pollution to Climate Change, Second Edition, Wiley Interscience., 2006.

Shiraiwa, M., Berkemeier, T. and Seinfeld, J. H.: Molecular corridors and kinetic regimes in the multiphase chemical evolution of secondary organic aerosol, , 8323–8341, doi:10.5194/acp-14-8323-2014, 2014.

Simpson, C. D., Paulsen, M., Dills, R. L., Liu, L. S. and Kalman, D. A.: Determination of Methoxyphenols in Ambient Atmospheric Particulate Matter : Tracers for Wood Combustion, Environ. Sci. Technol., 39(2), 631–637, 2005.

Simpson, I. J., Akagi, S. K., Barletta, B., Blake, N. J., Choi, Y., Diskin, G. S., Fried, A., Fuelberg, H. E., Meinardi, S., Rowland, F. S., Vay, S. A., Weinheimer, A. J., Wennberg, P. O., Wiebring, P., Wisthaler, A., Yang, M., Yokelson, R. J., Blake, D. R., Science, A. and Sciences, P.: Boreal forest fire emissions in fresh Canadian smoke plumes : C 1 -C 10 volatile organic compounds (VOCs), CO 2 , CO , NO 2 , NO , HCN and, , 6445–6463, doi:10.5194/acp-11-6445-2011, 2011.

Smith, J. D., Sio, V., Yu, L., Zhang, Q. and Anastasio, C.: Secondary Organic Aerosol Production from Aqueous Reactions of Atmospheric Phenols with an Organic Triplet Excited State, Environ. Sci. Technol., 2014.

Smith, J. D., Kinney, H. and Anastasio, C.: Phenolic carbonyls undergo rapid aqueous photodegradation to form low-volatility , light-absorbing products, Atmos. Environ., 126, 36–44, doi:10.1016/j.atmosenv.2015.11.035, 2016.

Sorvajärvi, T., DeMartini, N., Rossi, J. and Toivonen, J.: In situ measurement technique for simultaneous detection of K, KCl, and KOH vapors released during combustion of solid biomass fuel in a single particle reactor, Appl. Spectrosc., 68(2), 179–184, doi:10.1366/13-07206, 2014.

Sun, Y. L., Zhang, Q., Anastasio, C. and Sun, J.: Insights into secondary organic aerosol formed via aqueous-phase reactions of phenolic compounds based on high resolution mass spectrometry, Atmos. Chem. Phys., doi:10.5194/acp-10-4809-2010, 2010.

Talukdar, R. K., Burkholder, J. B., Schmoltner, A. M., Roberts, J. M., Wilson, R. R. and Ravishankara, A. R.: Investigation of the loss processes for peroxyacetyl nitrate in the atmosphere: UV photolysis and reaction with OH, J. Geophys. Res., 100(D7), doi:10.1029/95jd00545, 1995.

Wang, Y., Hu, M., Xu, N., Qin, Y., Wu, Z., Zeng, L., Huang, X. and He, L.: Chemical composition and light absorption of carbonaceous aerosols emitted from crop residue burning: Influence of combustion efficiency, Atmos. Chem. Phys., 20(22), 13721–13734, doi:10.5194/acp-20-13721-2020, 2020.

Weiss-Penzias, P., Jaffe, D. A., Swartzendruber, P., Dennison, J. B., Chand, D., Hafner, W. and Prestbo, E.: Observations of Asian air pollution in the free troposphere at Mount Bachelor Observatory during the spring of 2004, J. Geophys. Res. Atmos., doi:10.1029/2005JD006522, 2006.

Westerling, A. L. R.: Increasing western US forest wildfire activity: Sensitivity to changes in the timing of spring, Philos. Trans. R. Soc. B Biol. Sci., 371(1696), doi:10.1098/rstb.2015.0178, 2016.

Wigder, N. L., Jaffe, D. A. and Saketa, F. A.: Ozone and particulate matter enhancements from regional

wildfires observed at Mount Bachelor during 2004-2011, Atmos. Environ., doi:10.1016/j.atmosenv.2013.04.026, 2013.

Wolfe, G. M., Nicely, J. M., St, J. M., Hanisco, T. F., Liao, J. and Oman, L. D.: Mapping hydroxyl variability throughout the global remote troposphere via synthesis of airborne and satellite formaldehyde observations, , 116(23), 11171–11180, doi:10.1073/pnas.1821661116, 2019.

Wu, H., Taylor, J. W., Langridge, J. M., Yu, C., Allan, J. D., Szpek, K., Cotterell, M. I., Williams, P. I., Flynn, M., Barker, P., Fox, C., Allen, G., Lee, J. and Coe, H.: Rapid transformation of ambient absorbing aerosols from West African biomass burning, Atmos. Chem. Phys., 21(12), 9417–9440, doi:10.5194/acp-21-9417-2021, 2021.

Yokelson, R. J., Crounse, J. D., DeCarlo, P. F., Karl, T., Urbanski, S., Atlas, E., Campos, T., Shinozuka, Y., Kapustin, V., Clarke, A. D., Weinheimer, A., Knapp, D. J., Montzka, D. D., Holloway, J., Weibring, P., Flocke, F., Zheng, W., Toohey, D., Wennberg, P. O., Wiedinmyer, C., Mauldin, L., Fried, A., Richter, D., Walega, J., Jimenez, J. L., Adachi, K., Buseck, P. R., Hall, S. R. and Shetter, R.: Emissions from biomass burning in the Yucatan, Atmos. Chem. Phys., 9(15), 5785–5812, doi:10.5194/acp-9-5785-2009, 2009.

Young, D. E., Kim, H., Parworth, C., Zhou, S., Zhang, X., Cappa, C. D., Seco, R., Kim, S. and Zhang, Q.: Influences of emission sources and meteorology on aerosol chemistry in a polluted urban environment: Results from DISCOVER-AQ California, Atmos. Chem. Phys., 16(8), 5427–5451, doi:10.5194/acp-16-5427-2016, 2016.

Yu, L., Smith, J., Laskin, A., Anastasio, C., Laskin, J. and Zhang, Q.: Chemical characterization of SOA formed from aqueous-phase reactions of phenols with the triplet excited state of carbonyl and hydroxyl radical, Atmos. Chem. Phys., 14(24), 13801–13816, doi:10.5194/acp-14-13801-2014, 2014.

Yu, L., Smith, J., Laskin, A., M George, K., Anastasio, C., Laskin, J., M Dillner, A. and Zhang, Q.: Molecular transformations of phenolic SOA during photochemical aging in the aqueous phase: Competition among oligomerization, functionalization, and fragmentation, Atmos. Chem. Phys., 16(7), 4511–4527, doi:10.5194/acp-16-4511-2016, 2016.

Zauscher, M. D., Wang, Y., Moore, M. J. K., Gaston, C. J. and Prather, K. A.: Air quality impact and physicochemical aging of biomass burning aerosols during the 2007 San Diego wildfires, Environ. Sci. Technol., 47(14), 7633–7643, doi:10.1021/es4004137, 2013.

Zhang, L. and Jaffe, D. A.: Trends and sources of ozone and sub-micron aerosols at the Mt. Bachelor Observatory (MBO) during 2004–2015, Atmos. Environ., doi:10.1016/j.atmosenv.2017.06.042, 2017.

Zhang, Q., Jimenez, J. L., Canagaratna, M. R., Ulbrich, I. M., Ng, N. L., Worsnop, D. R. and Sun, Y.: Understanding atmospheric organic aerosols via factor analysis of aerosol mass spectrometry: A review, Anal. Bioanal. Chem., doi:10.1007/s00216-011-5355-y, 2011.

Zhang, Q., Zhou, S., Collier, S., Jaffe, D., Onasch, T., Shilling, J., Kleinman, L. and Sedlacek, A.: Understanding composition, formation, and aging of organic aerosols in wildfire emissions via combined mountain top and airborne measurements, ACS Symp. Ser., 1299, 363–385, doi:10.1021/bk-2018-1299.ch018, 2018.

Zhou, S., Collier, S., Jaffe, D. A., Briggs, N. L., Hee, J., Iii, A. J. S., Kleinman, L., Onasch, T. B. and Zhang, Q.: Regional influence of wildfires on aerosol chemistry in the western US and insights into atmospheric aging of biomass burning organic aerosol, Atmos. Chem. Phys., 17(3), doi:10.5194/acp-17-2477-2017, 2017.

Zhou, S., Collier, S., Jaffe, D. A. and Zhang, Q.: Free tropospheric aerosols at the Mt. Bachelor Observatory: More oxidized and higher sulfate content compared to boundary layer aerosols, Atmos. Chem. Phys., doi:10.5194/acp-19-1571-2019, 2019.

4. Source Apportionment of Soot Particles and Aqueous-Phase Processing of Black Carbon Coatings in an Urban Environment

This chapter has been accepted in Atmospheric Chemistry and Physics:
Farley, R. N., Collier, S., Cappa, C. D., Williams, L. R., Onasch, T. B., Russell, M., Kim, H. and Zhang, Q.: Source Apportionment of Soot Particles and Aqueous-Phase Processing of Black Carbon Coatings in an Urban Environment, Atmos. Chem. Phys. Discuss, (August), 1–34, 2023.

4.1 Abstract

The impacts of soot particles on climate and human health depend on the concentration of black carbon (BC) as well as the thickness and composition of the coating material, i.e., organic and inorganic compounds internally mixed with BC. In this study, the size-resolved chemical composition of BC-containing aerosol was measured using a high-resolution soot-particle aerosol mass spectrometer (SP-AMS) during wintertime in Fresno, California, a location influenced by abundant combustion emissions and frequent fog events. Concurrently, particle optical properties were measured to investigate the BC absorption enhancement. Positive matrix factorization (PMF) analysis was performed on the SP-AMS mass spectral measurements to explore the sources of soot particles and the atmospheric processes affecting the properties of BC coatings. The analysis revealed that residential wood burning and traffic are the dominant sources of soot particles. Alongside primary soot particles originating from biomass burning ($BBOA_{BC}$) and vehicles (HOA_{BC}) two distinct types of processed BC-containing aerosol were identified: fog-related oxidized organic aerosol ($FOOA_{BC}$) and winter-background OOA_{BC} ($WOOA_{BC}$). Both types of OOA_{BC} showed evidence of having undergone aqueous processing, albeit with differences. The concentration of $FOOA_{BC}$ was substantially elevated during fog events, indicating the formation of aqueous secondary organic aerosol (aqSOA) within fog droplets. On the other hand, $WOOA_{BC}$ was present at a relatively consistent concentration throughout the winter and is likely related to the formation of secondary organic aerosol (SOA) in both the gas phase and aerosol liquid water. By comparing the chemical properties and temporal variations of $FOOA_{BC}$ and $WOOA_{BC}$, we gain insights into the key aging processes of BC aerosol. It was found that aqueous-phase reactions facilitated by fog droplets had a

significant impact on the thickness and chemical composition of BC coatings, thereby affecting the light absorption and hygroscopic properties of soot particles. These findings underscore the important role of chemical reactions occurring within clouds and fogs and influencing the climate forcing of BC aerosol in the atmosphere.

4.2 Introduction

Soot particles, also known as black carbon (BC) aerosol, are produced during the incomplete combustion of biomass and fossil fuels. BC strongly absorbs solar radiation and significantly influences regional and global climate. Indeed, it is considered the second largest global warming agent after CO_2 (IPCC, 2021; Kumar et al., 2018; Ramanathan and Carmichael, 2008). In addition to direct effects on radiative forcing, BC aerosol can also alter cloud properties by acting as cloud condensation nuclei (CCN), increase cloud evaporation rates, and impede atmospheric mixing (Bond and Bergstrom, 2006; Koch and Del Genio, 2010; Petäjä et al., 2016).

Soot particles are often emitted as highly fractal structures, but can become internally mixed with secondary organic aerosol (SOA) and inorganic species through condensation and coagulation processes (Bhandari et al., 2019; Zhang et al., 2008), resulting in compaction into a spherical shape (Lee et al., 2019). The mixing state and coating composition of BC have important implications for the optical properties and climatic impacts of soot aerosol. Although BC itself is hydrophobic, the mixing with hydrophilic material can convert soot particles into effective CCN, thereby promoting cloud formation and increasing the BC wet deposition rate (Wu et al., 2019). Furthermore, the presence of coating material can enhance the light absorption of BC through the so-called lensing effect (Cappa et al., 2012; Peng et al., 2016). The magnitude of this enhancement is dependent on the coating composition, with absorptive material such as brown carbon (BrC) having a smaller enhancement compared to non-absorbing coatings (Lack and Cappa, 2010). However, the extent of these impacts remains uncertain, and further research is necessary

to better constrain the representation of BC in models. This requires measurements of the mixing state, coating material composition, and optical properties of soot particles in the ambient atmosphere.

Aqueous phase chemical reactions occurring in aerosol liquid water (ALW) and cloud/fog droplets can contribute to the formation of particulate matter and ultimately lead to degraded air quality. One example is the partitioning of water-soluble organic gases into the aqueous phase, where they can react to produce highly oxidized, low volatility compounds. These compounds, generally referred to as aqueous-phase SOA (aqSOA), can remain in the particle phase upon water evaporation (Bianco et al., 2020; Ervens et al., 2011, 2018; Gilardoni et al., 2016; Kim et al., 2019; Sun et al., 2010; Tomaz et al., 2018). The concentrated solute conditions of ALW promote the formation of oligomers and other high molecular weight compounds, while the higher water content conditions found in fog/cloud droplets favor the production of smaller carboxylic acids such as acetic, formic and oxalic acid (Charbouillot et al., 2012; Ervens et al., 2011; Lim et al., 2010). After water evaporation, the residual material is internally mixed with any included BC, or can coagulate with BC particles, resulting in soot particles with high non-BC content and larger particle sizes. (Collier et al., 2018; Meng and Seinfeld, 1994). The occurrence of aqueous-phase reactions are therefore expected to have a significant impact on the thickness and composition of BC coatings, ultimately impacting the optical properties of the soot aerosol (Cao et al., 2022; Cappa et al., 2019). However, a thorough understanding of how aqueous-phase reactions affect ambient soot particles and their optical properties is still lacking.

The San Joaquin Valley (SJV) of California provides an ideal location for studying the impacts of aqueous-phase reactions and fog processing on anthropogenic soot particles (Chen et al., 2018; Collett et al., 1998; Collier et al., 2018; Ge et al., 2012a; Herckes et al., 2015; Kim et al., 2019). This region experiences high levels of humidity and frequent radiation fog events during winter (Collett et al., 1998; Herckes et al., 2015). Moreover, the SJV faces significant air pollution challenges, with severe wintertime particulate matter (PM) pollution episodes and high concentrations of black carbon due to a combination

of elevated anthropogenic emissions and stagnant meteorology (Chen et al., 2018, 2020; Ge et al., 2012b; Parworth et al., 2017; Prabhakar et al., 2017; Sun et al., 2022; Watson et al., 2021; Young et al., 2016). Previous studies using aerosol mass spectrometry (AMS) have demonstrated that particulate matter less than 1μm in diameter (PM_1) during winter in the SJV is strongly influenced by combustion sources, including residential woodburning (RWB) and vehicle exhaust (Betha et al., 2018; Chen et al., 2018; Ge et al., 2012b; Sun et al., 2022; Young et al., 2016). Furthermore, the abundant volatile organic compounds (VOCs) co-emitted from these sources contribute to the formation of secondary organic aerosols (SOA) through both gas-phase and condensed-phase reactions (Chen et al., 2018; Ge et al., 2012b; Kim et al., 2019; Lurmann et al., 2006; Young et al., 2016).

In this study, we investigated the aqueous-phase processing of soot particles using a Soot-Particle Aerosol Mass Spectrometer (SP-AMS) deployed in Fresno, which is the largest city in the SJV with a population of approximately 500,000. In particular, we compared a multi-day fog event (high-fog) to a period with less fog (low-fog) to examine how fog droplet processing influences the chemical, physical and optical properties of soot aerosol. The SP-AMS was modified by removing the thermal vaporizer, leaving it solely equipped with the laser vaporizer. This setup allowed us to selectively measure BC-containing particles and analyze the refractory BC (rBC) and chemical composition of associated non-refractory coatings in real-time. Positive matrix factorization analysis of SP-AMS spectra was used to evaluate the importance of aqueous-phase reactions within fog droplets in shaping the properties of soot particles. SP-AMS ion fragments unique to fog processing were identified, offering valuable information for future ambient measurements aimed at identifying aerosol that has undergone fog/cloud processing. These results provide new insights into the role of aqueous processing in influencing the characteristics of BC-containing particles.

4.3 Experimental Methods

4.3.1 Sampling site and Instrumentation

Measurements were collected between December 19, 2014 and January 13, 2015 at the University of California Cooperative Extension (36°48'35.26"N, 119°46'42.00"W) in Fresno, CA. An Aerodyne SP-AMS was used to obtain the size-resolved concentration of refractory black carbon (rBC) and associated coating material at 5-minute time resolution. The instrument is similar in design to the Aerodyne high-resolution time-of-flight aerosol mass spectrometer (HR-AMS) but includes a 1064 nm Nd:YAG intracavity laser vaporizer for the vaporization of absorbing material such as rBC (DeCarlo et al., 2006; Onasch et al., 2012). The tungsten thermal vaporizer was physically removed from the instrument in order to only measure aerosol species (i.e. organics, nitrate, sulfate, chloride, ammonium) mixed with rBC. Further details of the sampling setup, operation of the SP-AMS and the configuration of collocated instruments are described in section S1.1 and reported in Collier et al. (2018) and Cappa et al. (2018).

Aerosol absorption was measured at 405 and 532 nm using a dual wavelength cavity ringdown/photoacoustic spectrometer (CRD-PAS) and 870nm using a photoacoustic extinctiometer (PAX). Details on the processing of the optical measurements can be found in Cappa et al. (2018) and in section S1.2.

4.3.2 SP-AMS Data Analysis and Source Apportionment via ME-2

SP-AMS measurements were processed in the Squirrel (V. 1.57) and PIKA (V. 1.16) analysis toolkits within the Igor Pro environment. The concentration of rBC was calculated using the sum of C_1^+-C_{10}^+. Organic species also contribute to the signal at C_1^+, therefore rBC contribution to C_1^+ was constrained using the ratio of C_1^+/C_3^+ measured for regal black during instrument calibration. High resolution peak fitting was performed in a similar manner to Collier et al. (2018) with the following modifications. Additional nitrogen-containing organic fragments were included in the ion list. The following refractory metals were also fit: K^+, Rb^+, K_2Cl^+, $K_2NO_3^+$, and $K_3SO_4^+$. Each of these compounds have a significant negative mass defect

with few other possible molecular formulae at the exact m/z ratio, allowing for their unambiguous identification. Organic aerosol elemental ratios including the molar ratios of oxygen-to-carbon (O/C) and hydrogen-to-carbon (H/C) reported here are calculated using the improved ambient method (Canagaratna et al., 2015b).

Positive Matrix Factorization (PMF) analysis was performed on the SP-AMS data matrix using the multilinear engine 2 (ME-2) solver within the Source Finder (SoFi) software (Canonaco et al., 2013; Paatero, 1999; Paatero and Tapper, 1994). The PMF factors associated with rBC aerosol resolved in this study are notated with a "BC" subscript to differentiate them from the NR-PM_1 factors identified in Chen et al (2018). Inputs for PMF included the high-resolution (HR) organic fragments between *m/z* 12-150, unit mass resolution (UMR) signal between *m/z* 151-307 and major inorganic ion fragments. Specifically, C_2^+ through C_5^+ were included for rBC, NO^+ and NO_2^+ for nitrate, Cl^+ and HCl^+ for chloride, SO^+, SO_2^+, HSO_2^+, SO_3^+, HSO_3^+ and $H_2SO_4^+$ for sulfate, NH^+, NH_2^+ and NH_3^+ for ammonium, and K^+ and Rb^+ for metals. Inclusion of inorganic fragments in PMF analysis constrains the rotational ambiguity of the solution and provides additional insight into the physical meaning of the factors (Sun et al., 2012; Zhou et al., 2017). For more information about ME-2 analysis please refer to section S1.3.

To calculate the species dependent mass within each BC-containing particle type, the fragments corresponding with organics, nitrate, sulfate, chloride, ammonium, rBC and K were segregated and scaled by the species dependent relative ionization efficiency (RIE) and the coating thickness dependent collection efficiency (CE) as described in Collier et al. (2018). The RIE values for nitrate, sulfate and ammonium were determined using the thermal vaporizer, and the RIE using the laser vaporizer may vary slightly from this. An RIE of 2.9 was used for potassium (Drewnick et al., 2006) while Rb and potassium containing salts are presented in nitrate equivalent concentration. The potassium RIE was derived using a ToF-AMS equipped with a thermal vaporizer and it is possible the laser vaporizer RIE is varies from this.

4.4 Results and Discussion

4.4.1 Soot Aerosol Composition and Properties in Fresno and the Influence of Fog Processing

The meteorological conditions during the sampling period were typical of winter in the San Joaquin Valley and were characterized by cool and humid weather with average (± σ) temperature of 9.9 ± 4.7°C and relative humidity (RH) of 83 ± 16% (Fig. C4a). The average wind speed was low (0.54 ± 0.32 m/s), indicating stagnant conditions that limited the dispersion of pollutants. Elevated rBC concentration was observed throughout the campaign, with an average of 1.04 ± 0.77 μg m^{-3} (Fig. C4c), due to a prevalence of combustion sources in this area.

Between Jan 7th and Jan 13th, 2015, a multiday fog event occurred, providing an opportunity for us to study the effect of fog processing on aerosol composition and properties. The visibility measured at the Fresno Yosemite International Airport, located approximately 10 km away from the sampling site, clearly indicates the persistent nature of the fog event, as the visibility remained below four km for seven consecutive days (Fig. 4.1, Fig. C4b). In contrast, the preceding, low-fog period between Dec 20th and Jan 4th, 2015 experienced colder and drier conditions. Fog events were less frequent during this period, and when they did occur (e.g., on Dec 21st, Dec 23rd and Dec 31st 2014), they were relatively short-lived, with visibility values below four km for 8 to 14 hours for each occurrence. However, despite the reduced occurrence of fog events, the RH reached 100% nearly every night, suggesting favorable nighttime conditions for the occurrence of aqueous-phase processing within aerosol liquid water (ALW).

A key feature of our study was that the SP-AMS was configured to exclusively measure rBC-containing aerosols. This allowed us to utilize the ratio of the total mass of inorganic and organic material to the mass of rBC ($R_{Coat/BC}$) as a metric for estimating the thickness of coatings on soot particles. In addition, because only 17% of total PM_1 mass was associated with rBC (Chen et al., 2018; Collier et al., 2018), the background concentrations of secondary species in our measurements were lower in comparison to the aggregated aerosols allowing for enhanced sensitivity in detecting subtle compositional changes arising from the production of secondary aerosol through aqueous-phase processing.

To gain insights into the changes associated with secondary aerosol formation during fog processing and understand the intricate chemical transformations occurring within the soot aerosol population, we compare the size-resolved chemical composition of submicrometer particles containing BC ($PM_{1,BC}$) between the high-fog period (Jan 7- Jan 13, 2015) and the low-fog period (Dec. 20 – Jan 4). A $PM_{2.5}$ cyclone was included in the sampling line prior to a diffusion dryer preventing the direct sampling of liquid fog droplets larger than 2.5 µm. Instead, the aerosol composition measured during fog events represents the composition of interstitial particles. As illustrated in Fig. 4.1c, the $PM_{1,BC}$ concentration

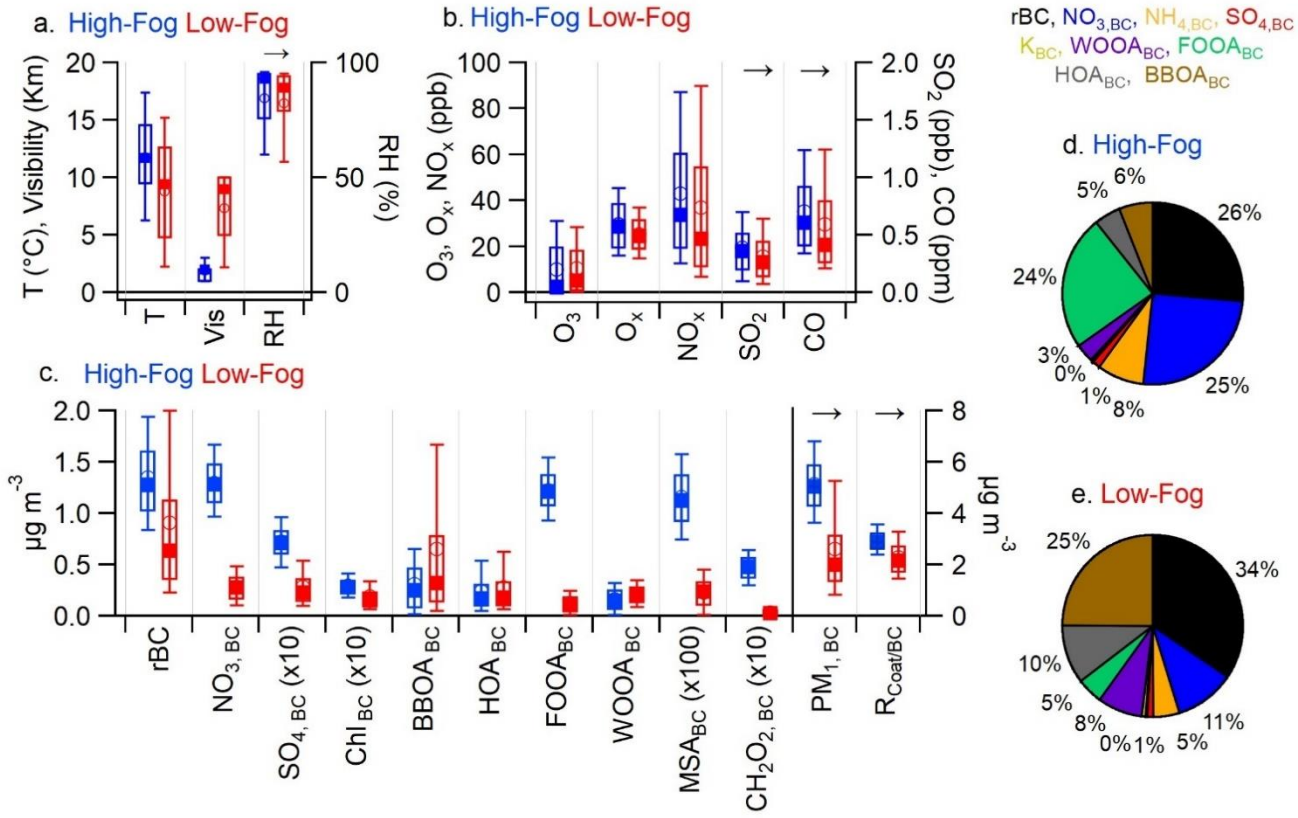

Figure 4.1: Comparison of (a) meteorological variables, (b) gas phase compounds and (c) aerosol phase species between the high-fog (blue symbols) and low-fog (red symbols) periods. The solid and open markers indicate the median and mean respectively, the box indicates the 25th-75th percentile, and whiskers indicate 10th-90th percentiles. $R_{Coat/BC}$ is the dimensionless ratio between the coating mass and rBC mass. (d) Average soot particle composition during the high-fog period. (e) Average soot particle composition during the low-fog period.

increased substantially from 2.6 ± 2.0 μg m^{-3} during the low-fog period to 5.1 ± 1.3 μg m^{-3} during the high-fog period, accompanied by significant changes in the soot aerosol composition. A t-test revealed that the concentrations of directly emitted species, including rBC ($p < 0.01$) and gas-phase CO ($p < 0.05$) displayed statistically significant increases during the high-fog period (Fig. 4.1). This increase is likely associated with the accumulation of pollutants from combustion sources facilitated by the stagnant, windless conditions and decreased boundary layer height. The low-fog period also coincided with the winter holidays, and it is possible that the emission patterns of primary sources, such as residential wood-burning and vehicle traffic varied between the two periods.

The $R_{Coat/BC}$ value increased by a relatively small, but statistically significant amount from 2.30 ± 0.86 during the low-fog period to 2.92 ± 0.45 during the high-fog period ($p < 0.01$; Fig. 4.1c). The increase of $R_{Coat/BC}$ during the fog event was attributed to the accumulation of secondary species, including nitrate, sulfate, ammonium and oxidized organics (Fig. 4.1c, C4). These observations indicate an enhanced production of secondary aerosol species facilitated by aqueous-phase reactions within fog droplets and underscore the profound influence of fog processing on aerosol composition and physical properties.

Nitrate exhibited the most significant increase on soot particles during the high-fog period, with the concentration of $NO_{3,\,BC}$ rising by a factor of five, from 0.28 ± 0.14 μg m^{-3} during the low-fog period to 1.29 ± 0.31 μg m^{-3} (Fig. 4.1c). Its contribution to the $PM_{1,BC}$ mass also increased considerably from 11% to 25% (Fig. 4.1d, 4.1e). These observations provide clear evidence that the presence of fog droplets promoted the formation of nitrate on BC particles. Particulate nitrate in the atmosphere is formed via multiple pathways. One of the pathways involves the gas-phase reaction between NO_2 and the OH radical, resulting in the formation of HNO_3, a highly water-soluble compound which rapidly partitions into liquid droplets (Finlayson-Pitts and Pitts, 1997). Upon the evaporation of water, the abundant ammonia present in the SJV region inhibits the evaporation of nitrate.

Another pathway for nitrate formation involves the heterogeneous uptake and subsequent hydrolysis of N_2O_5. N_2O_5 is formed through the reaction of NO_2 and NO_3 radical, which itself is formed by the reaction between NO_2 and O_3 (Ravishankara, 1997). As both N_2O_5 and its precursor, the NO_3 radical, are quickly photolyzed during the daytime, nitrate formation via the N_2O_5 pathway is typically considered important only at night while the OH pathway dominates during the day. However, previous studies have demonstrated that during fog/cloud events, the reduced transmission of solar radiation, coupled with an elevated droplet surface area, can make N_2O_5 hydrolysis a significant source of nitrate even during the daytime (Brown et al., 2016; Wu et al., 2021a; Zhang et al., 2022). Thus, the suppressed solar radiation during the high-fog period may result in elevated daytime steady-state concentrations of NO_3 radical and N_2O_5. Furthermore, the suppressed solar radiation will also likely lead to decrease in the steady state concentration of the OH radical, further reducing the role of the OH pathway. Together, this suggests that the N_2O_5 formation pathway could be an important factor contributing to the elevated concentrations of nitrate seen during the high-fog period.

The concentration of sulfate was also enhanced in soot aerosols during the high-fog period, exhibiting a 2.5-fold increase compared to the low-fog period (Fig. 4.1). Since SO_2 concentrations were comparable between the two periods, aqueous-phase reactions occurring within fog droplets likely played a role in the increasing sulfate concentration during the high-fog period. This observation aligns with the well-established understanding that SO_2 undergoes rapid conversion to SO_4^{2-} through aqueous-phase reactions (Seinfeld and Pandis, 2006).

Organic compounds were the most abundant species on soot aerosol, contributing 38% and 48% of $PM_{1,BC}$ mass during the high-fog period and low-fog period, respectively. The Org_{BC} was significantly higher during the high-fog period, increasing from 1.25 ± 1.13 μg m^{-3} to 1.96 ± 0.57 μg m^{-3}. Additionally, the composition of Org_{BC} differed between the two periods showing evidence of fog-induced increases of

oxygenated organic species in soot aerosols (Fig. 4.1c). The detailed discussion of this process is provided in the subsequent sections.

Another important species present in $PM_{1,BC}$ in Fresno is potassium, with an average concentration of 53 ± 50 ng m^{-3} and accounting for between 0.7% and 4% of $PM_{1,BC}$ (Fig 4.2). K^+ is emitted directly from the combustion of biomass and serves as an inert tracer for biomass burning emissions as, unlike levoglucosan, K^+ does not degrade during atmospheric processing (Andreae, 1983). However, there is significant variation of the chemical form of potassium in the atmosphere. Although K^+ is usually emitted as KCl or KOH, these compounds undergo rapid acid displacement reactions with H_2SO_4 and HNO_3 to form K_2SO_4 and KNO_3 (Cao et al., 2019; Li et al., 2013; van Lith et al., 2008; Sorvajärvi et al., 2014) . KCl, K_2SO_4 and KNO_3 have been identified previously in aerosols within BB plumes (Li et al., 2003, 2010) and have been detected with mass spectrometry as K_2Cl^+ (*m/z* 112.896), $K_2NO_3^+$ (*m/z* 139.915), and $K_3SO_4^+$ (*m/z* 212.843) (Pratt et al., 2010; Shen et al., 2019; Wang et al., 2020a). Similarly, Rb^+ is also associated with BB emissions (Artaxo et al., 1994; Rivellini et al., 2020). Quantification of K^+ is generally challenging within the AMS as potassium can undergo thermal ionization on the vaporizer surface, leading to highly uncertain ionization efficiency (Drewnick et al., 2015). Even in the absence of the thermal vaporizer, it is possible that potassium can undergo thermal ionization upon the BC particle surface during the vaporization process. However, previous studies have demonstrated a strong correlation between the K signal measured by an AMS and the K^+ concentration measured by collocated ion chromatography attached to a Particle Into Liquid Sampler (PILS), indicating that the AMS-measured K signals can be effectively utilized to determine the temporal variations in particulate potassium concentration (Parworth et al., 2017).

The dominant form of potassium measured was K^+, which exhibited a strong correlation with BBOA (r^2 = 0.93) and Rb^+ (r^2 = 0.78). However, K_2Cl^+, $K_2NO_3^+$ and $K_3SO_4^+$ were also unambiguously identified (Fig. 4.2). The concentration of K_2Cl^+ is sporadic and increased substantially during periods influenced by fresh RWB emissions. Interestingly, K_2Cl^+ concentration remained low throughout the high-fog period,

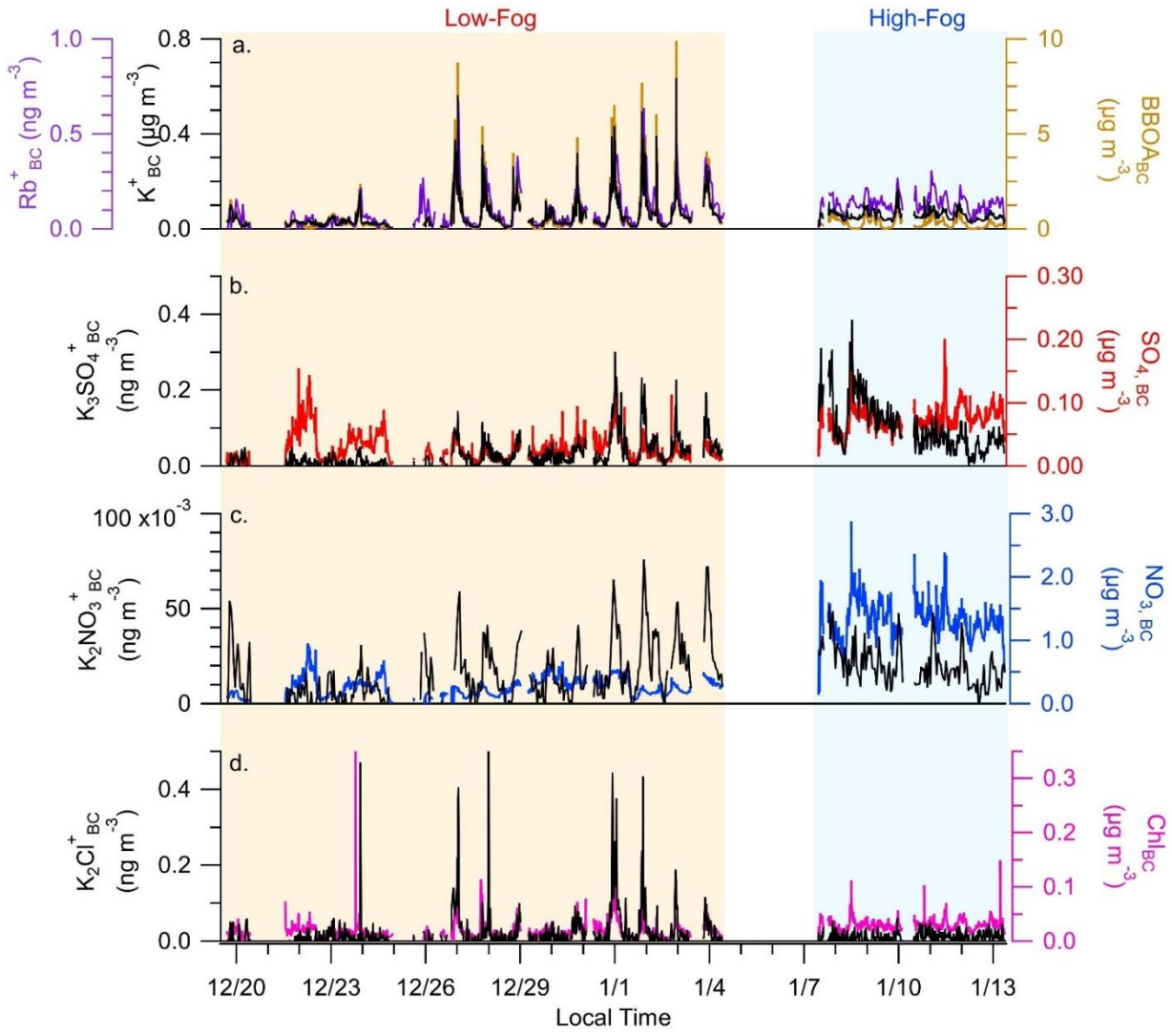

Figure 4.2: Temporal variation of (a) K^+_{BC}, Rb^+_{BC} and $BBOA_{BC}$, (b) $K_3SO_4^+$ and $SO_{4,BC}$, (c) $K_2NO_3^+$ and $NO_{3,BC}$ and (d) K_2Cl^+ and Chl_{BC}.

suggesting that the presence of fog droplets may facilitate the physical or chemical removal of KCl. In contrast, $K_3SO_4^+$ concentrations were elevated during the high-fog period compared to the low-fog period. The correlations between $K_3SO_4^+$ and $SO_{4,BC}$ concentrations showed variable slopes, gradually decreasing over the course of the high-fog period (Fig. 4.2b). The concentration of $K_2NO_3^+$ was considerably lower than the other forms of potassium, despite the abundance of nitrate in the SJV. Parworth et al (2017) found low concentrations of gas-phase HNO_3 likely resulting from the rapid formation of ammonium nitrate due to the high ammonia concentrations. Hence, the low concentrations of K_2NO_3 may be

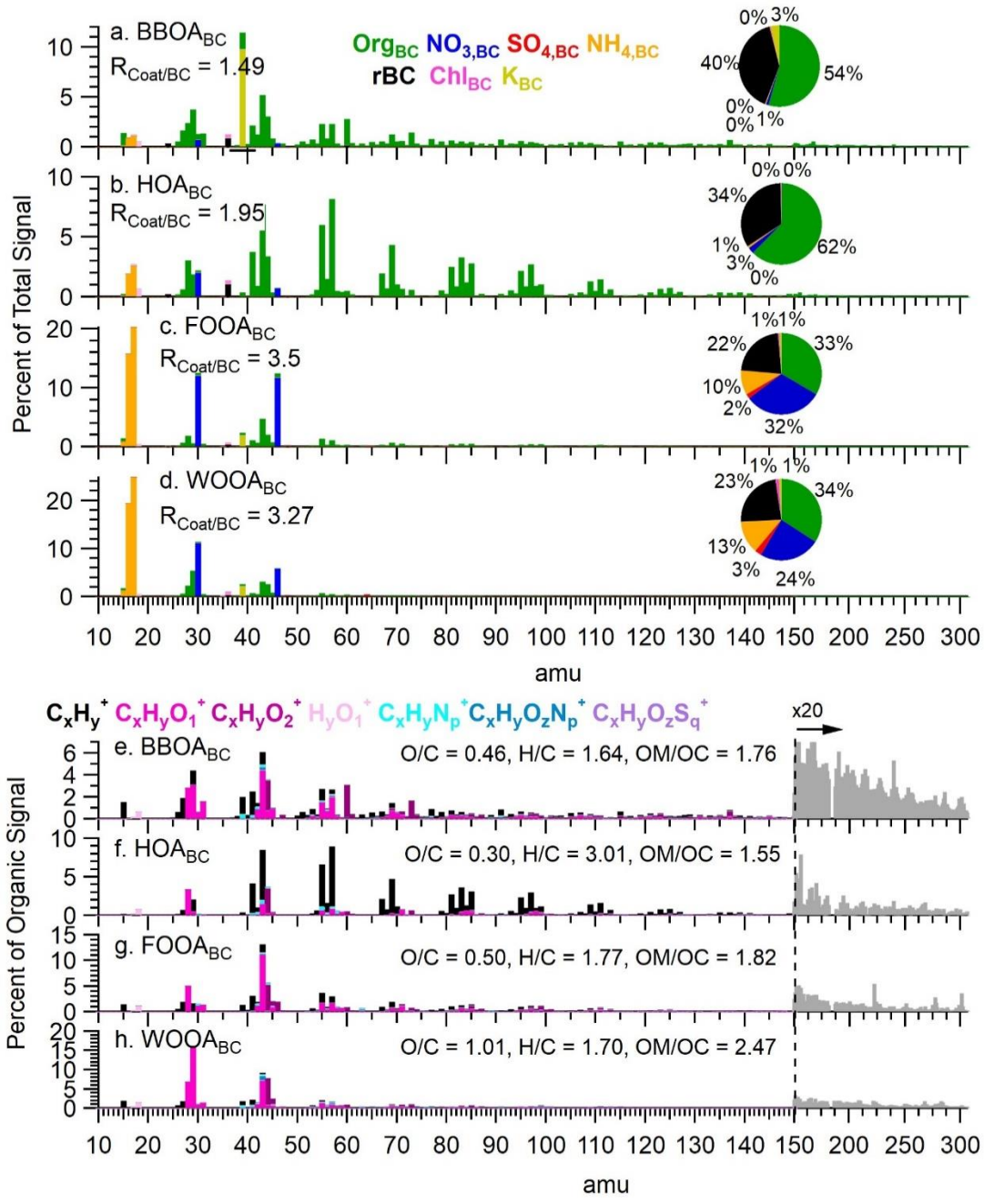

Figure 4.3: (a-d) Mass spectra of rBC containing PMF factors colored by species. y-axis is percent of total nitrate equivalent signal. Pie chart insets depict the mass fraction of each species. (e-h) Organic HRMS Spectra of the PMF factors colored by ion family. Unit mass resolution data was used at values greater than 150 amu, and are scaled by 20 for clarity.

attributed to insufficient HNO_3 levels to form significant amounts of KNO_3 through acid replacement reactions.

4.4.2 Sources and Organic Coating Processing of Soot Particles in Fresno

Through source apportionment analysis that included both organic and inorganic species, we identified four soot particle types. These included a biomass burning organic aerosol ($BBOA_{BC}$) associated with residential wood burning activity, hydrocarbon like organic aerosol (HOA_{BC}) related to vehicle emissions, fog-related oxidized organic aerosol ($FOOA_{BC}$) connected with aqueous phase processing occurring with fog droplets, and winter-background oxidized organic aerosol ($WOOA_{BC}$) associated with both aqueous phase and photochemical processes. The first of these two ($BBOA_{BC}$ and HOA_{BC}) are named according to their primary emission source, while the $FOOA_{BC}$ and $WOOA_{BC}$ are named based on the pathways by which the BC was coated and processed following emission. Biomass burning and vehicles are believed to be the original sources of the BC in $FOOA_{BC}$ and $WOOA_{BC}$, however the primary source signature has degraded or been overshadowed by secondary aerosol formation during atmospheric processing.

Among these, $BBOA_{BC}$ exhibited the highest concentration, with an average concentration of 0.55 $\mu g\ m^{-3}$, accounting for 37% of the OA_{BC} mass over the duration of the campaign. As shown in Fig. 4.3a, the $BBOA_{BC}$ spectrum had significant contributions from the $C_2H_4O_2^+$ (*m/z* = 60) and $C_3H_5O_2^+$ (*m/z* = 73) fragments, both of which are markers for anhydrous sugars such as levoglucosan released during the combustion of biomass (Aiken et al., 2010; Alfarra et al., 2007; Cubison et al., 2011). The organic mass in this factor showed a fraction of signal at *m/z* 60 (f_{60}) of 3.0%, and an O/C of 0.46 indicating $BBOA_{BC}$ likely represents freshly emitted soot particles from BB. Furthermore, Fig. 4.3a shows that $BBOA_{BC}$ had little contribution from inorganic compounds except for K^+, which accounted for 3.4% of the total factor mass. Additionally, $BBOA_{BC}$ displayed the the lowest $R_{Coat/BC}$ (1.49) among the four factors, suggesting that fresh wood smoke aerosol at this site was predominantly thinly coated.

The $BBOA_{BC}$ concentration was higher during the low-fog period, which can be attributed to an increased residential wood burning (RWB) activity due to the colder temperatures and the winter holidays

(Fig. 4.1c, Fig. 4.2a). It is also possible that the lower $BBOA_{BC}$ concentration during the high-fog period was due to rapid fog processing of fresh wood smoke aerosol into OOA, removing the BB source signatures. The time series analysis shows comparable diurnal patterns of $BBOA_{BC}$ concentrations during both periods, with peak concentrations occurring between 19:00-24:00 and a minor increase observed between 7:00-10:00 (Fig. C6a). These results are consistent with previous observations of prevalent RWB activity in Fresno during the winter season (Betha et al., 2018; Ge et al., 2012b; Sun et al., 2022; Young et al., 2016).

The HOA_{BC} factor likely represents soot particles emitted by vehicle traffic and accounted for 18% of OA mass on BC particles. Its mass spectrum was primarily composed of $C_xH_y^+$ ions, displaying an enhancement of the $C_nH_{2n-1}^+$ and $C_nH_{2n+1}^+$ ion series (Fig. 4.3) which is characteristic of fossil fuel combustion (Canagaratna et al., 2004; Collier et al., 2015; Zhang et al., 2005a). HOA_{BC} was the least oxidized factor identified in this study, with an O/C of 0.30. It displayed a slightly elevated contribution from inorganic nitrate, which accounted for 3% of the total factor mass, possibly due to the rapid oxidation of NO_x co-emitted from vehicles. Black carbon accounts for 34% of the total factor mass, yielding an average $R_{Coat/BC}$ of 1.95.

The average organic concentrations of HOA_{BC} during the low-fog and high-fog periods were 0.30±0.32 μg m^{-3} and 0.24±0.23 μg m^{-3}, respectively, indicating relatively consistent emissions of soot particles from vehicular sources throughout the campaign. However, the diurnal profiles of HOA_{BC} showed notable differences between the two periods (Fig. C6b). During the high-fog period, two diurnal peaks of similar magnitudes were observed. The peak in the morning (09:00-10:00) corresponds to rush hour, while the peak in the evening (19:00-23:00) is influenced by a combination of rush hour, decreasing boundary layer height and other, late night combustion activity. In contrast, during the low-fog period, the morning rush-hour peak was nearly absent and the evening peak occurred two hours earlier. These

differences may be due to different traffic patterns during the winter holidays, or differences in boundary layer height between the two periods.

The two OOA_{BC} factors showed distinct spectral and temporal features, suggesting that they may represent soot particles processed through different atmospheric pathways, with coatings formed via different precursor sources or secondary formation processes. The concentration of $FOOA_{BC}$ showed a dramatic increase during the high-fog period, rising by over a factor of 10 from 0.18 ± 0.13 μg m^{-3} to 2.2 ± 0.5 μg m^{-3} (Fig. 4.1). In contrast to this, $WOOA_{BC}$ did not exhibit significantly different concentrations between the two periods. Overall, the organic matter in the $FOOA_{BC}$ factor was less oxidized than the $WOOA_{BC}$ factor, with O/C ratios of 0.50 and 1.01, respectively. The O/C ratio of the $FOOA_{BC}$ is comparable to the O/C ratios observed in residual particles formed from the atomization of fog waters collected in Fresno (Kim et al., 2019). The $FOOA_{BC}$ spectrum is dominated by the $C_2H_3O^+$ fragment and shows a stronger influence from $C_xH_y^+$ fragments (Fig. 4.3). On the other hand, the $WOOA_{BC}$ factor has a higher contribution of oxygen-containing fragments such as the CO_2^+ at *m/z* 44. Furthermore, the $WOOA_{BC}$ factor also exhibits an enhanced fraction of organic mass at *m/z* 29, dominated by the CHO^+ fragment (Fig. 4.3), a marker that has been previously associated with aqSOA (Gilardoni et al., 2016). Nearly all of the nitrate, sulfate and ammonium mass is attributed to the OOA_{BC} factors, indicating the significant contribution of secondary inorganic species as coating material on processed BC aerosol in Fresno. Nitrate and sulfate accounted for 32% and 2% of the total $FOOA_{BC}$ mass and 24% and 3% of the total $WOOA_{BC}$ mass.

The diurnal profile of $FOOA_{BC}$ shows relatively little variation during the high-fog period, with a slight decrease observed at 08:00, and a maximum at 13:00 (Fig. C6c). This decrease in the morning coincided with the lowest visibility values and may be attributed to fog scavenging, or the growth of particles beyond the 1 μm transmission range of the SP-AMS. Based on our findings, we deduce that the organic matter in $FOOA_{BC}$ represents SOA formed through aqueous phase processing within liquid fog droplets.

The $WOOA_{BC}$ concentration shows notably different diurnal profiles between the two periods (Fig C6d). Although the concentration is flat during the low-fog period, this factor showed a notable daytime peak between 08:00 and 20:00 during the high-fog period, indicating the role of photochemical reactions in the formation of $WOOA_{BC}$. During the low-fog period, aqueous-phase processes likely occurred primarily in concentrated aerosol liquid water (ALW) under subsaturated conditions rather than in relatively dilute droplets under foggy conditions. We hypothesize that $WOOA_{BC}$ represents a general OOA factor internally mixed with BC, influenced by SOA formed through aqueous processing in ALW, as well as gas phase photo-oxidation.

Although solar radiation was slightly reduced during the high-fog period compared to the low-fog period, the mixing ratios of gas-phase O_3 and odd oxygen ($O_x = O_3 + NO_2$ (Herndon et al., 2008; Wood et al., 2010)) were similar between the two periods, suggesting comparable photochemical activity (Fig. C11). The role of photochemistry in SOA production was further investigated using the correlation of the aerosol species and O_x (Fig. C9). Overall, there were low correlations ($r^2 < 0.2$) between the concentration of both OOA_{BC} factors and O_x, suggesting that photochemical processes were unable to explain all SOA formation. When normalized to the rBC concentration, a slight increase in $WOOA_{BC}$/rBC was seen at high O_x values during the daytime ($r^2 = 0.32$), supporting that $WOOA_{BC}$ production was influenced by daytime photochemical processes during the low-fog period. However, the concentrations of nitrate and sulfate showed negligible changes with varying O_x levels, supporting the important contribution of aqueous phase reactions in the production of these species.

The soot particles represented by the $FOOA_{BC}$ and $WOOA_{BC}$ factors displayed larger $R_{Coat/BC}$ than the soot particles represented by the $BBOA_{BC}$ and HOA_{BC} factors, with $R_{Coat/BC}$ values of 3.50 and 3.27, respectively. These larger values are consistent with the accumulation of secondary material onto BC particles or the coagulation with non-BC containing secondary particles during atmospheric processing. However, the $R_{Coat/BC}$ observed in our study is considerably lower than values reported in studies that

analyzed heavily processed PM_1 using laser-only SP-AMS, where $R_{Coat/BC}$ values were found to exceed 10 (Healy et al., 2015; Lee et al., 2017; Wang et al., 2017). Therefore, we infer that $FOOA_{BC}$ and $WOOA_{BC}$ likely represent BC particles coated with secondary materials that have undergone limited processing.

Both OOA_{BC} factors also show a minor contribution from K and chloride in the coating material (Fig. 4.3, Fig. C5), indicating that RWB is a notable source of the processed soot particles at this site. This hypothesis is supported by the slightly elevated f_{C2H4O2} signal observed in the mass spectra of both $FOOA_{BC}$ and $WOOA_{BC}$ (0.74% and 0.84%, respectively). To estimate the influence of processed BB emissions on the two OOA_{BC} factors, we utilized K as an inert tracer. The K mass concentration associated with the $FOOA_{BC}$ and $WOOA_{BC}$ factors was multiplied by the BC/K ratio observed in the $BBOA_{BC}$ factor. Assuming a constant BC/K ratio for BB aerosol during atmospheric processing, this calculation resulted in a BB-influenced (BB-inf) fraction of 43% for $FOOA_{BC}$ and 49% for $WOOA_{BC}$. The ratio of BB-inf OOA_{BC} to BBOA was significantly higher ($p < 0.01$) during the high-fog period than the low-fog period, suggesting that the presence of droplets coupled with the stagnant conditions resulted in a higher abundance of processed BBOA (Fig C10). These results also highlight the importance of RWB emissions to the total BC budget in this location.

Due to the abundant $NH_{3(g)}$ emissions in SJV, aerosols are typically neutralized (Parworth et al., 2017; Young et al., 2016). Interestingly, the $BBOA_{BC}$, HOA_{BC} and $FOOA_{BC}$ factors all exhibited a ratio of measured ammonium to predicted ammonium ($NH_{4,meas}/NH_{4,pred}$) less than 1, with ratios of 0.80, 0.93 and 0.96 respectively, indicating an apparent deficit of ammonium. Although this may suggest the presence of acidic aerosol (Zhang et al., 2007), it is more likely due to the presence of the potassium salts of sulfate, nitrate and chloride. In contrast to this, the calculated $NH_{4,meas}/NH_{4,pred}$ ratio for the $WOOA_{BC}$ factor is 1.47, indicating an excess of ammonium associated with this factor. This excess may indicate the presence of organic acids, as suggested by the elevated CO_2^+ and CHO_2^+ signals, which have been proposed as tracers for organic acids (Jiang et al., 2021; Sorooshian et al., 2010; Yatavelli et al., 2015). Additionally, as the

organic matter in $WOOA_{BC}$ has the highest N/C ratio (0.032) among all factors resolved in this study, the elevated ammonium signal could also be contributed by amino compounds, which can fragment into NH_x^+ ions within the AMS (Ge et al., 2014).

Chen et al. (2018) conducted source apportionment analysis of NR-PM_1 using a co-located HR-ToF-AMS, and a comparison with their results provides insight into the differences between the bulk NR-PM_1 composition and the black carbon containing fraction. Four PMF factors were also identified for the source apportionment of NR-PM_1 including $BBOA_{NR\text{-}PM1}$ (O/C = 0.47, H/C = 1.7), $HOA_{NR\text{-}PM1}$ (O/C = 0.11, H/C = 1.8), Nitrate-related OOA ($NOOA_{NR\text{-}PM1}$; O/C = 0.44, H/C = 1.7) and very oxygenated OA ($VOOA_{NR\text{-}PM1}$; O/C = 0.78, H/C = 1.7) (Chen et al., 2018). Due to the two vaporization methods resulting in different fragmentation patterns (Avery et al., 2020; Canagaratna et al., 2015a) the temporal features of each factor are compared rather than a direct comparison of the spectra. The scatter plots of the time series (not shown) reveal a strong correlation between $BBOA_{BC}$ and $BBOA_{NR\text{-}PM1}$, with an r^2 value of 0.81 and a slope of 0.14 obtained through orthogonal distance regression with an intercept of zero. Likewise, the correlation between $HOA_{NR\text{-}PM1}$ and HOA_{BC} was high (r^2 = 0.70). Therefore, the two primary OA factors, HOA and BBOA were combined and displayed in Figure 4.4b. There was no statistical difference in the slope of ΣPOA_{BC} and $\Sigma POA_{NR\text{-}PM1}$ during the two periods. Overall, approximately 12% of POA mass was mixed with rBC in PM_1 during this study assuming the same RIE in the laser and tungsten vaporizer.

The temporal behavior of the OOA factors differ dramatically between the NR-PM_1 and $PM_{1,BC}$ solutions (Fig. 4.4a), suggesting that atmospheric processing may have impacted the non-BC containing fraction differently than the BC containing fraction. The time series of $FOOA_{BC}$ shows a strong correlation with $NOOA_{NR\text{-}PM1}$ (r^2 = 0.80) and no correlation with $VOOA_{NR\text{-}PM1}$ (r^2 = 0.01). However, the $NOOA_{NR\text{-}PM1}$ concentration also shows periods of elevated concentrations during the low-fog period signifying that $NOOA_{NR\text{-}PM1}$ is not unique to fog processing. Cappa et al. (2018) argues that this factor may be formed through various nocturnal oxidation pathways including aqueous-phase reactions and nitrate radical

chemistry. The $WOOA_{BC}$ time series shows no correlation ($r^2 < 0.1$) with either $OOA_{NR\text{-}PM1}$ factor. The correlation between ΣOOA_{BC} and $\Sigma OOA_{NR\text{-}PM1}$ is moderate during both periods, however the slope increases from 0.055 in the low-fog period to 0.12 in the high-fog period and the difference is statistically significant ($p < 0.01$). The steeper slope in the presence of fog suggests that droplet processing creates a more homogenous aerosol population, with a larger portion of secondary material internally mixed with rBC.

Approximately 4% of total sulfate is internally mixed with rBC (Fig. 4.4c). The percent of sulfate mixed with black carbon is slightly enhanced during the low-fog period (4.6% of total sulfate in PM_1 vs. 3.9% during high-fog period; $p < 0.05$). Although the concentration of $NO_{3,BC}$ increased by a factor of five during the high-fog period as discussed above, the fraction mixed with rBC is still low during the high-fog period (8.6%of total NO_3 in PM_1, in contrast to 6.4% during the low-fog period; $p < 0.01$).

4.4.3 Effect of Fog Processing on Soot Particle Size Distribution

The size distribution of soot particles changed significantly over the course of the campaign, peaking at larger sizes (600-700 nm in D_{va}) during the high-fog event consistent with cloud/fog processing (Fig. 4.5; Collier et al., 2018; Eck et al., 2012; Ge et al., 2012a). The average size distribution of each PMF factor was calculated by performing linear decompositions of the average size resolved mass spectra (Fig. 4.5), following the method described by Ge et al., (2012b). To examine the effects of fog processing, the decomposition was performed separately for the low-fog and high-fog periods. The HOA_{BC} and $BBOA_{BC}$ factors show slightly different size distributions between the two periods, with the size mode for each factor shifting to smaller diameters during the high-fog period (Fig. 4.5a-b). Specifically, the BBOA size distribution shifts from a peak at 300nm to 180nm in D_{va}, while the HOA size distribution shifts from a broad peak ranging from 200nm to 400nm to a narrower peak between 100nm and 300nm D_{va}. Additionally, during the low-fog period both HOA_{BC} and $BBOA_{BC}$ size distributions extended to particle sizes larger than 500nm D_{va}, while this tail is completely absent during the high-fog period. As the size

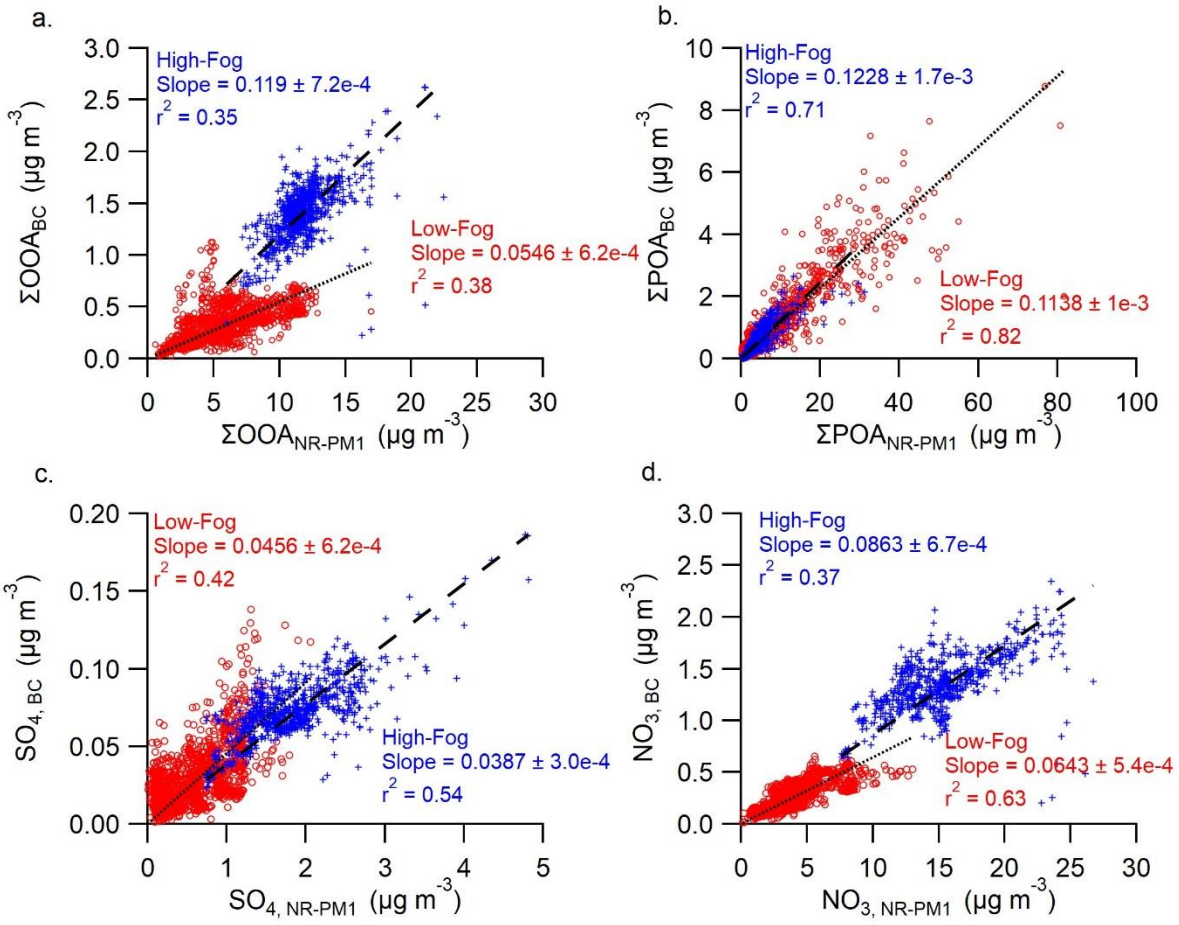

Figure 4.4: Correlation between the (a) sum of OOA factors, (b) sum of POA factors, (c) sulfate and (d) nitrate from SP-AMS and HR-AMS. Data is separated between the low-fog period (Red circles) and high-fog period (blue crosses). The orthogonal distance regressions forced through the origin are also shown for the low-fog (dotted line) and high-fog periods (dashed lines) with fitting parameters included on the figure.

distributions of freshly emitted POAs are likely similar between the two periods, the observed shift towards smaller sizes during the high-fog period may be attributed to rapid wet deposition or droplet scavenging, which selectively removes larger particles from the aerosol population.

The $FOOA_{BC}$ size distribution shows a single mode, peaking at 700nm, which is consistent with droplet processing. On the other hand, the $WOOA_{BC}$ factor appears to contribute more to smaller

accumulation mode particles compared to the $FOOA_{BC}$ factor. This behavior could be due to the condensation of SOA species produced in the gas phase through photochemical processes.

Due to the changes in the aerosol size distributions discussed above, the size dependent $PM_{1,BC}$ composition varied significantly between the two periods (Fig. 4.5e, f). During the high-fog period, small soot particles with D_{va} < 200nm are primarily composed of rBC and the POA species. Larger particles are predominantly coated with $FOOA_{BC}$ and ammonium nitrate. Interestingly, the coating thickness exhibits a strong size dependence, increasing from $R_{coating/BC}$ <1 at 100nm to nearly 6 at 1µm. In contrast, the composition was less variable across the size range during the low-fog period. The rBC fraction remained relatively constant for different sized particles, yielding only a minor increase in coating thicknesses at larger particle sizes.

4.4.4 aqSOA Formation on Soot Particles

The prolonged fog event and high concentrations of liquid water during the high-fog period provide an opportunity to explore the formation of aqSOA in the ambient atmosphere. Table 4.1 lists the changes in the concentration of HR-AMS ion fragments related to different sources, including organic acids, methanesulfonic acid, BBOA and vehicle emissions.

Methanesulfonic acid (MSA, CH_3SO_3H) or its salt – mesylate ($CH_3SO_3^-$) is often used as a marker for aqueous phase processing and has been previously identified in aerosol and fog water in Fresno (Ge et al., 2012b; Kim et al., 2019). Here, two previously identified AMS marker ions for MSA, $CH_2SO_2^+$ and $CH_3SO_2^+$, are observed to be well separated from adjacent ions and are used to estimate the MSA_{BC} concentration. The slope of the signal intensities of these two ions was 0.37 (r^2 = 0.71), which is similar to the ratio seen for pure MSA sampled in the laboratory and suggests that these fragments are primarily produced by MSA (Ge et al., 2012a). The total concentration of MSA in soot particles was estimated using the following formula:

$$\mathrm{MSA_{BC}} = \left(\mathrm{CH_2SO^+_{2,BC}} + \mathrm{CH_3SO^+_{2,BC}}\right) / 0.119 \quad (1)$$

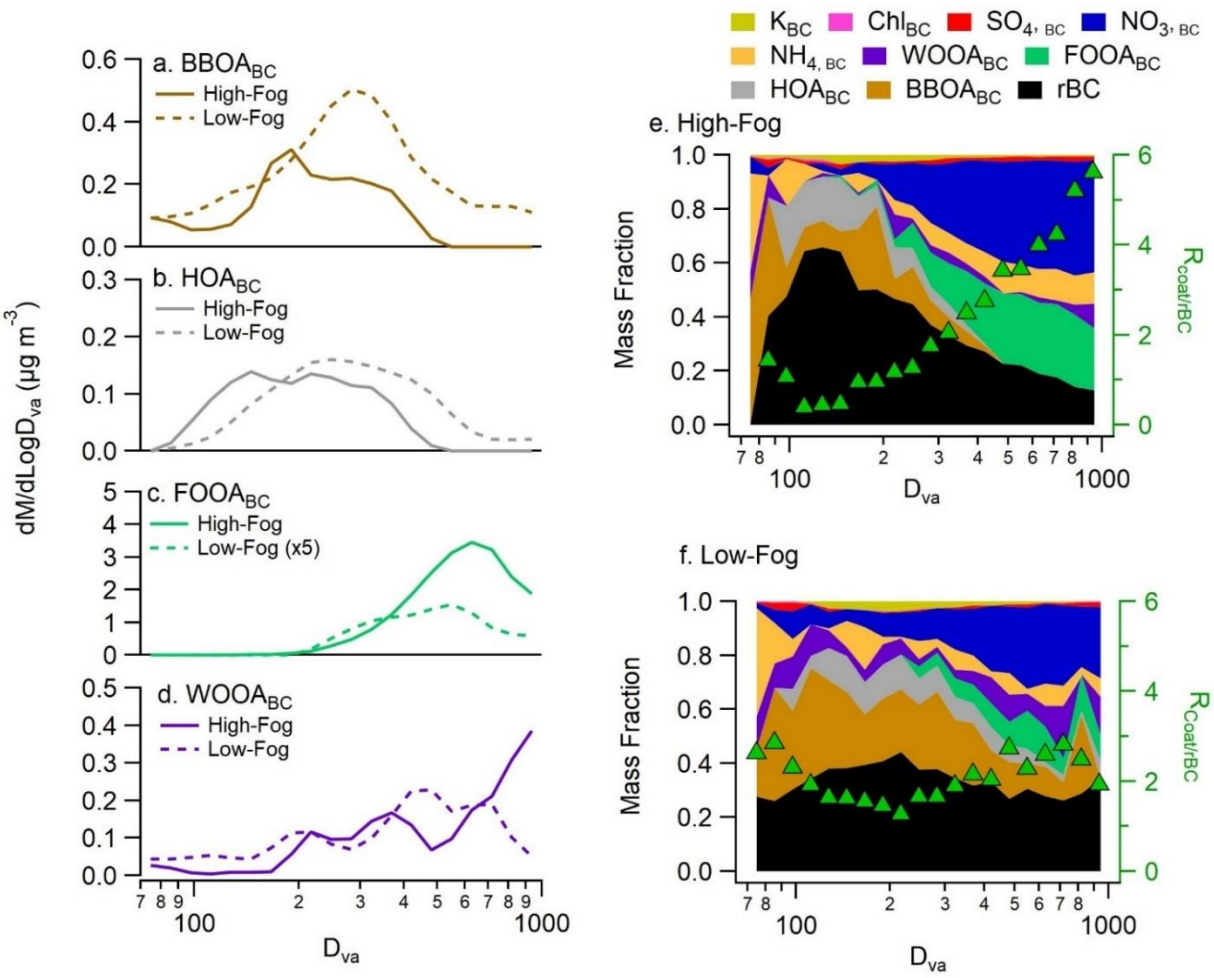

Figure 4.5: (a-d) Average size distributions of soot particle factors during both the high-fog period and low-fog period. Average aerosol composition as a function of size for the (e) high-fog period and (f) low-fog period. Size dependent coating thickness as a function of size is shown in the green triangles.

where $CH_2SO_2^+{}_{BC}$ and $CH_3SO_2^+{}_{BC}$ are the measured mass concentrations of these two ions and 0.119 is their fractional contribution to the total mass spectra of pure MSA reported in Ge et al, (2012a). The MSA_{BC} concentration during the low-fog period was 2.3 ± 1.9 ng m^{-3} and during the high-fog period it was approximately 5 times higher (11.6 ± 3.3 ng m^{-3}; Fig. 4.1c, Table 4.1). Ge et al. (2012a) reported an average MSA concentration of 18 ng m^{-3} in NR-PM$_1$ for the same site during winter 2010, and the lower concentration measured in our study is consistent with only capturing the MSA present in the rBC fraction. The MSA_{BC} concentration during the high-fog period corresponds to 0.59% of OA_{BC} mass, similar to the

0.5% reported by Ge et al. (2012a). Only the $CH_3SO_2^+$ fragment was included in the PMF analysis, and this fragment was mainly attributed to the $FOOA_{BC}$ factor (67%) and the $WOOA_{BC}$ factor (23%), with a minor contribution from $BBOA_{BC}$ (9%). This highlights the influence of aqSOA on both OOA_{BC} factors.

Organic acids are an important component of OA and have been found to contribute up to 50% of OA mass in some ambient samples (Sorooshian et al., 2010; Yatavelli et al., 2015). These compounds, often highly oxidized, have the potential to enhance the CCN ability of the aerosol. In HR-AMS datasets, CO_2^+ (*m/z* 44) is often used as a marker for organic acids and CHO_2^+ (*m/z* 45) has also been proposed as a marker fragment for these compounds (Duplissy et al., 2011; Jiang et al., 2021; Ng et al., 2011). At the study location, the CO_2^+ fragment shows contributions from all the PMF factors, emphasizing the diverse sources of this fragment. Indeed, 38% of CO_2^+ is associated with the two primary factors, indicating the presence of either directly emitted organic acids or other oxygenated functional groups that produce this fragment. In contrast, CHO_2^+ appears to be strongly associated with secondary processes. Nearly all of the signal from this fragment is attributed to the OOA_{BC} factors, with 35% and 62% of its measured signal apportioned to $WOOA_{BC}$ and $FOOA_{BC}$, respectively.

Here we also propose the use of the $CH_2O_2^+$ ion (*m/z* 46) as a novel tracer fragment for fog/cloud droplet processing. Interestingly, 98% of mass of this ion is apportioned to the $FOOA_{BC}$ factor, and a strong correlation ($r^2 = 0.88$) is seen between the timeseries of $CH_2O_2^+$ and $FOOA_{BC}$. Based on the SP-AMS spectra of pure oxalic acid measured in the laboratory, as well as the NIST data base spectra, we hypothesize that this fragment is generated from oxalic acid ($HO_2C\text{-}CO_2H$) or its conjugate base, oxalate ($C_2O_4^{2-}$; Fig. C13). Oxalate is one of the most abundant atmospheric carboxylates and is mainly produced through cloud processing of water soluble compounds such as glyoxal and methylglyoxal (Collett et al., 2008; Ho et al., 2007; Miyazaki et al., 2009; Nah et al., 2018; Tan et al., 2010; Wang et al., 2010) and phenols (Jiang et al., 2021; Sun et al., 2010; Yu et al., 2014). The volatility of ammonium oxalate has previously been found to be several orders of magnitude lower than oxalic acid, making this the most likely form in the ammonia

rich environment of the SJV (Paciga et al., 2014). The $CH_2O_2^+$ fragment has also been identified in aqueous phase OOA PMF factors in Xi'an and Beijing (Duan et al., 2021; Sun et al., 2016) and in cloud droplets following illumination (Schurman et al., 2018). Other possible formation pathways of oxalate are the fragmentation of larger dicarboxylic acids (Ervens et al., 2011) or primary emission from biomass burning (Wang et al., 2007). In this study, we see no significant relationship between $CH_2O_2^+$ and $BBOA_{BC}$ (r^2 = 0.02). This finding is in contrast to measurements in China, where primary BB emissions accounted for 30% of the oxalate mass (Yang et al., 2014).

Table 4.1: Comparison of average (± 1SD) concentration of relevant organic tracer ions during the high-fog period and low-fog period.

Fragment Ion	High-Fog ($ng\ m^{-3}$)	Low-Fog ($ng\ m^{-3}$)	Notes	Reference
CO_2^+	189 ± 57.4	100. ± 75.9	Organic acid tracer	Duplissy et al., 2011
CHO_2^+	30.9 ± 7.37	11.9 ± 6.53	Organic acid tracer	Jiang et al., 2021
$CH_2O_2^+$	47.5 ± 14.2	3.06 ± 4.34	Fog processing tracer	This work
$CH_3SO_2^+$	1.37 ± 0.427	0.277 ± 0.273	MSA tracer	Ge et al., 2012a
$C_2H_4O_2^+$	46.1 ± 27.1	51.6 ± 66.0	BBOA tracer	Cubison et al., 2011
$C_4H_9^+$	74.6 ± 39.8	50.6 ± 54.7	HOA tracer	Zhang et al., 2005

It is important to note that in ambient measurements, the HR-AMS signal at m/z 46 is typically dominated by NO_2^+ (45.9929 amu), and the ability to resolve $CH_2O_2^+$ (46.0055 amu) depends on the resolution of the instrument. Figure C13c displays the high-resolution peak fitting of the signal at *m/z* 46, confirming that the signal attributed to $CH_2O_2^+$ is robust and not an artifact resulting from the high-resolution fitting algorithm. According to the NIST database, other common mono- and di-carboxylic acids do not show significant production of this specific fragment. Formic acid is an exception; however, due to its high volatility, this compound is not expected to be present in the particle phase.

Previous studies have used the strong correlation between oxalic acid and sulfate across various ambient conditions to assess the extent of cloud processing experienced by an air parcel (Hilario et al., 2021; Sorooshian et al., 2006; Yu et al., 2005). While sulfate production is dependent on the liquid water content of the droplets, aqSOA production, including the formation of oxalate, is limited by the uptake of oxidants to the droplet, and is therefore dependent on droplet surface area (Ervens et al., 2014; McVay and Ervens, 2017). Figure 4.6 depicts the correlation between the different organic acid tracers discussed above and sulfate (Fig 4.6a,c,e) or nitrate (Fig 4.6b,d,f). Notably, $CH_2O_2^+$ shows significant enhancement and a strong correlation with both sulfate and nitrate during the high-fog period (Fig. 4.6a,b, Table 4.1). In contrast, the periods of elevated sulfate concentrations during the low-fog period are not associated with elevated concentrations of $CH_2O_2^+$. This variation in slope between the two periods suggests that while aqueous-phase processes can lead to sulfate formation during the low-fog period, the conditions are not conducive to the formation of the parent compound of $CH_2O_2^+$. We hypothesize that this compound is instead formed through processes occurring in the droplets, which only occur during the high-fog period. Unlike sulfate, nitrate can be produced through both photochemical and heterogeneous reactions as discussed earlier. Furthermore, due the semi-volatile nature of ammonium nitrate, its concentration can be influenced by gas-particle partitioning, which is driven by atmospheric conditions and particle acidity. Despite these complications, a discernible relationship between $CH_2O_2^+$ and nitrate is still seen during the high-fog period (Fig 4.6b). This highlights the important role of fog processing in controlling the formation of particulate nitrate as has been seen in previous, bulk aerosol measurements in Fresno (Chen et al., 2018).

The relationship between the CHO_2^+ fragment and sulfate are comparable between both periods (Fig. 4.6a), indicating that similar processes govern the enhancement of both species. Finally, CO_2^+ shows a negligible overall correlation with sulfate (Fig 4.6e). This finding is expected as CO_2^+ can be produced through the fragmentation of a multitude of compounds unrelated to aqueous-phase processing. The

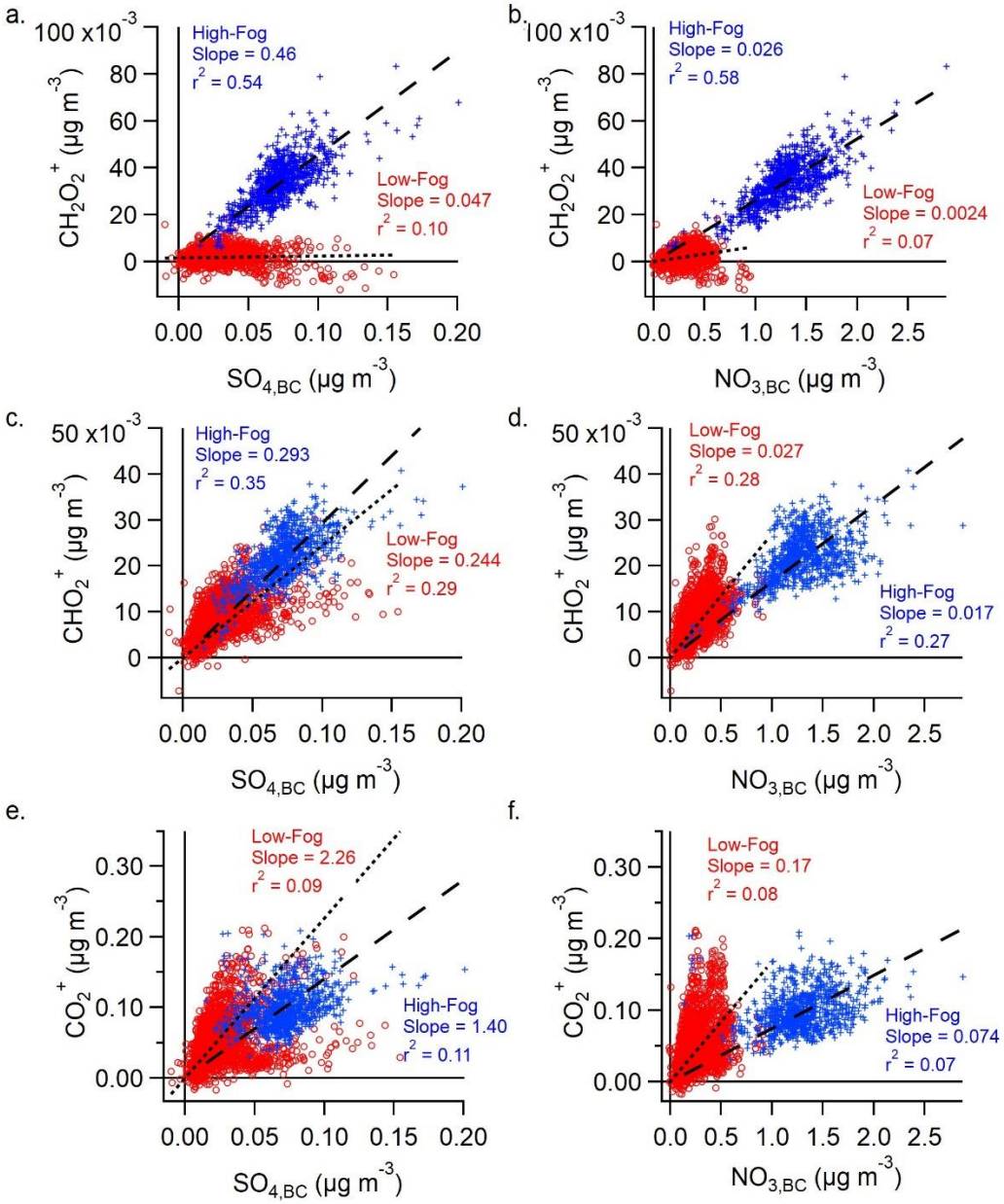

Figure 4.6: Correlations between carboxylic acid tracers and (a,c,e) sulfate or (b,d,f) nitrate. Data is separated between the low-fog period (Red circles, dotted line) and high-fog period (blue crosses, dashed line). Trend lines are orthogonal distance regressions and forced through the origin.

relationship between CHO_2^+ and $SO_{4,BC}$ (Fig. 4.6c) as well as CO_2^+ and $SO_{4,BC}$ (Fig. 4.6e) during the low-fog period shows a variation in slope with time, resulting in the overall low correlation, emphasizing the different sources of these species.

4.4.5 Influence of aqueous-phase processing on soot particle absorption properties and hygroscopicity

The soot particle composition as a function of $R_{Coat/BC}$ is shown in Fig. 4.7. The results reveal that the BC-containing POA factors are the dominant components when the rBC particles were thinly coated (i.e., $R_{Coat/BC} < 2$). However, as the coating thickness increased, the contributions of $FOOA_{BC}$ and nitrate become more prominent. Interestingly, the mass fraction of $FOOA_{BC}$ reaches a peak at an $R_{coat/BC}$ of 4, followed by a decrease at higher coating thickness. This suggests that during fog events, processed soot particles are likely removed from the atmosphere through wet deposition or advected away from the sampling site prior to becoming thickly coated. Instead, thickly coated soot particles ($R_{Coat/BC} > 4$) at this site are dominated by ammonium nitrate, HOA_{BC} and $WOOA_{BC}$. Previous studies have identified thickly coated HOA aerosol originating from diesel emissions, due to the rapid condensation of lubricating oils onto rBC aerosol (Carbone et al., 2019; Willis et al., 2016). Additionally, the higher mass fraction of $WOOA_{BC}$ at large $R_{coat/BC}$ values suggests the presence of particles that have undergone significant processing, possibly representing regionally transported aerosols.

Figure 4.7 also depicts the average rBC absorption enhancement (E_{abs}) for each $R_{coat/BC}$ bin. E_{abs} describes the relative increase in the mass absorption coefficient (MAC) of coated BC compared to pure BC due to the lensing effect (Cappa et al., 2012; Lack and Cappa, 2010). Details on the calculation of E_{abs} can be found in section S1.2 and Cappa et al. (2019). Although no clear monotonic trend of E_{abs} with coating thickness is observed, there is an increase in E_{abs} between $R_{coat/BC}$ of 2.5 to 4, followed by a subsequent decrease at larger $R_{Coat/BC}$ (Fig. 4.7). This observation suggests that the observed E_{abs} is dependent not only on coating thickness, but also on the composition of the coating material. A high fraction of secondary material, particularly oxidized organic formed through fog processing, may contribute to a stronger absorption enhancement. However, it is important to consider that the particular dependence of E_{abs} on $R_{coat/BC}$ could also be due to heterogeneity in the aerosol mixing state, the presence of brown carbon, or changes in the size distribution, as discussed in section 3.4. Regardless, our results

agree with previous studies that have identified the critical role of secondary species in influencing E_{abs} (Liu et al., 2015; Xie et al., 2019; Zhang et al., 2018c; Zheng et al., 2022).

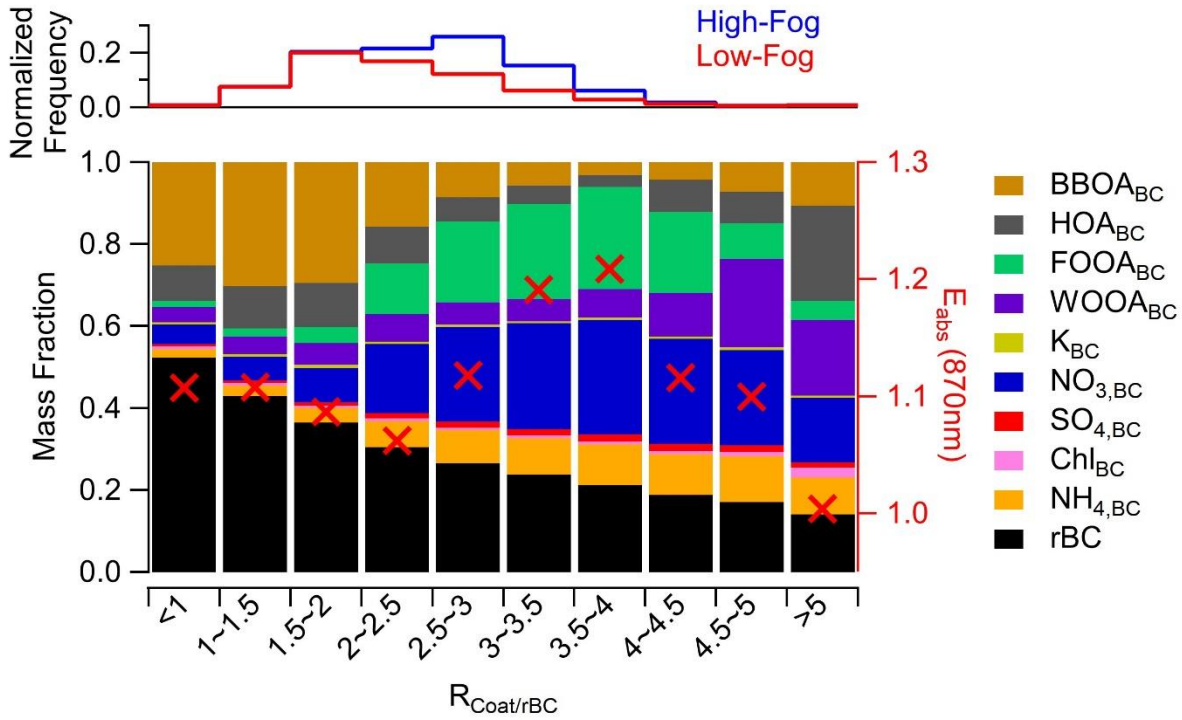

Figure 4.7: Fractional mass contribution of aerosol species binned by rBC coating thickness. Red crosses indicate the average absorption enhancement for each bin. The top panel shows the normalized frequency of the occurrence of different coating thicknesses, separated between the two periods.

The presence of hygroscopic coating material on rBC aerosol greatly increases the ability for the soot particles to take up water. This can allow them to act as cloud condensation nuclei, and alter their impact on cloud properties. To explore this, the ALW associated with inorganic compounds present in BC-containing particles ($ALWC_{E\text{-}AIM,BC}$) was estimated using the Extended Aerosol Inorganic Model (E-AIM) (Clegg et al., 1998) and the ALW associated with organics ($ALWC_{Org,BC}$) was estimated using the parameterization introduced in Petters and Kreidenweis (2007). The total ALWC associated with BC ($ALWC_{BC}$) was calculated as the sum of these two components. A detailed description of the ALWC calculations is included in section S1.3. The average $ALWC_{BC}$ increased from 2.8 ± 2.5 μg m^{-3} during the low-fog period to 8.5 ± 5.6 μg m^{-3} during the high-fog period (Fig. C14). The $ALWC_{BC}$ shows a strong diurnal

profile driven by the temporal variation of RH, indicating that aqueous processing within ALW may be prevalent at night throughout the entire campaign. However, the 3-fold increase that is seen during the high-fog period is a result of the high concentrations of ammonium nitrate and other hygroscopic coating material. The $ALWC_{BC}$ associated with organics (average 26%) is similar to measurements made in Beijing (30%) and other urban areas globally (21%) (Jin et al., 2020; Nguyen et al., 2016). The high concentrations of $ALWC_{BC}$ estimated here highlight that despite the hydrophobicity of the rBC core of the soot aerosol, the presence of ammonium nitrate and oxidized organic material allows soot particles to uptake water and provide sites for aqueous phase processing. Fog conditions generally have relatively low ambient supersaturation values, therefore it is necessary for particles to be sufficiently hygroscopic to initially activate and undergo droplet processing. However, following this initial activation further aqueous phase processing significantly increases the particle hygroscopicity.

4.5 Conclusions

BC-containing aerosol was sampled in a polluted, urban environment in the San Joaquin Valley of California, where residential wood burning and vehicle emissions are the main sources of soot particles. The presence of a persistent multiday fog event provided an excellent opportunity for a comprehensive case study on the effects of droplet processing on the chemical, physical and optical properties of soot aerosol. Through source apportionment analysis, two distinct BC-containing OOA factors were resolved: one related to fog processing ($FOOA_{BC}$) and the other representing a general winter OOA ($WOOA_{BC}$) impacted by both photochemical and aqueous phase reactions. $CH_2O_2^+$ was identified as a unique HRMS fragment that was only detectable in soot particles during the high-fog period and is proposed as an HR-AMS tracer ion for fog and cloud processing. This fragment is thought to originate from dicarboxylates, such as oxalate, which is produced through droplet processes. Although caution is advised when peak fitting is performed on this ion due to its close proximity to NO_2^+, $CH_2O_2^+$ may be useful for identifying ambient aqSOA formed through droplet processing.

Our results demonstrate that soot aerosols in Fresno are enriched with $FOOA_{BC}$ and inorganic ammonium nitrate during the winter fog event. Both components are hygroscopic, and in conjunction with the larger aerosol size distribution, suggest that soot particles that have undergone cloud or fog processing may serve as effective cloud condensation nuclei. This finding has important implications for accurately modelling the removal rate of black carbon from the atmosphere in global climate models. Furthermore, we observed a correlation between the BC absorption enhancement (E_{abs}) and $FOOA_{BC}$ fraction. Further research is needed to determine whether this relationship is primarily influenced by the coating composition, or if it is influenced by covariation with aerosol morphology and size.

References

Aiken, A. C., De Foy, B., Wiedinmyer, C., Decarlo, P. F., Ulbrich, I. M., Wehrli, M. N., Szidat, S., Prevot, A. S. H., Noda, J., Wacker, L., Volkamer, R., Fortner, E., Wang, J., Laskin, A., Shutthanandan, V., Zheng, J., Zhang, R., Paredes-Miranda, G., Arnott, W. P., Molina, L. T., Sosa, G., Querol, X. and Jimenez, J. L.: Mexico city aerosol analysis during MILAGRO using high resolution aerosol mass spectrometry at the urban supersite (T0)-Part 2: Analysis of the biomass burning contribution and the non-fossil carbon fraction, Atmos. Chem. Phys., 10(12), 5315–5341, doi:10.5194/acp-10-5315-2010, 2010.

Alfarra, M. R., Prevot, A. S. H., Szidat, S., Sandradewi, J., Weimer, S., Lanz, V. A., Schreiber, D., Mohr, M. and Baltensperger, U.: Identification of the mass spectral signature of organic aerosols from wood burning emissions, Environ. Sci. Technol., doi:10.1021/es062289b, 2007.

Andreae, M. O.: Soot carbon and excess fine potassium: Long-range transport of combustion-derived aerosols, Science (80-.)., 220(4602), 1148–1151, doi:10.1126/science.220.4602.1148, 1983.

Artaxo, P., Gerab, F., Yamasoe, M. A. and Martins, J. V: Fine mode aerosol composition at three long-term atmospheric monitoring sites in the Amazon Basin, J. Geophys. Res., 99(Dll), 22857–22868, 1994.

Avery, A. M., Williams, L. R., Fortner, E. C., Robinson, W. A. and Onasch, T. B.: Particle detection using the dual-vaporizer configuration of the soot particle Aerosol Mass Spectrometer (SP-AMS), Aerosol Sci. Technol., 55(3), 254–267, doi:10.1080/02786826.2020.1844132, 2020.

Betha, R., Russell, L. M., Chen, C. L., Liu, J., Price, D. J., Sanchez, K. J., Chen, S., Lee, A. K. Y., Collier, S. C., Zhang, Q., Zhang, X. and Cappa, C. D.: Larger Submicron Particles for Emissions With Residential Burning in Wintertime San Joaquin Valley (Fresno) than for Vehicle Combustion in Summertime South Coast Air Basin (Fontana), J. Geophys. Res. Atmos., 123(18), 10,526-10,545, doi:10.1029/2017JD026730, 2018.

Bhandari, J., Chandrakar, K. K., Kinney, G., Cantrell, W., Shaw, R. A., Mazzoleni, L. R., Girotto, G., Sharma, N., Gorkowski, K., Gilardoni, S., Decesari, S., Facchini, M. C., Zanca, N., Pavese, G., Esposito, F., Dubey, M. K., Aiken, A. C., Chakrabarty, R. K., Moosmüller, H., Onasch, T. B., Zaveri, R. A., Scarnato, B. V, Fialho, P. and Mazzoleni, C.: Extensive Soot Compaction by Cloud Processing from Laboratory and Field Observations, , (May), 1–12, doi:10.1038/s41598-019-48143-y, 2019.

Bianco, A., Passananti, M., Brigante, M. and Mailhot, G.: Photochemistry of the cloud aqueous phase: A

review, Molecules, 25(2), 1–23, doi:10.3390/molecules25020423, 2020.

Bond, T. C. and Bergstrom, R. W.: Light absorption by carbonaceous particles: An investigative review, Aerosol Sci. Technol., 27–67, doi:10.1080/02786820500421521, 2006.

Brown, S. S., Dubé, W. P., Tham, Y. J., Zha, Q., Xue, L., Poon, S., Wang, Z., Blake, D. R., Tsui, W., Parrish, D. D. and Wang, T.: Nighttime chemistry at a high altitude site above Hong Kong, J. Geophys. Res. Atmos., (3), 2457–2475, doi:10.1002/2015JD024566.Received, 2016.

Canagaratna, M. R., Jayne, J. T., Ghertner, D. A., Herndon, S., Shi, Q., Jimenez, J. L., Silva, P. J., Williams, P., Lanni, T., Drewnick, F., Demerjian, K. L., Kolb, C. E. and Worsnop, D. R.: Chase studies of particulate emissions from in-use New York City vehicles, Aerosol Sci. Technol., 38(6), 555–573, doi:10.1080/02786820490465504, 2004.

Canagaratna, M. R., Massoli, P., Browne, E. C., Franklin, J. P., Wilson, K. R., Onasch, T. B., Kirchstetter, T. W., Fortner, E. C., Kolb, C. E., Jayne, J. T., Kroll, J. H. and Worsnop, D. R.: Chemical compositions of black carbon particle cores and coatings via soot particle aerosol mass spectrometry with photoionization and electron ionization, J. Phys. Chem. A, 119(19), 4589–4599, doi:10.1021/jp510711u, 2015a.

Canagaratna, M. R., Jimenez, J. L., Kroll, J. H., Chen, Q., Kessler, S. H., Massoli, P., Hildebrandt Ruiz, L., Fortner, E., Williams, L. R., Wilson, K. R., Surratt, J. D., Donahue, N. M., Jayne, J. T. and Worsnop, D. R.: Elemental ratio measurements of organic compounds using aerosol mass spectrometry: Characterization, improved calibration, and implications, Atmos. Chem. Phys., 15(1), doi:10.5194/acp-15-253-2015, 2015b.

Canonaco, F., Crippa, M., Slowik, J. G., Baltensperger, U. and Prévôt, A. S. H.: SoFi, an IGOR-based interface for the efficient use of the generalized multilinear engine (ME-2) for the source apportionment: ME-2 application to aerosol mass spectrometer data, Atmos. Meas. Tech., doi:10.5194/amt-6-3649-2013, 2013.

Cao, L. M., Wei, J., He, L. Y., Zeng, H., Li, M. L., Zhu, Q., Yu, G. H. and Huang, X. F.: Aqueous aging of secondary organic aerosol coating onto black carbon: Insights from simultaneous L-ToF-AMS and SP-AMS measurements at an urban site in southern China, J. Clean. Prod., 330(November 2021), 129888, doi:10.1016/j.jclepro.2021.129888, 2022.

Cao, W., Martí-Rosselló, T., Li, J. and Lue, L.: Prediction of potassium compounds released from biomass during combustion, Appl. Energy, 250(May), 1696–1705, doi:10.1016/j.apenergy.2019.05.106, 2019.

Cappa, C. D., Onasch, T. B., Massoli, P., Worsnop, D. R., Jobson, B. T., Kolesar, K. R., Lack, D. A., Lerner, B. M. and Li, S.: Radiative Absorption Enhancements Due to the Mixing State of Atmospheric Black Carbon, Science (80-.)., (August), 1078–1082, 2012.

Cappa, C. D., Zhang, X., Russell, L. M., Collier, S., Lee, A. K. Y., Chen, C. L., Betha, R., Chen, S., Liu, J., Price, D. J., Sanchez, K. J., McMeeking, G. R., Williams, L. R., Onasch, T. B., Worsnop, D. R., Abbatt, J. and Zhang, Q.: Light Absorption by Ambient Black and Brown Carbon and its Dependence on Black Carbon Coating State for Two California, USA, Cities in Winter and Summer, J. Geophys. Res. Atmos., 124(3), 1550–1577, doi:10.1029/2018JD029501, 2019.

Carbone, S., Timonen, H. J., Rostedt, A., Happonen, M., Keskinen, J., Ristimaki, J., Korpi, H., Artaxo, P., Worsnop, D., Canonaco, F., Prévôt, A. S. H., Hillamo, R., Saarikoski, S., Keskinen, J., Ristimaki, J., Korpi, H., Artaxo, P., Canagaratna, M., Worsnop, D., Canonaco, F., Prévôt, A. S. H., Hillamo, R. and Saarikoski, S.: Distinguishing fuel and lubricating oil combustion products in diesel engine exhaust particles, Aerosol

Sci. Technol., 53(5), 594–607, doi:10.1080/02786826.2019.1584389, 2019.

Charbouillot, T., Gorini, S., Voyard, G., Parazols, M., Brigante, M., Deguillaume, L., Delort, A. M. and Mailhot, G.: Mechanism of carboxylic acid photooxidation in atmospheric aqueous phase: Formation, fate and reactivity, Atmos. Environ., 56, 1–8, doi:10.1016/j.atmosenv.2012.03.079, 2012.

Chen, C. L., Chen, S., Russell, L. M., Liu, J., Price, D. J., Betha, R., Sanchez, K. J., Lee, A. K. Y., Williams, L., Collier, S. C., Zhang, Q., Kumar, A., Kleeman, M. J., Zhang, X. and Cappa, C. D.: Organic Aerosol Particle Chemical Properties Associated With Residential Burning and Fog in Wintertime San Joaquin Valley (Fresno) and With Vehicle and Firework Emissions in Summertime South Coast Air Basin (Fontana), J. Geophys. Res. Atmos., 123(18), 10,707-10,731, doi:10.1029/2018JD028374, 2018.

Chen, J., Yin, D., Zhao, Z., Kaduwela, A. P., Avise, J. C., DaMassa, J. A., Beyersdorf, A., Burton, S., Ferrare, R., Herman, J. R., Kim, H., Neuman, A., Nowak, J. B., Parworth, C., Scarino, A. J., Wisthaler, A., Young, D. E. and Zhang, Q.: Modeling air quality in the San Joaquin valley of California during the 2013 Discover-AQ field campaign, Atmos. Environ. X, 5, 100067, doi:10.1016/j.aeaoa.2020.100067, 2020.

Clegg, S. L., Brimblecombe, P. and Wexler, A. S.: Thermodynamic model of the system H+-NH4+-SO42-NO 3--H2O at tropospheric temperatures, J. Phys. Chem. A, 102(12), 2137–2154, doi:10.1021/jp973042r, 1998.

Collett, J. L., Hoag, K. J., Sherman, D. E., Bator, A. and Richards, L. W.: Spatial and temporal variations in San Joaquin Valley fog chemistry, Atmos. Environ., 33(1), 129–140, doi:10.1016/S1352-2310(98)00136-8, 1998.

Collett, J. L., Herckes, P., Youngster, S. and Lee, T.: Processing of atmospheric organic matter by California radiation fogs, Atmos. Res., 87, 232–241, doi:10.1016/j.atmosres.2007.11.005, 2008.

Collier, S., Zhou, S., Kuwayama, T., Forestieri, S., Brady, J., Zhang, M., Kleeman, M., Cappa, C., Bertram, T. and Zhang, Q.: Organic PM emissions from vehicles: Composition, O/C ratio, and dependence on PM concentration, Aerosol Sci. Technol., 49(2), 86–97, doi:10.1080/02786826.2014.1003364, 2015.

Collier, S., Williams, L. R., Onasch, T. B., Cappa, C. D., Zhang, X., Russell, L. M., Chen, C. L., Sanchez, K. J., Worsnop, D. R. and Zhang, Q.: Influence of Emissions and Aqueous Processing on Particles Containing Black Carbon in a Polluted Urban Environment: Insights From a Soot Particle-Aerosol Mass Spectrometer, J. Geophys. Res. Atmos., 123(12), 6648–6666, doi:10.1002/2017JD027851, 2018.

Cubison, M. J., Ortega, A. M., Hayes, P. L., Farmer, D. K., Day, D., Lechner, M. J., Brune, W. H., Apel, E., Diskin, G. S., Fisher, J. A., Fuelberg, H. E., Hecobian, A., Knapp, D. J., Mikoviny, T., Riemer, D., Sachse, G. W., Sessions, W., Weber, R. J., Weinheimer, A. J., Wisthaler, A. and Jimenez, J. L.: Effects of aging on organic aerosol from open biomass burning smoke in aircraft and laboratory studies, Atmos. Chem. Phys., doi:10.5194/acp-11-12049-2011, 2011.

DeCarlo, P. F., Kimmel, J. R., Trimborn, A., Northway, M. J., Jayne, J. T., Aiken, A. C., Gonin, M., Fuhrer, K., Horvath, T., Docherty, K. S., Worsnop, D. R. and Jimenez, J. L.: Field-deployable, high-resolution, time-of-flight aerosol mass spectrometer, Anal. Chem., doi:10.1021/ac061249n, 2006.

Drewnick, F., Hings, S. S., Curtius, J., Eerdekens, G. and Williams, J.: Measurement of fine particulate and gas-phase species during the New Year's fireworks 2005 in Mainz, Germany, Atmos. Environ., 40(23), 4316–4327, doi:10.1016/j.atmosenv.2006.03.040, 2006.

Drewnick, F., Diesch, J. M., Faber, P. and Borrmann, S.: Aerosol mass spectrometry: Particle-vaporizer interactions and their consequences for the measurements, Atmos. Meas. Tech., 8(9), 3811–3830,

doi:10.5194/amt-8-3811-2015, 2015.

Duan, J., Huang, R., Gu, Y., Lin, C., Zhong, H., Wang, Y., Yuan, W., Ni, H., Yang, L., Chen, Y., Worsnop, D. R. and Dowd, C. O.: The formation and evolution of secondary organic aerosol during summer in Xi'an : Aqueous phase processing in fog-rain days, Sci. Total Environ., 756, 144077, doi:10.1016/j.scitotenv.2020.144077, 2021.

Duplissy, J., Decarlo, P. F., Dommen, J., Alfarra, M. R., Metzger, A., Barmpadimos, I. and Prevot, A. S. H.: Relating hygroscopicity and composition of organic aerosol particulate matter, Atmos. Chem. Phys., 1155–1165, doi:10.5194/acp-11-1155-2011, 2011.

Eck, T. F., Holben, B. N., Reid, J. S., Giles, D. M., Rivas, M. A., Singh, R. P., Tripathi, S. N., Bruegge, C. J., Platnick, S., Arnold, G. T., Krotkov, N. A., Carn, S. A., Sinyuk, A., Dubovik, O., Arola, A., Schafer, J. S., Artaxo, P., Smirnov, A., Chen, H. and Goloub, P.: Fog- and cloud-induced aerosol modification observed by the Aerosol Robotic Network (AERONET), J. Geophys. Res., 117, 1–18, doi:10.1029/2011JD016839, 2012.

Ervens, B., Turpin, B. J., Weber, R. J., Brunswick, N. and Sciences, A.: Secondary organic aerosol formation in cloud droplets and aqueous particles (aqSOA): a review of laboratory , field and model studies, Atmos. Chem. Phys., 11069–11102, doi:10.5194/acp-11-11069-2011, 2011.

Ervens, B., Sorooshian, A., Lim, Y. B. and Turpin, B. J.: Key parameters controlling OH-initiated formation of secondary organic aerosol in the aqueous phase (aqSOA), , 3997–4016, doi:10.1002/2013JD021021.Received, 2014.

Ervens, B., Sorooshian, A., Aldhaif, A. M., Shingler, T., Crosbie, E., Ziemba, L., Campuzano-Jost, P., Jimenez, J. L. and Wisthaler, A.: Is there an aerosol signature of chemical cloud processing?, Atmos. Chem. Phys., 18(21), 16099–16119, doi:10.5194/acp-18-16099-2018, 2018.

Finlayson-Pitts, B. J. and Pitts, J. N.: Tropospheric Air Pollution : Ozone , Airborne Toxics , Polycyclic Aromatic Hydrocarbons , and Particles, Science (80-.)., 276(May), 1997.

Ge, X., Zhang, A. Q., Sun, D. Y., C, B. C. R. R. and A, A. S.: Effect of aqueous-phase processing on aerosol chemistry and size distributions in Fresno , California , during wintertime, , 221–235, 2012a.

Ge, X., Setyan, A., Sun, Y. and Zhang, Q.: Primary and secondary organic aerosols in Fresno, California during wintertime: Results from high resolution aerosol mass spectrometry, J. Geophys. Res. Atmos., 117(18), 1–15, doi:10.1029/2012JD018026, 2012b.

Ge, X., Shaw, S. L. and Zhang, Q.: Toward understanding amines and their degradation products from postcombustion CO2 capture processes with aerosol mass spectrometry, Environ. Sci. Technol., 48(9), 5066–5075, doi:10.1021/es4056966, 2014.

Gilardoni, S., Massoli, P., Paglione, M., Giulianelli, L., Carbone, C., Rinaldi, M., Decesari, S., Sandrini, S., Costabile, F., Gobbi, G. P., Pietrogrande, M. C., Visentin, M., Scotto, F., Fuzzi, S. and Facchini, M. C.: Direct observation of aqueous secondary organic aerosol from biomass-burning emissions, Proc. Natl. Acad. Sci., doi:10.1073/pnas.1602212113, 2016.

Healy, R. M., Wang, J. M., Jeong, C., Lee, A. K. Y., Willis, M. D., Jaroudi, E., Zimmerman, N., Hilker, N., Murphy, M., Eckhardt, S., Stohl, A., Abbatt, J. P. D., Wenger, J. C. and Evans, G. J.: Journal of Geophysical Research : Atmospheres, , 6619–6633, doi:10.1002/2015JD023382.Received, 2015.

Herckes, P., Marcotte, A. R., Wang, Y. and Collett, J. L.: Fog composition in the Central Valley of

California over three decades, Atmos. Res., 151, 20–30, doi:10.1016/j.atmosres.2014.01.025, 2015.

Herndon, S. C., Onasch, T. B., Wood, E. C., Kroll, J. H., Canagaratna, M. R., Jayne, J. T., Zavala, M. A., Knighton, W. B., Mazzoleni, C., Dubey, M. K., Ulbrich, I. M., Jimenez, J. L., Seila, R., de Gouw, J. A., de Foy, B., Fast, J., Molina, L. T., Kolb, C. E. and Worsnop, D. R.: Correlation of secondary organic aerosol with odd oxygen in Mexico City, Geophys. Res. Lett., 35(15), 1–6, doi:10.1029/2008GL034058, 2008.

Hilario, M. R. A., Crosbie, E., Bañaga, P. A., Betito, G., Braun, R. A., Cambaliza, M. O., Corral, A. F., Cruz, M. T., Dibb, J. E., Lorenzo, G. R., MacDonald, A. B., Robinson, C. E., Shook, M. A., Simpas, J. B., Stahl, C., Winstead, E., Ziemba, L. D. and Sorooshian, A.: Particulate Oxalate-To-Sulfate Ratio as an Aqueous Processing Marker: Similarity Across Field Campaigns and Limitations, Geophys. Res. Lett., 48(23), 1–13, doi:10.1029/2021GL096520, 2021.

Ho, K. F., Cao, J. J., Lee, S. C., Kawamura, K., Zhang, R. J., Chow, J. C. and Watson, J. G.: Dicarboxylic acids , ketocarboxylic acids , and dicarbonyls in the urban atmosphere of China, J. Geophys. Res., 112, 1–12, doi:10.1029/2006JD008011, 2007.

IPCC: Climate Change 2021: The Physical Science Basis. Contribution of Working Group I to the Sixth Assessment Report of the Intergovernmental Panel on Climate Change, edited by V. Masson-Delmotte, P. Zhai, A. Pirani, S. L. Connors, C. Pean, S. Berger, N. Caud, Y. Chen, L. Goldfarb, M. I. Gomis, M. Huang, K. Leitzell, E. Lonnoy, J. B. . Matthews, T. K. Maycock, T. Waterfield, O. Yelekci, R. Yu, and B. Zhou, Cambridge University Press, United Kingdom and New York, NY, USA., 2021.

Jiang, W., Misovich, M. V., Hettiyadura, A. P. S., Laskin, A., McFall, A. S., Anastasio, C. and Zhang, Q.: Photosensitized Reactions of a Phenolic Carbonyl from Wood Combustion in the Aqueous Phase - Chemical Evolution and Light Absorption Properties of AqSOA, Environ. Sci. Technol., 55(8), 5199–5211, doi:10.1021/acs.est.0c07581, 2021.

Jin, X., Wang, Y., Li, Z., Zhang, F., Xu, W., Sun, Y., Fan, X., Chen, G., Wu, H., Ren, J., Wang, Q. and Cribb, M.: Significant contribution of organics to aerosol liquid water content in winter in Beijing , China, Atmos. Chem. Phys., 901–914, 2020.

Kim, H., Collier, S., Ge, X., Xu, J., Sun, Y., Jiang, W., Wang, Y., Herckes, P. and Zhang, Q.: Chemical processing of water-soluble species and formation of secondary organic aerosol in fogs, Atmos. Environ., 200(August 2018), 158–166, doi:10.1016/j.atmosenv.2018.11.062, 2019.

Koch, D. and Del Genio, A. D.: Black carbon semi-direct effects on cloud cover: Review and synthesis, Atmos. Chem. Phys., 10(16), 7685–7696, doi:10.5194/acp-10-7685-2010, 2010.

Kumar, N. K., Corbin, J. C., Bruns, E. A., Massabó, D., Slowik, J. G., Drinovec, L., Močnik, G., Prati, P., Vlachou, A., Baltensperger, U., Gysel, M., El-Haddad, I. and Prévôt, A. S. H.: Production of particulate brown carbon during atmospheric aging of residential wood-burning emissions, Atmos. Chem. Phys., 18(24), 17843–17861, doi:10.5194/acp-18-17843-2018, 2018.

Lack, D. A. and Cappa, C. D.: Impact of brown and clear carbon on light absorption enhancement , single scatter albedo and absorption wavelength dependence of black carbon, Atmos. Chem. Phys., 4207–4220, doi:10.5194/acp-10-4207-2010, 2010.

Lee, A. K. Y., Chen, C. L., Liu, J., Price, D. J., Betha, R., Russell, L. M., Zhang, X. and Cappa, C. D.: Formation of secondary organic aerosol coating on black carbon particles near vehicular emissions, Atmos. Chem. Phys., 17(24), 15055–15067, doi:10.5194/acp-17-15055-2017, 2017.

Lee, A. K. Y., Rivellini, L. H., Chen, C. L., Liu, J., Price, D. J., Betha, R., Russell, L. M., Zhang, X. and Cappa, C.

D.: Influences of Primary Emission and Secondary Coating Formation on the Particle Diversity and Mixing State of Black Carbon Particles, Environ. Sci. Technol., 53(16), 9429–9438, doi:10.1021/acs.est.9b03064, 2019.

Li, B., Sun, Z., Li, Z., Aldén, M., Jakobsen, J. G., Hansen, S. and Glarborg, P.: Post-flame gas-phase sulfation of potassium chloride, Combust. Flame, 160(5), 959–969, doi:10.1016/j.combustflame.2013.01.010, 2013.

Li, J., Pósfai, M., Hobbs, P. V. and Buseck, P. R.: Individual aerosol particles from biomass burning in southern Africa: 2. Compositions and aging of inorganic particles, J. Geophys. Res. D Atmos., 108(13), 1–12, doi:10.1029/2002jd002310, 2003.

Li, W. J., Shao, L. Y. and Buseck, P. R.: Haze types in Beijing and the influence of agricultural biomass burning, Atmos. Chem. Phys., 10(17), 8119–8130, doi:10.5194/acp-10-8119-2010, 2010.

Lim, Y. B., Tan, Y., Perri, M. J., Seitzinger, S. P. and Turpin, B. J.: Aqueous chemistry and its role in secondary organic aerosol (SOA) formation, Atmos. Chem. Phys., doi:10.5194/acp-10-10521-2010, 2010.

van Lith, S. C., Jensen, P. A., Frandsen, F. J. and Glarborg, P.: Release to the gas phase of inorganic elements during wood combustion. Part 2: Influence of fuel composition, Energy and Fuels, 22(3), 1598–1609, doi:10.1021/ef060613i, 2008.

Liu, S., Aiken, A. C., Gorkowski, K., Dubey, M. K., Cappa, C. D., Williams, L. R., Herndon, S. C., Massoli, P., Fortner, E. C., Chhabra, P. S., Brooks, W. A., Onasch, T. B., Jayne, J. T., Worsnop, D. R., Sharma, N., Mazzoleni, C., Xu, L., Ng, N. L., Liu, D., Allan, J. D., Pre, S. H. and Lee, J. D.: Enhanced light absorption by mixed source black and brown carbon particles in UK winter, Nat. Commun., doi:10.1038/ncomms9435, 2015.

Lurmann, F. W., Brown, S. G., McCarthy, M. C. and Roberts, P. T.: Processes Influencing Secondary Aerosol Formation in the San Joaquin Valley During Winter, J. Air Waste Manag. Assoc., 56(12), 1679–1693, doi:10.1080/10473289.2006.10464573, 2006.

McVay, R. and Ervens, B.: A microphysical parameterization of aqSOA and sulfate formation in clouds, Geophys. Res. Lett., 44(14), 7500–7509, doi:10.1002/2017GL074233, 2017.

Meng, Z. and Seinfeld, J. H.: On the Source of the Submicrometer Droplet Mode of Urban and Regional Aerosols On the Source of the Submicrometer Droplet Mode of Urban and Regional Aerosols, Aerosol Scien, 6826, doi:10.1080/02786829408959681, 1994.

Miyazaki, Y., Aggarwal, S. G., Singh, K. and Gupta, P. K.: Dicarboxylic acids and water-soluble organic carbon in aerosols in New Delhi , India , in winter : Characteristics and formation processes, J. Geophys. Res., 114, 1–12, doi:10.1029/2009JD011790, 2009.

Nah, T., Guo, H., Sullivan, A. P., Chen, Y., Tanner, D. J., Nenes, A., Russell, A., Lee Ng, N., Gregory Huey, L. and Weber, R. J.: Characterization of aerosol composition, aerosol acidity, and organic acid partitioning at an agriculturally intensive rural southeastern US site, Atmos. Chem. Phys., 18(15), 11471–11491, doi:10.5194/acp-18-11471-2018, 2018.

Ng, N. L., Canagaratna, M. R., Jimenez, J. L., Chhabra, P. S., Seinfeld, J. H. and Worsnop, D. R.: Changes in organic aerosol composition with aging inferred from aerosol mass spectra, Atmos. Chem. Phys., 11(13), 6465–6474, doi:10.5194/acp-11-6465-2011, 2011.

Nguyen, T. K. V, Zhang, Q., Jimenez, J. L., Pike, M. and Carlton, A. G.: Liquid Water : Ubiquitous

Contributor to Aerosol Mass, , doi:10.1021/acs.estlett.6b00167, 2016.

Onasch, T. B., Trimborn, A., Fortner, E. C., Jayne, J. T., Kok, G. L., Williams, L. R., Davidovits, P. and Worsnop, D. R.: Soot particle aerosol mass spectrometer: Development, validation, and initial application, Aerosol Sci. Technol., doi:10.1080/02786826.2012.663948, 2012.

Paatero, P.: The Multilinear Engine—A Table-Driven, Least Squares Program for Solving Multilinear Problems, Including the n-Way Parallel Factor Analysis Model, J. Comput. Graph. Stat., 8(4), 854–888, doi:10.1080/10618600.1999.10474853, 1999.

Paatero, P. and Tapper, U.: Positive matrix factorization: A non-negative factor model with optimal utilization of error estimates of data values, Environmetrics, doi:10.1002/env.3170050203, 1994.

Paciga, A. L., Riipinen, I. and Pandis, S. N.: Effect of ammonia on the volatility of organic diacids, Environ. Sci. Technol., 48(23), 13769–13775, doi:10.1021/es5037805, 2014.

Parworth, C., Young, D. E., Kim, H., Zhang, X., Cappa, C. D., Collier, S. and Zhang, Q.: Wintertime water-soluble aerosol composition and particle water content in Fresno, California, J. Geophys. Res. Atmos., 122, 3155–3170, doi:10.1002/2016JD026173, 2017.

Peng, J., Hu, M., Guo, S., Du, Z., Zheng, J., Shang, D., Levy, M. and Zeng, L.: Markedly enhanced absorption and direct radiative forcing of black carbon under polluted urban environments, , doi:10.1073/pnas.1602310113, 2016.

Petäjä, T., Järvi, L., Kerminen, V. M., Ding, A. J., Sun, J. N., Nie, W., Kujansuu, J., Virkkula, A., Yang, X., Fu, C. B., Zilitinkevich, S. and Kulmala, M.: Enhanced air pollution via aerosol-boundary layer feedback in China, Sci. Rep., 6, doi:10.1038/SREP18998, 2016.

Petters, M. D. and Kreidenweis, S. M.: A single parameter representation of hygroscopic growth and cloud condensation nucleus activity, Atmos. Chem. Phys., 13(2), 1081–1091, doi:10.5194/acp-13-1081-2013, 2007.

Prabhakar, G., Parworth, C. L., Zhang, X., Kim, H., Young, D. E., Beyersdorf, A. J., Ziemba, L. D., Nowak, J. B., Bertram, T. H., Faloona, I. C., Zhang, Q. and Cappa, C. D.: Observational assessment of the role of nocturnal residual-layer chemistry in determining daytime surface particulate nitrate concentrations, Atmos. Chem. Phys., 17(23), 14747–14770, doi:10.5194/acp-17-14747-2017, 2017.

Pratt, K. A., Heymsfield, A. J., Twohy, C. H., Murphy, S. M., DeMott, P. J., Hudson, J. G., Subramanian, R., Wang, Z., Seinfeld, J. H. and Prather, K. A.: In situ chemical characterization of aged biomass-burning aerosols impacting cold wave clouds, J. Atmos. Sci., 67(8), 2451–2468, doi:10.1175/2010JAS3330.1, 2010.

Ramanathan, V. and Carmichael, G.: Global and regional climate changes due to black carbon, Nat. Geosci., 1(4), 221–227, doi:10.1038/ngeo156, 2008.

Ravishankara, A. R.: Heterogeneous and multiphase chemistry in the troposphere, Science (80-.)., 276(5315), 1058–1065, doi:10.1126/science.276.5315.1058, 1997.

Rivellini, L. H., Adam, M. G., Kasthuriarachchi, N. and Lee, A. K. Y.: Characterization of carbonaceous aerosols in Singapore: Insight from black carbon fragments and trace metal ions detected by a soot particle aerosol mass spectrometer, Atmos. Chem. Phys., 20(10), 5977–5993, doi:10.5194/acp-20-5977-2020, 2020.

Schurman, M. I., Boris, A., Desyaterik, Y. and Collett, J. L.: Aqueous Secondary Organic Aerosol Formation in Ambient Cloud Water Photo-Oxidations, Aerosol Air Qual. Res., 15–25, doi:10.4209/aaqr.2017.01.0029, 2018.

Seinfeld, J. H. and Pandis, S. N.: Atmospheric Chemistry and Physics. From Air Pollution to Climate Change, Second Edition, Wiley Interscience., 2006.

Shen, X., Saathoff, H., Huang, W., Mohr, C., Ramisetty, R. and Leisner, T.: Understanding atmospheric aerosol particles with improved particle identification and quantification by single-particle mass spectrometry, Atmos. Meas. Tech., 12(4), 2219–2240, doi:10.5194/amt-12-2219-2019, 2019.

Sorooshian, A., Varutbangkul, V., Brechtel, F. J., Ervens, B., Feingold, G., Bahreini, R., Murphy, S. M., Holloway, J. S., Atlas, E. L., Buzorius, G., Jonsson, H., Flagan, R. C. and Seinfeld, J. H.: Oxalic acid in clear and cloudy atmospheres: Analysis of data from International Consortium for Atmospheric Research on Transport and Transformation 2004, J. Geophys. Res. Atmos., 111(23), 1–17, doi:10.1029/2005JD006880, 2006.

Sorooshian, A., Murphy, S. M., Hersey, S., Bahreini, R., Jonsson, H., Flagan, R. C. and Seinfeld, J. H.: Constraining the contribution of organic acids and AMS m/z 44 to the organic aerosol budget: On the importance of meteorology, aerosol hygroscopicity, and region, Geophys. Res. Lett., 37(21), 1–5, doi:10.1029/2010GL044951, 2010.

Sorvajärvi, T., DeMartini, N., Rossi, J. and Toivonen, J.: In situ measurement technique for simultaneous detection of K, KCl, and KOH vapors released during combustion of solid biomass fuel in a single particle reactor, Appl. Spectrosc., 68(2), 179–184, doi:10.1366/13-07206, 2014.

Sun, P., Farley, R. N., Li, L., Srivastava, D., Niedek, C. R., Li, J., Wang, N., Cappa, C. D., Pusede, S. E., Yu, Z., Croteau, P. and Zhang, Q.: PM2.5 composition and sources in the San Joaquin Valley of California : A long-term study using ToF-ACSM with the capture vaporizer, Environ. Pollut., 292(PA), 118254, doi:10.1016/j.envpol.2021.118254, 2022.

Sun, Y., Du, W., Fu, P., Wang, Q., Li, J., Ge, X., Zhang, Q., Zhu, C. and Ren, L.: Primary and secondary aerosols in Beijing in winter : sources , variations and processes, Atmos. Chem. Phys., 8309–8329, doi:10.5194/acp-16-8309-2016, 2016.

Sun, Y. L., Zhang, Q., Anastasio, C. and Sun, J.: Insights into secondary organic aerosol formed via aqueous-phase reactions of phenolic compounds based on high resolution mass spectrometry, Atmos. Chem. Phys., doi:10.5194/acp-10-4809-2010, 2010.

Sun, Y. L., Zhang, Q., Schwab, J. J., Yang, T., Ng, N. L. and Demerjian, K. L.: Factor analysis of combined organic and inorganic aerosol mass spectra from high resolution aerosol mass spectrometer measurements, Atmos. Chem. Phys., doi:10.5194/acp-12-8537-2012, 2012.

Tan, Y., Carlton, A. G., Seitzinger, S. P. and Turpin, B. J.: SOA from methylglyoxal in clouds and wet aerosols: Measurement and prediction of key products, Atmos. Environ., 44(39), 5218–5226, doi:10.1016/j.atmosenv.2010.08.045, 2010.

Tomaz, S., Cui, T., Chen, Y., Sexton, K. G., Roberts, J. M., Warneke, C., Yokelson, R. J., Surratt, J. D. and Turpin, B. J.: Photochemical Cloud Processing of Primary Wildfire Emissions as a Potential Source of Secondary Organic Aerosol, Environ. Sci. Technol., doi:10.1021/acs.est.8b03293, 2018.

Wang, G., Xie, M., Hu, S., Gao, S., Tachibana, E. and Kawamura, K.: Dicarboxylic acids, metals and isotopic compositions of C and N in atmospheric aerosols from inland China: Implications for dust and

coal burning emission and secondary aerosol formation, Atmos. Chem. Phys., 10(13), 6087–6096, doi:10.5194/acp-10-6087-2010, 2010.

Wang, J., Zhang, Q., Chen, M., Collier, S., Zhou, S., Ge, X., Xu, J., Shi, J., Xie, C., Hu, J., Ge, S., Sun, Y. and Coe, H.: First Chemical Characterization of Refractory Black Carbon Aerosols and Associated Coatings over the Tibetan Plateau (4730 m a.s.l), Environ. Sci. Technol., 51(24), 14072–14082, doi:10.1021/acs.est.7b03973, 2017.

Wang, J., Ye, J., Liu, D., Wu, Y., Zhao, J., Xu, W., Xie, C., Shen, F., Zhang, J., Ohno, P. E., Qin, Y., Zhao, X., T. Martin, S., Lee, A. K. Y., Fu, P., J. Jacob, D., Zhang, Q., Sun, Y., Chen, M. and Ge, X.: Characterization of submicron organic particles in Beijing during summertime: Comparison between SP-AMS and HR-AMS, Atmos. Chem. Phys., 20(22), 14091–14102, doi:10.5194/acp-20-14091-2020, 2020.

Wang, Y., Zhuang, G., Chen, S., An, Z. and Zheng, A.: Characteristics and sources of formic, acetic and oxalic acids in PM2.5 and PM10 aerosols in Beijing, China, Atmos. Res., 84(2), 169–181, doi:10.1016/j.atmosres.2006.07.001, 2007.

Watson, J. G., Cao, J., Wang, X. and Chow, J. C.: PM2.5 pollution in China's Guanzhong Basin and the USA's San Joaquin Valley mega-regions, Faraday Discuss., 226, 255–289, doi:10.1039/d0fd00094a, 2021.

Willis, M. D., Healy, R. M., Riemer, N., West, M., Wang, J. M., Jeong, C., Wenger, J. C., Evans, G. J., Abbatt, J. P. D. and Lee, A. K. Y.: Quantification of black carbon mixing state from traffic : implications for aerosol optical properties, , 4693–4706, doi:10.5194/acp-16-4693-2016, 2016.

Wood, E. C., Canagaratna, M. R., Herndon, S. C., Onasch, T. B., Kolb, C. E., Worsnop, D. R., Kroll, J. H., Knighton, W. B., Seila, R., Zavala, M., Molina, L. T., Decarlo, P. F., Jimenez, J. L., Weinheimer, A. J., Knapp, D. J., Jobson, B. T., Stutz, J., Kuster, W. C. and Williams, E. J.: Investigation of the correlation between odd oxygen and secondary organic aerosol in Mexico City and Houston, Atmos. Chem. Phys., 10(18), 8947–8968, doi:10.5194/acp-10-8947-2010, 2010.

Wu, C., Liu, L., Wang, G., Zhang, S., Li, G., Lv, S., Li, J., Wang, F., Meng, J. and Zeng, Y.: Important contribution of N2O5 hydrolysis to the daytime nitrate in Xi'an , China during haze periods : Isotopic analysis and WRF-Chem model simulation, Environ. Pollut., 288(July), 117712, doi:10.1016/j.envpol.2021.117712, 2021.

Wu, Y., Liu, D., Wang, J., Shen, F., Chen, Y., Cui, S., Ge, S., Wu, Y., Chen, M. and Ge, X.: Characterization of Size-Resolved Hygroscopicity of Black Carbon-Containing Particle in Urban Environment, Environ. Sci. Technol., 53(24), 14212–14221, doi:10.1021/acs.est.9b05546, 2019.

Xie, C., Xu, W., Wang, J., Liu, D., Ge, X., Zhang, Q., Wang, Q., Du, W., Zhao, J., Zhou, W., Li, J., Fu, P., Wang, Z., Worsnop, D. and Sun, Y.: Light absorption enhancement of black carbon in urban Beijing in summer, Atmos. Environ., 213(May), 499–504, doi:10.1016/j.atmosenv.2019.06.041, 2019.

Yang, F., Gu, Z., Feng, J., Liu, X. and Yao, X.: Biogenic and anthropogenic sources of oxalate in PM 2 . 5 in a mega city , Shanghai, Atmos. Res., 138, 356–363, doi:10.1016/j.atmosres.2013.12.006, 2014.

Yatavelli, R. L. N., Mohr, C., Stark, H., Day, D. A. and Thompson, S. L.: Estimating the contribution of organic acids to northern hemispheric continental organic aerosol, Geophys. Res. Lett., 44, 6084–6090, doi:10.1002/2015GL064650.Received, 2015.

Young, D. E., Kim, H., Parworth, C., Zhou, S., Zhang, X., Cappa, C. D., Seco, R., Kim, S. and Zhang, Q.: Influences of emission sources and meteorology on aerosol chemistry in a polluted urban environment: Results from DISCOVER-AQ California, Atmos. Chem. Phys., 16(8), 5427–5451, doi:10.5194/acp-16-5427-

2016, 2016.

Yu, J. Z., Huang, X. F., Xu, J. and Hu, M.: When aerosol sulfate goes up, so does oxalate: Implication for the formation mechanisms of oxalate, Environ. Sci. Technol., 39(1), 128–133, doi:10.1021/es049559f, 2005.

Yu, L., Smith, J., Laskin, A., Anastasio, C., Laskin, J. and Zhang, Q.: Chemical characterization of SOA formed from aqueous-phase reactions of phenols with the triplet excited state of carbonyl and hydroxyl radical, Atmos. Chem. Phys., 14(24), 13801–13816, doi:10.5194/acp-14-13801-2014, 2014.

Zhang, G., Hu, X., Sun, W., Yang, Y., Guo, Z. and Fu, Y.: A comprehensive study about the in-cloud processing of nitrate through coupled measurements of individual cloud residuals and cloud water, EGUsphere, (April), 1–39 [online] Available from: https://doi.org/10.5194/egusphere-2022-178, 2022.

Zhang, Q., Rami Alfarra, M., Worsnop, D. R., Allan, J. D., Coe, H., Canagaratna, M. R. and Jimenez, J. L.: Deconvolution and quantification of hydrocarbon-like and oxygenated organic aerosols based on aerosol mass spectrometry, Environ. Sci. Technol., 39(13), 4938–4952, doi:10.1021/es048568l, 2005.

Zhang, Q., Jimenez, J. L., Worsnop, D. R. and Canagaratna, M.: A case study of urban particle acidity and its influence on secondary organic aerosol, Environ. Sci. Technol., 41(9), 3213–3219, doi:10.1021/es061812j, 2007.

Zhang, R., Khalizov, A. F., Pagels, J., Zhang, D., Xue, H. and Mcmurry, P. H.: Variability in morphology , hygroscopicity , and optical properties of soot aerosols during atmospheric processing, Proc. Natl. Acad. Sci., 105(30), 10291–10296, 2008.

Zhang, Y., Favez, O., Canonaco, F., Liu, D., Prévôt, A. S. H., Gros, V. and Albinet, A.: Evidence of major secondary organic aerosol contribution to lensing effect black carbon absorption enhancement, Clim. Atmos. Sci., (November), doi:10.1038/s41612-018-0056-2, 2018.

Zheng, H., Kong, S., Chen, N. and Wu, C.: Secondary inorganic aerosol dominated the light absorption enhancement of black carbon aerosol in Wuhan, Central China, Atmos. Environ., 287(July), 119288, doi:10.1016/j.atmosenv.2022.119288, 2022.

Zhou, S., Collier, S., Jaffe, D. A., Briggs, N. L., Hee, J., Iii, A. J. S., Kleinman, L., Onasch, T. B. and Zhang, Q.: Regional influence of wildfires on aerosol chemistry in the western US and insights into atmospheric aging of biomass burning organic aerosol, Atmos. Chem. Phys., 17(3), doi:10.5194/acp-17-2477-2017, 2017.

5. Chemical Properties and Single Particle Mixing State of Soot Aerosol in Houston during the TRACER Campaign

This chapter has been submitted to Atmospheric Chemistry and Physics: Farley, R. N., Lee, J. E., Rivellini, L., Lee, A. K. Y., Porto, R. D., Cappa, C. D., Gorkowski, K., Shawon, A. S., Benedict, K. B., Allison, C., Dubey, M. K. and Zhang, Q.: Chemical Properties and Single Particle Mixing State of Soot Aerosol in Houston during the TRACER Campaign, Atmos. Chem. Phys. Discuss., 2023.

5.1 Abstract

A high-resolution soot particle aerosol mass spectrometer (SP-AMS) was used to selectively measure refractory black carbon (rBC) and its associated coating material using both the ensemble size-resolved mass spectral mode and the event trigger single particle (ETSP) mode in Houston, Texas in summer 2022. This study was conducted as part of the Department of Energy Atmospheric Radiation Measurement (ARM) program's Tracking Aerosol Convection Interactions Experiment (TRACER) field campaign. The study revealed an average (± 1s) rBC concentration of 103 ± 176 ng m^{-3}. Additionally, the coatings on the BC particles were primarily composed of organics (59%; 219 ± 260 ng m^{-3}) and sulfate (26%; 94 ± 55 ng m^{-3}). Positive matrix factorization (PMF) analysis of the ensemble mass spectra of BC-containing particles resolved four distinct types of soot aerosol, including an oxidized organic aerosol ($OOA_{BC,PMF}$) factor associated with processed primary organic aerosol, an inorganic sulfate factor ($SO_{4,BC,PMF}$), an oxidized rBC factor ($O\text{-}BC_{PMF}$), and a mixed mineral dust/biomass burning aerosol factor with significant contribution from potassium ($K\text{-}BB_{BC,PMF}$). Additionally, K-Means clustering analysis of the single particle mass spectra identified eight different clusters, including soot particles enriched in hydrocarbon like organic aerosol ($HOA_{BC,ETSP}$), sulfate ($SO_{4,BC,ETSP}$), two types of rBC, OOA ($OOA_{BC,ETSP}$), chloride ($Cl_{BC,ETSP}$) and nitrate ($NO_{3,BC,ETSP}$). The single particle measurements demonstrate substantial variation in BC coating thickness with coating-to-rBC mass ratios ranging from 0.1 to 100. The mixing state index (χ), which denotes the degree of homogeneity of the soot aerosol, varied from 4 to 94% with a median of 40%, indicating that the aerosol population lies in between internal and external mixing but has large temporal and source type variability. In addition, a significant fraction of BC-containing

particles, a majority enriched with oxidized organics and sulfate, exhibit sufficiently high κ values and diameters conducive to activation as cloud nuclei under atmospherically relevant supersaturation conditions. This finding bears significance in comprehending the activation of rBC-containing particles as cloud droplets and the origins of CCN in urban areas. Our analysis highlights the complex nature of soot aerosol and underscore the need to comprehend its variability across different environments for accurate assessment of climate change.

5.2 Introduction

Soot aerosol, predominantly emitted from the incomplete combustion of fossil fuels and biomass, strongly absorbs solar radiation and contributes to positive climate forcing (Bond et al., 2013; IPCC, 2021; Ramanathan and Carmichael, 2008). The microphysical and optical properties of soot aerosol are profoundly influenced by the mixing state of black carbon (BC) and aerosol constituents internally mixed with BC (Cappa et al., 2012). The properties of ambient soot aerosol undergo dynamic variations during their aging processes in the atmosphere, such as the condensation of low-volatility or semi-volatile vapors, coagulation with preexisting aerosol and heterogenous oxidation.

When freshly emitted, soot aerosol is often hydrophobic, but condensation of hygroscopic material, such as secondary organic aerosol (SOA) or inorganic salts, enables soot to act as cloud condensation nuclei (CCN) and alter cloud properties (Lambe et al., 2015; Motos et al., 2019; Wu et al., 2019; Zuberi et al., 2005). Additionally, the rate at which BC is scavenged by wet deposition, and therefore its atmospheric lifetime, is controlled by the hygroscopicity of its coating (Emerson et al., 2018; Yang et al., 2019). The presence of non-absorbing coating materials can also enhance aerosol light absorption through the so-called lensing effect, leading to disparities between optical models and observations (Cappa et al., 2012, 2019; Fierce et al., 2020; Lack and Cappa, 2010; Lee et al., 2022a; Xie et al., 2019). The competition between the absorption enhancement and reduced lifetime from internal mixing of BC significantly effects its climate impacts and is not well understood (Hodnebrog et al., 2014).

Understanding the chemical and microphysical properties of soot aerosol and the complexities associated with its mixing state, which involves the interaction and incorporation of BC with other aerosol components, is crucial for comprehending its impact on the climate system and refining climate change assessment. Process level modelling studies with detailed mixing state treatments show that current simple model parameterizations can bias the climate forcing of BC (Fierce et al., 2017)

To address this problem, the present study investigates the intricate properties and dynamic variations of mixed soot particles with state-of-the-art chemical and microphysical instruments to determine their influence on cloud development in Houston, TX. This study is part of the DOE Sponsored TRacking Aerosol Convection Interactions Experiment (TRACER), which aims to unravel the interactions between clouds and aerosols in urban areas. Houston is a subtropical city heavily impacted by anthropogenic emissions from gasoline and diesel vehicles, cargo ships, and petrochemical industries (Al-Naiema et al., 2018; Bean et al., 2016; Schulze et al., 2018; Yoon et al., 2020). The abundance of soot particle sources and the high levels of photochemical activity in Houston make it an ideal location for studying urban soot aerosol characteristics and atmospheric processing.

Previous ambient measurements in Houston have reported average BC concentrations ranging between 0.31 and 0.80 μg m^{-3} (Levy et al., 2013; Yoon et al., 2020). Additionally, a study utilizing ambient vapors within an environmental chamber in Houston found that after 18 hours of atmospheric processing, monodisperse BC aerosol is transformed from a highly fractal morphology into spherical particles with a significant simultaneous increase in absorption enhancement (E_{abs}) (Peng et al., 2016). Another study by Levy et al. (2013) utilized measurements of BC aerosol effective density to probe the mixing state of soot particles in Houston and found that although the soot particles were often internally mixed with other species, an externally mixed BC population was also present during rush hour.

Despite the importance of soot aerosol at this site, detailed measurements of the composition and properties of BC-containing aerosol have not been performed in Houston. A particularly significant gap in knowledge pertains to the mixing states of soot aerosols. In this study, a soot particle aerosol mass spectrometers (SP-AMS) configured with only the laser vaporizer was used to selectively measure submicrometer particles (PM_1) containing black carbon. Additionally, a co-located dual-vaporizer SP-AMS, equipped with a $PM_{2.5}$ inlet was deployed concurrently to provide measurements of the bulk $PM_{2.5}$ composition. Comprehensive measurements of aerosol optical properties were also collected to explore the effects of mixing state and coating composition on light absorption. Here, we report the results of ensemble and single particle measurements of BC-containing aerosol and use them understand how size resolved mixing leads to compositional differences between BC-containing and BC-free aerosols.

5.3 Methods

5.3.1 Sampling Location and Instrumentation

Measurements were performed at a U.S. Department of Energy (DOE) managed site at the La Porte Municipal Airport (29.670, -95.058) from Jun 28 to Aug 1, 2022, as a part of the TRACER intensive operating period. The La Porte site is located approximately 30km ESE of downtown Houston and is surrounded by residential and commercial areas (Fig. D1). The Port of Houston and Houston Ship Channel (HSP) are located about 5 km to the northeast and there are multiple refineries and other industrial and petrochemical plants located in the region. Although there was an active small aircraft runway nearby, we see no evidence of aircraft emissions impacting our measurements.

A suite of instrumentation for the comprehensive characterization of aerosol chemical and optical properties was housed in a temperature-controlled trailer owned by the Los Alamos National Laboratory (Fig. D1). Among them, two high-resolution time-of-flight soot particle aerosol mass spectrometers (SP-AMS; Aerodyne Inc., Billerica MA.) were deployed simultaneously. One SP-AMS was operated in the laser-only configuration, allowing for the measurement of BC-containing PM_1, while the

other SP-AMS incorporated both a laser and thermal vaporizer and a $PM_{2.5}$ aerodynamic lens system, aiming to characterize both BC-containing and non-refractory $PM_{2.5}$ (NR-$PM_{2.5}$) (Avery et al., 2020; Williams et al., 2013). Details of supporting instrumentation is provided in section S1.1

5.3.2 SP-AMS measurement and data processing

The laser-only SP-AMS utilized in this study was modified by removing the tungsten thermal vaporizer in order to selectively detect particles containing black carbon. The SP-AMS is described in detail in previous publications (DeCarlo et al., 2006; Onasch et al., 2012). Briefly, ambient aerosols are sampled through an aerodynamic lens system and sorted based on their vacuum aerodynamic diameter (D_{va}) within the Particle Time of Flight (PToF) chamber. A Nd-YAG intracavity (1064nm) laser is utilized to selectively vaporize particles containing absorbing material, such as rBC. The resulting gaseous molecules are ionized using 70 eV electron impact ionization and measured using high resolution time of flight mass spectrometry. The mass spectrometer was operated in the "V" mode, providing higher sensitivity at the cost of lower resolution ($m/\Delta m$ = 2500) and was programmed to switch between three different sampling modes: the ensemble mass spectrum (MS) mode, the efficient particle time of flight (ePToF) size mode, and the event trigger single particle (ETSP) mode (DeCarlo et al., 2006; Onasch et al., 2012).

MS and ePToF measurements were analyzed in the SQUIRREL (v. 1.65C) and PIKA (v. 1.25C) analysis toolkits within the IGOR Pro (v. 8.04) environment and concentrations were determined from the high-resolution peak fittings. Ambient rBC was quantified using the sum of C_1^+ to C_{10}^+. As the signal at C_1^+ can be influenced by both organics and rBC, the C_1^+ related to rBC was constrained using the ratio of C_3^+ to C_1^+ measured during the regal black calibration (0.65). The limit of detection (LOD) for each species was determined as 3σ during filtered air measurements when a HEPA filter was placed upstream of the SP-AMS. The LOD for 5 min averaging was 106, 17, 6, 11, 12, 2 ng m^{-3} for organics, rBC, sulfate,

nitrate, chloride and ammonium, respectively. Additional details of SP-AMS operation and calibration is provided in section S1.2.

5.3.3 Positive matrix factorization analysis of ensemble mass spectra

Source apportionment of the ensemble mass spectra was performed by positive matrix factorization (PMF) analysis using the PMF evaluation tool (PET) (Paatero and Tapper, 1994; Ulbrich et al., 2009). Organic and inorganic ions were included in the PMF matrix to reduce rotational ambiguity as well as to explore the distribution of inorganic species across the factors (Sun et al., 2012). This included HR organic ions between 12-120 amu, major ions related to rBC, sulfate and nitrate and UMR signal between *m/z* 121-307. PMF Solutions up to 8 factors were assessed based on mass spectral and temporal features. Four meaningful factors were identified and includes an oxidized organic aerosol factor ($OOA_{BC,PMF}$), an oxidized black carbon factor ($O\text{-}BC_{PMF}$), an inorganic sulfate factor ($SO_{4,BC,PMF}$), and a mixed biomass burning/mineral dust factor ($K\text{-}BB_{BC,PMF}$).

5.3.4 Event trigger single particle (ETSP) data processing and K-means clustering

The Event Trigger Single Particle mode was used to explore the mixing state of individual ambient particles, as done previously (Lee et al., 2019; Ma et al., 2023; Willis et al., 2019; Ye et al., 2018). The vaporization, ionization, and detection processes are identical to what is described above, however rather than averaging the measured signals across all MS extractions, individual extractions (single particle events) are identified and saved if the signal at predefined *m/z* values is above a set threshold. Table S1 shows the three regions of interest (ROIs), consisting of individual or a range of *m/z* values used to trigger particle events and the corresponding ion thresholds needed at each ROI. *m/z* 36 and 43 were selected to target rBC and OA, respectively. ROI 3 encompassed the total signal within the range of 46-150 amu, allowing for capturing particle events containing sulfate, nitrate and/or high molecular weight organics. Note that the settings were altered slightly after the first week to better target OA.

The unit mass resolution (UMR) data was processed in Tofware v2.5.13 prior to inputting into the Cluster Input Preparation Panel (CIPP), a tool developed by Lee et al. (2015), to identify real particle events. For each event, the total ion signal was defined as the sum of all ions except for *m/z* 14 (N^+), 16 (O^+), 18 (H_2O^+ and $^{18}O^+$), 20 (Ar^{2+}) 28 (N_2^+), 32 (O_2^+), and 40 (Ar^+), as they are significantly influenced by air signal. A simplified fragmentation table using the same fragmentation ratios as those from the ensemble measurements (Allan et al., 2004) was used to quantify the contribution of different aerosol species. The minimum ion threshold was set as the average number of ions plus three standard deviations in the particle-free regions (defined as 10-50 nm and 2000-4000 nm), and any events falling below this threshold were discarded. Throughout the campaign, organized into 1-week segments, the minimum ion threshold varied slightly, ranging between 21-27 ions. Additionally, events were considered valid if the signal of any individual species (rBC, sulfate, nitrate, chloride, potassium) exceeded the average plus three standard deviations of that species within the particle-free region.

In total, 14,699 single particle events were identified and imported for K-means clustering. Clustering was performed within Igor Pro v. 8.04 using the Cluster Analysis Panel (CAP) (Lee et al., 2015). Prior to clustering analysis, additional, noisy ions were removed including *m/z* 15 ($^{15}N^+$), 17 (NH_3^+, HO^+), 19 ($H_2{}^{18}O^+$), 22 ($CO_2{}^{2+}$), 182 ($^{182}W^+$), 183 ($^{183}W^+$) and 186 ($^{186}W^+$). Single particle spectra were normalized to the total ion signal. Solutions up to 15 clusters were analyzed based on change in Euclidian distance as well as the spectral features, size distributions and temporal patterns of each class (Figure D2).

The chosen solution included 12 classes, however clusters that showed similar features were merged for a more coherent representation (Fig. D3). Specifically, sulfate signal was found to be split between three different clusters: one predominantly comprising *m/z* 64 (SO_2^+), another featuring elevated *m/z* 48 (SO^+), and a third with elevated *m/z* 80 (SO_3^+) and 81 (HSO_3^+). Although these spectra may potentially hold intrinsic significance (e.g., aerosol acidity), it is more likely that this splitting behavior captures statistical variability in sulfate fragmentation. Consequently, these clusters were

combined. Two OOA-like clusters were also identified, showing comparable size distributions and temporal trends. However, due to limitations in the UMR signal, it was not possible to discern meaningful differences between these clusters and they were combined. Finally, one cluster displayed signal spikes at seemingly random masses (*m/z* 76, 112, 130, 145), making it challenging to provide a physically meaningful interpretation. Given the limited occurrence of these events (< 0.5% of particle count), these spectra were assumed to be noise and were discarded from further analysis. NH_x^+ ions were not included in the particle clustering analysis; therefore, ammonium mass associated with each cluster was estimated assuming particle neutralization.

5.3.5 Quantification of Aerosol Mixing State and Estimation of Single Particle Hygroscopicity

The aerosol mixing state was quantified using the metrics presented in Riemer and West (2013). The single particle diversity (D_i) describes the number of chemical components in a single particle, weighted by the mass fraction of each component. The components used in this analysis were Org, rBC, sulfate, nitrate, chloride, and potassium. D_i varies from 1 when a particle is composed of only a single component, to the total number of species (in this work 6) when every species composes equal mass fractions. D_i is calculated using the following formula

$$D_i = \prod_{a=1}^{A} (p_i^a)^{-p_i^a} \quad (2)$$

where p_i^a is the mass fraction of species *a* within particle *i* measured in the ETSP mode. The average single particle diversity (D_α) is the weighted average of D_i across an aerosol population and is calculated as

$$D_\alpha = \prod_{i=1}^{N} (D_i)^{p_i} \quad (3)$$

where p_i is the mass fraction of particle *i* in the population. D_γ measures the bulk population diversity and is calculated as

$$D_\gamma = \prod_{a=1}^{A} (p^a)^{-p^a} \quad (4)$$

where p^a is the mass fraction of species *a* in the aerosol population measured in the ensemble mode.

While D_i and D_α were calculated based on the single particle spectra from ETSP measurements, D_γ is a parameter derived from the ensemble measurements. As the ensemble MS and ETSP measurements were carried out sequentially at 20 min interval, hourly averages of D_α and D_γ were calculated to determine the mixing state index (χ). χ describes the degree of population homogeneity and varies from 0%, signifying a fully external mixture, to 100%, which indicates a fully internal mixture and is defined as

$$\chi = \frac{D_\alpha - 1}{D_\gamma - 1} \quad (5)$$

The hygroscopicity of individual particles was predicted using Zdanovskii-Stokes-Robinson (ZSR) mixing rule and the hygroscopicity parameter (κ) introduced in Petters and Kreidenweis (2007). Details of these calculations is given in sections S1.4 and S1.5.

5.4 Results

5.4.1 Overview of Soot Aerosol Composition and Properties in Houston during TRACER

Meteorological conditions during TRACER were hot and humid, typical of summertime conditions at this subtropical site (Fig. D4). The average (±1σ) temperature was 29 ± 3°C and average RH was 72 ± 13% with strong diurnal variation. Throughout the measurement period there were several heavy precipitation events, however these rarely lasted longer than a few hours. The wind showed a consistent diurnal profile with weak (< 2 m/s) southerly/southwesterly winds overnight and stronger (> 5 m/s) southeasterly winds in the afternoon (Fig. D5). This pattern is a result of a strong sea-breeze dynamic previously identified in the Houston area and results in the accumulation of local emissions overnight, followed by the advection of marine or processed airmasses during the day (Banta et al., 2005; Caicedo et al., 2019; Li et al., 2020).

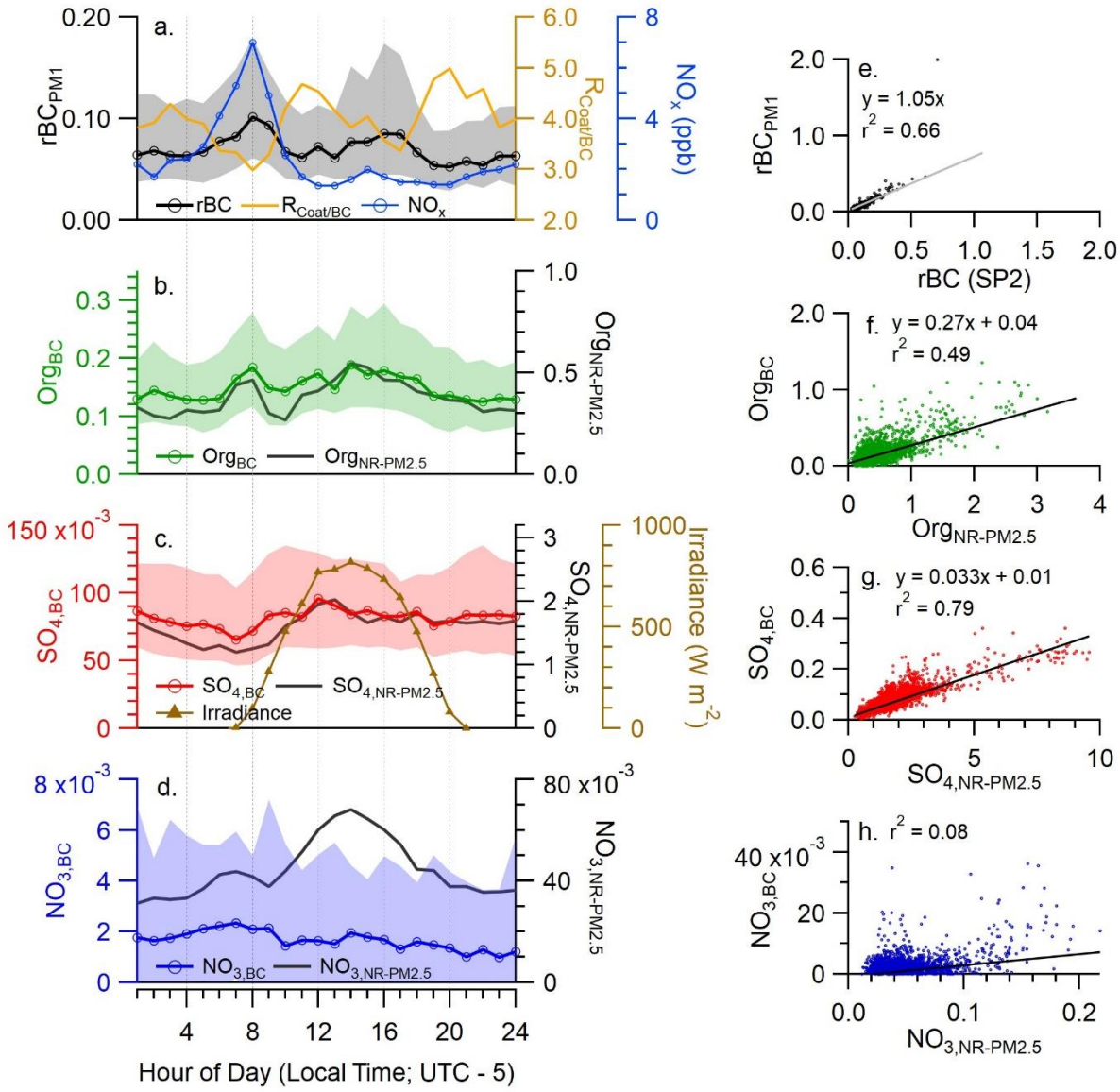

Figure 5.1: (a) diurnal profile of rBC concentration, coating to rBC mass ratio ($R_{coat/BC}$) and gas-phase NO_x. (b-e) diurnal profile of aerosol species mixed with BC (colored traces with markers) and present in the NR-$PM_{2.5}$ fraction (black traces). (e) Correlation between rBC measured by SP-AMS and co-located SP2. (f-h) scatterplot between species concentration present in BC fraction and NR-$PM_{2.5}$ fraction. Trend lines are orthogonal distance regression. All units are in μg m^{-3}, except for $R_{Coat/BC,}$ which is a dimensionless value.

The average black carbon concentration was 0.10 ± 0.18 μg m^{-3}, which is significantly lower than the average of 0.31 ± 0.22 μg m^{-3} measured in May 2009 (Levy et al., 2013) and 0.80 ± 0.69 μg m^{-3} measured in September 2013 (Yoon et al., 2020). However, both of those prior measurements were

conducted at the University of Houston, which is closer to the urban core of Houston. The rBC concentration measured by the laser-only SP-AMS agrees well with a co-located SP2 (Slope = 1.05, r^2 = 0.67, Figure 5.1e) and the dual-vaporizer SP-AMS with a $PM_{2.5}$ inlet (Slope = 1.14, r^2 = 0.62; Fig. D6). The slightly higher rBC concentration measured by the dual vaporizer SP-AMS may be due to additional rBC mass present in the 1 – 2.5 μm range. Additionally, the relationship between the SP-AMS rBC and the $PM_{2.5}$ aerosol absorption at 532nm, determined using orthogonal distance fitting constrained to an intercept of 0, yields a slope of 13.8 $m^2\ g^{-1}$ (r^2 = 0.46). This value is higher than the expected MAC of pure black carbon of 7.5 ± 1.2 $m^2\ g^{-1}$ (Bond and Bergstrom, 2006; Liu et al., 2020), and can be explained by absorption from dust particles, absorbing material present between 1 – 2.5 μm or absorption enhancement due to BC mixing state (Cappa et al., 2012; Lack and Cappa, 2010). Further analysis of the aerosol optical properties will be included in a separate publication.

The diurnal pattern of rBC concentration shows a weak bimodal cycle, with higher concentrations seen in the morning and early afternoon and lower concentrations in the evening and overnight (Fig. 5.1a). The morning peak at 08:00 local time coincides with high gas-phase NO_x and CO concentrations and is likely related to fresh vehicle emissions during rush hour (Fig. 5.1a, D5). Due to the high boundary layer height in the afternoon (2-3km), the increase of rBC between 16:00-17:00 is likely due to a combination of elevated vehicle emissions, industrial emissions, and the regional transport of BC-containing aerosol.

The soot aerosol coating thickness was estimated using the parameter $R_{Coat/BC}$, calculated by taking the mass ratio of coating material to refractory black carbon. The term "coating material" is used to refer to the total inorganic and organic species found within the soot particles and does not imply knowledge of particle morphology or the coating being present as a layer on the black carbon core. Figure 5.2a presents the frequency of $R_{coat/BC}$ occurrences for the entire campaign. Each ensemble $R_{Coat/BC}$ measurement represents the average mass ratio of all submicrometer soot particles sampled

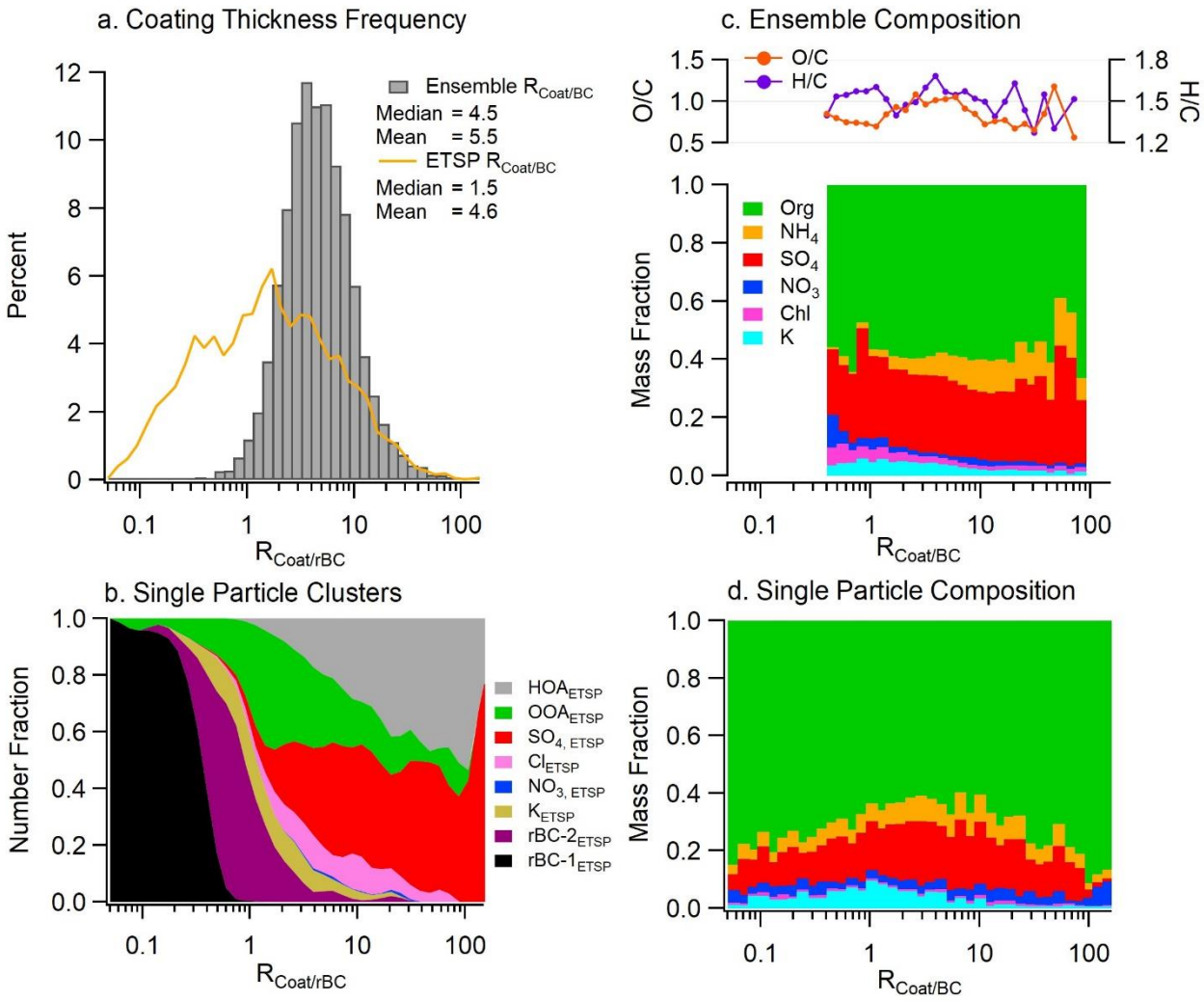

Figure 5.2: (a) normalized frequency of $R_{coat/BC}$ from the ensemble and ETSP measurements. (b) Frequency of each single particle class as a function of $R_{Coat/BC}$. (c) Average mass fraction of ensemble measurements, divided by $R_{coat/BC}$, and the O/C and H/C ratios of the organic coating. (d) Average mass fraction of single particle measurements, divided by $R_{coat/BC}$.

during the five-minute averaging period, while the $R_{coat/BC}$ calculated from the single particle measurements represents the mass ratios for individual soot particles. The frequency histograms of $R_{coat/BC}$ display log-normal distributions for both the ensemble and single particle measurements, but with substantially different median values of 4.5 and 1.5, respectively (Fig. 5.2a). The ensemble $R_{coat/BC}$ measurements agree well with previous measurements in urban areas, which typically vary between 1-10 (Collier et al., 2018; Healy et al., 2015; Wang et al., 2020a). However, there were periods of thickly

coated particles with $R_{Coat/rBC}$ values exceeding 10, indicating that a portion of the soot aerosol at this site may have undergone extensive atmospheric processing. The distribution of $R_{coat/BC}$ measured by ETSP highlights a population of nearly uncoated BC particles with $R_{coat/BC}$ less than 1, indicating substantial variation in the rBC mixing state. The diurnal profile of ensemble $R_{Coat/BC}$ appears inversely related to the rBC concentration, with the lowest values occurring in the morning and afternoon (Fig 5.1a). These time intervals are likely influenced by fresh, local emissions from vehicles or industrial sources, showing similar $R_{Coat/BC}$ values to previous measurements taken near roadways (Lee et al., 2017). The soot aerosol coating is dominated by organic material (59%) followed by sulfate (25%) and ammonium (9%) (Fig. 5.3a). Potassium contributes 3% while nitrate and chloride each 1%. Figure 5.2 also shows the chemical composition of rBC coatings at different $R_{coat/BC}$ values, determined from both ensemble spectra (Fig. 5.2c) and single particle spectra (Fig. 5.2d). Overall, as the $R_{coat/BC}$ ratio increases, the coating composition remains similar with a slight increase in the sulfate mass fraction, which is consistent with the formation of secondary aerosol upon atmospheric aging. Further details regarding the single particle composition across varying $R_{coat/BC}$ values, along with insights into particle mixing states, are provided in the subsequent sections.

The diurnal cycle of Org_{BC} is similar to that of rBC and shows a slight morning increase (Fig. 5.1b). The diurnal profiles of both rBC and Org_{BC} show minima between 19:00 and 23:00, indicating the transport of cleaner, marine airmasses to the site. The $SO_{4,BC}$ profile shows little diurnal variation, highlighting its regional sources (Fig 5.1c). The ratio of $SO_{4,BC}$ to rBC peaks between 20:00 and 23:00 possibly due to long-range transport of sulfate-rich aerosol. The observed $SO_{4,BC}$ concentration was unlikely to be significantly impacted by sea salt emissions, as the SP-AMS signals for $NaCl^+$, Cl^+ and HCl^+ were low despite these ions being detectable with the laser vaporizer if internally mixed with rBC. Instead, we hypothesize that $SO_{4,BC}$ is primarily attributed to ammonium sulfate formed from the oxidation of either marine-derived DMS or SO_2 from anthropogenic sources such as crude oil processing

or other petrochemical industries (Ahmed et al., 2021; Rivera et al., 2010). We see little evidence for other forms of sulfate, such as methanesulfonic acid (MSA), primarily due to the absence of marker ions for MSA, such as $CH_3SO_2^+$ and $CH_4SO_3^+$

Figure 5.1b-d also shows the diurnal profiles of non-refractory $PM_{2.5}$ (NR-$PM_{2.5}$) collected by the collocated dual vaporizer SP-AMS in laser-off mode (Section S1.1). The comparison of each species between the laser-only SP-AMS and the laser-off SP-AMS provides insights into the percent of mass internally mixed with rBC. This assumes that the mass of refractory organics, sulfate, nitrate and chloride material internally mixed with BC is low, and that negligible non-refractory mass is present between 1-2.5 µm. On average, approximately 27% of organic mass during this study is internally mixed with rBC, however, this fraction exhibits considerable temporal variation, as indicated by the moderate r^2 of 0.49 (Fig. 5.1f). Overall, both Org_{BC} and $Org_{NR\text{-}PM2.5}$ show similar diurnal profiles (Fig 5.1b) however a slightly higher proportion of organic mass is mixed with rBC at night and during the morning hours, with the fraction decreasing in the afternoon. This pattern is consistent with vehicles and industrial sources emitting an internal mixture of rBC and organics, while SOA production tends to enhance the growth of BC-free aerosols due to their higher surface area fraction. Supporting this hypothesis, only 3% of sulfate mass is mixed with rBC, despite a stronger correlation between $SO_{4,BC}$ and non-refractory SO_4 (r^2 = 0.79; Fig. 5.1g). As sulfate is primarily formed through secondary processes in the atmosphere, this limited presence of sulfate on soot particles indicates that the bulk of sulfate is externally mixed from rBC. Like SOA, the condensation of sulfate is likely to occur on all particles, however the higher particle surface area of non-BC-containing aerosol will increase the fraction externally mixed from rBC. Furthermore, aerosol liquid water content is likely to be higher on particles free of rBC due to increased hygroscopicity, which promotes the aqueous phase formation of sulfate on non-BC-containing particles.

Nitrate, another secondary aerosol species, presents at low concentrations within both the rBC fraction and the NR-$PM_{2.5}$ fraction. High ambient temperatures throughout the measurement period

likely promote the partitioning of inorganic nitrate into the gas-phase. The negligible correlation between $NO_{3,BC}$ and $NO_{3,NR\text{-}PM2.5}$, coupled with their different diurnal patterns (Fig. 5.1h), highlights the overall externally mixed nature of nitrate and soot aerosol, and suggests different sources of nitrate between

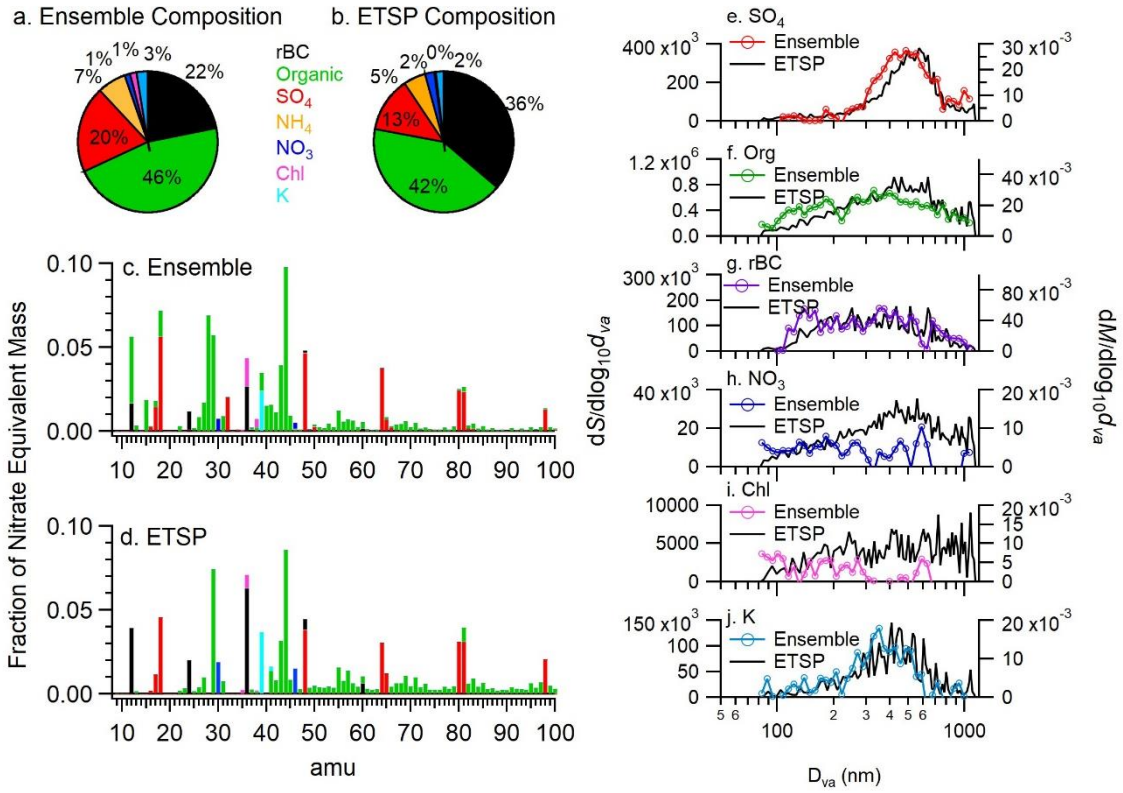

Figure 5.3: Average fractional composition of total $PM_{1,BC}$ measured by (a) high-resolution ensemble measurements and (b) ETSP measurements. (c) Average mass spectrum of ensemble measurements and (d) average mass spectrum of all single particle events measured by ETSP mode. (e-j) Comparison of species dependent size distributions for ensemble measurements (colored line) and ETSP measurements (black line). Bulk size distributions are mass weighted (against right y axes), while ETSP measurements are signal weighted (against left y axes).

the two fractions. Additionally, differences in the aerosol water content or acidity between BC-containing and BC-free particles could also play a role in the weak correlation.

5.4.2 Single-particle characteristics of soot aerosol

Using the SP-AMS ETSP mode, we were able to further probe the single-particle composition and mixing state of BC-containing aerosol. Although the 14699 single particle spectra recorded only represent a small subset of ambient BC-containing aerosol, a comparison of the average composition, mass spectral features and species-dependent size distributions measured during ETSP mode and ensemble mode indicates that the sampled single particles are generally representative of the soot population (Fig. *5*.3). The mass fraction of rBC in $PM_{1,BC}$ was significantly higher in the single-particle measurements compared to the ensemble measurements, accounting for 36% of $PM_{1,BC}$ in comparison to 22% for the ensemble measurements. Concurrently, the $SO_{4.BC}$ mass fraction decreased from 20% measured during ensemble mode to 13% during ETSP mode. These differences could potentially arise from biases created by the specific *m/z* triggers selected for this study as has been observed previously (Lee et al., 2019). For example, one of the three triggers used was *m/z* 36 (C_3^+), which may introduce a bias towards events with high *m/z* 36 signal. Differences also appear when comparing the average mass spectra of all ensemble measurements (Fig. 5.3c) and all single particle events (Fig. 5.3d) which likely arise due to variations between the HR and UMR fragmentation tables (Allan et al., 2004), in addition to the biases discussed above.

Despite these differences, the species dependent size distributions for $SO_{4,BC}$, $Org_{BC,}$ rBC and K_{BC} are similar between the bulk ensemble and ETSP measurements suggesting that there is minimal systemic bias as a function of particle size (Fig. 5.3). However, the ETSP size distribution for $SO_{4,BC}$ and Org_{BC} are slightly shifted towards larger particle sizes. Additionally, the ensemble rBC size distribution shows an additional mode at small sizes. These differences may be attributed to larger particles generating more ions and thereby having a higher statistical likelihood of triggering an ETSP event.

Although rBC or other absorbing material is required for vaporization and subsequent detection with the laser-only SP-AMS configuration, 49% of the ETSP spectra measured had no detectable rBC.

The fraction of particles with no rBC was highest for the particle types with thickest coatings including $HOA_{BC,ETSP}$ (62%), $SO_{4,BC,ETSP}$ (45%) and $OOA_{BC,ETSP}$ (35%) particle clusters (Table D3). These seemingly rBC-free particles may represent events in which the particles did not overlap well with the laser vaporizer, resulting in temperatures that were sufficient to vaporize non-refractory coating material but not the rBC core (Onasch et al., 2012; Willis et al., 2014). Another possibility is that these particles were extremely thickly coated with only a small BC core, and the energy supplied by the laser vaporizer was only sufficient to vaporize the coating material, leaving the rBC intact. Finally, semi-volatile, BC-free particles may be thermally vaporized on heated internal surfaces, such as the ion filament, despite the absence of the tungsten vaporizer. This could be especially relevant for the $NO_{3,BC,ETSP}$ cluster due to the high volatility of ammonium nitrate. However, it is important to note that this cluster comprises only 247 particles, representing only 1.6% of the total single particles detected (Fig. 5.5g). Particles without rBC signal were included for the clustering analysis, but necessarily excluded from the calculation of $R_{coat/BC}$.

5.4.3 Sources and Atmospheric Processing of Soot Aerosol

PMF analysis of the ensemble high-resolution mass spectra of soot particles resolved four distinct soot particle types characterized by distinct spectral features and tracer ions. These types include an oxidized organic aerosol ($OOA_{BC,PMF}$) factor, an oxidized rBC-rich factor ($O\text{-}BC_{PMF}$), a sulfate-rich factor ($SO_{4,BC,PMF}$), and a mixed biomass burning/mineral dust factor ($BB\text{-}K_{BC,PMF}$).

The $OOA_{BC,PMF}$ factor has an average concentration of 0.10 ± 0.19 μg m^{-3}, constituting 29% of the $PM_{1,BC}$ mass (Fig. 5.4). This soot type is primarily composed of organic species, which contribute 79% of the mass, with the rest of the mass comprised of rBC (14%), nitrate (4%) and sulfate (3%). The organic fraction is moderately oxidized with an O/C of 0.68 and shows enhanced levels of $C_2H_3O^+$ and CO_2^+, two markers for SOA (Ng et al., 2011). However, there is also an enhancement of $C_xH_y^+$ fragments, including $C_3H_3^+$ (*m/z* 39.02), $C_3H_5^+$ (m/z 41.04) $C_4H_7^+$ (*m/z* 55.05), $C_4H_9^+$ (*m/z* 57.07), which are frequently used as

markers for hydrocarbon like OA (HOA) (Al-Naiema et al., 2018; Ge et al., 2012b; Young et al., 2016). Based on this, we conclude that this factor likely represents processed soot aerosol with coatings containing a mixture of SOA and oxidized primary OA. Additionally, 80% of the nitrate signal is attributed to this factor. The concentration of this factor peaks in the afternoon, consistent with secondary photochemical production (Fig. D7). However, there is also a minor increase corresponding with morning rush hour, emphasizing the contribution of primary aerosol (Fig. D7a). The time series shows the highest concentrations on Jun 28th – Jun 29th during which back trajectories are related to long range transport from the continental U.S (Fig. D8).

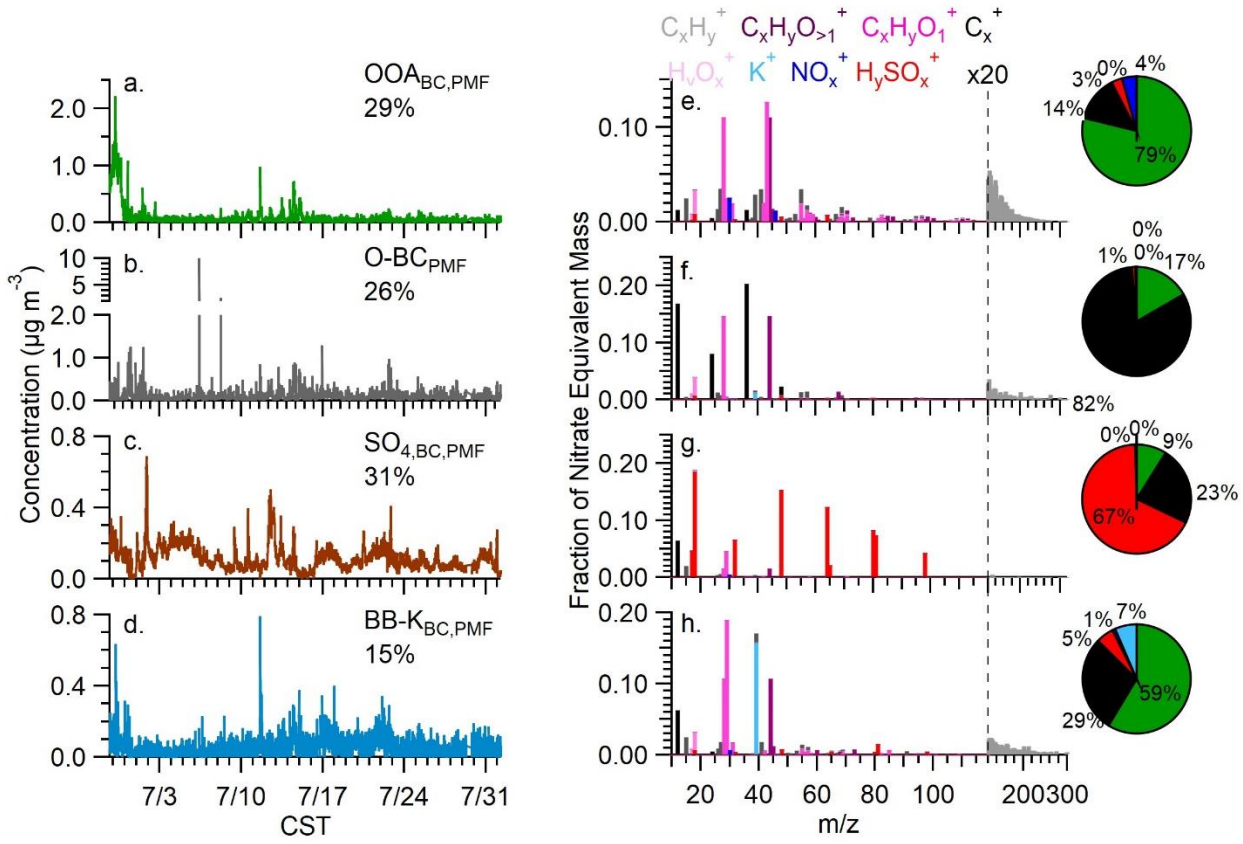

Figure 5.4: (a-d) Concentration time series of the PMF factors. Values reported are percent of total $PM_{1,BC}$. (e-h) Normalized, nitrate-equivalent mass spectra of PMF factors. Pie charts show the mass fraction of each species after applying species depedent RIE.

The O-BC_{PMF} spectrum is dominated by the $C_{1\text{-}3}^+$ peaks, with the rBC and organic fragments contributing 82% and 17% of the mass respectively. The most abundant organic fragment is CO_2^+ and the spectrum also shows an enhancement of the $C_3O_2^+$ ion (*m/z* 67.99). These ions serve as a marker for oxidized functional groups on the soot surface (Falk et al., 2021; Ma et al., 2023). Elevated $C_3O_2^+$ and CO_2^+ signals have also been identified in POA emitted from diesel and gasoline vehicles and in soot particles emitted from wood or fossil fuel combustion (Carbone et al., 2019; Collier et al., 2015; Corbin et al., 2014, 2015). There is also slightly enhanced signal from reduced hydrocarbons such as $C_4H_7^+$ (*m/z* 55.05) and $C_4H_9^+$ (*m/z* 57.07), indicating that traffic emissions may be a source of this particle type. Indeed, the diurnal profile shows a clear increase at 7:00 and a minor increase at 16:00 local time, consistent with typical rush hours (Fig. D7b). Based on these temporal features, we conclude that this factor likely represents emissions from both gasoline light duty vehicles and industrial or diesel vehicle sources. The average concentration of O-BC_{PMF} was 0.102 ± 0.193 μg m^{-3}, however, sporadic spikes were also seen, with concentrations occasionally reaching 10 μg m^{-3}. The most intense of these instances occurred on Jul 7th, coinciding with a plume observed near the site, however the fuel type for this event is unknown (Fig. 5.4b).

The $SO_{4,BC,PMF}$ factor is dominated by $H_ySO_x^+$ ions which contribute 67% of the factor mass, along with relatively minor contribution from rBC (23%) and organics (9%) . The time series shows a consistent background presence of this factor throughout the measurement period, with an average loading of 0.117 ± 0.071 μg m^{-3} (31% of $PM_{1,BC;}$ Fig. 5.4c). The low organic content suggests that this factor is mainly comprised of inorganic sulfate that has condensed onto ambient rBC particles. Overall, $SO_{4,BC,PMF}$ accounts for over 90% of the measured sulfate mass within soot aerosol. Rather than being associated with a specific source region, this factor appears to be a component of the regional background and is likely influenced by offshore sources (Fig. D8d).

An important source of non-sea salt sulfate in coastal regions is the oxidation of dimethyl sulfide (DMS), a byproduct from phytoplankton activity (Andreae, 1990; Andreae et al., 1985; Bates et al., 1992). Additionally, Bates et al. (2008) estimated that marine vessel emissions were the dominant source of sulfate over the Gulf of Mexico in 2006. However, recent regulations implemented in 2020 limit the sulfur content in marine heavy fuel oil to 0.1% by mass within the North American Emissions Control Area (ECA) and 0.5% in international waters (IMO, 2020). These policies have led to a noteworthy 80% reduction in SO_x emissions and 72% reduction in PM_1 emissions associated with shipping (Anastasopolos et al., 2021; Watson-Parris et al., 2022; Yu et al., 2020). Consequently, marine vessel emissions may contribute a smaller amount of sulfate and PM in this study compared to previous campaigns. Further discussion regarding the identification of shipping emissions is provided in section 3.3.

The fourth factor, denoted as BB-$K_{BC,PMF}$, is notable for a significant contribution from K^+ and accounts for 95% of the total K^+ mass observed within soot aerosol. The average loading of BB-$K_{BC,PMF}$ was 0.058 ± 0.059 μg m^{-3} with potassium contributing 7% of the total mass. The remaining mass consists of organic (59%), rBC (29%) and sulfate (5%). We propose that this factor represents a composite of biomass burning (BB) soot aerosol intermixed with mineral dust. Several key indicators support this hypothesis. K^+ is often used as a molecular marker for biomass combustion processes (Andreae, 1983) and the BB-$K_{BC,PMF}$ spectrum shows a slight increase in $C_2H_4O_2^+$ (*m/z* 60) and $C_3H_5O_2^+$ (*m/z* 73), which are markers for anhydrous sugars such as levoglucosan that are commonly emitted during BB processes (Cubison et al., 2011). However, the K^+ time series also shows multi-day events between Jul 16th and Jul 23rd which coincide with enhancements of coarse-mode aerosol volume ($V_{P,1\text{-}10\mu m}$) and aerosol light absorption. These events are likely related to Saharan mineral dust transported from West Africa (Fig D9a, Gorkowski et al., in Prep). The presence of Saharan dust in the Houston area has been well documented (Bates et al., 2008; Bozlaker et al., 2013, 2019; Das et al., 2022), and the HYSPLIT concentration-weighted back trajectories for this period indicate an obvious source region close to West

Africa (Fig D8e). Fe^+, another major component Saharan dust, shows sporadic enhancements throughout the campaign and these occurrences often, but not always, coincide with elevated concentrations of K^+ (Fig D9). Likewise, Na^+ was also intermittently detected, however this element appears to be related to biomass burning aerosol as highlighted by the simultaneous increases of Na^+ and $C_2H_4O_2^+$ (Figure D9). While Na^+ has previously been identified in BB aerosol (Jahn et al., 2021), not all periods with elevated $C_2H_4O_2^+$ coincide with Na^+ increases. This suggests that only certain fuel types or combustion conditions emit Na^+. Previous SP-AMS have linked Na^+ with vehicle emissions (Rivellini et al., 2020), however we observe low correlations ($r^2 < 0.1$) between Na^+ and HOA marker ions such as $C_4H_7^+$ and $C_4H_9^+$.

5.4.4 Origins of soot particle according to single particle measurements

Eight distinct BC particle types were identified by applying K-means clustering to the ETSP measurements (Fig. 5.5). These include a hydrocarbon-like OA ($HOA_{BC,ETSP}$), two rBC-rich classes displaying different amounts of BC content ($rBC\text{-}1_{ETSP}$ and $rBC\text{-}2_{ETSP}$), an oxidized OA classes ($OOA_{BC,ETSP}$), a sulfate-rich class ($SO_{4,\ BC,ETSP}$), a chloride-rich class ($Cl_{BC,ETSP}$), a nitrate-rich class ($NO_{3,\ BC,ETSP}$) and a potassium-rich class ($K_{BC,ETSP}$).

$HOA_{BC,ETSP}$ is the most abundant particle type by number, with 3851 particle counts (26%). The average spectrum displays characteristic hydrocarbon peaks at *m/z* 41, 43, 55, 57, 69 and 71 consistent with previous measurements of vehicle exhaust (Fig 5.5a) (Canagaratna et al., 2004; Collier et al., 2015). The elevated *m/z* 44 signal indicates the aerosol has undergone some degree of processing (Willis et al., 2016; Zhang et al., 2005b). The diurnal profile shows two increases at 6:00-8:00 and 15:00-16:00 local time, corresponding with morning and afternoon rush hours, respectively (Figure D7e). C_x^+ peaks only account for 5% of the average total mass within this aerosol type, indicating substantial coating mass. Additionally, The $HOA_{BC,ETSP}$ class shows a broad mass-based size distribution between 200—1000 nm in D_{va}. This is in contrast to other AMS measurements, which often identify HOA with size distributions in

sizes less than 150 nm (Collier et al., 2015; Lee et al., 2019; Ulbrich et al., 2012; Zhang et al., 2005b). The larger particle size and small mass fraction of rBC observed here suggests that the particles grouped in the $HOA_{BC,ETSP}$ class are a result of the rapid condensation of lubricating oil and other low volatility vapors onto BC cores, or the coagulation of BC-free HOA-like particles with BC-containing particles within the vehicle exhaust system. While previous studies have detected lubricating oil signatures in vehicle POA (Collier et al., 2015; Sonntag et al., 2012; Worton et al., 2014), these results provide direct evidence that the smaller particles identified in these previous studies may be externally mixed from rBC. It is also possible that these particles may originate from other fossil fuel combustion sources, such as emissions from heavy fuel oil used in ship traffic. Direct measurements of ultra-low sulfur diesel fuel emissions, similar to what ships use near shore and in U.S. ports, show spectra similar to vehicle emissions (Price et al., 2017). Two particle classes, rBC-1_{ETSP} and rBC-2_{ETSP}, were identified, each accounting for 9% and 10% of the particle number, respectively. Both classes are dominated by C_x^+ fragments but the amount of coating material differs. The soot particles in the rBC-1_{ETSP} class are nearly uncoated, with nearly all particles having $R_{Coat/BC}$ less than 1. In contrast to this, those in the rBC-2_{ETSP} class have higher contributions from organics, sulfate and potassium with rBC accounting for 49% of mass on average. Both rBC-1_{ETSP} and rBC-2_{ETSP} show increased concentrations in the afternoon, concurrent with the increases in HOA_{ETSP}, OOA_{PMF} and O-BC_{PMF}. However, unlike these other particle types, little enhancement of rBC-1_{ETSP} and rBC-2_{ETSP} is seen during morning rush hour. This suggests the presence of local, non-vehicle rBC sources or meteorological conditions conducive to the transport of fresh emissions to the sampling site during the afternoon and are likely related to industrial emissions or gas flaring. Direct measurements of PM emissions from gas-flaring activity observed extremely thinly coated soot particles with BC mass fraction between 80-96% (Fortner et al., 2012). The presence of sulfate (7%) and potassium (3%) in rBC-2_{ETSP} may indicate co-emission from refineries or biomass burning, respectively. The organic signal at *m/z* 60 appears to be elevated, further supporting the

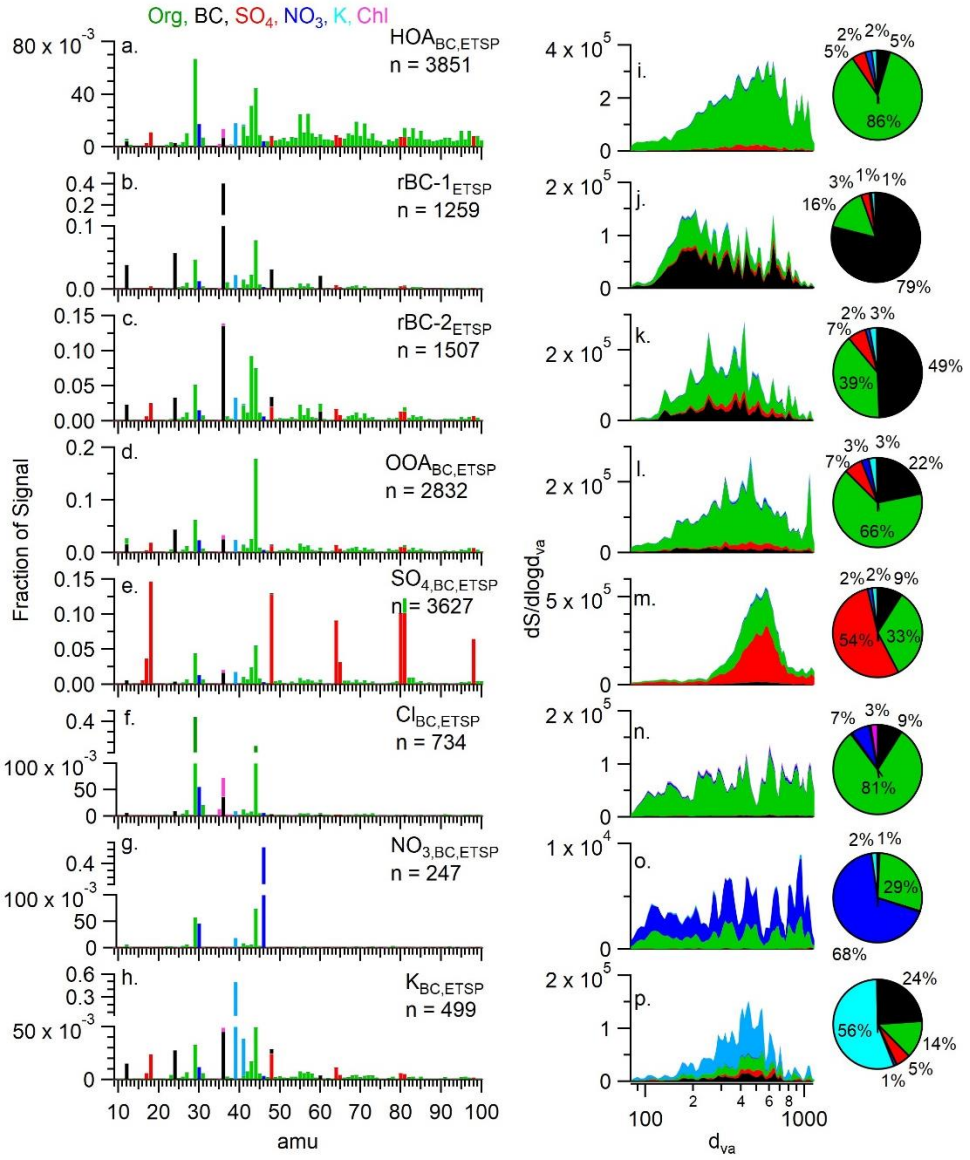

Figure 5.5: (a-h) Average mass spectra of each ETSP cluster calculated using K-means clustering. Number of particles in each class is also displayed. (i-p) Signal weighted size distribution of each cluster. Pie charts display the mass fraction of each aerosol species.

influence of BB. However, the attribution of *m/z* 60 between C_4^+ and organic fragments in the ETSP analysis is uncertain. Additionally, the size distribution shifted from a peak at 200nm for rBC-1_{ETSP} to

400nm for rBC-2_{ETSP}, consistent with the condensation of secondary material.

The average spectrum of the $OOA_{BC,ETSP}$ particle cluster was dominated by *m/z* 44, suggesting significant oxidation of the organic material. Indeed, the fraction of mass at *m/z* 44 (f_{44}) for $OOA_{BC,ETSP}$ is higher than that of $OOA_{BC,PMF}$, indicating that particles within this cluster are more oxidized than the PMF factor. The diurnal profile of this class is relatively flat with only a modest increase in the afternoon, suggesting that $OOA_{BC,ETSP}$ represents regionally transported background aerosols that have undergone photochemical processing. Similar to the $SO_{4,BC,PMF}$ factor, soot particles in the $SO_{4,BC,ETSP}$ class show a large contribution from H_ySO_x fragments, with sulfate accounting for 54% of the total mass on average. The majority of the rest of the material is composed of organic species (33%) and rBC (9%). These particles likely represent the incorporation of inorganic sulfate and other secondary organic material with rBC particles through processes such as condensation or coagulation. Given that most of the sulfate signal was attributed to this particle class, this indicates that particulate sulfate, which is primarily formed through the secondary oxidation of $SO_{2(g)}$, is generally externally mixed from organic aerosol. This class shows the largest size mode, peaking at 600 nm. As sulfate is efficiently produced in the aqueous phase, this contribution of mass in the droplet mode is consistent with aqueous phase production. $SO_{4,\ BC,ETSP}$ consisted of thickly coated particles, with a median coating thickness of 9.5 (Fig. 5.2b).

The average spectrum of soot particles within the $Cl_{BC,ETSP}$ cluster is primarily composed of *m/z* 29 and 44. However it is notable as the only particle class with measurable chloride, which accounts for 2.5% of the mass. The average cluster mass spectrum shows minor enhancements of *m/z* 60 and 73, suggesting a potential association with oxidized BB aerosol. Particles of this type were relatively infrequent, only accounting for 5% of the measured particles.

The $K_{BC,ETSP}$ shows the highest contribution of K^+, accounting for 56% of the average particle mass in this cluster. The average spectrum shows minor contribution from *m/z* 36 (C_3^+) and *m/z* 44 (CO_2^+). This is in

contrast to $K_{BC,PMF}$ which shows a significantly higher contribution from oxidized organic fragments. Recent single particle measurements of ambient biomass burning emissions revealed that some types of BBOA particles are relatively enriched with K^+ compared with other BBOA particle types (Lee et al., 2016). Furthermore, a near-roadside study in Fontana identified a similar K^+ dominated particle cluster that the authors attributed to vehicle emissions (Lee et al., 2019). However, the Fontana K-class displayed a smaller average diameter and more signal at *m/z* 43 and 55 than the $K_{BC,ETSP}$ cluster identified in this work. The low contribution of markers for primary HOA (i.e. *m/z* 55, 57) and BBOA (i.e. *m/z* 60, 73), in conjunction with the presence of secondary material such as sulfate, suggests that particles of this type have undergone atmospheric processing. From this, we conclude that the $K_{BC,ETSP}$ class represents a subset of relatively aged potassium-containing particles from sources such as vehicles, biomass burning and/or mineral dust. This class only consisted of 499 particles (3.4% of total) with a size distribution peaking at 400-600nm.

Finally, the nitrate class was the least abundant with only 247 particles (1.5%). The average spectrum is dominated by *m/z* 46 (NO_2^+) with only a small enhancement of *m/z* 30 (NO^+) and *m/z* 44. Overall, nitrate accounted for an average of 68% of particle mass in this cluster. The extremely low contribution from rBC is consistent with the overall external mixing state of nitrate and rBC as discussed previously.

5.4.5 Sources of Refractory Metal in Soot Aerosol

An advantage of the laser vaporization utilized in the SP-AMS is the ability to detect refractory metal compounds internally mixed with rBC (Bibi et al., 2021; Cao et al., 2022; Carbone et al., 2015; Rivellini et al., 2020). Heavy fuel oil combustion from shipping activity is typically associated with the emission of heavy metals, such as vanadium (V) and nickel (Ni) (Popovicheva et al., 2012; Rivellini et al., 2020). Indeed, a previous study concluded that shipping activities are the primary source of V-rich aerosol in the Houston region (Bozlaker et al., 2019). Two events with elevated V^+ concentration are detailed in Figure D10. These events coincided with increases in particulate sulfate and rBC, supporting

the role of shipping related emissions, however there is negligible correlation ($r^2 < 0.05$) between V^+ and sulfate for the entire campaign, indicating that primary ship emissions are not the major source of sulfate for most of this campaign.

Finally, there is a noticeable increase in K^+ and Fe^+ levels on the night of Jul 4, which we attribute to firework activity. A previous SP-AMS study found enhancement of various metal species, including these ions, when fireworks were used (Bibi et al., 2021). However, the primary firework tracer identified in Bibi et al., (2021) was Sr^+, which was absent in our data. The lack of Sr^+ may be due to significantly lower concentrations during this campaign, or the utilization of different types of fireworks.

5.4.6 Black Carbon Mixing State

Figure 5.6a presents the distribution of single particle diversity (D_i) for each of the particle classes. D_i is a measurement of the effective number of species present in individual species and ranges from 1 to 6 in this work. Particles in the $HOA_{BC,ETSP}$ (average $D_i = 1.5$) and $OOA_{BC,ETSP}$ (average $D_i = 1.9$) classes show low

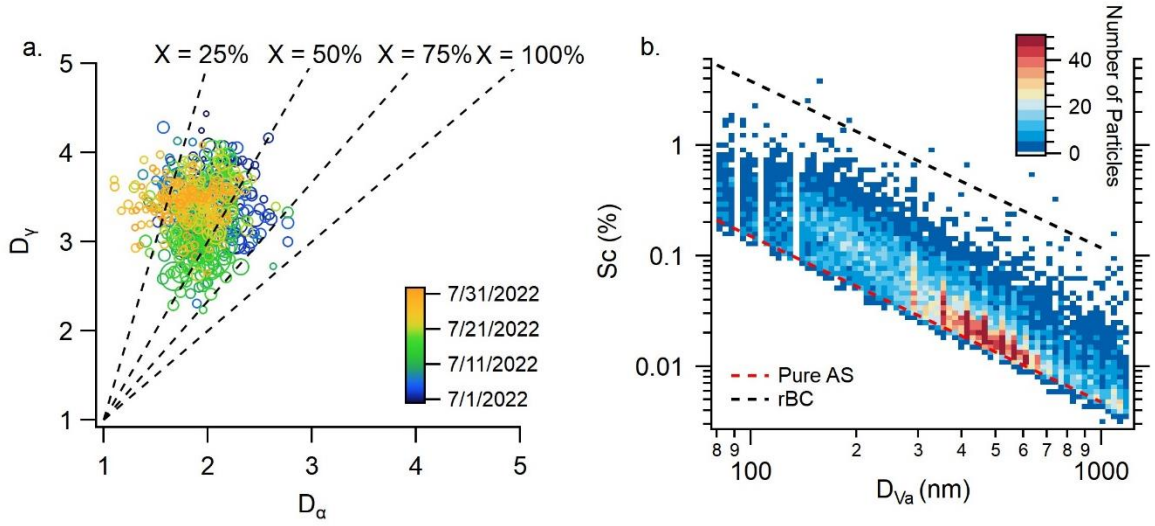

Figure 7: (a) Mixing state diagram depicting the relationship between bulk particle diversity (D_γ), average single particle diversity (D_α). The dashed lines indicate the resulting mixing state index (χ). Points are sized by $PM_{1,rBC}$ concentration and colored by sampling date. (b) Bivariate histogram of estimated particle critical supersaturation and particle diameter. Dashed lines represent uncoated rBC ($\kappa = 0.001$) and pure ammonium sulfate ($\kappa = 0.61$).

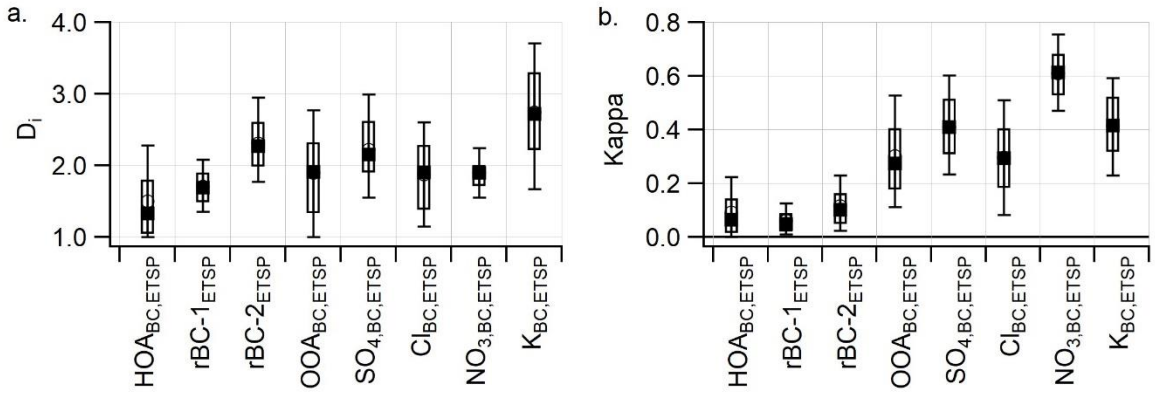

Figure 6: (a) Single particle diversity (D_i) for each cluster type. (b) Predicted hygroscopicity for individual particles, divided by particle class. The solid and open markers indicate the median and mean respectively, the box indicates the 25th-75th percentile, and whiskers indicate 10th-90th percentiles.

D_i values as the composition is dominated by organic aerosol. Likewise, particles in the $rBC\text{-}1_{ETSP}$ class also shows low D_i as they have a high mass fraction of rBC. In contrast, $rBC\text{-}2_{ETSP}$ (average D_i = 2.3), $SO_{4,ETSP}$ (2.2) and K_{ETSP} (2.7) display the highest diversity. All three of these classes likely consist of particles that have undergone atmospheric processing with significant contribution from secondary material such as organics and sulfate as well as primary species such as rBC and K. This highlights the role of photochemical processing in modulating the aerosol mixing state.

The mixing state index (χ) indicates the degree of aerosol heterogeneity and ranges between 0% (fully externally mixed) and 100% (fully internally mixed). In this study, the hourly averages of χ range from 5% to 95%, with an average of 41 ± 13% (Fig. 5.7a). The bulk aerosol diversity (D_γ) calculated from the ensemble measurements exhibits a daytime decrease, indicating reduced aerosol population diversity during the day (Fig. D7n). This decrease corresponds to elevated mass fractions of organics and sulfate. In contrast to this, the single particle diversity (D_α) shows little diurnal variation, with only a slight decrease in the afternoon. As a result, there is an overall daytime increase in the mixing state index (χ). Our results indicate that the production of SOA and sulfate coatings on rBC through photochemical

processes results in a more internally mixed, homogenous aerosol population. Finally, at night, sulfate concentration remains elevated, while organic and rBC decrease, resulting in an increase in D_γ but a decrease in the mixing state index. In contrast to these results, Lee et al. (2019) reported elevated values for both D_α and D_γ during rush hour in Fontana, CA, where the rapid secondary formation of particulate nitrate played a key role in rBC mixing state. The observed differences can be explained by the complex combination of rBC sources in Houston and differences in aerosol acidity.

5.4.7 Effect of Mixing State on Particle Hygroscopicity

The ability for a particle to act as a CCN is governed by its bulk hygroscopicity. Previous studies have used measurements of single particle composition to quantitatively predict their hygroscopicity. These estimates have been found to agree well with direct measurements of water uptake using instruments such as a hygroscopic tandem differential mobility analyzer (HTDMA) (Gysel et al., 2007; Healy et al., 2014; Petters and Kreidenweis, 2007; Wang et al., 2020b). Figure 5.6b shows the predicted hygroscopicity parameter κ for the BC-containing particles measured in this study grouped by particle classes. Details about the calculation of κ, estimation of single particle O/C and H/C values, and the necessary assumptions are provided in S1.4.

Among the eight particle classes, the $HOA_{BC,ETSP}$ and $rBC\text{-}1_{ETSP}$ classes show the lowest hygroscopicity, with average κ of 0.09 and 0.06, respectively. Although most particles in the $HOA_{BC,ETSP}$ class have a low rBC volume fraction, the organic species present are chemically reduced and display extremely low κ_{org} values, resulting in a decrease in overall particle hygroscopicity (Fig D11). This is consistent with direct measurements of motor oil and diesel emissions, which show little hygroscopic growth (Fofie et al., 2018; Lambe et al., 2011). Despite the presence of relatively hygroscopic coating material on $rBC\text{-}1_{ETSP}$ and $rBC\text{-}2_{ETSP}$, the high rBC volume fraction result in extremely low overall κ for both classes. However, the $rBC\text{-}2_{ETSP}$ class shows slightly higher κ values than $rBC\text{-}1_{ETSP}$ due to a higher fraction of oxidized organic material and inorganic sulfate.

The median predicted κ for $OOA_{BC,ETSP}$ of 0.27 agrees well with SOA produced in laboratory and chamber experiments, as well as OOA measured in other field studies (Chang et al., 2010; Fofie et al., 2018). Additionally, due to the high mass fraction of sulfate in $SO_{4,BC,ETSP}$ particles, the κ value approaches that of pure ammonium sulfate (0.61) for a subpopulation of this particle type. Similarly, the κ value for $NO_{3,BC,ETSP}$ and $K_{BC,ETSP}$ approach that of ammonium nitrate (0.67) and potassium sulfate (0.69), respectively. As these inorganic salts are hygroscopic, the overall hygroscopicity of these particles are highest.

5.5 Conclusions

This study involved the measurements of both the bulk and single particle composition of soot particles using a SP-AMS operated in the laser-only configuration. Material internally mixed with BC had a significant contribution from secondary aerosol species, including oxidized organic aerosol and inorganic sulfate. This finding highlights the importance of atmospheric aging processes affecting soot aerosol characteristics in urban environments. The utilization of two different source apportionment techniques in this study, namely PMF of the ensemble measurements and K-Means clustering of the single particle measurements, yields complimentary results. Although PMF analysis of the ensemble spectra failed to isolate a factor related to HOA, either due to low signal intensity or a similar temporal profile as other OA sources, the simultaneous application of the ETSP mode successfully identified particles exhibiting HOA-like spectra. Additionally, both source apportionment techniques revealed the presence of nearly pure rBC particles with extremely small amounts of coating material. For instance, the average $R_{coat/BC}$ for the oxidized rBC factor ($O\text{-}BC_{PMF}$) was only 0.24 while the median value for the $rBC\text{-}1_{ETSP}$ single particle cluster was 0.20.

A significant limitation in the ETSP data interpretation is the reliance on UMR mass spectra due to the extremely low ion counts for individual particle events. This introduces uncertainty when distinguishing different aerosol species that share isobaric ions, such as C_4^+ and SO^+ or C_5^+ and $C_2H_4O_2^+$.

Additionally, the lack of high-resolution spectra hinders the differentiation of isobaric ions representing distinct organic ion families, such as $C_4H_7^+$ and $C_3H_3O^+$ at *m/z* 55, which would otherwise contribute to more robust differentiation between POA and SOA factors, such as HOA and OOA.

The utilization of single particle measurements also allowed for a detailed analysis of the BC mixing state. The average mixing state index (χ) was determined to be 41 ± 13%, indicating that the aerosol population demonstrated an intermediate between internal and external mixing. Notably, these values align with the χ values measured at two other cities, including a near roadside location in Fontana, CA (48%) and a downtown location in Pittsburgh, PA (43%) (Lee et al., 2019; Ye et al., 2018). κ-Köhler theory was utilized to estimate critical supersaturation values at which these particles would activate into cloud droplets (Fig. 5.7b). Many of the BC-containing particles had undergone atmospheric processing and exhibited mixing with hygroscopic material. Consequently, a significant fraction of the soot particles demonstrates sufficiently high κ values and diameters to activate under atmospherically relevant supersaturation values. Among the classes identified, the $OOA_{BC,ETSP}$ and $SO_{4,\ BC,ETSP}$ type particles appear to be particularly relevant for CCN activity, given their combined attributes of abundance, hygroscopicity and size distribution. This finding has important implications for understanding the activation of rBC containing particles into cloud droplets and the sources of CCN in urban locations.

References

Ahmed, M., Rappenglück, B., Das, S. and Chellam, S.: Source apportionment of volatile organic compounds, CO, SO2 and trace metals in a complex urban atmosphere, Environ. Adv., 6, 100127, doi:10.1016/j.envadv.2021.100127, 2021.

Al-Naiema, I. M., Hettiyadura, A. P. S., Wallace, H. W., Sanchez, N. P., Madler, C. J., Karakurt Cevik, B., Bui, A. A. T., Kettler, J., Griffin, R. J. and Stone, E. A.: Source apportionment of fine particulate matter in Houston, Texas: Insights to secondary organic aerosols, Atmos. Chem. Phys., 18(21), 15601–15622, doi:10.5194/acp-18-15601-2018, 2018.

Allan, J. D., Delia, A. E., Coe, H., Bower, K. N., Alfarra, M. R., Jimenez, J. L., Middlebrook, A. M., Drewnick, F., Onasch, T. B., Canagaratna, M. R., Jayne, J. T. and Worsnop, D. R.: A generalised method for the extraction of chemically resolved mass spectra from Aerodyne aerosol mass spectrometer data, J. Aerosol Sci., 35(7), 909–922, doi:10.1016/j.jaerosci.2004.02.007, 2004.

Anastasopolos, A. T., Sofowote, U. M., Hopke, P. K., Rouleau, M., Shin, T., Dheri, A., Peng, H., Kulka, R., Gibson, M. D., Farah, P. and Sundar, N.: Air quality in Canadian port cities after regulation of low-sulphur marine fuel in the North American Emissions Control Area, Sci. Total Environ., 791, 147949, doi:10.1016/j.scitotenv.2021.147949, 2021.

Andreae, M. O.: Soot carbon and excess fine potassium: Long-range transport of combustion-derived aerosols, Science (80-.)., 220(4602), 1148–1151, doi:10.1126/science.220.4602.1148, 1983.

Andreae, M. O.: Ocean-atmosphere interactions in the global biogeochemical sulfur cycle, Mar. Chem., 30(C), 1–29, doi:10.1016/0304-4203(90)90059-L, 1990.

Andreae, M. O., Ferek, R. J., Bermond, F., Byrd, K. P., Engstrom, R. T., Hardin, S., Houmere, P. D., Lemarrec, F. and Raemdonck, H.: Dimethyl sulfide in the Marine atmosphere, J. Geophys. Res., 100(D12), doi:10.1029/95jd02374, 1985.

Avery, A. M., Williams, L. R., Fortner, E. C., Robinson, W. A. and Onasch, T. B.: Particle detection using the dual-vaporizer configuration of the soot particle Aerosol Mass Spectrometer (SP-AMS), Aerosol Sci. Technol., 55(3), 254–267, doi:10.1080/02786826.2020.1844132, 2020.

Banta, R. M., Senff, C. J., Nielsen-Gammon, J., Darby, L. S., Ryerson, T. B., Alvarez, R. J., Sandberg, S. R., Williams, E. J. and Trainer, M.: A bad air day in Houston, Bull. Am. Meteorol. Soc., 86(5), 657–669, doi:10.1175/BAMS-86-5-657, 2005.

Bates, T. S., Lamb, B. K., Guenther, A., Dignon, J. and Stoiber, R. E.: Sulfur emissions to the atmosphere from natural sourees, J. Atmos. Chem., 14(1–4), 315–337, doi:10.1007/BF00115242, 1992.

Bates, T. S., Quinn, P. K., Coffman, D., Schulz, K., Covert, D. S., Johnson, J. E., Williams, E. J., Lerner, B. M., Angevine, W. M., Tucker, S. C., Brewer, W. A. and Stohl, A.: Boundary layer aerosol chemistry during TexAQS / / GoMACCS 2006 : Insights into aerosol sources and transformation processes, J. Geophys. Res., 113, 1–18, doi:10.1029/2008JD010023, 2008.

Bean, J. K., Faxon, C. B., Leong, Y. J., Wallace, H. W., Cevik, B. K., Ortiz, S., Canagaratna, M. R., Usenko, S., Sheesley, R. J., Griffin, R. J. and Ruiz, L. H.: Composition and sources of particulate matter measured near Houston, TX: Anthropogenic-biogenic interactions, Atmosphere (Basel)., 7(5), doi:10.3390/atmos7050073, 2016.

Bibi, Z., Coe, H., Brooks, J., Williams, P. I., Reyes-Villegas, E., Priestley, M., Percival, C. J. and Allan, J. D.: Technical note: A new approach to discriminate different black carbon sources by utilising fullerene and metals in positive matrix factorisation analysis of high-resolution soot particle aerosol mass spectrometer data, Atmos. Chem. Phys., 21(13), 10763–10777, doi:10.5194/acp-21-10763-2021, 2021.

Bond, T. C. and Bergstrom, R. W.: Light absorption by carbonaceous particles: An investigative review, Aerosol Sci. Technol., 27–67, doi:10.1080/02786820500421521, 2006.

Bond, T. C., Doherty, S. J., Fahey, D. W., Forster, P. M., Berntsen, T., Deangelo, B. J., Flanner, M. G., Ghan, S., Kärcher, B., Koch, D., Kinne, S., Kondo, Y., Quinn, P. K., Sarofim, M. C., Schultz, M. G., Schulz, M., Venkataraman, C., Zhang, H., Zhang, S., Bellouin, N., Guttikunda, S. K., Hopke, P. K., Jacobson, M. Z., Kaiser, J. W., Klimont, Z., Lohmann, U., Schwarz, J. P., Shindell, D., Storelvmo, T., Warren, S. G. and Zender, C. S.: Bounding the role of black carbon in the climate system: A scientific assessment, J. Geophys. Res. Atmos., 118(11), 5380–5552, doi:10.1002/jgrd.50171, 2013.

Bozlaker, A., Prospero, J. M., Fraser, M. P. and Chellam, S.: Quantifying the contribution of long-range saharan dust transport on particulate matter concentrations in Houston, Texas, using detailed elemental

analysis, Environ. Sci. Technol., 47(18), 10179–10187, doi:10.1021/es4015663, 2013.

Bozlaker, A., Prospero, J. M., Price, J. and Chellam, S.: Identifying and Quantifying the Impacts of Advected North African Dust on the Concentration and Composition of Airborne Fine Particulate Matter in Houston and Galveston, Texas, J. Geophys. Res. Atmos., 124(22), 12282–12300, doi:10.1029/2019JD030792, 2019.

Caicedo, V., Rappenglueck, B., Cuchiara, G., Flynn, J., Ferrare, R., Scarino, A. J., Berkoff, T., Senff, C., Langford, A. and Lefer, B.: Bay Breeze and Sea Breeze Circulation Impacts on the Planetary Boundary Layer and Air Quality From an Observed and Modeled DISCOVER-AQ Texas Case Study, J. Geophys. Res. Atmos., 124(13), 7359–7378, doi:10.1029/2019JD030523, 2019.

Canagaratna, M. R., Jayne, J. T., Ghertner, D. A., Herndon, S., Shi, Q., Jimenez, J. L., Silva, P. J., Williams, P., Lanni, T., Drewnick, F., Demerjian, K. L., Kolb, C. E. and Worsnop, D. R.: Chase studies of particulate emissions from in-use New York City vehicles, Aerosol Sci. Technol., 38(6), 555–573, doi:10.1080/02786820490465504, 2004.

Cao, L. M., Wei, J., He, L. Y., Zeng, H., Li, M. L., Zhu, Q., Yu, G. H. and Huang, X. F.: Aqueous aging of secondary organic aerosol coating onto black carbon: Insights from simultaneous L-ToF-AMS and SP-AMS measurements at an urban site in southern China, J. Clean. Prod., 330(November 2021), 129888, doi:10.1016/j.jclepro.2021.129888, 2022.

Cappa, C. D., Onasch, T. B., Massoli, P., Worsnop, D. R., Jobson, B. T., Kolesar, K. R., Lack, D. A., Lerner, B. M. and Li, S.: Radiative Absorption Enhancements Due to the Mixing State of Atmospheric Black Carbon, Science (80-.)., (August), 1078–1082, 2012.

Cappa, C. D., Zhang, X., Russell, L. M., Collier, S., Lee, A. K. Y., Chen, C. L., Betha, R., Chen, S., Liu, J., Price, D. J., Sanchez, K. J., McMeeking, G. R., Williams, L. R., Onasch, T. B., Worsnop, D. R., Abbatt, J. and Zhang, Q.: Light Absorption by Ambient Black and Brown Carbon and its Dependence on Black Carbon Coating State for Two California, USA, Cities in Winter and Summer, J. Geophys. Res. Atmos., 124(3), 1550–1577, doi:10.1029/2018JD029501, 2019.

Carbone, S., Onasch, T., Saarikoski, S., Timonen, H., Saarnio, K., Sueper, D., Rönkkö, T., Pirjola, L., Haÿrinen, A., Worsnop, D. and Hillamo, R.: Characterization of trace metals on soot aerosol particles with the SP-AMS: Detection and quantification, Atmos. Meas. Tech., 8(11), 4803–4815, doi:10.5194/amt-8-4803-2015, 2015.

Carbone, S., Timonen, H. J., Rostedt, A., Happonen, M., Keskinen, J., Ristimaki, J., Korpi, H., Artaxo, P., Worsnop, D., Canonaco, F., Prévôt, A. S. H., Hillamo, R., Saarikoski, S., Keskinen, J., Ristimaki, J., Korpi, H., Artaxo, P., Canagaratna, M., Worsnop, D., Canonaco, F., Prévôt, A. S. H., Hillamo, R. and Saarikoski, S.: Distinguishing fuel and lubricating oil combustion products in diesel engine exhaust particles, Aerosol Sci. Technol., 53(5), 594–607, doi:10.1080/02786826.2019.1584389, 2019.

Chang, R. Y., Slowik, J. G., Shantz, N. C., Vlasenko, A., Liggio, J., Sjostedt, S. J. and Leaitch, W. R.: The hygroscopicity parameter (κ) of ambient organic aerosol at a field site subject to biogenic and anthropogenic influences : relationship to degree of aerosol oxidation, Atmos. Chem. Phys., 5047–5064, doi:10.5194/acp-10-5047-2010, 2010.

Collier, S., Zhou, S., Kuwayama, T., Forestieri, S., Brady, J., Zhang, M., Kleeman, M., Cappa, C., Bertram, T. and Zhang, Q.: Organic PM emissions from vehicles: Composition, O/C ratio, and dependence on PM concentration, Aerosol Sci. Technol., 49(2), 86–97, doi:10.1080/02786826.2014.1003364, 2015.

Collier, S., Williams, L. R., Onasch, T. B., Cappa, C. D., Zhang, X., Russell, L. M., Chen, C. L., Sanchez, K. J., Worsnop, D. R. and Zhang, Q.: Influence of Emissions and Aqueous Processing on Particles Containing Black Carbon in a Polluted Urban Environment: Insights From a Soot Particle-Aerosol Mass Spectrometer, J. Geophys. Res. Atmos., 123(12), 6648–6666, doi:10.1002/2017JD027851, 2018.

Corbin, J. C., Sierau, B., Gysel, M., Laborde, M., Keller, A., Kim, J., Petzold, A., Onasch, T. B., Lohmann, U. and Mensah, A. A.: Mass spectrometry of refractory black carbon particles from six sources: Carbon-cluster and oxygenated ions, Atmos. Chem. Phys., 14(5), 2591–2603, doi:10.5194/acp-14-2591-2014, 2014.

Corbin, J. C., Lohmann, U., Sierau, B., Keller, A., Burtscher, H. and Mensah, A. A.: Black carbon surface oxidation and organic composition of beech-wood soot aerosols, Atmos. Chem. Phys., 15(20), 11885–11907, doi:10.5194/acp-15-11885-2015, 2015.

Cubison, M. J., Ortega, A. M., Hayes, P. L., Farmer, D. K., Day, D., Lechner, M. J., Brune, W. H., Apel, E., Diskin, G. S., Fisher, J. A., Fuelberg, H. E., Hecobian, A., Knapp, D. J., Mikoviny, T., Riemer, D., Sachse, G. W., Sessions, W., Weber, R. J., Weinheimer, A. J., Wisthaler, A. and Jimenez, J. L.: Effects of aging on organic aerosol from open biomass burning smoke in aircraft and laboratory studies, Atmos. Chem. Phys., doi:10.5194/acp-11-12049-2011, 2011.

Das, S., Miller, B. V., Prospero, J. M., Gaston, C. J., Royer, H. M., Blades, E., Sealy, P. and Chellam, S.: Coupling Sr-Nd-Hf Isotope Ratios and Elemental Analysis to Accurately Quantify North African Dust Contributions to PM2.5in a Complex Urban Atmosphere by Reducing Mineral Dust Collinearity, Environ. Sci. Technol., 56(12), 7729–7740, doi:10.1021/acs.est.2c01233, 2022.

DeCarlo, P. F., Kimmel, J. R., Trimborn, A., Northway, M. J., Jayne, J. T., Aiken, A. C., Gonin, M., Fuhrer, K., Horvath, T., Docherty, K. S., Worsnop, D. R. and Jimenez, J. L.: Field-deployable, high-resolution, time-of-flight aerosol mass spectrometer, Anal. Chem., doi:10.1021/ac061249n, 2006.

Emerson, E. W., Katich, J. M. and Farmer, D. K.: Direct Measurements of Dry and Wet Deposition of Black Carbon Over a Grassland, , 277–290, doi:10.1029/2018JD028954, 2018.

Falk, J., Korhonen, K., Malmborg, V. B., Gren, L., Eriksson, A. C., Karjalainen, P., Markkula, L., Bengtsson, P., Virtanen, A., Svenningsson, B., Pagels, J. and Kristensen, T. B.: Immersion Freezing Ability of Freshly Emitted Soot with Various Physico-Chemical Characteristics, Atmosphere (Basel)., 1–17, 2021.

Fierce, L., Riemer, N. and Bond, T. C.: Toward Reduced Representation of Mixing State For Simulating Aerosol Effects on Climate, Bull. Am. Meteorol. Soc., (May), 971–980, doi:10.1175/BAMS-D-16-0028.1, 2017.

Fierce, L., Onasch, T. B., Cappa, C. D., Mazzoleni, C., China, S., Bhandari, J., Davidovits, P., Al Fischer, D., Helgestad, T., Lambe, A. T., Sedlacek, A. J., Smith, G. D. and Wolff, L.: Radiative absorption enhancements by black carbon controlled by particle-to-particle heterogeneity in composition, Proc. Natl. Acad. Sci. U. S. A., 117(10), 5196–5203, doi:10.1073/pnas.1919723117, 2020.

Fofie, E. A., Donahue, N. M. and Asa-Awuku, A.: Cloud condensation nuclei activity and droplet formation of primary and secondary organic aerosol mixtures, Aerosol Sci. Technol., 6826, doi:10.1080/02786826.2017.1392480, 2018.

Fortner, E. C., Brooks, W. A., Onasch, T. B., Canagaratna, M. R., Massoli, P., Jayne, J. T., Franklin, J. P., Knighton, W. B., Wormhoudt, J., Worsnop, D. R., Kolb, C. E. and Herndon, S. C.: Particulate emissions measured during the TCEQ comprehensive flare emission study, Ind. Eng. Chem. Res., 51(39), 12586–

12592, doi:10.1021/ie202692y, 2012.

Ge, X., Setyan, A., Sun, Y. and Zhang, Q.: Primary and secondary organic aerosols in Fresno, California during wintertime: Results from high resolution aerosol mass spectrometry, J. Geophys. Res. Atmos., 117(18), 1–15, doi:10.1029/2012JD018026, 2012.

Gysel, M., Crosier, J., Topping, D. O., Whitehead, J. D., Bower, K. N., Cubison, M. J., Williams, P. I., Flynn, M. J., McFiggans, G. B. and Coe, H.: Closure study between chemical composition and hygroscopic growth of aerosol particles during TORCH2, Atmos. Chem. Phys., 7(24), 6131–6144, doi:10.5194/acp-7-6131-2007, 2007.

Healy, R. M., Evans, G. J., Murphy, M., Tritscher, T., Laborde, M., Weingartner, E., Gysel, M., Poulain, L., Kamilli, K. A., Wiedensohler, A., Connor, I. P. O., Mcgillicuddy, E., Sodeau, J. R. and Wenger, J. C.: Predicting hygroscopic growth using single particle chemical composition estimates, J. Geophys. Res. Atmos., 9567–9577, doi:10.1002/2014JD021888.Received, 2014.

Healy, R. M., Wang, J. M., Jeong, C., Lee, A. K. Y., Willis, M. D., Jaroudi, E., Zimmerman, N., Hilker, N., Murphy, M., Eckhardt, S., Stohl, A., Abbatt, J. P. D., Wenger, J. C. and Evans, G. J.: Journal of Geophysical Research : Atmospheres, , 6619–6633, doi:10.1002/2015JD023382.Received, 2015.

Hodnebrog, Ø., Myhre, G. and Samset, B.: How shorter black carbon lifetime alters its climate effect, Nat. Commun., (May), 1–7, doi:10.1038/ncomms6065, 2014.

IMO: International Maritime Organization (IMO) 2020, 2020.

IPCC: Climate Change 2021: The Physical Science Basis. Contribution of Working Group I to the Sixth Assessment Report of the Intergovernmental Panel on Climate Change, edited by V. Masson-Delmotte, P. Zhai, A. Pirani, S. L. Connors, C. Pean, S. Berger, N. Caud, Y. Chen, L. Goldfarb, M. I. Gomis, M. Huang, K. Leitzell, E. Lonnoy, J. B. . Matthews, T. K. Maycock, T. Waterfield, O. Yelekci, R. Yu, and B. Zhou, Cambridge University Press, United Kingdom and New York, NY, USA., 2021.

Jahn, L. G., Jahl, L. G., Bland, G. D., Bowers, B. B., Monroe, L. W. and Sullivan, R. C.: Metallic and crustal elements in biomass-burning aerosol and ash: Prevalence, significance, and similarity to soil particles, ACS Earth Sp. Chem., 5(1), 136–148, doi:10.1021/acsearthspacechem.0c00191, 2021.

Lack, D. A. and Cappa, C. D.: Impact of brown and clear carbon on light absorption enhancement , single scatter albedo and absorption wavelength dependence of black carbon, Atmos. Chem. Phys., 4207–4220, doi:10.5194/acp-10-4207-2010, 2010.

Lambe, A. T., Onasch, T. B., Massoli, P., Croasdale, D. R., Wright, J. P., Ahern, A. T., Williams, L. R., Worsnop, D. R., Brune, W. H. and Davidovits, P.: Laboratory studies of the chemical composition and cloud condensation nuclei (CCN) activity of secondary organic aerosol (SOA) and oxidized primary organic aerosol (OPOA), Atmos. Chem. Phys., doi:10.5194/acp-11-8913-2011, 2011.

Lambe, A. T., Ahern, A. T., Wright, J. P., Croasdale, D. R., Davidovits, P. and Onasch, T. B.: Oxidative aging and cloud condensation nuclei activation of laboratory combustion soot, J. Aerosol Sci., 79, 31–39, doi:10.1016/j.jaerosci.2014.10.001, 2015.

Lee, A. K. Y., Willis, M. D., Healy, R. M., Onasch, T. B. and Abbatt, J. P. D.: Mixing state of carbonaceous aerosol in an urban environment: Single particle characterization using the soot particle aerosol mass spectrometer (SP-AMS), Atmos. Chem. Phys., 15(4), 1823–1841, doi:10.5194/acp-15-1823-2015, 2015.

Lee, A. K. Y., Willis, M. D., Healy, R. M., Wang, J. M., Jeong, C. H., Wenger, J. C., Evans, G. J. and Abbatt, J.

P. D.: Single-particle characterization of biomass burning organic aerosol (BBOA): Evidence for non-uniform mixing of high molecular weight organics and potassium, Atmos. Chem. Phys., 16(9), 5561–5572, doi:10.5194/acp-16-5561-2016, 2016.

Lee, A. K. Y., Chen, C. L., Liu, J., Price, D. J., Betha, R., Russell, L. M., Zhang, X. and Cappa, C. D.: Formation of secondary organic aerosol coating on black carbon particles near vehicular emissions, Atmos. Chem. Phys., 17(24), 15055–15067, doi:10.5194/acp-17-15055-2017, 2017.

Lee, A. K. Y., Rivellini, L. H., Chen, C. L., Liu, J., Price, D. J., Betha, R., Russell, L. M., Zhang, X. and Cappa, C. D.: Influences of Primary Emission and Secondary Coating Formation on the Particle Diversity and Mixing State of Black Carbon Particles, Environ. Sci. Technol., 53(16), 9429–9438, doi:10.1021/acs.est.9b03064, 2019.

Lee, J. E., Gorkowski, K., Meyer, A. G., Benedict, K. B., Aiken, A. C. and Dubey, M. K.: Wildfire Smoke Demonstrates Significant and Predictable Black Carbon Light Absorption Enhancements, , doi:10.1029/2022GL099334, 2022.

Levy, M. E., Zhang, R., Khalizov, A. F., Zheng, J., Collins, D. R., Glen, C. R., Wang, Y., Yu, X. Y., Luke, W., Jayne, J. T. and Olaguer, E.: Measurements of submicron aerosols in Houston, Texas during the 2009 SHARP field campaign, J. Geophys. Res. Atmos., 118(18), 10,518-10,534, doi:10.1002/jgrd.50785, 2013.

Li, W., Wang, Y., Bernier, C. and Estes, M.: Identification of Sea Breeze Recirculation and Its Effects on Ozone in Houston, TX, During DISCOVER-AQ 2013, J. Geophys. Res. Atmos., 125(22), 1–21, doi:10.1029/2020JD033165, 2020.

Liu, F., Yon, J., Fuentes, A., Lobo, P., Gregory, J. and Corbin, J. C.: Review of recent literature on the light absorption properties of black carbon : Refractive index , mass absorption cross section , and absorption function, Aerosol Sci. Technol., 54(1), 33–51, doi:10.1080/02786826.2019.1676878, 2020.

Ma, M., Rivellini, L.-H., Kasthuriarachchi, N., Zhu, Q., Zong, Y., Yu, W., Yang, W., Kraft, M. and Lee, A. K. Y.: Effects of polyoxymethylene dimethyl ether (PODE n) blended fuel on diesel engine emission : Insight from soot-particle aerosol mass spectrometry and aethalometer measurements, Atmos. Environ. X, 18(March), doi:10.1016/j.aeaoa.2023.100216, 2023.

Motos, G., Schmale, J., Corbin, J. C., Zanatta, M., Baltensperger, U. and Gysel-Beer, M.: Droplet activation behaviour of atmospheric black carbon particles in fog as a function of their size and mixing state, Atmos. Chem. Phys., 19(4), 2183–2207, doi:10.5194/acp-19-2183-2019, 2019.

Ng, N. L., Canagaratna, M. R., Jimenez, J. L., Chhabra, P. S., Seinfeld, J. H. and Worsnop, D. R.: Changes in organic aerosol composition with aging inferred from aerosol mass spectra, Atmos. Chem. Phys., 11(13), 6465–6474, doi:10.5194/acp-11-6465-2011, 2011.

Onasch, T. B., Trimborn, A., Fortner, E. C., Jayne, J. T., Kok, G. L., Williams, L. R., Davidovits, P. and Worsnop, D. R.: Soot particle aerosol mass spectrometer: Development, validation, and initial application, Aerosol Sci. Technol., doi:10.1080/02786826.2012.663948, 2012.

Paatero, P. and Tapper, U.: Positive matrix factorization: A non-negative factor model with optimal utilization of error estimates of data values, Environmetrics, doi:10.1002/env.3170050203, 1994.

Peng, J., Hu, M., Guo, S., Du, Z., Zheng, J., Shang, D., Levy, M. and Zeng, L.: Markedly enhanced absorption and direct radiative forcing of black carbon under polluted urban environments, , doi:10.1073/pnas.1602310113, 2016.

Petters, M. D. and Kreidenweis, S. M.: A single parameter representation of hygroscopic growth and cloud condensation nucleus activity, Atmos. Chem. Phys., 13(2), 1081–1091, doi:10.5194/acp-13-1081-2013, 2007.

Popovicheva, O., Kireeva, E., Persiantseva, N., Timofeev, M., Bladt, H., Ivleva, N. P., Niessner, R. and Moldanová, J.: Microscopic characterization of individual particles from multicomponent ship exhaust, J. Environ. Monit., 14(12), 3101–3110, doi:10.1039/c2em30338h, 2012.

Price, D. J., Chen, C. L., Russell, L. M., Lamjiri, M. A., Betha, R., Sanchez, K., Liu, J., Lee, A. K. Y. and Cocker, D. R.: More unsaturated, cooking-type hydrocarbon-like organic aerosol particle emissions from renewable diesel compared to ultra low sulfur diesel in at-sea operations of a research vessel, Aerosol Sci. Technol., 51(2), 135–146, doi:10.1080/02786826.2016.1238033, 2017.

Ramanathan, V. and Carmichael, G.: Global and regional climate changes due to black carbon, Nat. Geosci., 1(4), 221–227, doi:10.1038/ngeo156, 2008.

Rivellini, L. H., Adam, M. G., Kasthuriarachchi, N. and Lee, A. K. Y.: Characterization of carbonaceous aerosols in Singapore: Insight from black carbon fragments and trace metal ions detected by a soot particle aerosol mass spectrometer, Atmos. Chem. Phys., 20(10), 5977–5993, doi:10.5194/acp-20-5977-2020, 2020.

Rivera, C., Mellqvist, J., Samuelsson, J., Lefer, B., Alvarez, S. and Patel, M. R.: Quantification of NO2 and SO2 emissions from the houston ship channel and texas city industrial areas during the 2006 texas air quality study, J. Geophys. Res. Atmos., 115(8), 1–10, doi:10.1029/2009JD012675, 2010.

Schulze, B. C., Wallace, H. W., Bui, A. T., Flynn, J. H., Erickson, M. H., Alvarez, S., Dai, Q., Usenko, S., Sheesley, R. J. and Griffin, R. J.: The impacts of regional shipping emissions on the chemical characteristics of coastal submicron aerosols near Houston , TX, Atmos. Chem. Phys., (x), 14217–14241, 2018.

Sonntag, D. B., Bailey, C. R., Fulper, C. R. and Baldauf, R. W.: Contribution of Lubricating Oil to Particulate Matter Emissions from Light-Duty Gasoline Vehicles in Kansas City, Environ. Sci. Technol., 2012.

Sun, Y. L., Zhang, Q., Schwab, J. J., Yang, T., Ng, N. L. and Demerjian, K. L.: Factor analysis of combined organic and inorganic aerosol mass spectra from high resolution aerosol mass spectrometer measurements, Atmos. Chem. Phys., doi:10.5194/acp-12-8537-2012, 2012.

Ulbrich, I. M., Canagaratna, M. R., Zhang, Q., Worsnop, D. R. and Jimenez, J. L.: Interpretation of organic components from Positive Matrix Factorization of aerosol mass spectrometric data, Atmos. Chem. Phys., doi:10.5194/acp-9-2891-2009, 2009.

Ulbrich, I. M., Canagaratna, M. R., Cubison, M. J., Zhang, Q., Ng, N. L., Aiken, A. C. and Jimenez, J. L.: Three-dimensional factorization of size-resolved organic aerosol mass spectra from Mexico City, Atmos. Meas. Tech., 195–224, doi:10.5194/amt-5-195-2012, 2012.

Wang, J., Ye, J., Liu, D., Wu, Y., Zhao, J., Xu, W., Xie, C., Shen, F., Zhang, J., Ohno, P. E., Qin, Y., Zhao, X., T. Martin, S., Lee, A. K. Y., Fu, P., J. Jacob, D., Zhang, Q., Sun, Y., Chen, M. and Ge, X.: Characterization of submicron organic particles in Beijing during summertime: Comparison between SP-AMS and HR-AMS, Atmos. Chem. Phys., 20(22), 14091–14102, doi:10.5194/acp-20-14091-2020, 2020a.

Wang, X., Ye, X., Chen, J., Wang, X., Yang, X., Fu, T. M., Zhu, L. and Liu, C.: Direct links between hygroscopicity and mixing state of ambient aerosols: Estimating particle hygroscopicity from their single-particle mass spectra, Atmos. Chem. Phys., 20(11), 6273–6290, doi:10.5194/acp-20-6273-2020, 2020b.

Watson-Parris, D., Christensen, M. W., Laurenson, A., Clewley, D., Gryspeerdt, E. and Stier, P.: Shipping regulations lead to large reduction in cloud perturbations, Proc. Natl. Acad. Sci. U. S. A., 119(41), doi:10.1073/pnas.2206885119, 2022.

Williams, L. R., Gonzalez, L. A., Peck, J., Trimborn, D., McInnis, J., Farrar, M. R., Moore, K. D., Jayne, J. T., Robinson, W. A., Lewis, D. K., Onasch, T. B., Canagaratna, M. R., Trimborn, A., Timko, M. T., Magoon, G., Deng, R., Tang, D., De La Rosa Blanco, E., Prévôt, A. S. H., Smith, K. A. and Worsnop, D. R.: Characterization of an aerodynamic lens for transmitting particles greater than 1 micrometer in diameter into the Aerodyne aerosol mass spectrometer, Atmos. Meas. Tech., 6(11), 3271–3280, doi:10.5194/amt-6-3271-2013, 2013.

Willis, M. D., Lee, A. K. Y., Onasch, T. B., Fortner, E. C., Williams, L. R., Lambe, A. T., Worsnop, D. R. and Abbatt, J. P. D.: Collection efficiency of the soot-particle aerosol mass spectrometer (SP-AMS) for internally mixed particulate black carbon, Atmos. Meas. Tech., doi:10.5194/amt-7-4507-2014, 2014.

Willis, M. D., Healy, R. M., Riemer, N., West, M., Wang, J. M., Jeong, C., Wenger, J. C., Evans, G. J., Abbatt, J. P. D. and Lee, A. K. Y.: Quantification of black carbon mixing state from traffic : implications for aerosol optical properties, , 4693–4706, doi:10.5194/acp-16-4693-2016, 2016.

Willis, M. D., Bozem, H., Kunkel, D., Lee, A. K. Y., Schulz, H., Burkart, J., Aliabadi, A. A., Herber, A. B., Richard Leaitch, W. and Abbatt, J. P. D.: Aircraft-based measurements of High Arctic springtime aerosol show evidence for vertically varying sources, transport and composition, Atmos. Chem. Phys., 19(1), 57–76, doi:10.5194/acp-19-57-2019, 2019.

Worton, D. R., Isaacman, G., Gentner, D. R., Dallmann, T. R., Chan, A. W. H., Ruehl, C., Kirchstetter, T. W., Wilson, K. R., Harley, R. A. and Goldstein, A. H.: Lubricating Oil Dominates Primary Organic Aerosol Emissions from Motor Vehicles, 2014.

Wu, Y., Liu, D., Wang, J., Shen, F., Chen, Y., Cui, S., Ge, S., Wu, Y., Chen, M. and Ge, X.: Characterization of Size-Resolved Hygroscopicity of Black Carbon-Containing Particle in Urban Environment, Environ. Sci. Technol., 53(24), 14212–14221, doi:10.1021/acs.est.9b05546, 2019.

Xie, C., Xu, W., Wang, J., Liu, D., Ge, X., Zhang, Q., Wang, Q., Du, W., Zhao, J., Zhou, W., Li, J., Fu, P., Wang, Z., Worsnop, D. and Sun, Y.: Light absorption enhancement of black carbon in urban Beijing in summer, Atmos. Environ., 213(May), 499–504, doi:10.1016/j.atmosenv.2019.06.041, 2019.

Yang, Y., Fu, Y., Lin, Q., Jiang, F., Lian, X., Li, L., Wang, Z., Zhang, G., Bi, X., Wang, X. and Sheng, G.: Recent advances in quantifying wet scavenging efficiency of black carbon aerosol, Atmosphere (Basel)., 10(4), 1–19, doi:10.3390/atmos10040175, 2019.

Ye, Q., Gu, P., Li, H. Z., Robinson, E. S., Lipsky, E., Kaltsonoudis, C., Lee, A. K. Y., Apte, J. S., Robinson, A. L., Sullivan, R. C., Presto, A. A. and Donahue, N. M.: Spatial Variability of Sources and Mixing State of Atmospheric Particles in a Metropolitan Area, Environ. Sci. Technol., 52(12), 6807–6815, doi:10.1021/acs.est.8b01011, 2018.

Yoon, S., Usenko, S. and Sheesley, R. J.: Fine and Coarse Carbonaceous Aerosol in Houston, TX, during DISCOVER-AQ, Atmosphere (Basel)., 11(482), 1–14, doi:10.3390/ATMOS11050482, 2020.

Young, D. E., Kim, H., Parworth, C., Zhou, S., Zhang, X., Cappa, C. D., Seco, R., Kim, S. and Zhang, Q.: Influences of emission sources and meteorology on aerosol chemistry in a polluted urban environment: Results from DISCOVER-AQ California, Atmos. Chem. Phys., 16(8), 5427–5451, doi:10.5194/acp-16-5427-2016, 2016.

Yu, C., Pasternak, D., Lee, J., Yang, M., Bell, T., Bower, K., Wu, H., Liu, D., Reed, C., Bauguitte, S., Cliff, S., Trembath, J., Coe, H. and Allan, J. D.: Characterizing the Particle Composition and Cloud Condensation Nuclei from Shipping Emission in Western Europe, Environ. Sci. Technol., 54(24), 15604–15612, doi:10.1021/acs.est.0c04039, 2020.

Zhang, Q., Worsnop, D. R., Canagaratna, M. R. and Jimenez, J. L.: Hydrocarbon-like and oxygenated organic aerosols in Pittsburgh: Insights into sources and processes of organic aerosols, Atmos. Chem. Phys., 5(12), 3289–3311, doi:10.5194/acp-5-3289-2005, 2005.

Zuberi, B., Johnson, K. S., Aleks, G. K., Molina, L. T., Molina, M. J. and Laskin, A.: Hydrophilic properties of aged soot, Geophys. Res. Lett., 32, 2–5, doi:10.1029/2004GL021496, 2005.

6. Conclusions

The sources and atmospheric evolution of PM remains a significant source of uncertainty within the earth system. The physical and chemical characteristics of these aerosols greatly impact the effects on global climate and human health. Ambient observations are needed to parametrize models and inform public policy. Through the analysis of a series of field deployments of a soot-particle aerosol mass spectrometer, we were able to obtain high-time resolution, size-resolved compositional information of ambient PM in a range of different atmospheric environments ranging from the remote free troposphere to urban and industrial locations. Important conclusions that can be drawn from this work include:

i. PM_1 in the remote troposphere of the Western U.S. is impacted by highly aged, low volatility BBOA during the summertime. BBOA accounted for an average 18% of the OA mass during the MBO19 field campaign with an average concentration of 0.22 μg sm^{-3} and correlated with biomass burning tracer species such as CO, rBC and acetonitrile. Through the comparison of wildfire plumes ranging in age from 10 hours to 10 days, it was found that BBOA became more oxidized, lower volatility and the shifted to a larger size mode with atmospheric processing. ΔOA/ΔCO was found to decrease with extended processing, at a rate of approximately −0.022 ppb ppb^{-1} day^{-1}, suggesting a net loss of BBOA relative to CO during long-range transport caused by processes such as evaporation, photolysis, and deposition.

ii. The measurements collected during the 2019 field campaign were compared to previous measurements of fresh wildfire emissions and the plume age was estimated using the decay of NO_x relative to CO. Rapid aerosol oxidation was seen in wildfire plumes as evidenced by increasing O/C and f_{44}. Through PMF analysis, distinct BBOA components with varying degrees of processing were identified. Notably, there was a rapid decrease in the mass fraction of fresh BBOA factors, replaced by more oxidized aerosol as the wildfire plumes aged. This transformation can be attributed to a

combination of volatilization of the more volatile fresh BBOA and the formation of less volatile, more oxidized BBOAs.

iii. The volatility of different BBOA types was quantitatively assessed using the volatility basis set (VBS) approach. With increased atmospheric processing, the aerosol mass distribution shifted from C* of 10^{1} to C* < 10^{-2}. The BBOA PMF factor identified in 2019 displayed the lowest volatility, with a significant mass fraction at C* < 10^{-7}. From this, the role of dilution driven aerosol evaporation was characterized. It was found that only 20-40% of the mass of the most processed BBOA components evaporated with dilution, while upwards of 80% of fresh BBOA components evaporated.

iv. Aqueous processing of aerosols within fog and cloud droplets has important implications on the chemical composition and physical properties of PM. BC-containing aerosol was sampled in a polluted, urban location and it was found that following extensive fog processing, soot aerosols were enriched with ammonium nitrate and a distinct secondary organic aerosol type. The $CH_2O_2^+$ ion fragment was identified as a promising mass spectral signature for aqueous phase processing in droplets, and is likely related to dicarboxylates, such as oxalate. Due to the hygroscopicity of these aerosol species, this greatly increases the cloud condensation nuclei activity of the black carbon containing aerosol fraction.

v. Ensemble and single particle measurements of black carbon containing aerosol were collected in Houston, TX. BC was found to be primarily internally mixed with secondary species such as oxidized organics and sulfate, highlighting the importance of atmospheric aging processes on soot aerosol characteristics in urban environments. The BC mixing state was quantitatively assessed, and the average mixing state index was found to be 41 ± 13%, indicating that the aerosol population was intermediate between internally and externally mixed. Furthermore, a significant fraction of BC particles was found to be mixed with hygroscopic material and estimated to activate under environmentally relevant super saturation conditions.

Appendix A: Supplementary Material for Persistent Influence of Wildfire Emissions in the Western United States and Characteristics of Aged Biomass Burning Organic Aerosols Under Clean Air Conditions

A1. Methods

A1.1 Sampling Site

The Mt Bachelor Observatory (MBO) is a mountaintop site within the Deschutes National Forest that has been operated for air quality studies since 2004. The observatory is located inside the summit lift building and is not accessible via road, and instead is only reached by chairlift or a ~1.5 km trail. Although the sampling site is above tree line, the surrounding forest is primarily coniferous. Active wildfires in the PNW during the sampling period and during the 2013 campaign period were detected by the Moderate Resolution Imaging Spectroradiometer (MODIS) aboard the Terra satellite are shown in Figure A1.

A schematic of the sampling system deployed during the campaign is shown in Figure A3. Ambient aerosols were sampled through an inlet approximately 7m above the ground, and passed through a $PM_{2.5}$ cyclone and ~5m of insulated, ½" O.D. stainless steel tubing (14 l/min; residence time = 2.7s). A ¼" flow splitter (Brechtel Manufacturing Inc.) was used to divide the flow between the SP-AMS and a Scanning Mobility Particle Sizer (SMPS).

A1.2 Soot-Particle Aerosol Mass Spectrometer

The SP-AMS allows for high time resolution measurements of NR-PM_1 and refractory black carbon (rBC). The instrument was run using 2 minute (Aug 1 – Aug 24 and Aug 30 – Sept 10) or 6 minute averaging (Aug 24 – Aug 30). The open and closed spectra were collected alternatively every 3 seconds for the averaging time, and the average closed spectrum was subtracted from the average open spectrum ("open – closed mode"). During the "laser on" mode, an Nd-YAG laser (1064nm) is operated perpendicular to the particle beam in addition to the standard tungsten vaporizer. Black carbon containing particles are able to absorb the laser radiation and heat to ~4000K, vaporizing particles

containing rBC. The laser mode was switched on every 2 hours and kept on for 1 hr to allow the system to fully equilibrate between modes. All SP-AMS concentrations are reported in STP conditions (273.15K, 101325Pa), and are notated with "μg sm^{-3}".

The ionization efficiency was calibrated using monodisperse ammonium nitrate particles (Canagaratna et al., 2007; Jayne et al., 2000). Relative ionization efficiencies (RIEs) of ammonium, sulfate and rBC were determined using ammonium nitrate, ammonium sulfate and regal black respectively (Onasch et al., 2012). RIEs of nitrate, ammonium, sulfate and rBC were determined to be 1.05, 3.5, 1.25 and 0.17. The default RIEs for organics (1.4) and chloride (1.3) were used. The collection efficiency (CE) for aerosol mass spectrometers with standard vaporizer has been previously found to be near 0.5 due to the bounce of particles off of the vaporizer (Matthew et al., 2008), and this value was used during all laser off periods. Particles that undergo laser vaporization, i.e., rBC and any species internally mixed with black carbon, do not experience particle bounce, and thus have a larger CE. To account for this, an orthogonal distance regression fit forced through the origin was found for the average concentration of each species in the 6 minutes following the laser switching on (or off) with respect to the average concentration of the 6 minutes preceding the laser switching on (or off). The two minutes immediately following the laser switching on were removed to allow time for the instrument to equilibrate. This was done in an attempt to compare the change in signal when the laser vaporizer was turned on while the instrument was sampling the same air mass. The slope of the fit line was used as a CE correction and applied to all laser on concentration. This adjusts the CE to 0.625 for organics and 0.55 for inorganics during laser on periods and a post-correction comparison shows a slope close to one for all species (Fig A4). The correction values found agree well with those reported in Avery et al., (2020)(Avery et al., 2020). Additionally, previous studies have found that the fragmentation pattern of OA may differ between laser on mode and laser off mode(Onasch et al., 2012). Figure A4d-e show the a

similar analysis for f_{44} and f_{C2H4O2}, and confirm that both of these species have a slope close to 1, therefore, no correction was applied.

The standard fragmentation table was adjusted to account for the interference from gas phase species based on particle-free mass spectra. Gas phase CO_2^+ interference was subtracted based on a clean period with SMPS volume concentration of ~0 $\mu m^3 m^{-3}$. Ammonium mass concentration was determined only from the NH_3^+ fragment due to the overwhelming O^+ peak causing significant interference to the NH_2^+ peak at *m/z* 16, and $^{15}N^+$ and CH_3^+ fragments causing interference with the NH^+ peak at *m/z* 15. The NH_2^+ and NH^+ concentrations were scaled to NH_3^+ using the average ratio found during ammonium nitrate and ammonium sulfate calibration (NH_2^+ = 0.828 * NH_3^+ and NH^+ = 0.065 * NH_3^+). Due to the low ambient ammonium concentrations, the NH_3^+ signal (*m/z* 17.02655) had a systematic positive bias caused by ringing from the OH^+ peak. This was solved by constraining an additional peak to the OH signal (exact mass = 17.0420, OH_{ring} = 0.0916 * OH^+). Following this, the ammonium time series was smoothed using a 3-point boxcar smoothing algorithm to account for erroneous spikes caused by noise at the NH_3^+ ion.

The PM_1 concentration measured by the SP-AMS correlated well with the calculated mass from the SMPS using composition dependent PM_1 density (Pearson r value of 0.95; Fig. A5). The mass scattering efficiency (MSE), calculated as the orthogonal distance regression between light scattering at 550nm and PM_1 concentration was found to be 4.14 $m^2 g^{-1}$, a value that is consistent with previous measurements at MBO (Laing et al., 2016), as well as MSE values seen in other aged BB plumes (Reid et al., 2004).

A1.3. Thermodenuder

A digitally controlled thermodenuder was included upstream of the SP-AMS to quantify aerosol volatility. The thermodenuder was based on the design of Fierz et al., 2007(Fierz et al., 2007) and consists of a heating stage and an adsorption stage. The adsorption section was wrapped in carbon

cloth to remove evaporated VOCs and prevent re-condensation. The thermodenuder was operated in 14 different temperature steps between 30 and 290°C for 12 minutes each. The first six minutes of each step bypassed the thermodenuder while the temperature was allowed to equilibrate (Bypass mode; BP), this was followed by 6 minutes of the sample passing through the thermodenuder (TD mode). The switching was activated by a digital output to ensure synchronization with the SP-AMS averaging period, and a 10 second waiting period was implemented prior to every SP-AMS sample to prevent any cross-contamination between TD and BP modes. The volatility of different ions and PM_1 species was quantified based on the mass fraction remaining (MFR) after passing through the thermodenuder. MFR at each thermodenuder temperature was determined as the slope of the orthogonal fit of the TD mass concentration and the average ambient concentration of the six minutes before and after the TD cycle, forced through the origin.

A1.4 Other Instrumentation

In addition to SP-AMS, real-time measurements available during the intensive campaign also included: 1) VOC concentrations at 1 minute time resolution (Proton Transfer Reaction – Mass Spectrometer; Ionicon Analytik PTR-TOF-MS 4000), 2) NO_x concentration at 5 minute time resolution (2 Channel photolytic; Air Quality Design), 3) CO concentration at 5 time resolution (Picarro G2S02 Cavity Ring Down Spectrometer), 4) aerosol absorption at 467nm, 530nm and 660nm at 5 time resolution (Tricolor absorption photometer; Brechtel Manufacturing), 5) aerosol scattering at 450nm, 550nm and 700nm at 5 time resolution (TSI Model 3563 Nephelometer), and 6) aerosol number distribution between 14 and 615 nm at 5 minute time resolution (a scanning mobility particle sizer (SMPS) system consisted of a TSI 3082 electrostatic classifier with a TSI 3776 water based condensation particle counter). In addition, general meteorological data are available at 5 time resolution.

A1.5 Positive Matrix Factorization analysis

The SP-AMS data matrix was prepared for PMF analysis as laid out in Zhang et al., (2011)(Zhang et al., 2011). Included in the PMF analysis were HRMS for organic ions from *m/z* 12-140, unit mass resolution (UMR) signal from *m/z* 141-440 and major inorganic ions: SO^+, SO_2^+, HSO_2^+, SO_3^+, HSO_3^+, $H_2SO_4^+$ for sulfate, NO^+, NO_2^+ for nitrate, NH_3^+ for ammonium and C_2^+ for black carbon. Chloride was not included due to low S/N ratio. The organic mass concentration in each factor was determined as sum of the concentration of all organic fragments after applying the relative ionization efficiency correction. The one to six factor solutions were explored with varying rotational space (-1 < FPEAK < 1, increments of 0.2) and were analyzed based on the mass spectral features, diurnal profiles, and correlations with external tracers. The final PMF solutions consisted of four factors; a low volatility oxygenated OA (LV-OOA), a semi-volatile oxygenated OA (SV-OOA), BBOA, and a noise factor. The noise factor only consisted of 3.0% of the total signal, with 94% of this being at >140 amu. There were time periods during the campaign with decreased S/N at high m/z ions due to RF interference, and this factor was useful in segregating and removing these noisy periods. Moving from three to four factor solution showed decreased residual as the noise factor was resolved with little change in the concentrations or mass spectra of the other factors, while the five factor solution showed the splitting of OOA factors, with minimal decrease of residual. Details of the three and five factor solutions are shown in Fig. A6 and Fig. A7 and a summary of the PMF diagnostic plots for the four factor solution is presented in Fig. A8. The PMF solutions were stable upon exploration of rotational variation, and an Fpeak value of 0 was chosen as this had the minimum Q/Q_{exp}.

During BBOP, Zhou et al. (2017) observed that as BBOA ages, f_{60} and the volatility of the aerosols decreased and O/C ratio increased. The authors resolved three distinct BBOA factors using PMF which include a fresh, semivolatile BBOA-1 (O/C = 0.35; f_{60} = 2.2%), an intermediately oxidized BBOA-2 (O/C = 0.60; f_{60} = 1.1%), and a highly oxidized BBOA-3 (O/C = 1.06; f_{60} ~ 0.1%) (Zhang et al., 2018a; Zhou et al.,

2017). The BBOA factor resolved during MBO19 was highly oxidized, and showed characteristics intermediate of the BBOP BBOA 2 and BBOA 3. Comparisons of the ion intensities between the MBO19 factor and the three BBOP BBOA factors is shown in Figure A12. The $C_xH_y^+$ ion family, which is a marker for chemically reduced OA, accounted for 30% of the signal in the MBO19 BBOA spectrum (Fig. 2.3a). This value is consistent with the fraction (28.5%) seen in the moderately aged BBOA-2 factor of BBOP, but it is lower than the fractions seen in fresh BBOA factors, where the $C_xH_y^+$ family can account for 47-62% of the signal (Elser et al., 2016; Hu et al., 2016; Mohr et al., 2012; Saarikoski et al., 2012; Struckmeier et al., 2016; Zhou et al., 2017). The BBOA mass spectrum also showed a significant contribution from high molecular weight fragments ($f_{m/z>100}$ = 16.1%), which is a common spectral feature of BBOA. Consistently, the thermal profile of the BBOA factor of MBO19 also falls between those of BBOA-2 and BBOA-3 of BBOP (Fig. 2.3d). The average (± 1□) BBOA concentration was 0.30 (±0.60) μg sm^{-3}, which accounted for 18% of the total OA mass on average during this study.

The SV-OOA factor showed a strong diurnal pattern indicative of boundary layer (BL) dynamics (Fig. 2.2e). In addition, the spectral and diurnal features of SV-OOA are very similar to the boundary layer OOA (BL-OOA) factor identified during BBOP (Zhou et al., 2017) (Fig. A12). The largest precursors of SOA in remote locations are biogenically emitted VOCs, including isoprene and monoterpenes (Hallquist et al., 2009; Xu et al., 2015). The average (± 1□) daytime mixing ratios of isoprene and monoterpenes measured during MBO19 were 307 (±241) and 117 (±79.5) pptv, respectively. Indeed, the SV-OOA mass spectrum showed enhancement of the $C_5H_6O^+$ ion (*m/z* 82), a tracer for isoprene oxidation products (Robinson et al., 2011). The f_{C5H6O} of the factor (0.32%) is consistent with other ambient studies in isoprene and monoterpene influenced locations, and is above the background level of 0.18% (Hu et al., 2015). The thermogram for SV-OOA showed a rapid decrease between 50 and 150°C, indicating the semi-volatile nature of the factor. These results indicate that the SV-OOA factor may represent a moderately oxidized, BL-originated SOA with influence from biogenic precursors.

The LV-OOA factor was highly oxidized and the time series correlated tightly with sulfate (r^2 = 0.95) and peaked between 02:00-09:00 when MBO was located above the MBL (Fig. 2.2c, 2.2f). The LV-OOA concentration was low (average of 0.1 μg sm^{-3}) and relatively stable throughout the campaign. The thermogram of this factor showed little evaporation until 150°C suggesting it was mainly composed of low volatility compounds. However, unlike the BBOA factor, complete evaporation of the LV-OOA factor was seen at temperatures above 220°C. Overall, LV-OOA represents a highly oxidized, regional background aerosol and accounts for 6% of OA during MBO19.

A1.6 Back trajectory Analysis and Photochemical Age calculation

Backward air mass trajectories were calculated using the Hybrid Single Particle Integrated Trajectory (HYSPLIT) model (Draxler, 1998). 72-hour back-trajectories were run at 1 hour intervals using the Global Data Assimilation System (GDAS) meteorological data (ftp://arlftp.arlhq.noaa.gov/pub/archives/gdas1). The summit of Mt. Bachelor is located ~1500m above model ground level in GDAS, therefore this value was used as back-trajectory starting elevation (Ambrose et al., 2011). Physical age of BB plumes were estimated by comparing the back trajectories with satellite detected fires (Fig A17-A21). Photochemical age was calculated based on the dilution corrected decay of toluene (ΔToluene/ΔCO and ΔToluene/ΔBenzene; Fig A23). Toluene, benzene and CO are all primary emissions from combustion, however toluene has greater reactivity towards atmospheric OH and can therefore be used to determine the time since emission by comparing the measured enhancement ratio to a known emission ratio(Roberts et al., 1984).

Previous aircraft studies have found variable emission ratios of toluene relative to CO in ambient BB plumes. For examples, fresh sampled plumes during WE-CAN in the Western U.S. found an average ΔToluene/ΔCO of 1.23 pptv/ppbv and up to 1.62 ptv/ppbv with a strong dependence on MCE(Permar et al., 2021). In the laboratory, Koss et al., (2018) recorded ratios up to 1.91 pptv/ppbv depedent on fuel type(Koss et al., 2018). The higher ΔToluene/ΔCO seen in this campaign, even during aged

plumes, is intriguing. It is possible that the BB plumes mixed with fresh vehicle emissions, which have significantly higher ΔToluene/ΔCO(Borbon et al., 2013), but this is unlikely due to the strong correlations between toluene and BBOA during the plumes, as well as the remote location. More likely, the elevated ratio is due to mixing of BB plumes of different ages. Another well-established metric for photochemical age is ΔToluene/ΔBenzene. The use of this metric may be better as it may take into account the dependence on fuel type and MCE. Similarly to ΔToluene/ΔCO, the ΔToluene/ΔBenzene values seen during this campaign were higher than expected based on ambient and laboratory studies. Permar et al., (2021) reports an average of 0.66 pptv/pptv during the WE-CAN campaign, and Koss et al., 2018 reports 0.53 pptv/pptv during FIREX. During MBO19, much larger values were seen, up to 3.4 pptv/pptv.

Due to this variable emission ratio and unknown oxidant concentration we do not attempt to quantify the absolute photochemical age. Instead, we compare the plumes to each other to explore the changes in aerosol chemistry as a function of relative age. Overall, the three different aging metrics agreed reasonably well (Fig. A24), and ΔToluene/ΔCO was focused on due to the tighter correlation with physical age.

A2. Figures

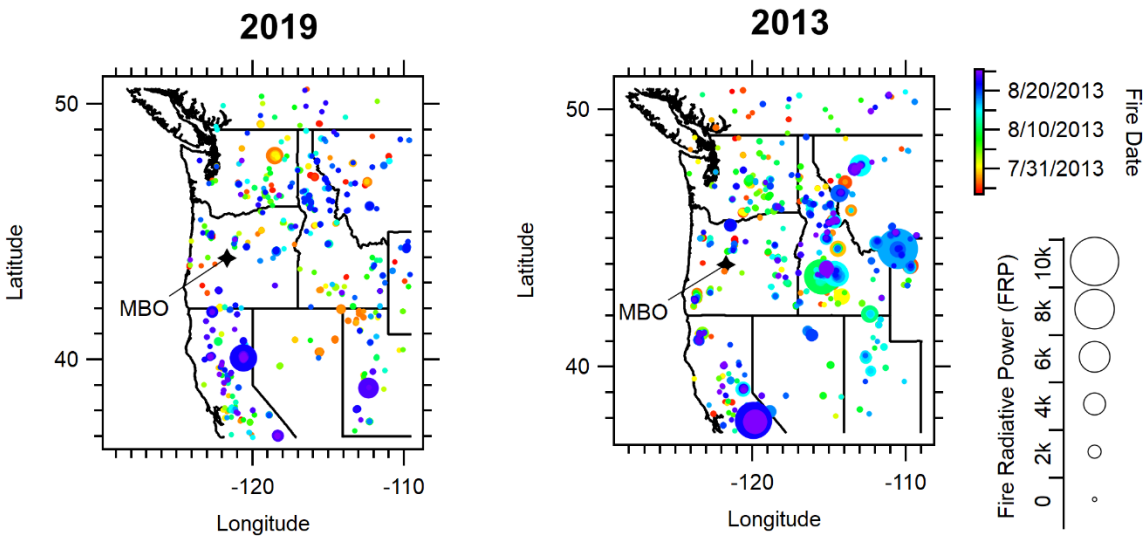

Figure A1: Comparison of MODIS satellite fire detections in the Pacific Northwest during the current study (left) and the 2013 BBOP study (right). Fire detections are colored by date, and sized by fire radiative power.

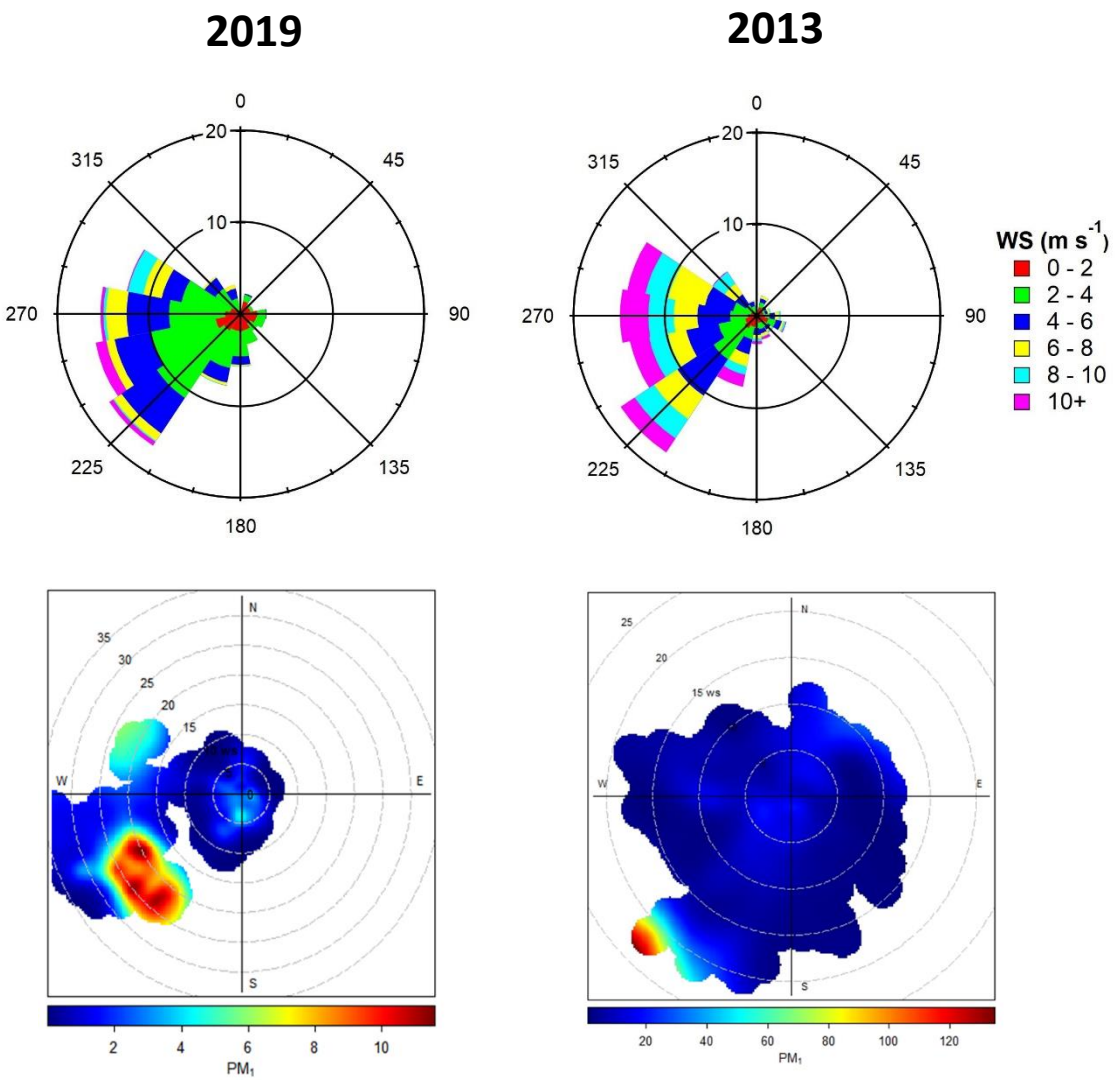

Figure A2: Wind roses (top) and bivariate polar plots (bottom) of PM_1 concentration in µg m^{-3} during the MBO19 campaign (left) and BBOP campaign (right). Notice different scale values on the polar plots.

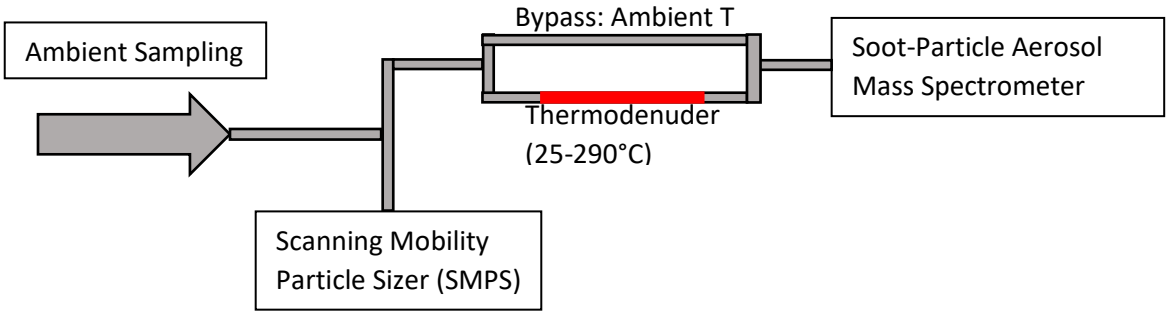

Figure A3: Schematic of sampling layout at Mt. Bachelor Observatory. Ambient air was sampled through a $PM_{2.5}$ cyclone. Flow was split between the SMPS and Thermodenuder/SP-AMS using a Brechtel flow splitter.

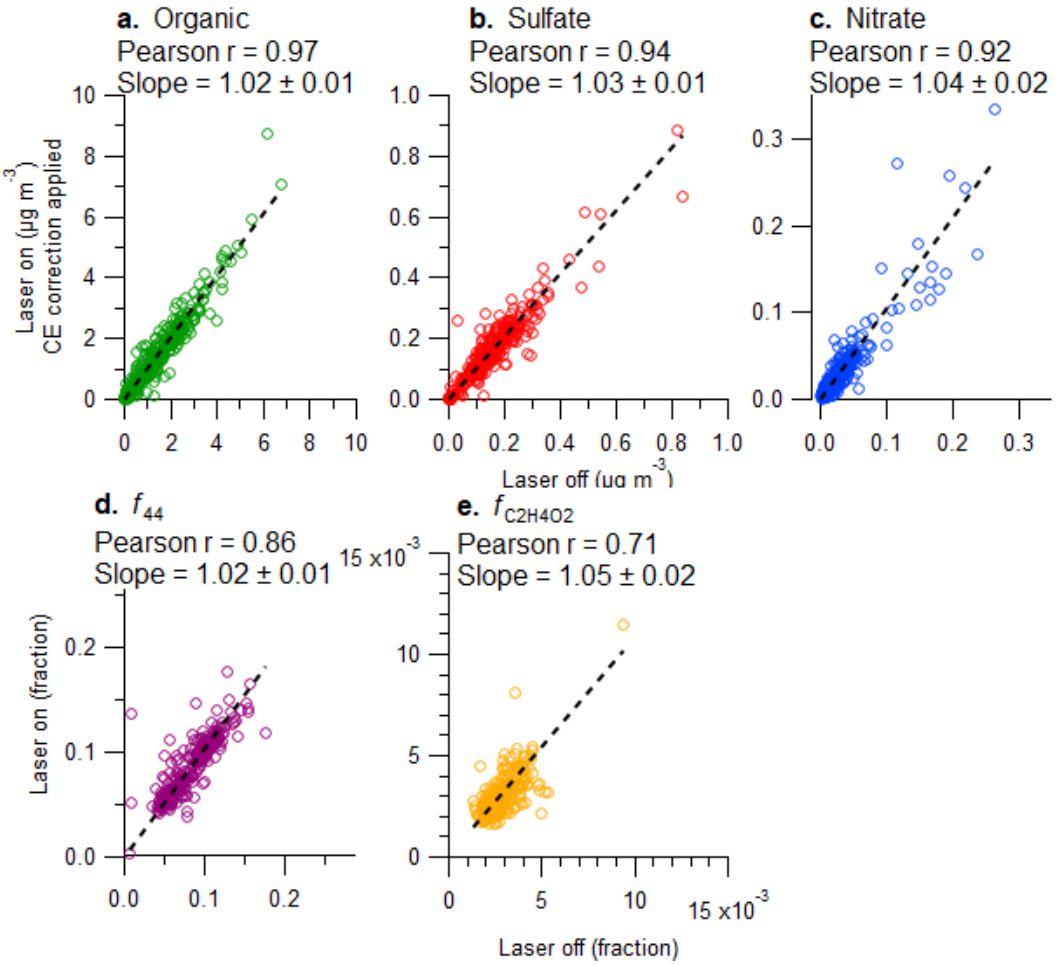

Figure A4: Comparison of laser on and laser off measurements after laser on collection efficiency correction factor has been applied. Plots show organics (a), sulfate (b), nitrate (c), f_{44} (d), f_{C2H4O2} (e). Determined from analysis of the high-resolution mass spectra. y-axis values are the average of 6 minutes immediately prior to laser turning off, or immediately following laser turning on. x-axis values are the average of 6 minutes immediately prior to laser turning on, or immediately following laser turning off. The slope was calculated using a orthogonal distance regression (±σ). Correction factor was found to be 1.25 for organics and 1.1 for inorganics. No correction was applied for f_{44} or f_{C2H4O2}.

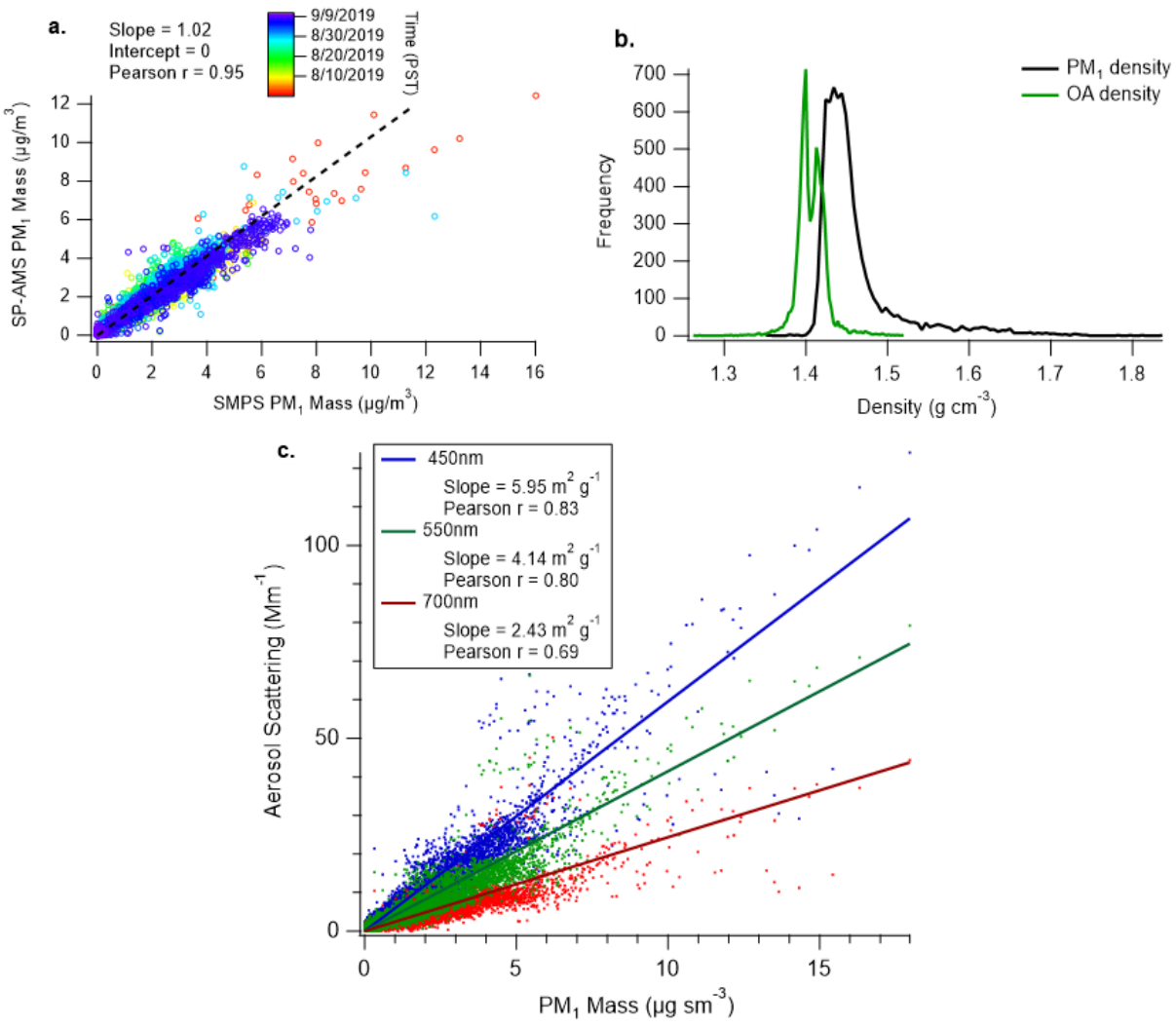

Figure A5: a. Comparison of PM_1 mass from SP-AMS and SMPS. Only periods with the SP laser on are included in this comparison, as the laser off periods will have a negative bias due to omission of rBC mass. SMPS aerosol mass is determined from the measured volume multiplied by the PM_1 composition dependent density based on SP-AMS speciation. The density of PM_1 was calculated using densities of ammonium sulfate (1.77 g cm^{-3}), ammonium nitrate (1.72 g cm^{-3}), and black carbon (BC, 1.8 g cm^{-3}). Time dependent density (g/cm^3) of OA was calculated using the following empirical relationship based on the elemental composition: (12+(H:C)+16(O:C)) / (7+5(H:C)+4.15(O:C)) (Kuwata et al., 2012). The frequency histogram of calculated PM_1 and OA densities is shown in b. Panel c shows the correlations between the aerosol mass scattering coefficient and PM_1 mass at three different wavelengths.

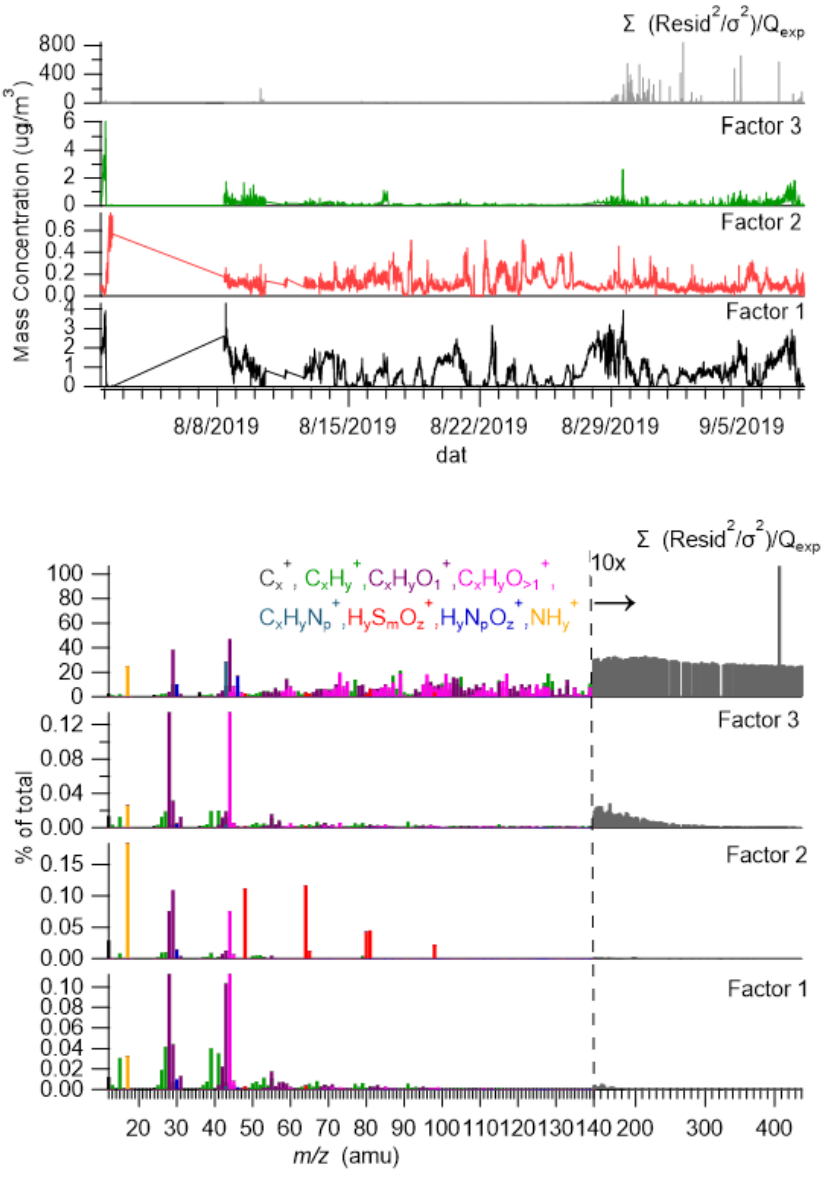

Figure A6: Factor time series and mass spectra of the three factor PMF solution.

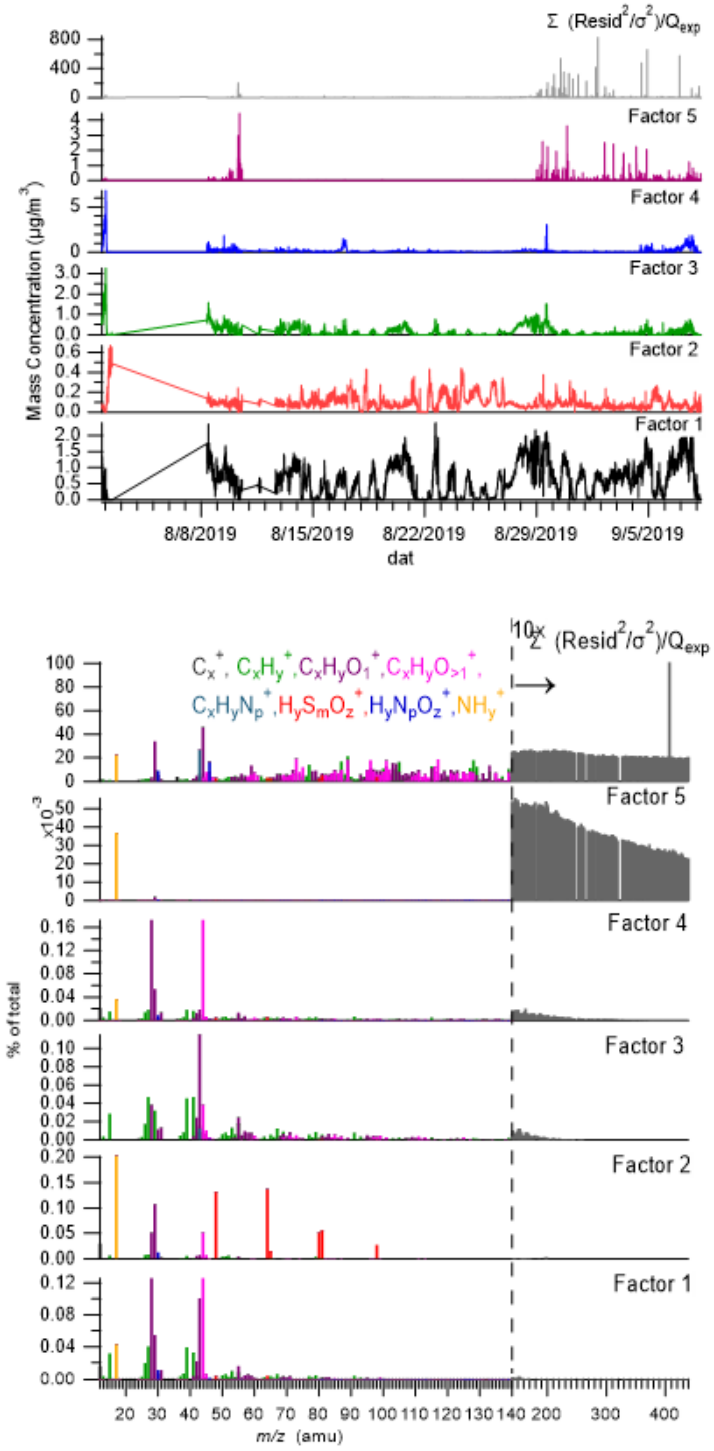

Figure A7: Factor time series and mass spectra of the five factor PMF solution.

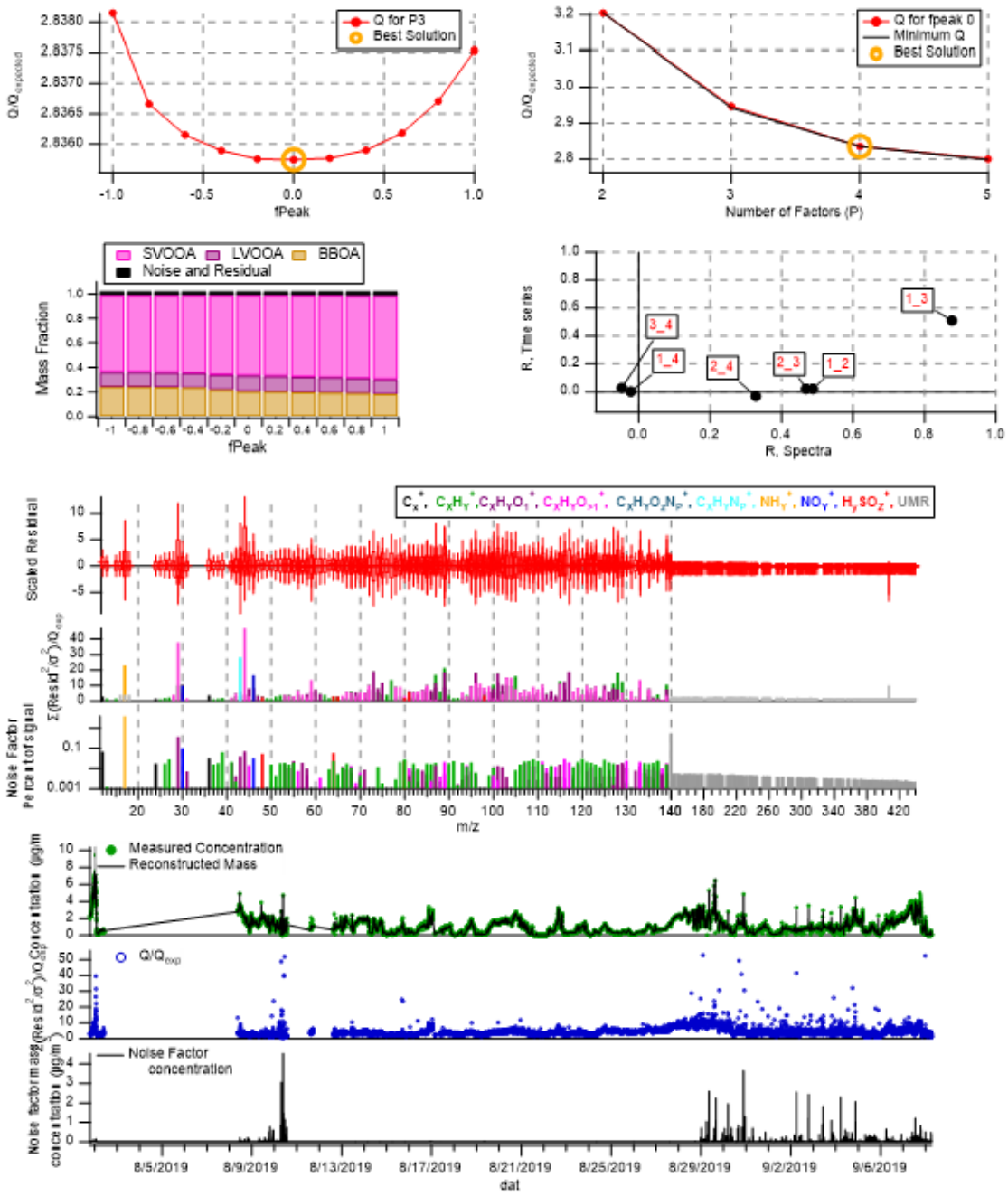

Figure A8: Key diagnostics for the four factor PMF solution. An fPeak value of 0 was chosen based on the local minimum of $Q/Q_{expected}$.

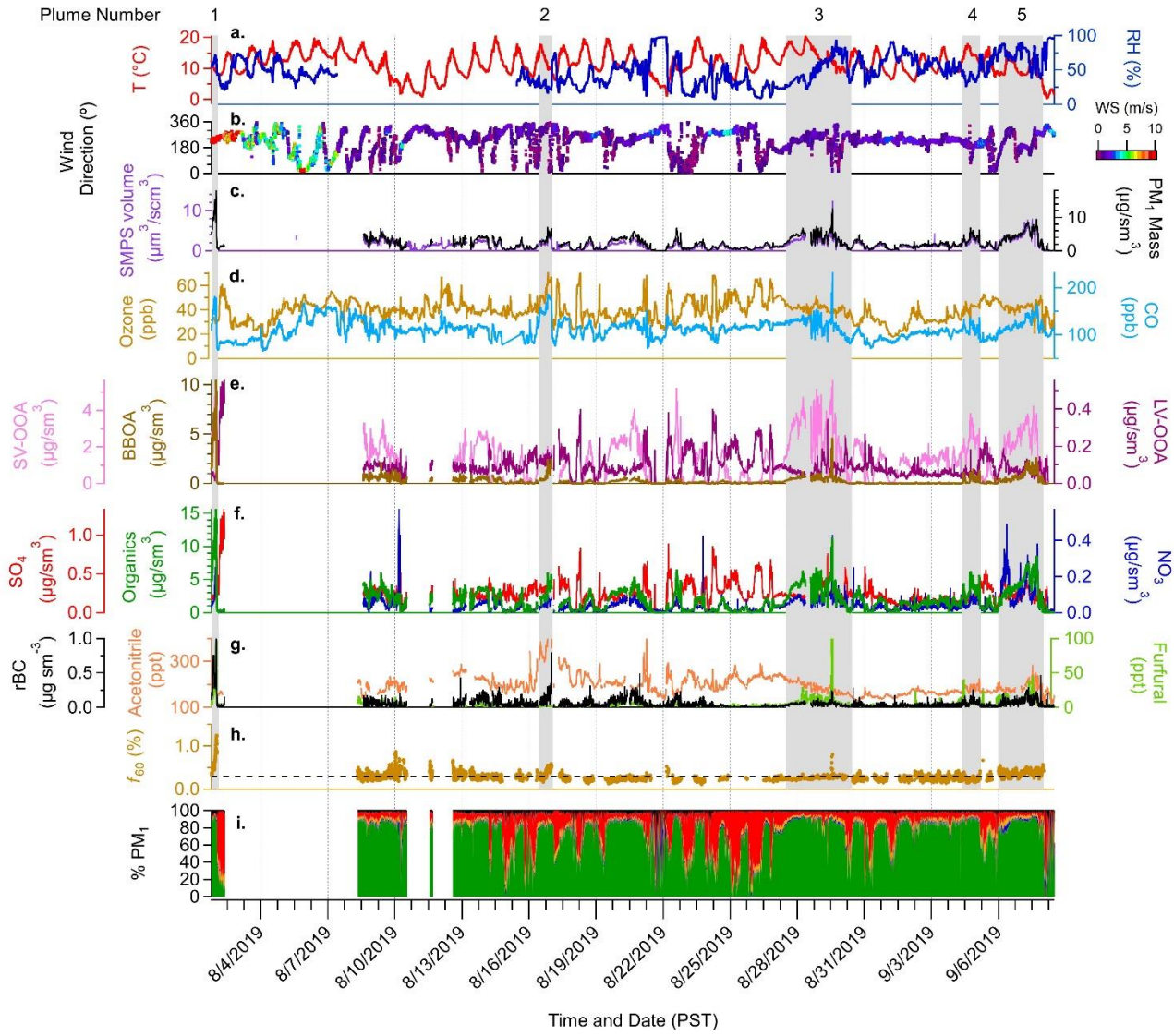

Figure A9: Time series of (a,b) meteorological conditions, (c) total SMPS and PM_1 concentration (d) gas phase species, (e) PMF factors, (f) organic, sulfate and nitrate concentration, (g) fraction of organic signal at *m/z* 60, corresponding to influence from anhydrous sugars. Dashed line corresponds to ambient background signal as described in Cubison et al., (2011). (h) Fractional contribution of each PM_1 species. Data gaps correspond to missing data due to instrument malfunctions, except in (g), where periods with low organic signal (<0.5μg m^{-3}) were also removed to reduce noise. Gray areas are plume periods defined in the text, and are numbered at the top

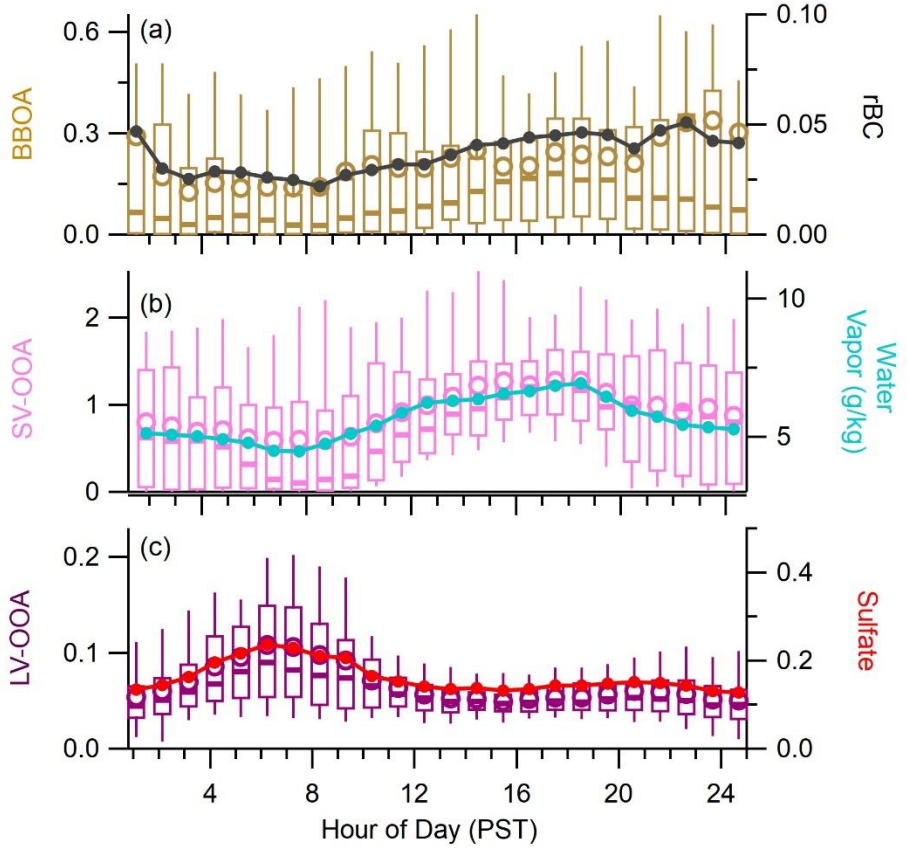

Figure A10: Diurnal variation of each OA factor. Whiskers denote 10th and 90th percentile, lower and upper bounds of the box denote 25th and 75th percentile. Lines and circles indicate the median and mean, respectively.

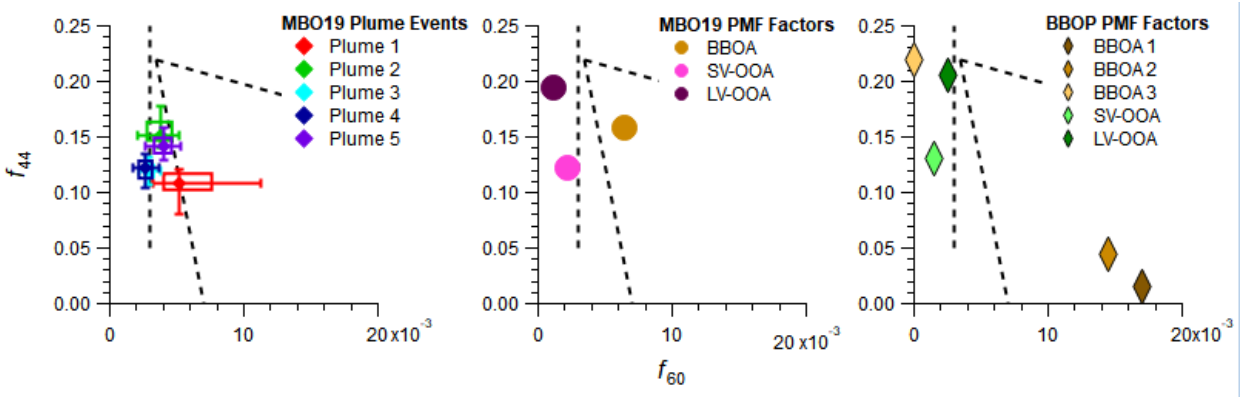

Figure A11: Similar to Figure 1b, however parameters are plotted separately to increase clarity.

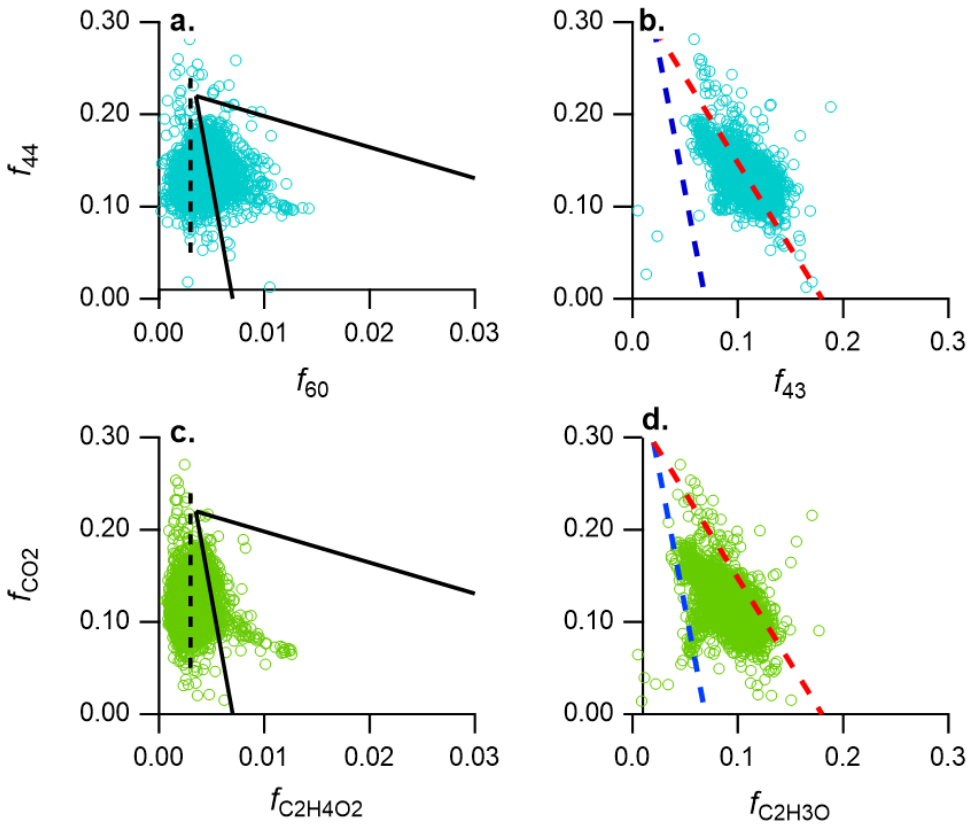

Figure A12: (a,b). Triangle plots showing fraction of signal at m/z 44 plotted against m/z 60 and m/z 43. On average, 94%, 87% and 95% of ion signal at m/z 44, 43 and 60 are due to CO_2^+, $C_2H_3O^+$ and $C_2H_4O_2^+$, respectively. The triangle plots only considering these major ions are shown in c. and d. Other isobaric ions include $C_2H_4O^+$ and $C_3H_8^+$ at m/z = 44, $C_3H_7^+$ at m/z = 43, and $C_3H_8O^+$ at m/z = 60.

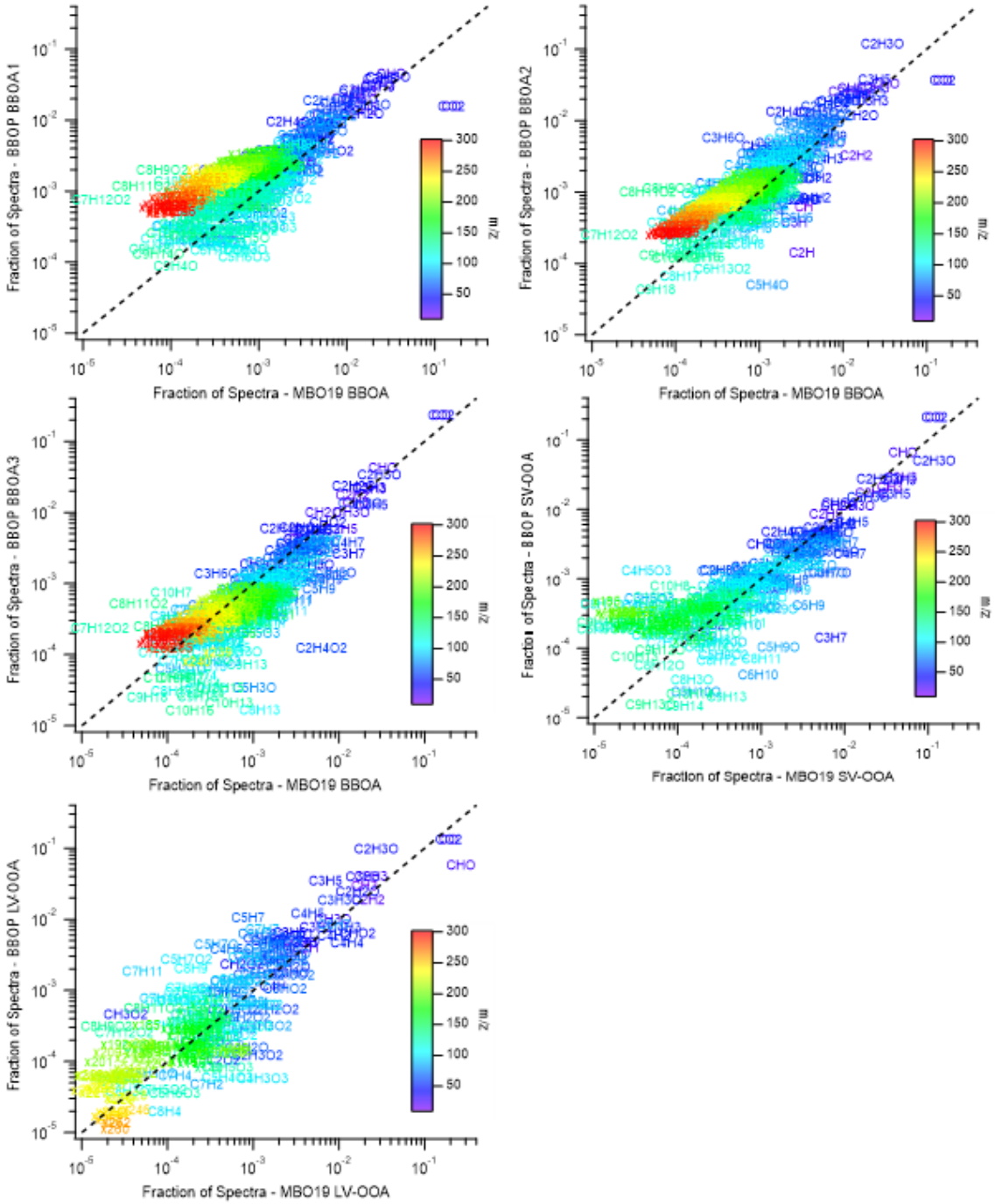

Figure A13: Comparisons of the PMF factors between the current (MBO19) study, and the 2013 BBOP study. All fragment between 12-300amu with fractional contribution $>10^{-5}$ in both studies are included. Fragments are color coded by molecular weight.

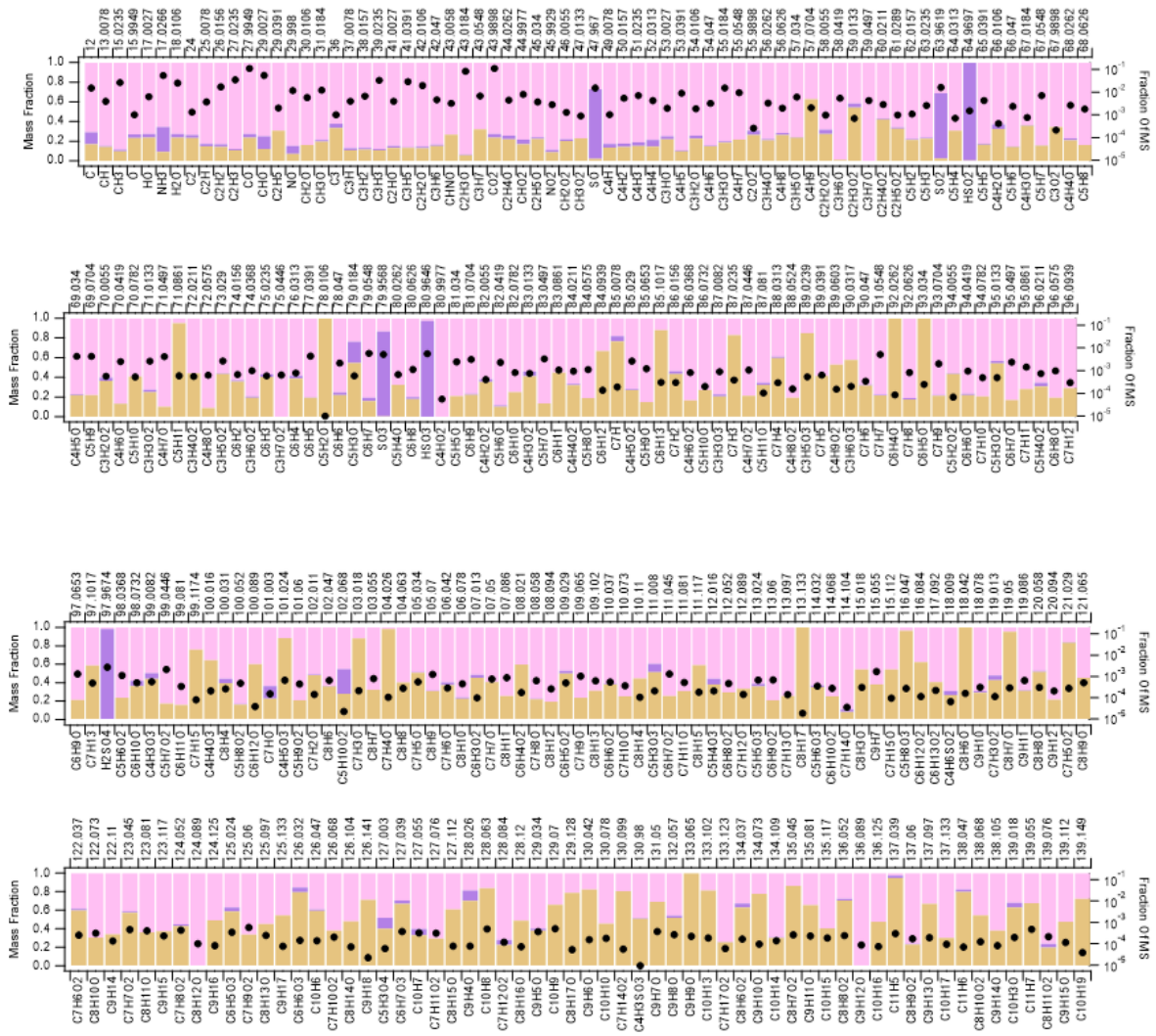

Figure A14: Mass fraction of ions included in PMF analysis attributed to each factor. Tan represents BBOA, Pink SV-OOA and Purple LV-OOA. Black dots show contribution of each ion to the average mass spectrum of the entire campaign.

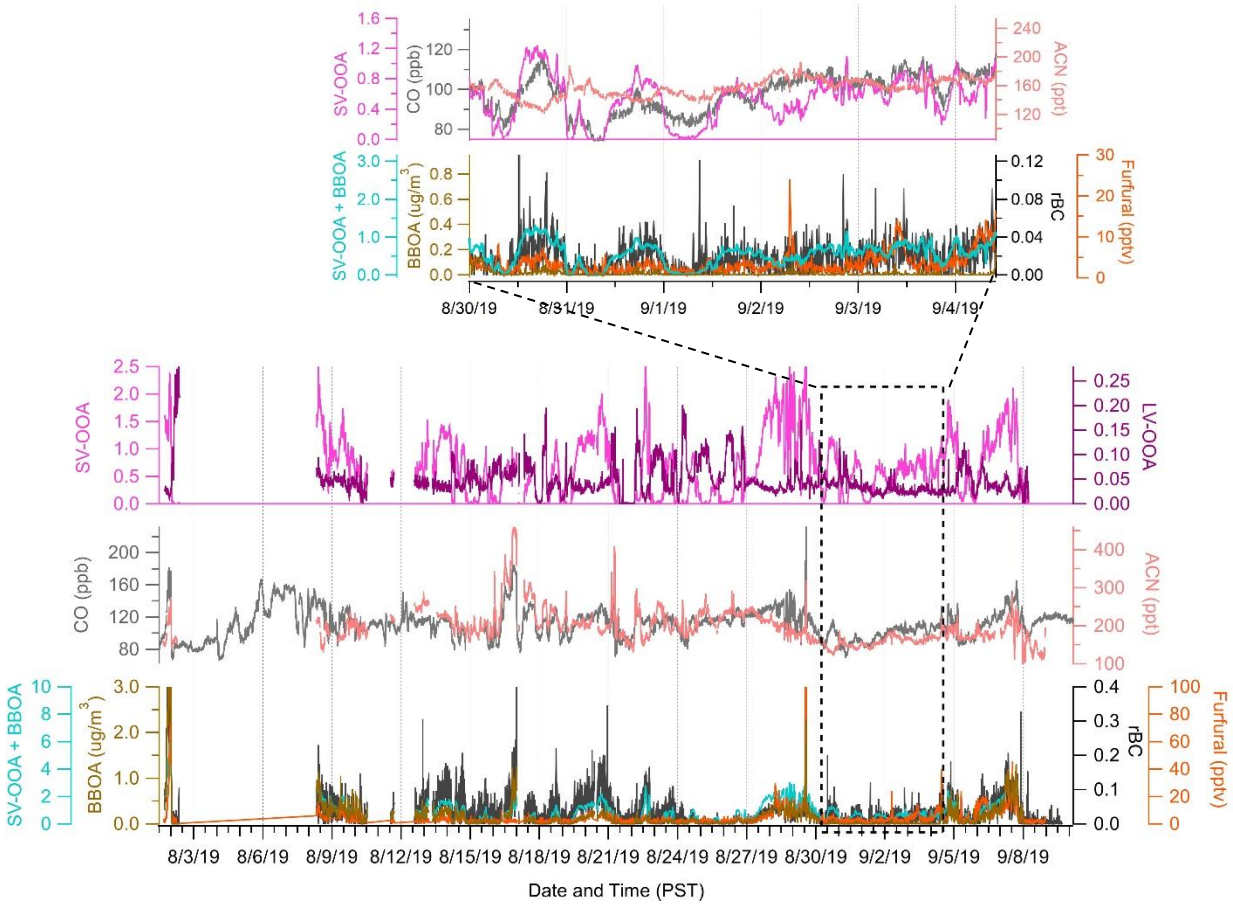

Figure A15: Time series comparison of PMF factors and BB tracer species.

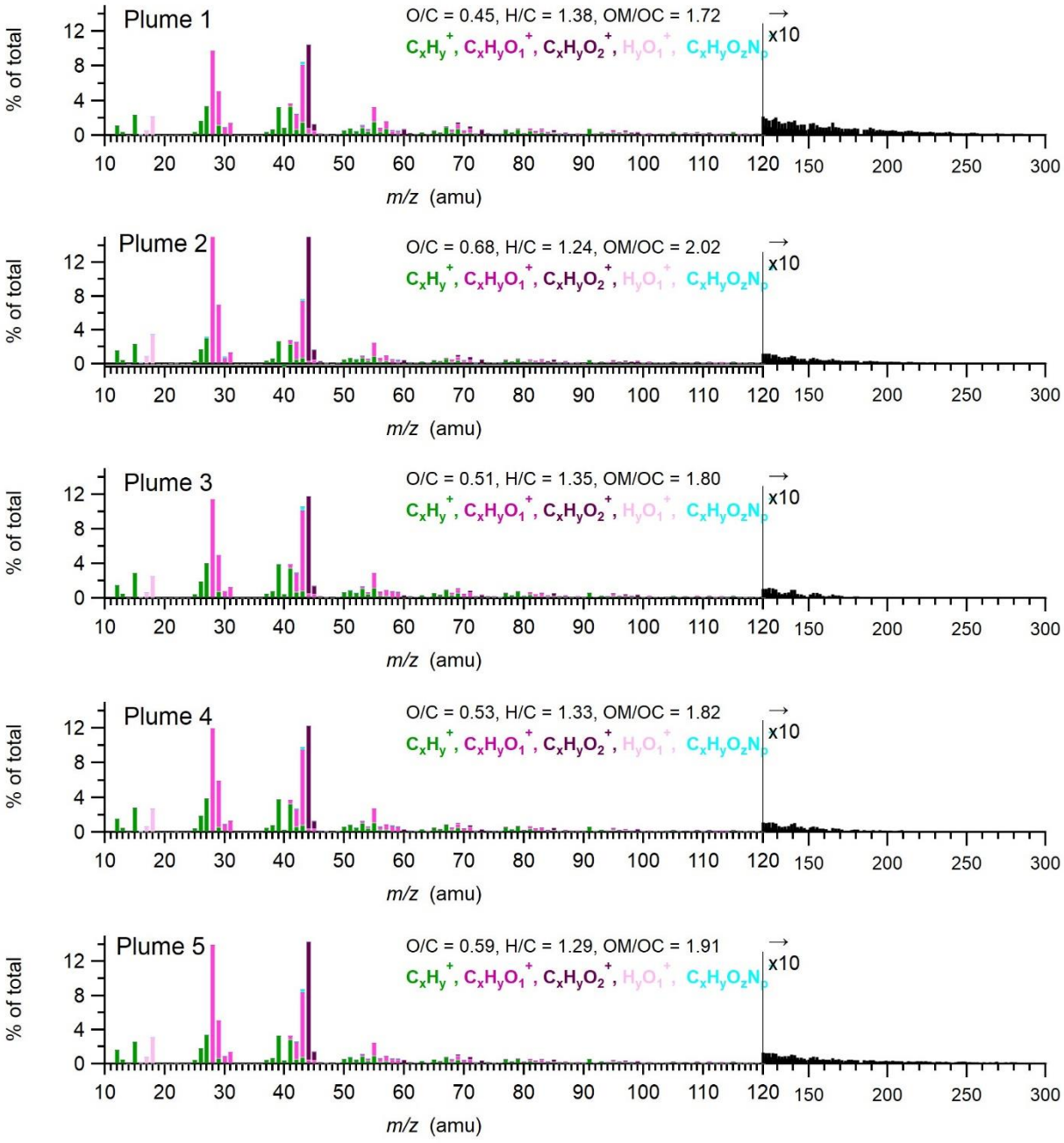

Figure A16: Average HR-MS spectra for each BB plume event.

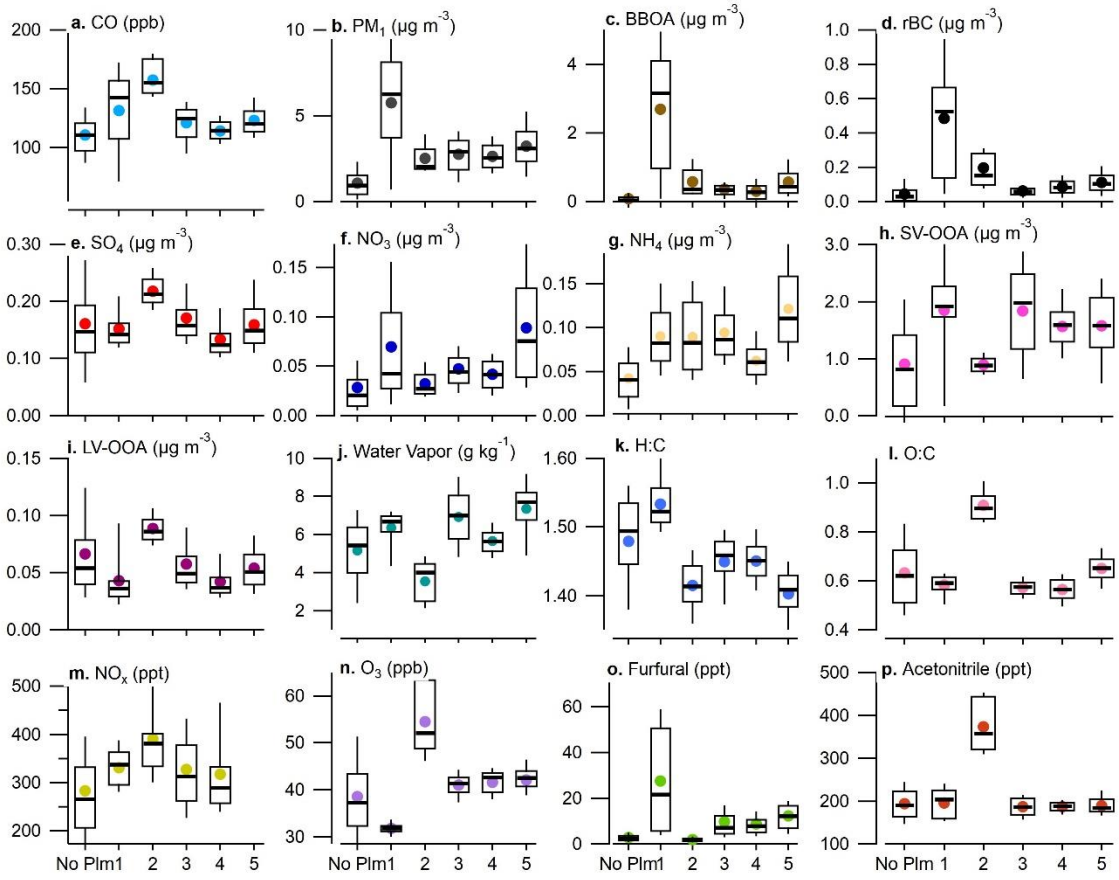

Figure A17: Box plot comparisons of key gas and particle phase species and parameters during each plume event. No Plm consists of all time points not included in one of the plumes, and still may have influence from biomass burning. Circle indicates the mean value, line indicates median value, and upper and lower bounds of the box indicates 25th – 75th percentile and whiskers indicate 10th-90th percentile.

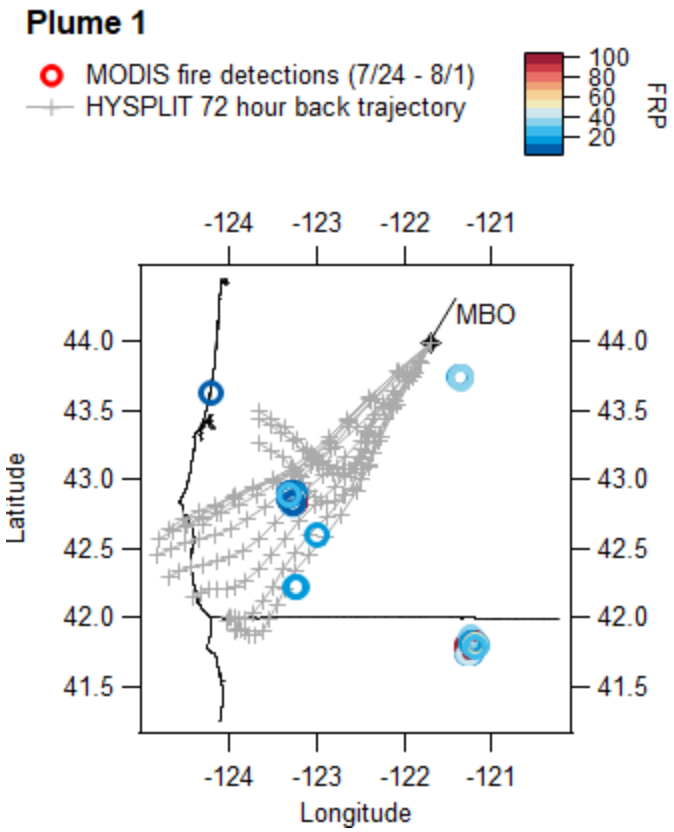

Figure A18: 72 hour HYSPLIT back trajectories initiated every hour for the duration of plume 1 with one symbol per hour.

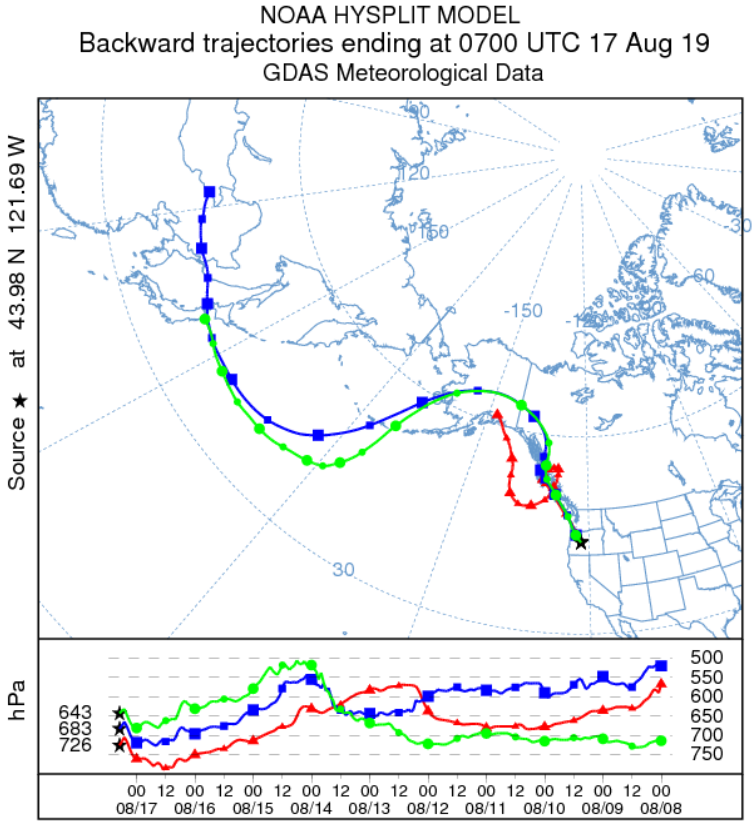

Figure A19: 10 day back trajectories for periods of peak PM_1 concentration during plume 2. The model is initialized at three different model heights: 1000m a.g.l (red trace), 1500m a.g.l. (blue trace) and 2000m a.g.l (green trace). Markers are placed at 12 hour intervals.

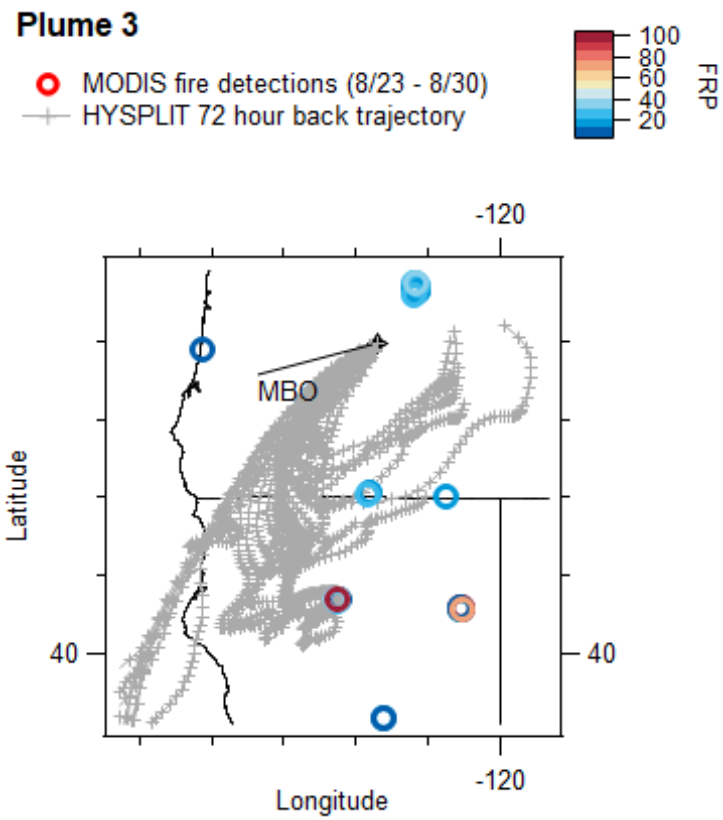

Figure A20: 72 hour HYSPLIT back trajectories initiated every hour for the duration of plume 3 with one symbol per hour.

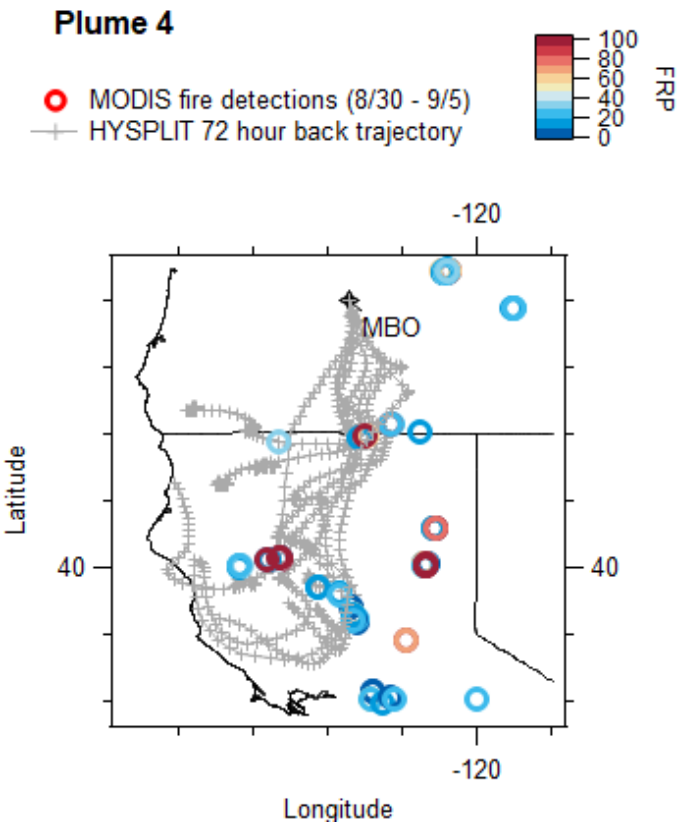

Figure A21: 72 hour HYSPLIT back trajectories initiated every hour for the duration of plume 4 with one symbol per hour.

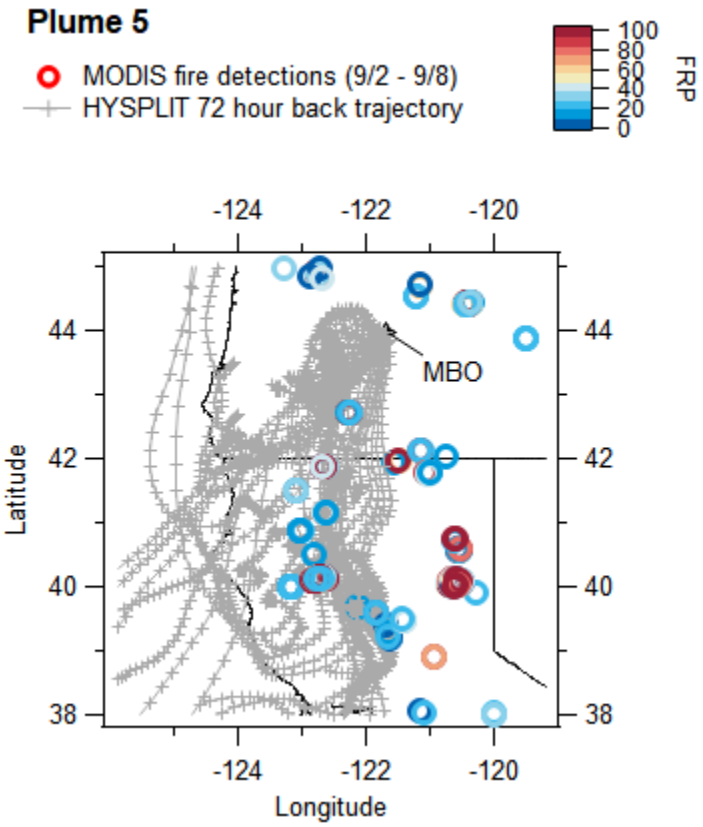

Figure A22: 72 hour HYSPLIT back trajectories initiated every hour for the duration of plume 5 with one symbol per hour

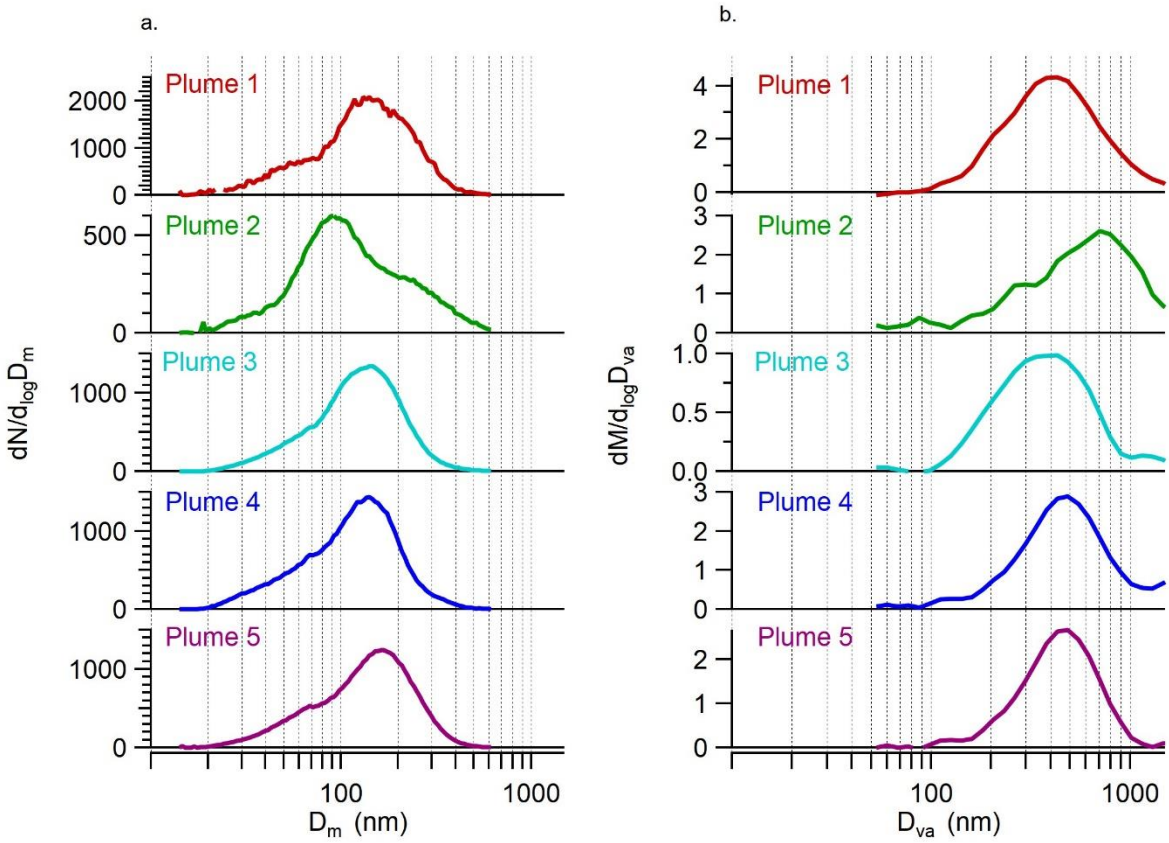

Figure A23: (a) Average number-based size distribution of PM_1 measured by SMPS and (b) average mass-based size distribution of organic aerosols measured by SP-AMS. Similar to Figure 5, but plotted separately to increase clarity.

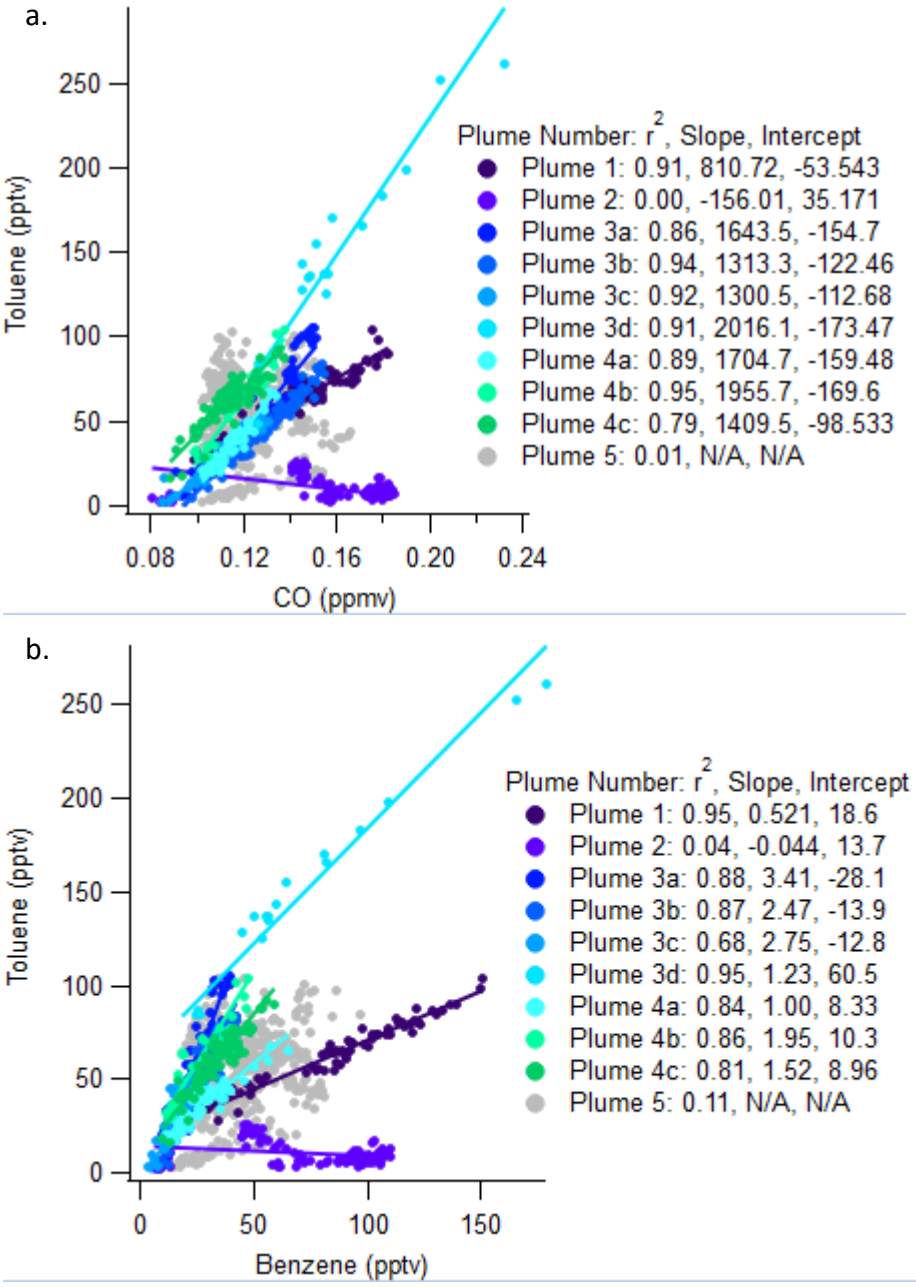

Figure A24: Scatterplots of (a) Toluene and CO and (b) Toluene and benzene. Trend lines are orthogonal distance regressions

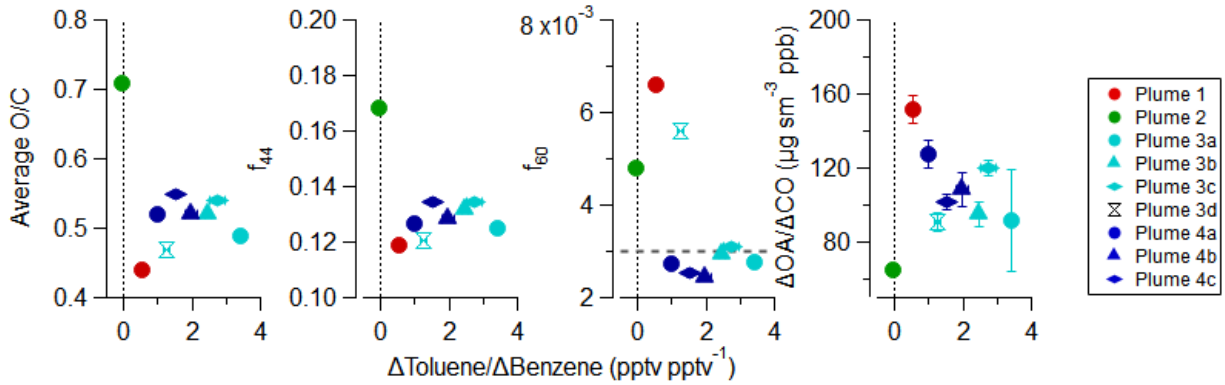

Figure A25: Similar to Figure 6, but using ΔToluene/ΔBenzene as photochemical age metric.

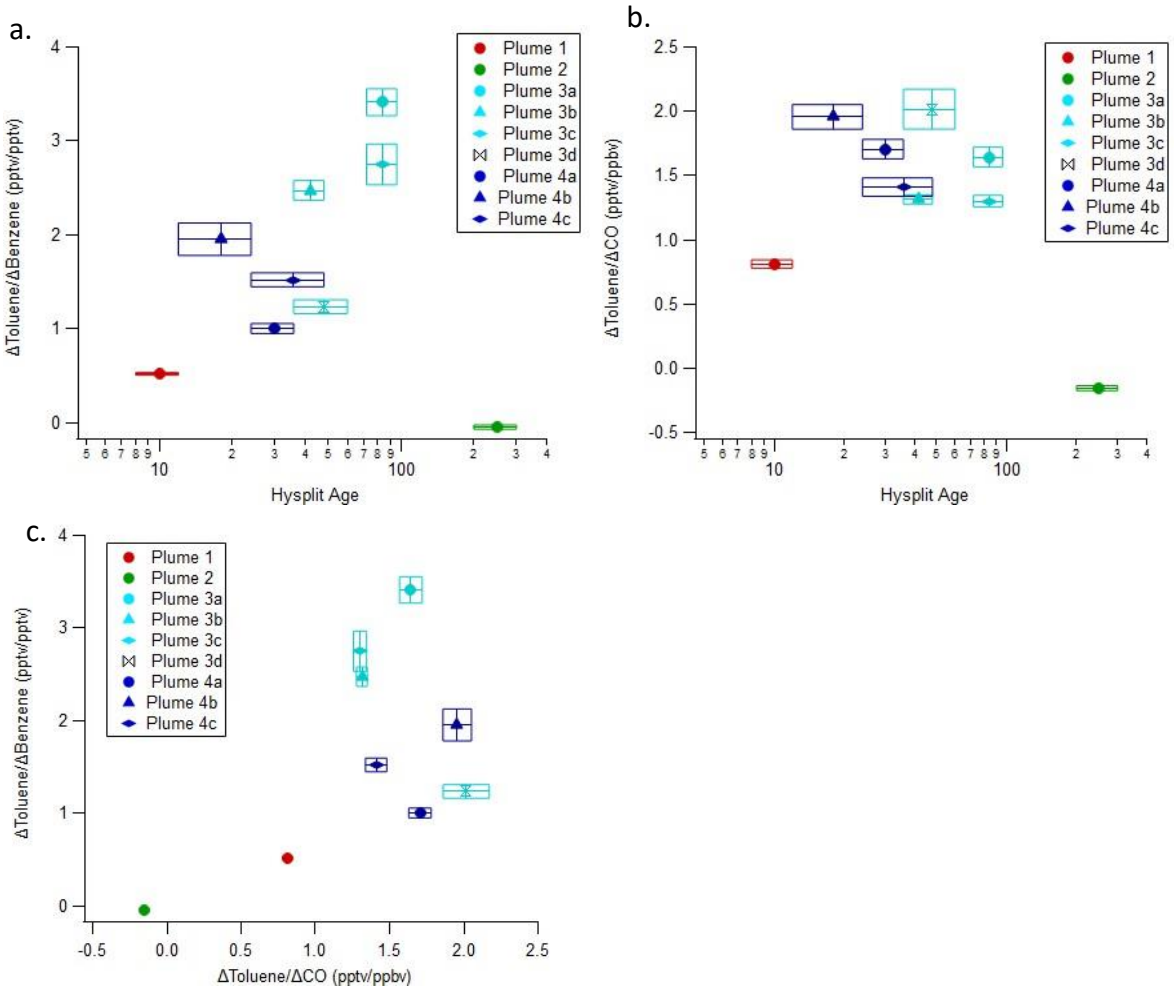

Figure A26: Intercomparison between physical age estimated from HYSPLIT analysis, and photochemical age calculated from toluene/CO and toluene/benzene

References

Ambrose, J. L., Reidmiller, D. R. and Jaffe, D. A.: Causes of high O3 in the lower free troposphere over the Pacific Northwest as observed at the Mt. Bachelor Observatory, Atmos. Environ., 45(30), 5302–5315, doi:10.1016/j.atmosenv.2011.06.056, 2011.

Avery, A. M., Williams, L. R., Fortner, E. C., Robinson, W. A. and Onasch, T. B.: Particle detection using the dual-vaporizer configuration of the soot particle Aerosol Mass Spectrometer (SP-AMS), Aerosol Sci. Technol., 55(3), 254–267, doi:10.1080/02786826.2020.1844132, 2020.

Borbon, A., Gilman, J. B., Kuster, W. C., Grand, N., Chevaillier, S., Colomb, A., Dolgorouky, C., Gros, V., Lopez, M., Holloway, J., Stutz, J., Petetin, H., Mckeen, S., Beekmann, M., Warneke, C., Parrish, D. D. and Gouw, J. A. De: Emission ratios of anthropogenic volatile organic compounds in northern mid-latitude megacities : Observations versus emission inventories in Los Angeles and Paris, J. Geophys. Res. Atmos., 118, 2041–2057, doi:10.1002/jgrd.50059, 2013.

Canagaratna, M. R., Jayne, J. T., Jimenez, J. L., Allan, J. D., Alfarra, M. R., Zhang, Q., Onasch, T. B., Drewnick, F., Coe, H., Middlebrook, A., Delia, A., Williams, L. R., Trimborn, A. M., Northway, M. J., DeCarlo, P. F., Kolb, C. E., Davidovits, P. and Worsnop, D. R.: Chemical and microphysical characterization of ambient aerosols with the aerodyne aerosol mass spectrometer, Mass Spectrom. Rev., 19(2), 173–181, doi:10.1002/mas.20115, 2007.

Elser, M., Huang, R., Wolf, R., Slowik, J. G., Wang, Q., Canonaco, F., Li, G., Bozzetti, C., Daellenbach, K. R., Huang, Y., Zhang, R., Li, Z., Cao, J., Baltensperger, U., El-haddad, I. and Prévôt, A. S. H.: New insights into PM 2 . 5 chemical composition and sources in two major cities in China during extreme haze events using aerosol mass spectrometry, Atmos. Chem. Phys., 3207–3225, doi:10.5194/acp-16-3207-2016, 2016.

Fierz, M., Vernooij, M. G. C. and Burtscher, H.: An improved low-flow thermodenuder, J. Aerosol Sci., doi:10.1016/j.jaerosci.2007.08.006, 2007.

Hallquist, M., Wenger, J. C., Baltensperger, U., Rudich, Y., Simpson, D., Claeys, M., Dommen, J., Donahue, N. M., George, C., Goldstein, A. H., Hamilton, J. F., Herrmann, H., Hoffmann, T., Iinuma, Y., Jang, M., Jenkin, M. E., Jimenez, J. L., Kiendler-Scharr, A., Maenhaut, W., McFiggans, G., Mentel, T. F., Monod, A., Prévôt, A. S. H., Seinfeld, J. H., Surratt, J. D., Szmigielski, R. and Wildt, J.: The formation, properties and impact of secondary organic aerosol: Current and emerging issues, Atmos. Chem. Phys., doi:10.5194/acp-9-5155-2009, 2009.

Hu, W., Hu, M., Hu, W., Jimenez, J. L., Yuan, B., Chen, W., Wang, M., Wu, Y., Chen, C., Wang, Z., Peng, J., Zeng, L. and Shao, M.: Chemical composition, sources, and aging process of submicron aerosols in beijing: Contrast between summer and winter, J. Geophys. Res. Atmos., 1955–1977, doi:10.1002/2015JD024020.Received, 2016.

Hu, W. W., Campuzano-Jost, P., Palm, B. B., Day, D. A., Ortega, A. M., Hayes, P. L., Krechmer, J. E., Chen, Q., Kuwata, M., Liu, Y. J., De Sá, S. S., McKinney, K., Martin, S. T., Hu, M., Budisulistiorini, S. H., Riva, M., Surratt, J. D., St. Clair, J. M., Isaacman-Van Wertz, G., Yee, L. D., Goldstein, A. H., Carbone, S., Brito, J., Artaxo, P., De Gouw, J. A., Koss, A., Wisthaler, A., Mikoviny, T., Karl, T., Kaser, L., Jud, W., Hansel, A., Docherty, K. S., Alexander, M. L., Robinson, N. H., Coe, H., Allan, J. D., Canagaratna, M. R., Paulot, F. and Jimenez, J. L.: Characterization of a real-time tracer for isoprene epoxydiols-derived secondary organic aerosol (IEPOX-SOA) from aerosol mass spectrometer measurements, Atmos. Chem. Phys., doi:10.5194/acp-15-11807-2015, 2015.

Jayne, J. T., Leard, D. C., Zhang, X., Davidovits, P., Smith, K. A., Kolb, C. E. and Worsnop, D. R.: Development of an aerosol mass spectrometer for size and composition analysis of submicron particles, Aerosol Sci. Technol., doi:10.1080/027868200410840, 2000.

Koss, A. R., Sekimoto, K., Gilman, J. B., Selimovic, V., Coggon, M. M., Zarzana, K. J., Yuan, B., Lerner, B. M., Brown, S. S., Jimenez, J. L., Krechmer, J., Roberts, J. M., Warneke, C., Yokelson, R. J. and De Gouw, J.: Non-methane organic gas emissions from biomass burning: Identification, quantification, and emission factors from PTR-ToF during the FIREX 2016 laboratory experiment, Atmos. Chem. Phys., 18(5), 3299–3319, doi:10.5194/acp-18-3299-2018, 2018.

Kuwata, M., Zorn, S. R. and Martin, S. T.: Using elemental ratios to predict the density of organic material composed of carbon, hydrogen, and oxygen, Environ. Sci. Technol., 46(2), 787–794, doi:10.1021/es202525q, 2012.

Laing, J. R., Jaffe, D. A. and Hee, J. R.: Physical and optical properties of aged biomass burning aerosol from wildfires in Siberia and the Western USA at the Mt . Bachelor Observatory, Atmos. Chem. Phys., 15185–15197, doi:10.5194/acp-16-15185-2016, 2016.

Matthew, B. M., Middlebrook, A. M. and Onasch, T. B.: Collection efficiencies in an aerodyne aerosol mass spectrometer as a function of particle phase for laboratory generated aerosols, Aerosol Sci. Technol., 42(11), 884–898, doi:10.1080/02786820802356797, 2008.

Mohr, C., Decarlo, P. F., Heringa, M. F., Chirico, R., Slowik, J. G., Richter, R., Reche, C., Alastuey, A., Querol, X., Seco, R., Crippa, M., Zimmermann, R., Baltensperger, U., Barcelona, D., Munchen, H. Z. and Mass, J.: Identification and quantification of organic aerosol from cooking and other sources in Barcelona using aerosol mass spectrometer data, Atmos. Chem. Phys., 1649–1665, doi:10.5194/acp-12-1649-2012, 2012.

Onasch, T. B., Trimborn, A., Fortner, E. C., Jayne, J. T., Kok, G. L., Williams, L. R., Davidovits, P. and Worsnop, D. R.: Soot particle aerosol mass spectrometer: Development, validation, and initial application, Aerosol Sci. Technol., doi:10.1080/02786826.2012.663948, 2012.

Permar, W., Wang, Q., Selimovic, V., Wielgasz, C., Yokelson, R. J., Hornbrook, R. S., Hills, A. J., Apel, E. C., Ku, I. T., Zhou, Y., Sive, B. C., Sullivan, A. P., Collett, J. L., Campos, T. L., Palm, B. B., Peng, Q., Thornton, J. A., Garofalo, L. A., Farmer, D. K., Kreidenweis, S. M., Levin, E. J. T., DeMott, P. J., Flocke, F., Fischer, E. V. and Hu, L.: Emissions of Trace Organic Gases From Western U.S. Wildfires Based on WE-CAN Aircraft Measurements, J. Geophys. Res. Atmos., 126(11), 1–29, doi:10.1029/2020JD033838, 2021.

Reid, J. S., Eck, T. F., Christopher, S. A., Koppmann, R., Dubovik, O., Eleuterio, D. P., Holben, B. N., Reid, E. A. and Zhang, J.: A review of biomass burning emissions part III: intensive optical properties of biomass burning particles, Atmos. Chem. Phys. Discuss., 4(5), 5201–5260, doi:10.5194/acpd-4-5201-2004, 2004.

Roberts, J. M., Fehsenfeld, F. C., Liu, S. C., Bollinger, M. J., Hahn, C., Albritton, D. L. and Sievers, R. E.: Measurements of aromatic hydrocarbon ratios and NOx concentrations in the rural troposphere: Observation of air mass photochemical aging and NOx removal, Atmos. Environ., 18(11), 2421–2432, doi:10.1016/0004-6981(84)90012-X, 1984.

Robinson, N. H., Hamilton, J. F., Allan, J. D., Langford, B., Oram, D. E., Chen, Q., Docherty, K., Farmer, D. K., Jimenez, J. L., Ward, M. W., Hewitt, C. N., Barley, M. H., Jenkin, M. E., Rickard, A. R., Martin, S. T., McFiggans, G. and Coe, H.: Evidence for a significant proportion of secondary organic aerosol from isoprene above a maritime tropical forest, Atmos. Chem. Phys., 11(3), 1039–1050, doi:10.5194/acp-11-1039-2011, 2011.

Saarikoski, S., Carbone, S., Decesari, S., Giulianelli, L., Angelini, F., Canagaratna, M., Ng, N. L. and Trimborn, A.: Chemical characterization of springtime submicrometer aerosol in Po Valley , Italy, Atmos. Chem. Phys., 8401–8421, doi:10.5194/acp-12-8401-2012, 2012.

Struckmeier, C., Drewnick, F., Fachinger, F., Gobbi, G. P. and Borrmann, S.: Atmospheric aerosols in Rome , Italy : sources , dynamics and spatial variations during two seasons, Atmos. Chem. Phys., 15277–15299, doi:10.5194/acp-16-15277-2016, 2016.

Xu, L., Suresh, S., Guo, H., Weber, R. J. and Ng, N. L.: Aerosol characterization over the southeastern United States using high-resolution aerosol mass spectrometry: Spatial and seasonal variation of aerosol composition and sources with a focus on organic nitrates, Atmos. Chem. Phys., 15(13), doi:10.5194/acp-15-7307-2015, 2015.

Zhang, Q., Jimenez, J. L., Canagaratna, M. R., Ulbrich, I. M., Ng, N. L., Worsnop, D. R. and Sun, Y.: Understanding atmospheric organic aerosols via factor analysis of aerosol mass spectrometry: A review, Anal. Bioanal. Chem., doi:10.1007/s00216-011-5355-y, 2011.

Zhang, Q., Zhou, S., Collier, S., Jaffe, D., Onasch, T., Shilling, J., Kleinman, L. and Sedlacek, A.: Understanding composition, formation, and aging of organic aerosols in wildfire emissions via combined mountain top and airborne measurements, ACS Symp. Ser., 1299, 363–385, doi:10.1021/bk-2018-1299.ch018, 2018.

Zhou, S., Collier, S., Jaffe, D. A., Briggs, N. L., Hee, J., Iii, A. J. S., Kleinman, L., Onasch, T. B. and Zhang, Q.: Regional influence of wildfires on aerosol chemistry in the western US and insights into atmospheric aging of biomass burning organic aerosol, Atmos. Chem. Phys., 17(3), doi:10.5194/acp-17-2477-2017, 2017.

Appendix B: Supplementary Material for Chemical Transformations of Biomass Burning Organic Aerosol within Wildfire Plumes - From Near-source to the Regional Scale

B1. Positive Matrix Factorization Analysis

Positive Matrix Factorization analysis was performed using the high-resolution mass spectral (HRMS) ions between 12-150 amu. Ions that had low S/N or were not included in the BBOA-3 factor were removed resulting in 332 ions. PMF was run independently for each of the G1 research flights and the number of factors was selected based on the temporal and spectral features. For each analysis, one factor was constrained to the BBOA-3 factor identified in Zhou et al (2017) using an *a*-value of 0 (Canonaco et al., 2013). Here we assume that this mass spectrum is representative of processed BBOA in the Pacific Northwest and is independent of variations between different wildfires. If the *a*-value is increased, the mass spectrum shows signatures of fresh BBOA, indicating it no longer represents processed emissions.

A three factor solution was identified for G1-0821b and G1-0806 and a four factor solution was identified for G1-0730b. For G1-0821b and G1-0806, these three factors correspond with fresh, aged and highly aged BBOA. Increasing from two to three factors results in a decrease in Q/Q_{exp} and residual, while moving to four factors results in non-meaningful splitting. For G1-0730b, a second, fresh BBOA factor is necessary to explain the variation in the aerosol composition.

B2. Identification of Wildfire Fuel Types

High resolution (30m x 30m resolution) vegetation maps were downloaded from Landscape Fire and Resource Management Planning Tools (https://landfire.gov/). Vegetation type from 2001 was used as all other periods were conducted after 2013, and were influenced by vegetation loss from the fire. The Colockum Tarps fire (G1-0730b) was dominated by shrubland and grassland type ecosystems (Table B1, Fig. B7) primarily corresponding to sagebrush and bluebunch wheatgrass. In contrast, the Government Flats fire (G1-0821b) was dominated by closed and open tree canopies, that were primarily

conifers including Grand Fir and Ponderosa Pine (Fig. B8). Fire plumes from G1-0806 and the MBO site are more difficult to analyze fuel type, as they likely encompass a mixture of emissions from different fires. Table B1 shows the fuel types during the three major fires that influenced these sites: Salmon River complex, Whisky Creek complex and Douglas Complex. We assume that the emissions sampled are a mixture of all three fires. All three of these fires were dominated by closed and open tree canopy ecosystems, primarily featuring mixed conifer forests (Douglas fir, Ponderosa pine, Sugar pine, California Black Oak) and Douglas fir-Western Hemlock.

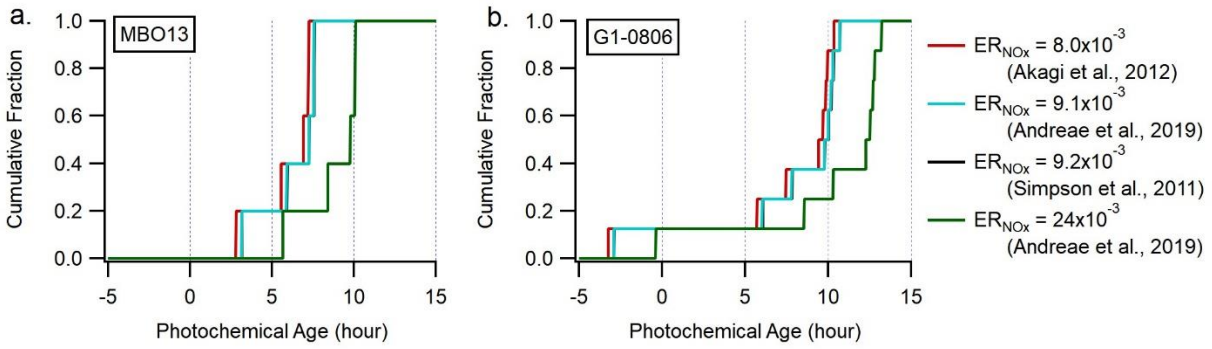

Figure B1: Sensitivity analysis of using different initial NO_x/CO values for (a) MBO13 plumes and (b) G1-0806 plumes

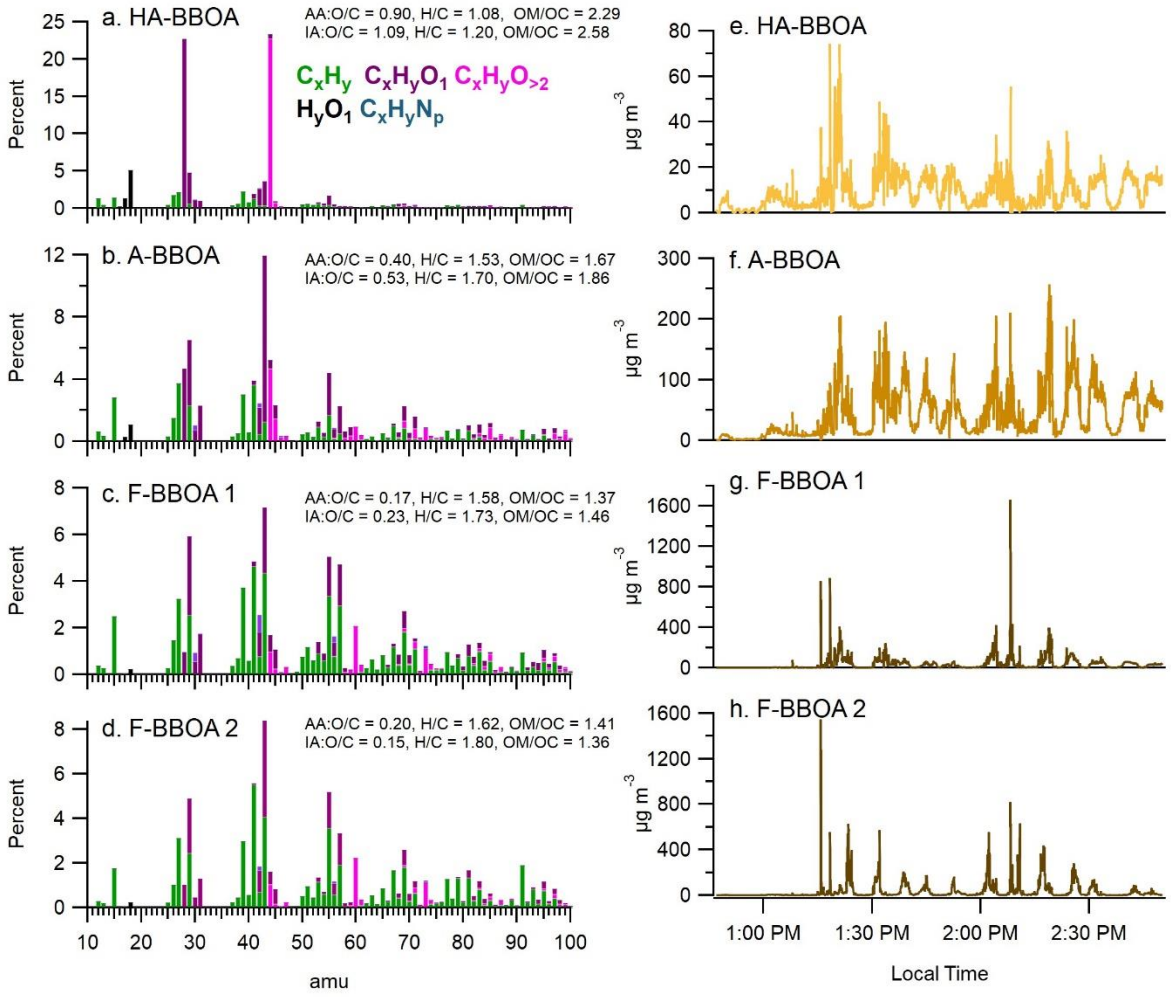

Figure B2: PMF spectra and time series of OA factors for G1-0730b

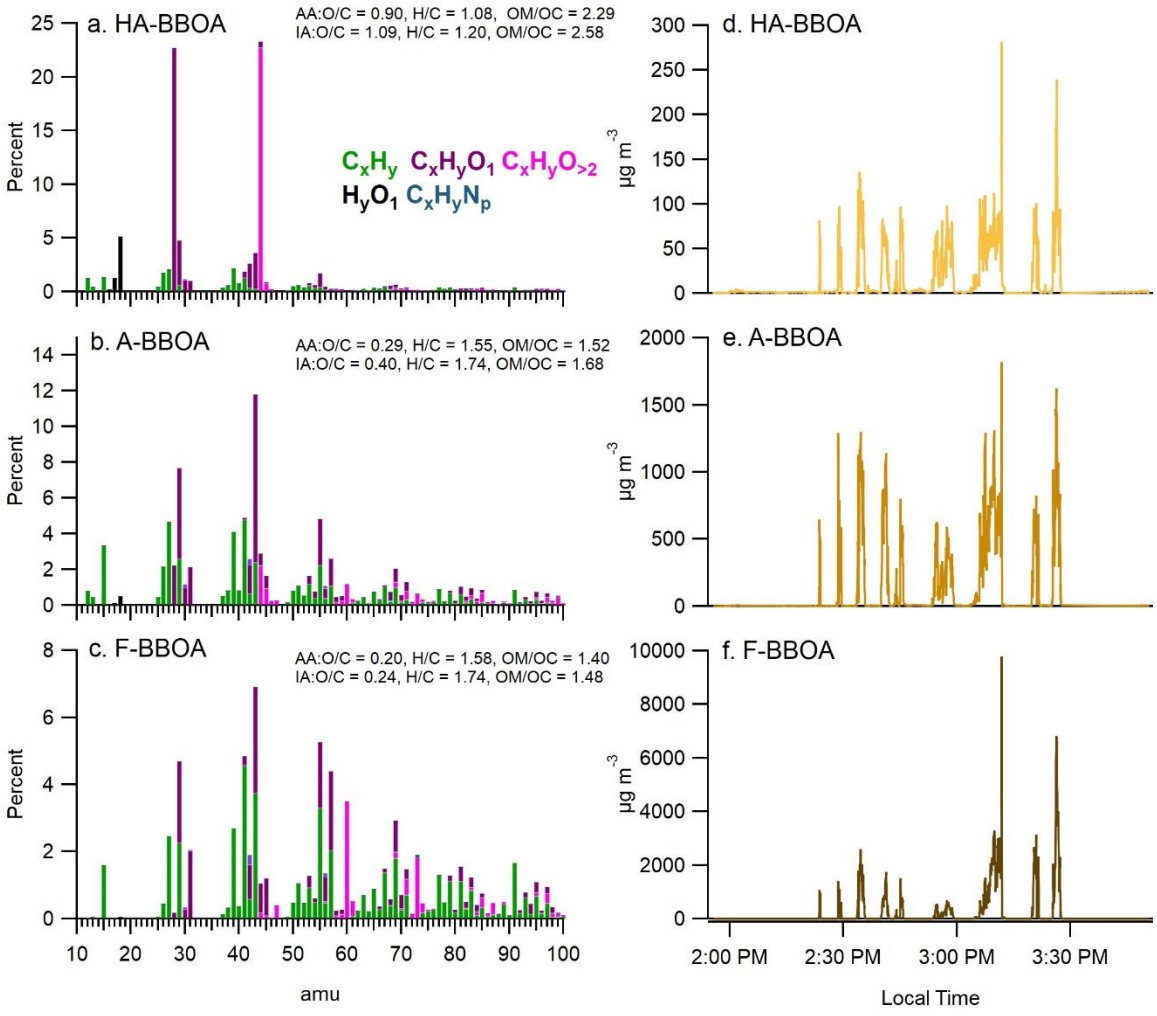

Figure B3: PMF spectra and time series of OA factors for G1-0821b

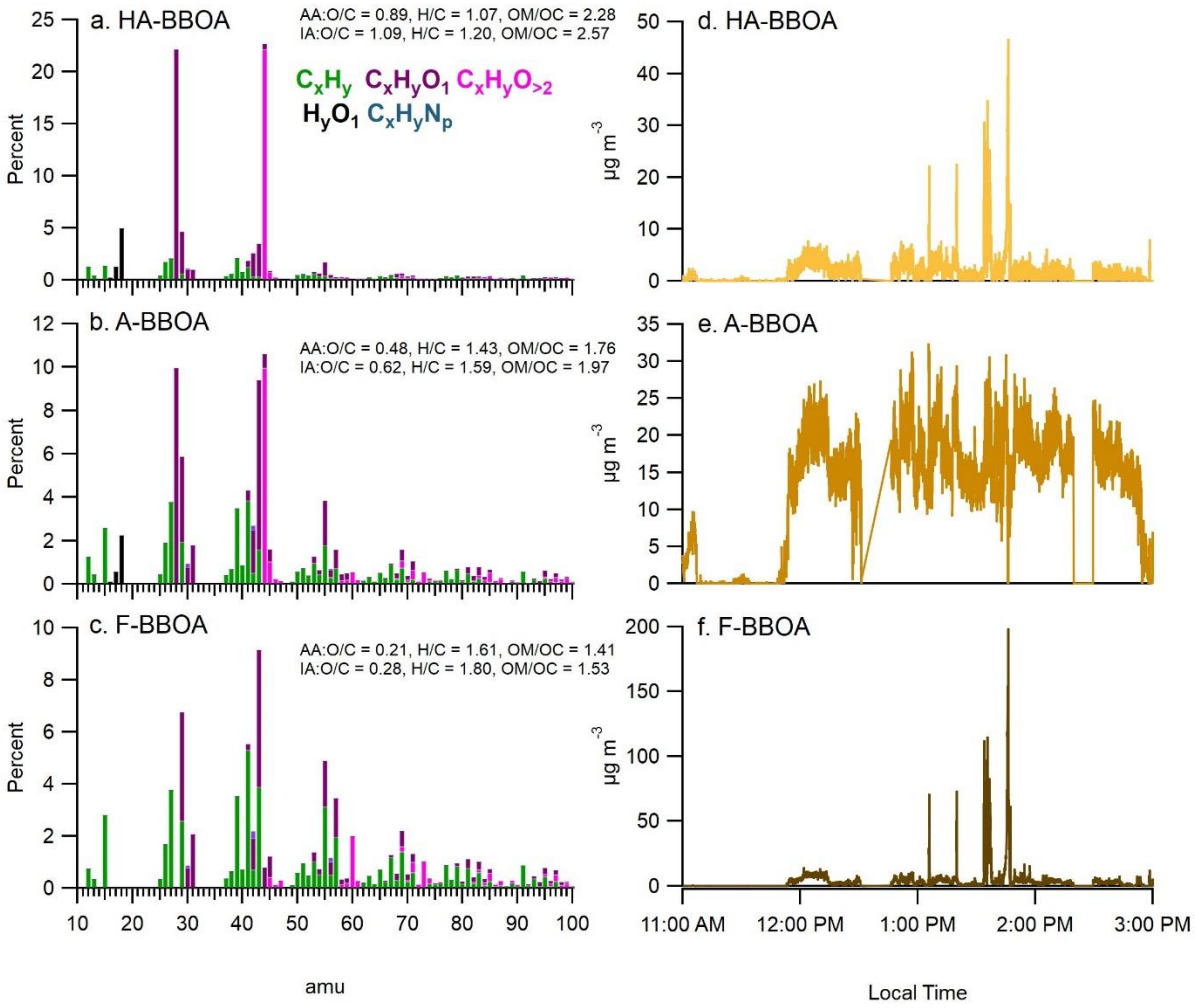

Figure B4: PMF spectra and time series of OA factors for G1-0806

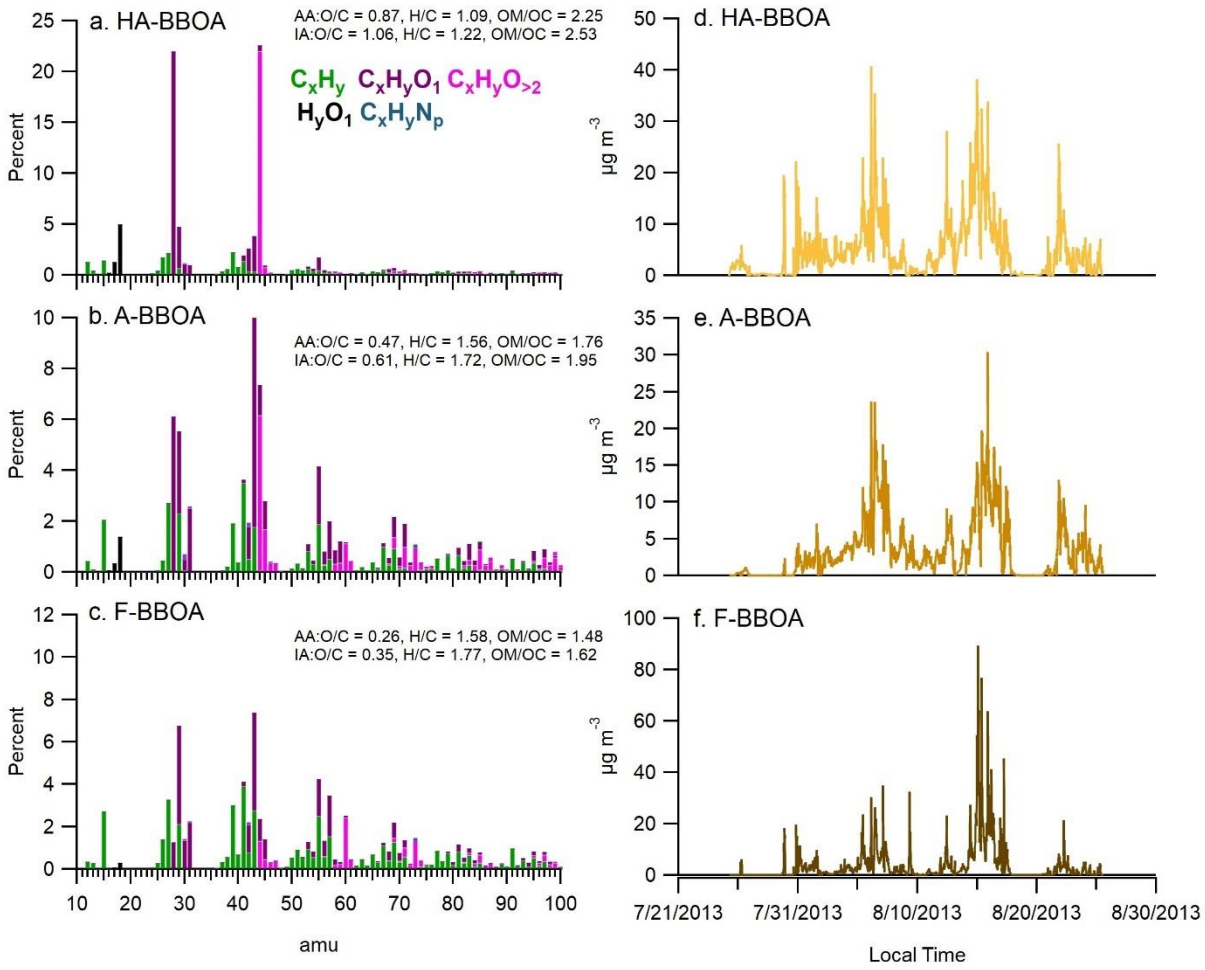

Figure B5: PMF spectra and time series of BBOA factors during BBOP at MBO

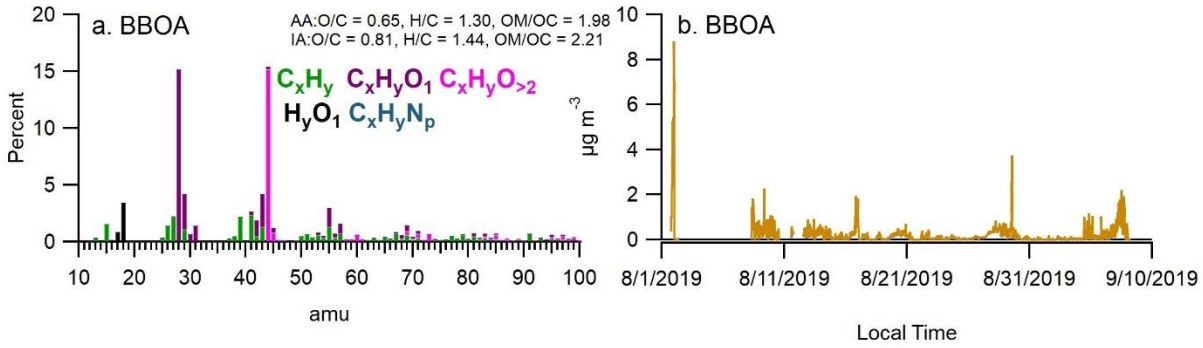

Figure B6: PMF spectra and time series of the BBOA factor during MBO-19

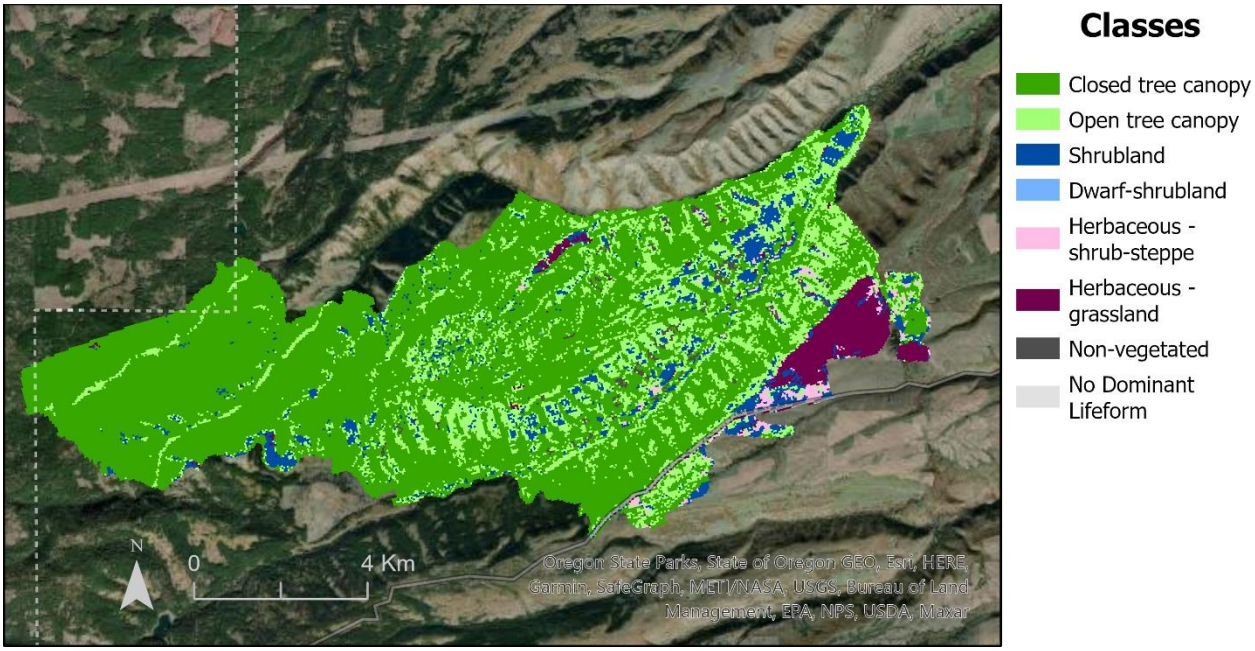

Figure B7: Map of the Government Flats fire extent, colored by fuel type. Fuel data was retrieved from Landscape Fire and Resource Management Planning Tools (https://landfire.gov/).

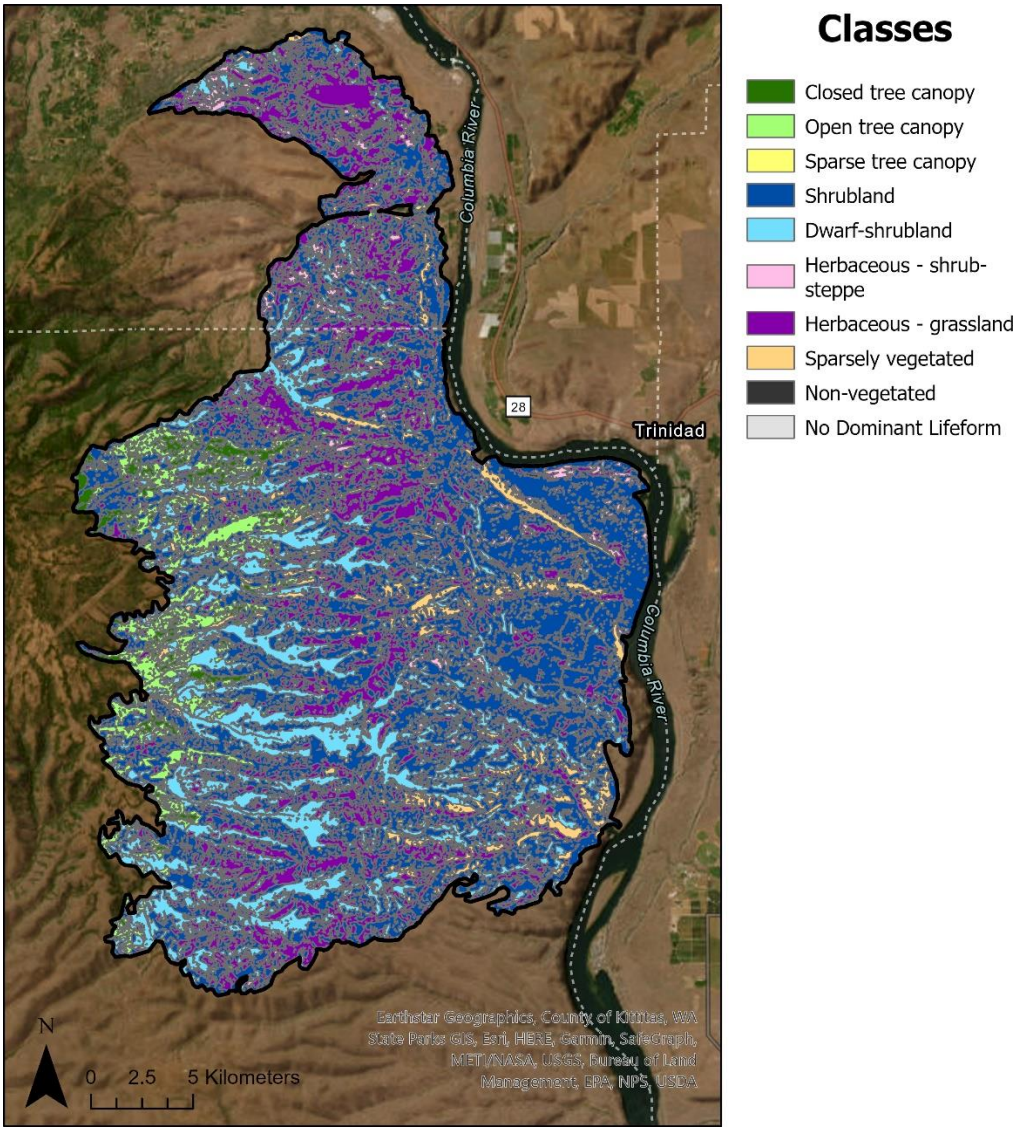

Figure B8: Map of the Colocknum Tarps fire extent, colored by fuel type. Fuel data was retrieved from Landscape Fire and Resource Management Planning Tools (https://landfire.gov/).

Table B1: Vegetation types in the area burned during each fire. N/A means no area of the corresponding type.

	Colockum Tarps Fire	Government Flats Fire	Salmon River Complex	Whiskey Creek Fire	Douglas Creek Complex
Closed tree canopy	2.5%	67.4%	51.7%	49.4%	69.7%
Open tree canopy	5.7%	20.1%	34.4%	49.5%	25.4%
Shrubland	45.7%	6.3%	10.2%	<1%	<1%
Dwarf-shrubland	14.9%	<1%	N/A	<1%	N/A
Herbaceous - grassland	23.0%	3.8%	2.3%	<1%	2.7%
Herbaceous - shrub-steppe	3.9%	1.2%	N/A	<1%	<1%
Sparsely vegetated	3.9%	N/A	N/A	N/A	N/A
Sparse tree canopy	<1%	N/A	<1%	N/A	N/A
No Dominant Lifeform	<1%	<1%	<1%	N/A	1.5%
Non-vegetated	<1%	<1%	<1%	N/A	<1%

Table B2: Coefficient values for trend lines shown in Figure 4. Fits are sigmoid curves in the form of $y = a + \left(\frac{b}{1+\exp\left(\frac{c-x}{d}\right)}\right)$

Parameter	a	b	c	d
O/C	0.272	0.651	11.88	4.83
f_{CO2}	-0.019	0.167	8.477	6.24
f_{C2H4O2}	0.099	-0.949	-7.18	4.75
f_{CHO2}	0.002	0.0048	2.69	1.15

References

Canonaco, F., Crippa, M., Slowik, J. G., Baltensperger, U. and Prévôt, A. S. H.: SoFi, an IGOR-based interface for the efficient use of the generalized multilinear engine (ME-2) for the source apportionment: ME-2 application to aerosol mass spectrometer data, Atmos. Meas. Tech., doi:10.5194/amt-6-3649-2013, 2013.

Zhou, S., Collier, S., Jaffe, D. A., Briggs, N. L., Hee, J., Iii, A. J. S., Kleinman, L., Onasch, T. B. and Zhang, Q.: Regional influence of wildfires on aerosol chemistry in the western US and insights into atmospheric aging of biomass burning organic aerosol, Atmos. Chem. Phys., 17(3), doi:10.5194/acp-17-2477-2017, 2017.

Appendix C: Supplementary Material for Source Apportionment of Soot Particles and Aqueous-Phase Processing of Black Carbon Coatings in an Urban Environment

C1. Methods

C1.1 Sampling Site

The measurements were performed at the University of California Cooperative Extension, an urban site in Fresno, CA. The sampling location was surrounded by residential neighborhoods and a commercial center and was approximately 500m from a nearby highway. Instrumentation was housed in a temperature regulated trailer and ambient air was sampled at 1 m^3 min^{-1} from 6m above ground level. A flow of 10 L min^{-1} was subsampled and passed through a diffusion drier and $PM_{2.5}$ cyclone prior to a split between the real time instrumentation, including a soot-particle aerosol mass spectrometer (SP-AMS), high resolution aerosol mass spectrometer (HR-AMS), Cavity Ring Down Photoacoustic Spectrometer (CRD-PAS), Particle absorption eXtinctiometer (PAX), single particle soot photometer (SP2) and scanning mobility particle sizer (SMPS). Meteorology, including wind speed, wind direction, temperature and relative humidity was measured using a Vaisala WXT520 weather transmitter. Trace gas measurements including NO and NO_2 (T200 M, Teledyne API), CO (T300, Teledyne API) were also measured at the field site.

C1.2 Aerosol Optical Measurements and Absorption Enhancement Calculations

Optical properties were measured at 405 and 532nm using the University of California Davis dual wavelength cavity ringdown/photoacoustic spectrometer (CRD-PAS) and at 870nm using a photoacoustic eXtinctiometer (PAX; DMT Inc.) (Cappa et al., 2019; Langridge et al., 2011).

The absorption enhancement (E_{abs}) of black carbon due to the lensing effect was calculated based on the mass absorption coefficient (MAC_{BC}), and is detailed in (Cappa et al., 2019). Specifically, MAC_{BC} was calculated as

$$MAC_{BC} = \frac{b_{abs}}{[BC]} \quad \text{(S1)}$$

where b_{abs} is the measured absorption and [BC] is the black carbon mass. Following this, the absorption enhancement was calculated as

$$E_{abs} = \frac{MAC_{BC}}{MAC_{BC,ref}} \quad \text{(S2)}$$

where the $MAC_{BC,ref}$ was determined as the MAC for pure, uncoated BC. $MAC_{BC,ref}$ values used for this campaign were 4.4 ± 0.2 $m^2\ g^{-1}$ (870 nm), 7.5 ± 0.5 $m^2\ g^{-1}$ (532 nm), 10.7 ± 0.6 $m^2\ g^{-1}$ (405 nm). This enhancement accounts for both the absorption due to coating material (i.e. BrC) and the lensing effect. Because of this, all analysis regarding E_{abs} was done at 870 nm to reduce the overall influence of BrC.

C1.3 ME-2 Analysis

The SP-AMS matrix was prepared for PMF analysis following previously established guidelines (Ulbrich et al., 2009; Zhang et al., 2011). Noisy ions with signal-to-noise ratio (S/N) < 0.2 were removed and S/N < 2 were down-weighted. Ions scaled to CO_2^+ (i.e., O^+, OH^+, H_2O^+, CO^+) were removed and recalculated following the analysis (Canonaco et al., 2013).

Initially, all solutions were allowed to vary freely, however it became evident that there was significant mixing between the hydrocarbon-like OA (HOA_{BC}) and biomass burning organic aerosol ($BBOA_{BC}$) factors. This was likely due to the proximity of combustion sources and similar patterns of emissions, leading to strong temporal correlations between the two factors. To correct for this, the $BBOA_{BC}$ and HOA_{BC} spectra were constrained using the *a*-value approach within the SoFi software (Canonaco et al., 2013). With this method, *a priori* spectra are provided by the user and the solution is allowed to vary based on a preselected *a*-value, ranging between 0 (fully constrained) and 1 (unconstrained). The $BBOA_{BC}$ anchor spectrum selected for this study was the profile resolved in the 4-factor unconstrained analysis. If the number of factors was increased beyond four during the unconstrained PMF analysis, splitting of the BBOA factor was seen. For the HOA_{BC} anchor spectrum, the HOA_{BC} spectrum resolved in the 5-factor unconstrained analysis was modified to remove the influence from BBOA. The 5-factor HOA_{BC} spectrum was selected as it had a smaller contribution from fragments

associated with BBOA, such as $C_2H_4O_2^+$, compared to the 4-factor solution. The spectrum was further modified by subtracting a portion of each ion signal based on its ratio to the $C_2H_4O_2^+$ ion in the $BBOA_{BC}$ spectrum until the f_{60} reached the established background value of 0.3% (Cubison et al., 2011). BC and other inorganic fragments were included in the anchor spectra, however the intensity of these ions in the HOA_{BC} anchor spectrum were not modified.

The 1 to 8 factor solutions were explored with *α*-values ranging from 0-0.8 for the $BBOA_{BC}$ and HOA_{BC} factors while the remaining factors were allowed to vary freely. A 4-factor solution with *α*-values of 0.4 for $BBOA_{BC}$ and HOA_{BC} was selected as the final solution. The spectra of the 3- and 5-factor solutions and the diagnostic plots are shown in Fig. C1-3. The 4-factor solution showed lower Q/Q_{exp} and improved residual over the 3-factor solution as a second OOA_{BC} factor was resolved (Fig. C3). However, moving from 4 to 5 factors resulted in further splitting of the OOA_{BC} factors with minimal additional chemical information. As the *α*-value was increased within the 4-factor solution, the $BBOA_{BC}$ factor remained similar, however the HOA_{BC} spectrum began to show signs of increasing BBOA "contamination". An *α*-value of 0.4 was selected as there was minimal improvement of Q/Q_{exp} at larger values and mixing of $BBOA_{BC}$ and HOA_{BC} remained minimized (Fig. C6b). Furthermore, previous studies have also found that *α*-values of 0.4 are optimum (Canonaco et al., 2020; Sun et al., 2022). Despite this, we note that there is a slightly elevated f_{60} (0.45%) within the HOA_{BC} mass spectrum, suggesting a minor BBOA influence. Finally, the rotational ambiguity of the solution was explored by varying the fpeak value from -1 to 1. Minimal change was seen with varying fpeak and a value of 0 was chosen.

C1.4 Thermodynamic modeling

Aerosol liquid water content associated with rBC ($ALWC_{BC}$) was estimated using the Extended Aerosol Inorganic Model (E-AIM) using model II (http://www.aim.env.uea.ac.uk/aim/aim.php) (Clegg et al., 1998). This model uses the concentrations of NH_4^+, NO_3^- and SO_4^{2-} measured by the SP-AMS as well as the ambient temperature and relative humidity. As no $NH_{3(g)}$ measurements were collected, the

model was run in reverse mode. The E-AIM model requires neutralized particles, therefore the charges were balanced using H^+ and OH^- as needed. E-AIM is not able to calculate the ALWC associated with organics ($ALWC_{Org}$), which previous research has been found to be non-negligible (Nguyen et al., 2016; Parworth et al., 2017). Instead $ALWC_{Org,\ rBC}$ was found using the following equation derived from (Petters and Kreidenweis, 2007)

$$\mathrm{ALWC_{Org,rBC}} = \frac{\mathrm{m_{Org}}\,\rho_w}{\rho_{\mathrm{Org}}}\frac{\kappa_{\mathrm{Org}}}{\left(\frac{1}{\mathrm{RH}}-1\right)} \quad \text{(S3)}$$

where m_{Org} is the measured OA mass from the SP-AMS, ρ_w is the density of water (1 g cm^{-3}), ρ_{Org} is the OA density, κ_{org} is the OA hygroscopicity parameter and RH is the measured relative humidity. ρ_{Org} was estimated based on the elemental composition with the following formula: ρ_{Org} = [(12 + H/C) + 16*(O/C) / 7 + 5*(H/C) + 4.15*(O/C)] (Kuwata et al., 2012). As there were no direct measurements of the hygroscopicity of the black carbon containing aerosols, κ_{org} was parameterized using the SP-AMS f_{44} with the following relationship

$$\kappa_{Org} = 2.2 * f_{44} - 0.13 \quad \text{(S4)}$$

as described in (Duplissy et al., 2011). The total $ALWC_{rBC}$ is assumed to be the sum of $ALWC_{E\text{-}AIM,rBC}$ and $ALWC_{Org,rBC}$ and the time series of each is shown in Fig. C14.

C2. Figures

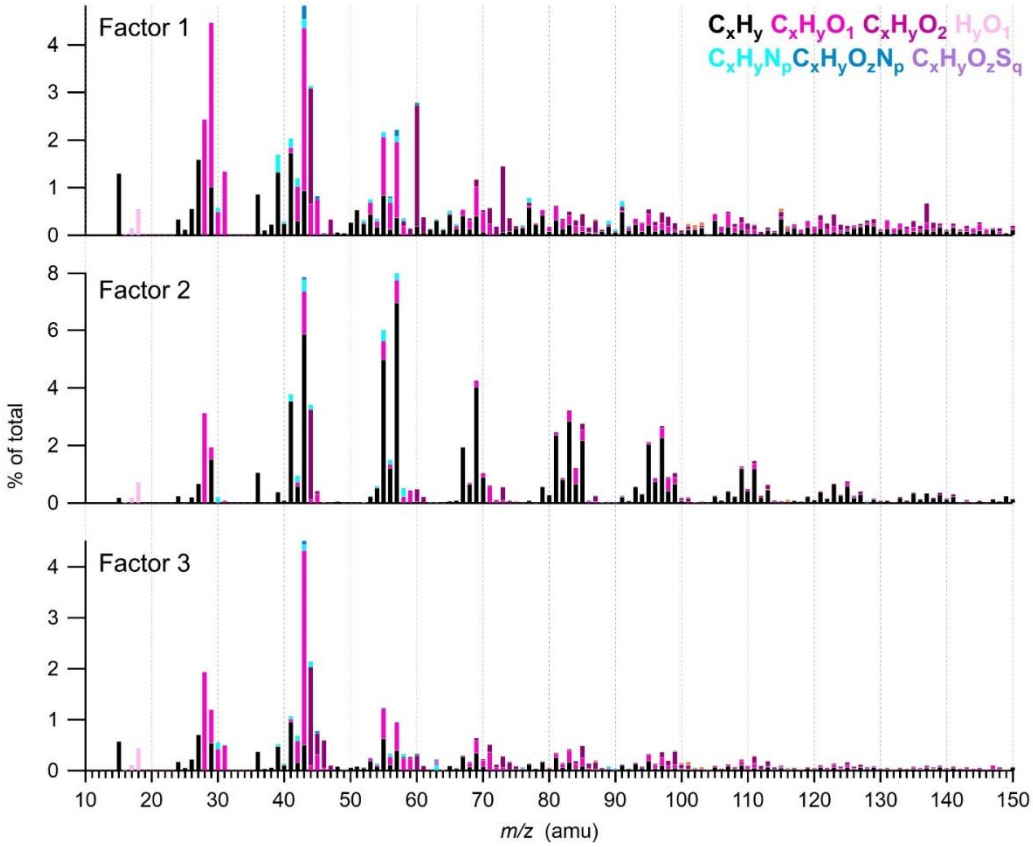

Figure C1: OA_{BC} spectra for three factor PMF solution. Factor 1 is constrained to BBOA and factor 2 is constrained to HOA with a values of 0.4.

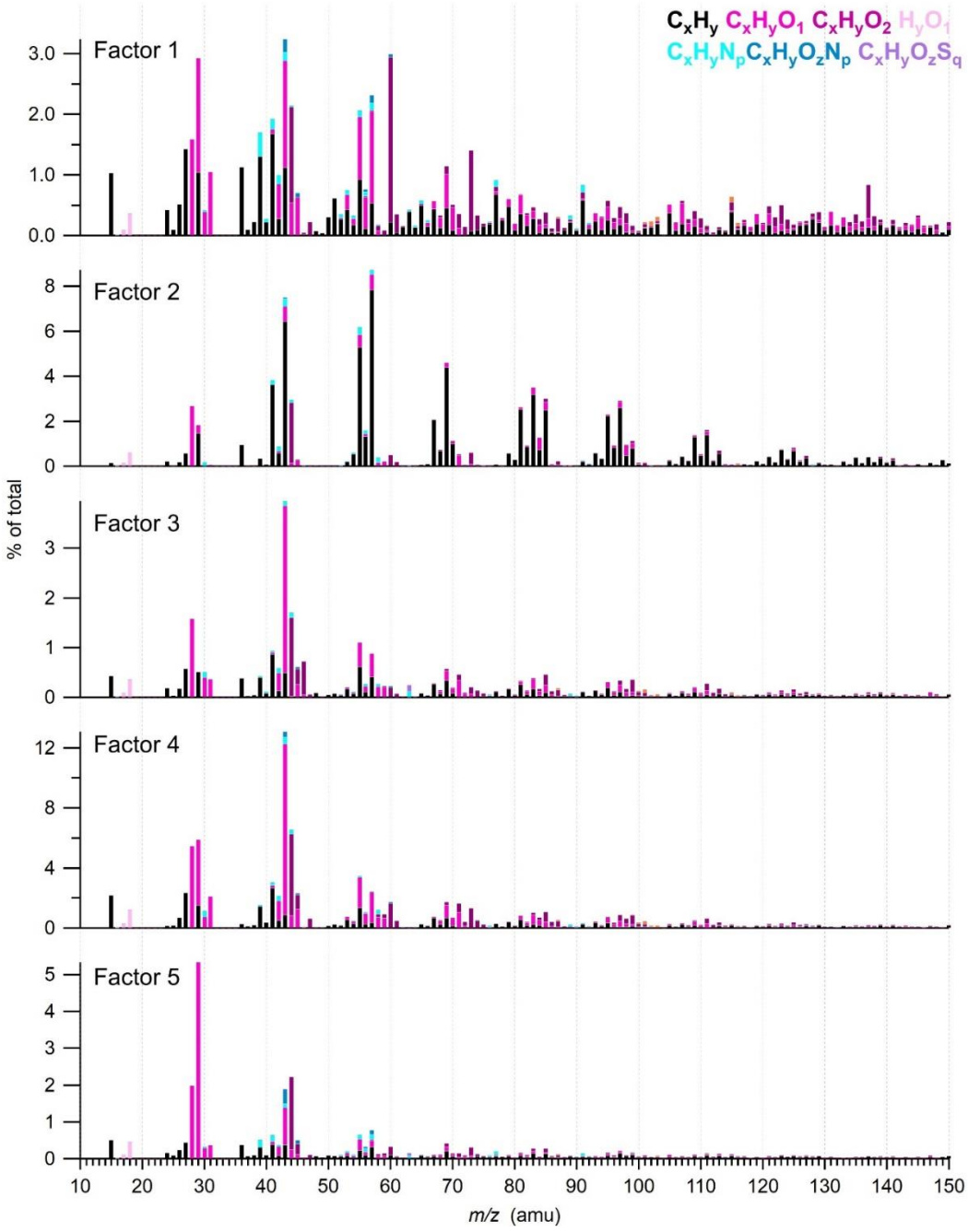

Figure C2: OABC spectra for five factor PMF solution. Factor 1 is constrained to BBOA and factor 2 is constrained to HOA with a values of 0.4.

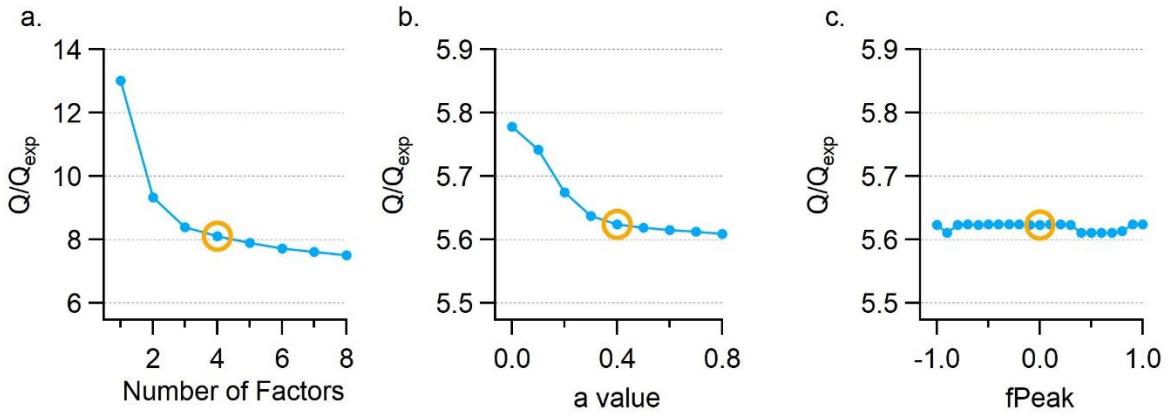

Figure C3: Change in Q/Qexp of PMF solution as function of (a) number of factors, (b) a-value, (c) fPeak. Values used in (a) are from the a-value of 0 and fPeak of 0. Values in (b) are for four factor solution and fPeak of 0. Values of (c) are for four factor solution and a-value of 0.4.

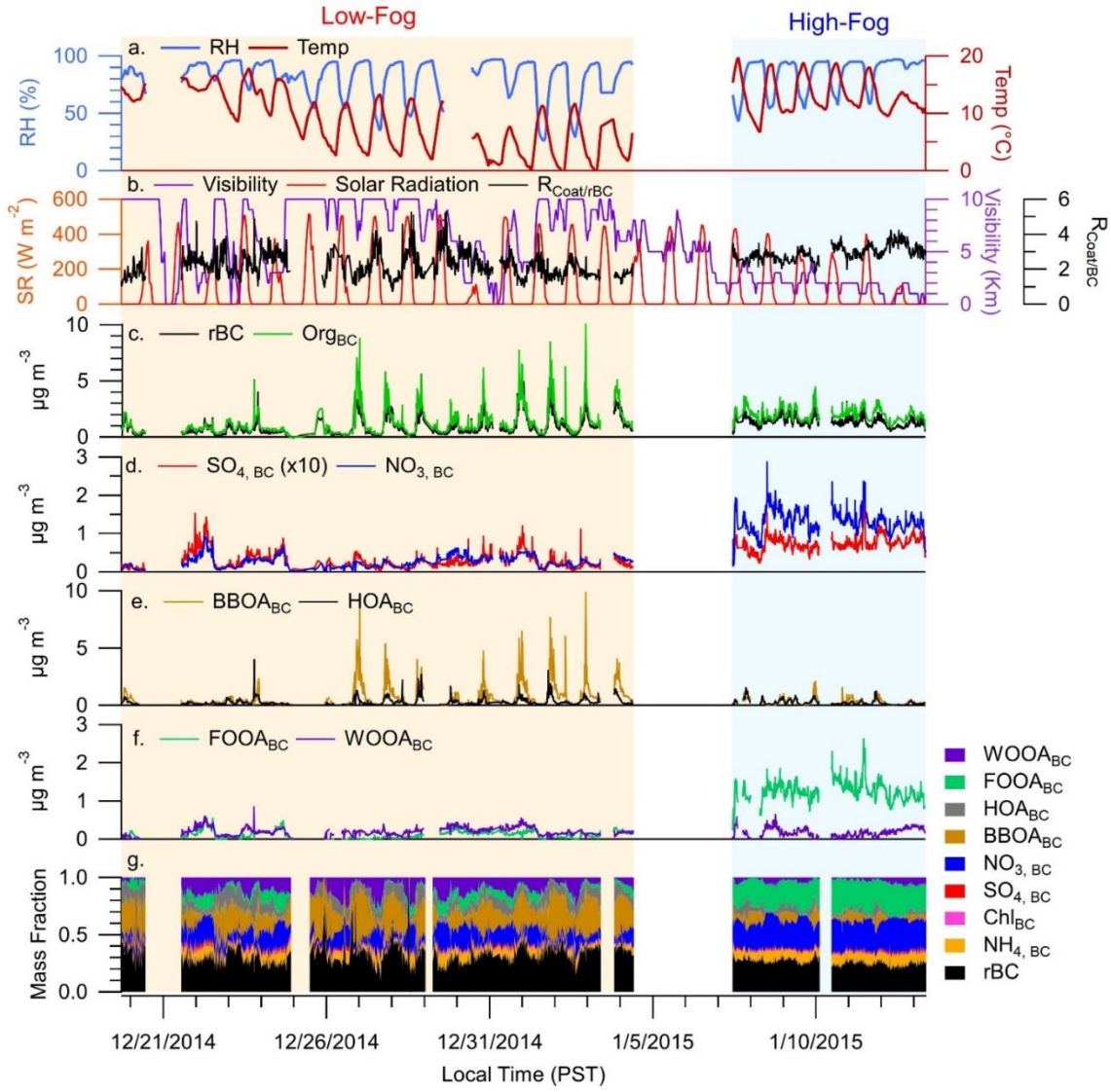

Figure C4: Time series of (a, b) meteorological parameters (b) bulk rBC coating thickness (c, d) PM1,BC species, (e,f) OABC factors resolved with PMF and (g) fractional contribution of each species to total PM1,BC. The blue background represents the fog case study period, while the orange background represents the contrasting low fog period. Gaps indicate missing data.

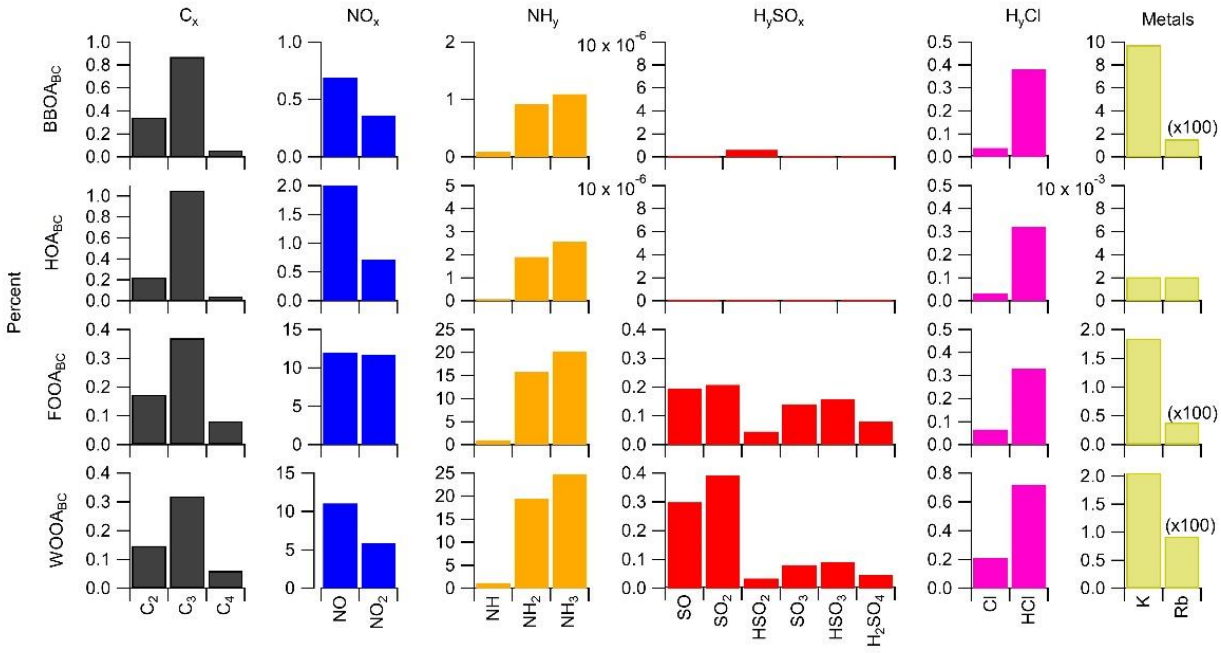

Figure C5: Distribution of inorganic ions across PMF factors, separated by chemical species. Axis values are percent of total nitrate equivalent signal.

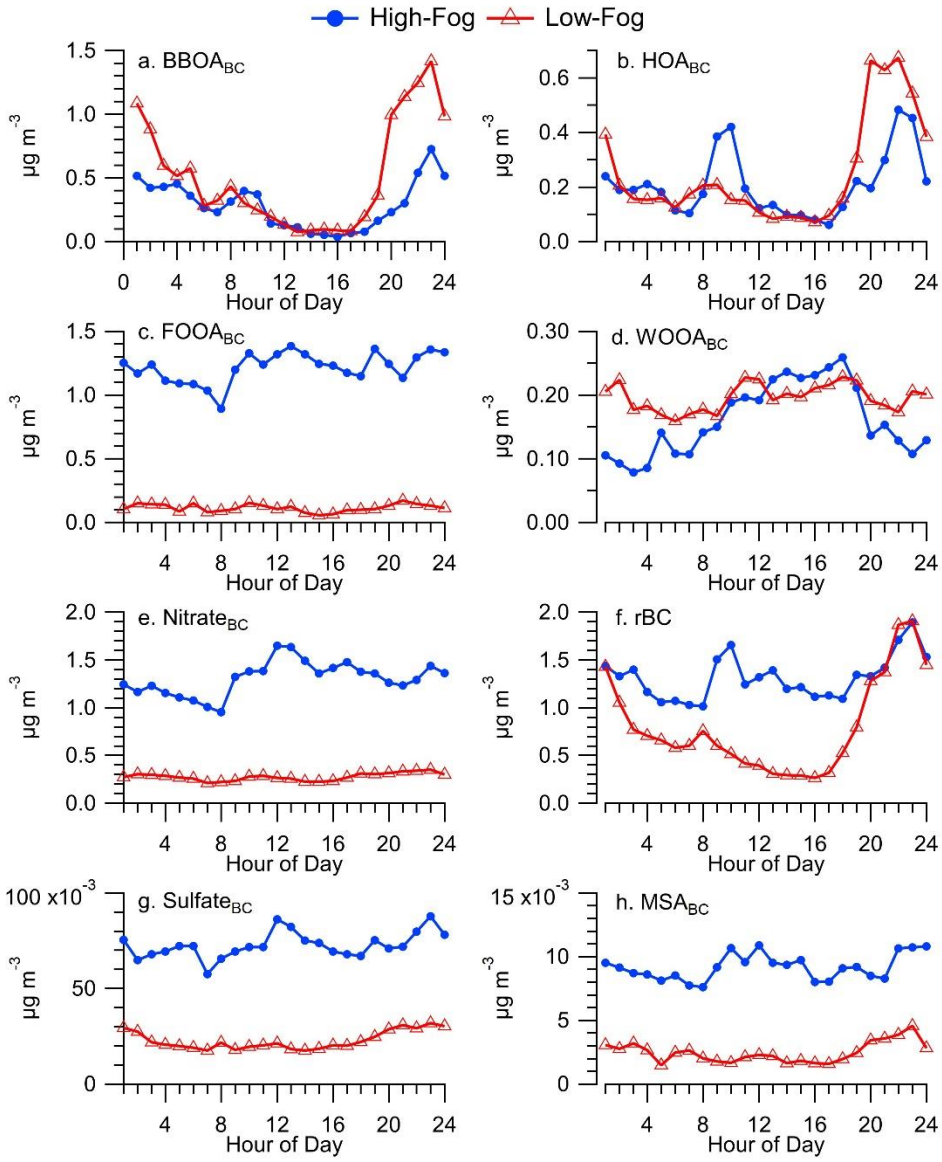

Figure C6: Diurnal profiles of hourly median concentration of (a) BBOA$_{BC}$, (b) HOA$_{BC}$, (c) FOOA$_{BC}$, (d) WOOA$_{BC}$, (e) Nitrate$_{BC}$, (f) rBC, (g) Sulfate$_{BC}$, (h) estimated MSA$_{BC}$. Concentration of each species is separated between the high-fog period and low-fog periods.

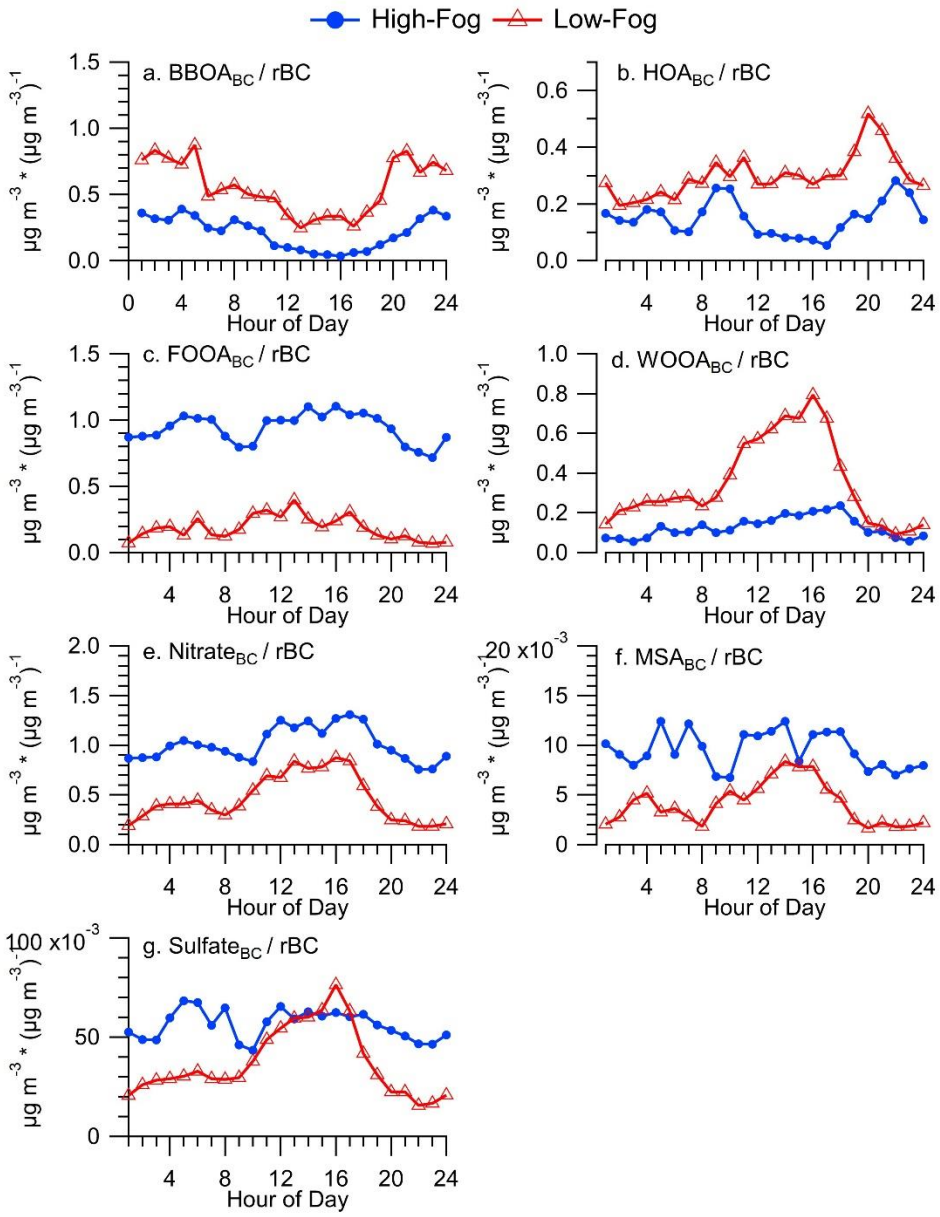

Figure C7: Same as Figure S6, however concentration is normalized by rBC concentration.

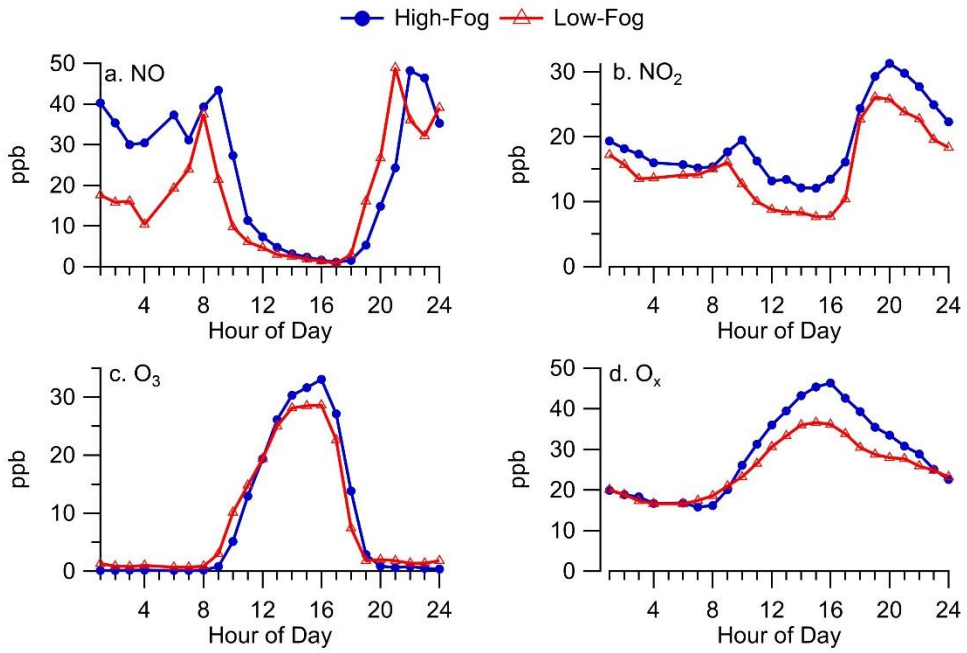

Figure C8: Diurnal profile of gas-phase species (a) NO, (b) NO_2, (c) O_3 and (d) O_x. O_x equals the sum of O_3 and NO_2.

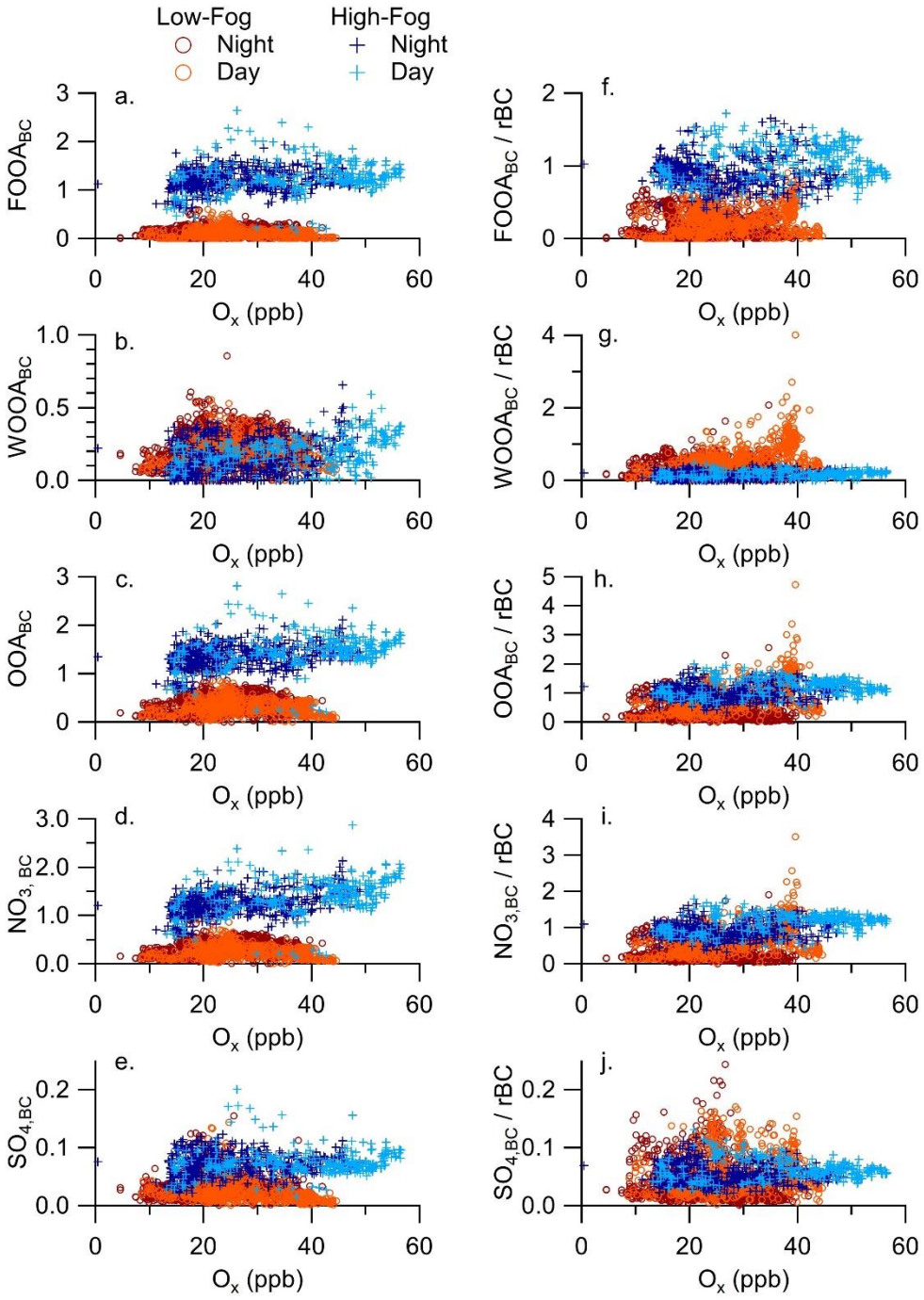

Figure C9: Relationship between (a) $FOOA_{BC}$, (b) $WOOA_{BC}$, (c) sum of $FOOA_{BC}$ and $WOOA_{BC}$, (d) $NO_{3,BC}$, (e) $SO_{4,BC}$ and O_x. (f-j) Same as (a-e) except concentration is normalized by rBC concentration. Data is separated between the fog period and low fog period as well as between day and night.

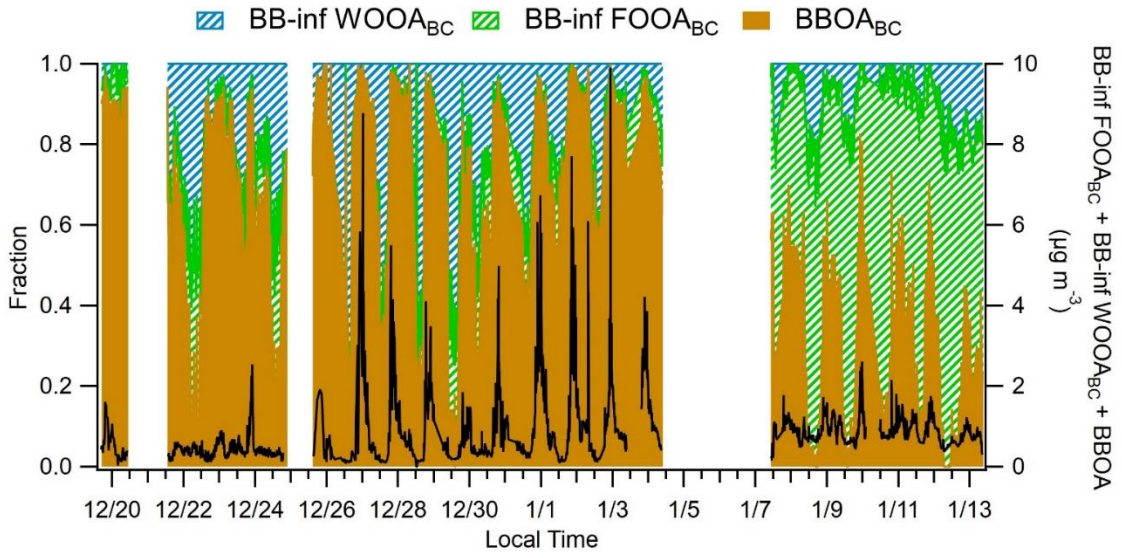

Figure C10: Fractional contribution of BB-influenced WOOA, BB-influenced FOOA and BBOA. Black trace is the sum of the three species.

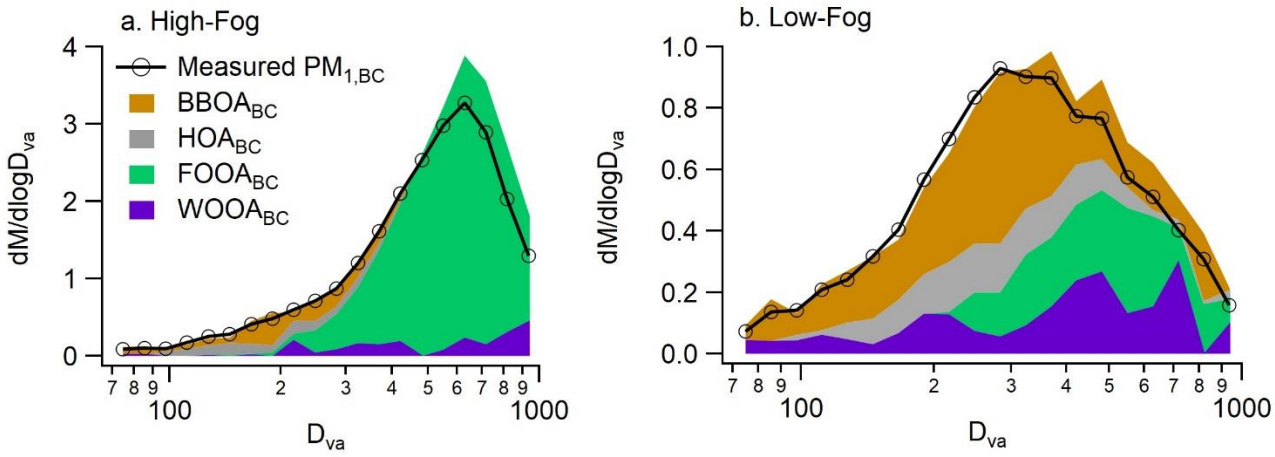

Figure C11: Comparison of SP-AMS measured $PM_{1,BC}$ size distribution (black line) and results of the linear decomposition of the size resolved mass spectra for the (a) fog period and (b) low fog period. Top panels show the scaled residual between the measured and modeled size distributions.

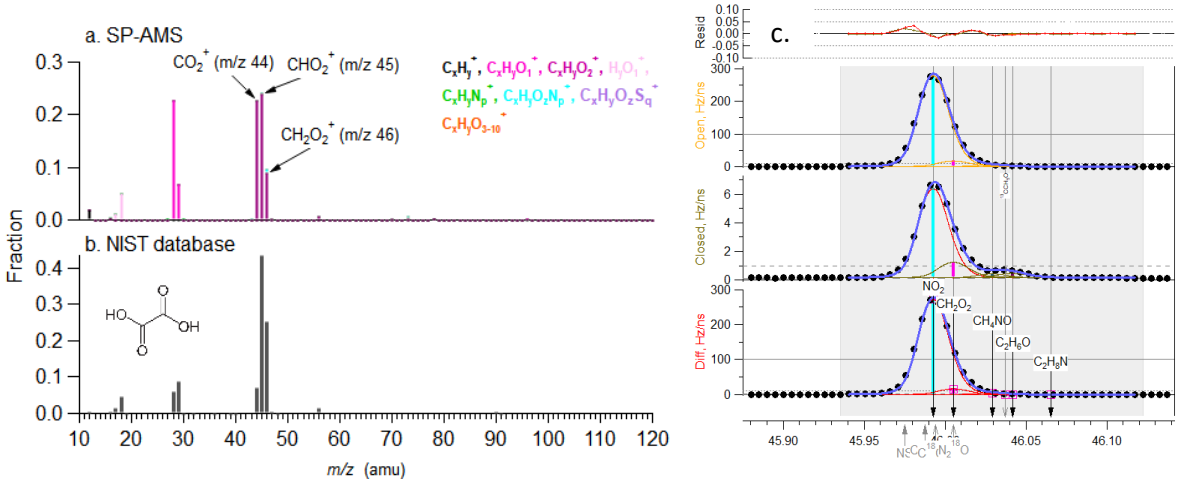

Figure C13: (a) SP-AMS mass spectrum of pure oxalic acid sampled in the laboratory. (b) Reference mass spectrum for oxalic acid from the NIST databases. (c) High resolution peak fitting of m/z 46 during a representative section of the fog period.

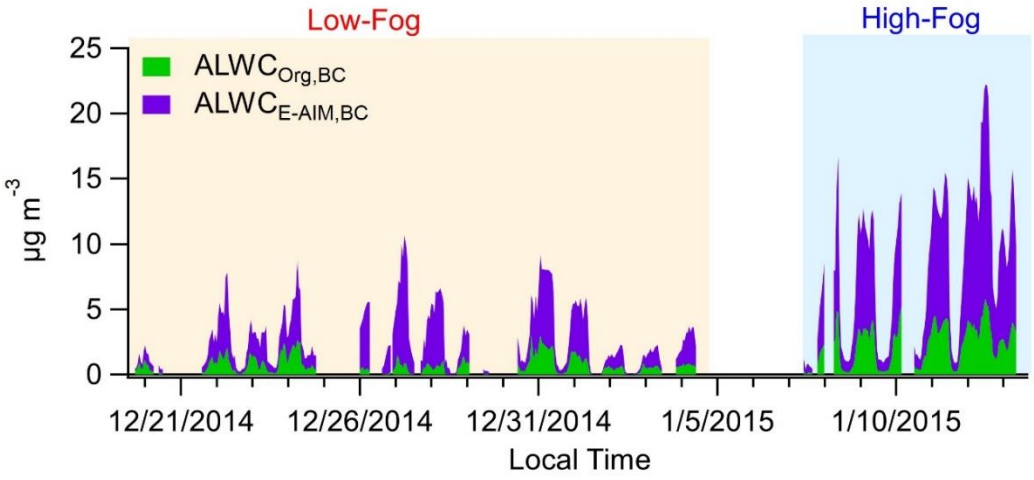

Figure C14: Stacked time series of ALWC$_{BC}$ associated with inorganics calculating using E-AIM (ALWC$_{E-AIM,BC}$) and ALWC$_{BC}$ associated with organics (ALWC$_{Org,BC}$).

References

Canonaco, F., Crippa, M., Slowik, J. G., Baltensperger, U. and Prévôt, A. S. H.: SoFi, an IGOR-based interface for the efficient use of the generalized multilinear engine (ME-2) for the source apportionment: ME-2 application to aerosol mass spectrometer data, Atmos. Meas. Tech., doi:10.5194/amt-6-3649-2013, 2013.

Canonaco, F., Tobler, A., Chen, G., Sosedova, Y., Slowik, J. G., Daellenbach, K. R., Elhaddad, I., Crippa, M., Huang, R., Baltensperger, U., Stephan, A. and Prévôt, H.: A new method for long-term source apportionment with time- dependent factor profiles and uncertainty assessment using SoFi Pro : application to one year of organic aerosol data, Atmos. Meas. Tech., (July), 1–39, 2020.

Cappa, C. D., Zhang, X., Russell, L. M., Collier, S., Lee, A. K. Y., Chen, C. L., Betha, R., Chen, S., Liu, J., Price, D. J., Sanchez, K. J., McMeeking, G. R., Williams, L. R., Onasch, T. B., Worsnop, D. R., Abbatt, J. and Zhang, Q.: Light Absorption by Ambient Black and Brown Carbon and its Dependence on Black Carbon Coating State for Two California, USA, Cities in Winter and Summer, J. Geophys. Res. Atmos., 124(3), 1550–1577, doi:10.1029/2018JD029501, 2019.

Clegg, S. L., Brimblecombe, P. and Wexler, A. S.: Thermodynamic model of the system H+-NH4+-SO42-NO 3--H2O at tropospheric temperatures, J. Phys. Chem. A, 102(12), 2137–2154, doi:10.1021/jp973042r, 1998.

Cubison, M. J., Ortega, A. M., Hayes, P. L., Farmer, D. K., Day, D., Lechner, M. J., Brune, W. H., Apel, E., Diskin, G. S., Fisher, J. A., Fuelberg, H. E., Hecobian, A., Knapp, D. J., Mikoviny, T., Riemer, D., Sachse, G. W., Sessions, W., Weber, R. J., Weinheimer, A. J., Wisthaler, A. and Jimenez, J. L.: Effects of aging on organic aerosol from open biomass burning smoke in aircraft and laboratory studies, Atmos. Chem. Phys., doi:10.5194/acp-11-12049-2011, 2011.

Duplissy, J., Decarlo, P. F., Dommen, J., Alfarra, M. R., Metzger, A., Barmpadimos, I. and Prevot, A. S. H.: Relating hygroscopicity and composition of organic aerosol particulate matter, Atmos. Chem. Phys., 1155–1165, doi:10.5194/acp-11-1155-2011, 2011.

Kuwata, M., Zorn, S. R. and Martin, S. T.: Using elemental ratios to predict the density of organic material composed of carbon, hydrogen, and oxygen, Environ. Sci. Technol., 46(2), 787–794, doi:10.1021/es202525q, 2012.

Langridge, J. M., Richardson, M. S., Lack, D., Law, D. and Murphy, D. M.: Aircraft instrument for comprehensive characterization of aerosol optical properties, part i: Wavelength-dependent optical extinction and its relative humidity dependence measured using cavity ringdown spectroscopy, Aerosol Sci. Technol., 45(11), 1305–1318, doi:10.1080/02786826.2011.592745, 2011.

Nguyen, T. K. V, Zhang, Q., Jimenez, J. L., Pike, M. and Carlton, A. G.: Liquid Water : Ubiquitous Contributor to Aerosol Mass, , doi:10.1021/acs.estlett.6b00167, 2016.

Parworth, C., Young, D. E., Kim, H., Zhang, X., Cappa, C. D., Collier, S. and Zhang, Q.: Wintertime water-soluble aerosol composition and particle water content in Fresno, California, J. Geophys. Res. Atmos., 122, 3155–3170, doi:10.1002/2016JD026173, 2017.

Petters, M. D. and Kreidenweis, S. M.: A single parameter representation of hygroscopic growth and cloud condensation nucleus activity, Atmos. Chem. Phys., 13(2), 1081–1091, doi:10.5194/acp-13-1081-2013, 2007.

Sun, P., Farley, R. N., Li, L., Srivastava, D., Niedek, C. R., Li, J., Wang, N., Cappa, C. D., Pusede, S. E., Yu, Z., Croteau, P. and Zhang, Q.: PM2.5 composition and sources in the San Joaquin Valley of California : A long-term study using ToF-ACSM with the capture vaporizer, Environ. Pollut., 292(PA), 118254, doi:10.1016/j.envpol.2021.118254, 2022.

Ulbrich, I. M., Canagaratna, M. R., Zhang, Q., Worsnop, D. R. and Jimenez, J. L.: Interpretation of organic components from Positive Matrix Factorization of aerosol mass spectrometric data, Atmos. Chem. Phys., doi:10.5194/acp-9-2891-2009, 2009.

Zhang, Q., Jimenez, J. L., Canagaratna, M. R., Ulbrich, I. M., Ng, N. L., Worsnop, D. R. and Sun, Y.: Understanding atmospheric organic aerosols via factor analysis of aerosol mass spectrometry: A review, Anal. Bioanal. Chem., doi:10.1007/s00216-011-5355-y, 2011.

Appendix D: Supplementary Material for Chemical Properties and Single Particle Mixing State of Soot Aerosol in Houston during the TRACER Campaign

D1. Methods

D1.1 Co-located Measurements at La Porte Field Site

Measurements of numerous aerosol chemical and physical properties were collected at the La Porte site during the TRACER campaign. Ambient aerosols were sampled from a mast approximately ten meters above ground level prior to passing through a nafion drier followed by a $PM_{2.5}$ cyclone (Fig. D1) . The flow was then split between all instrumentation within the trailer. In addition to the laser-only SP-AMS, a second, co-located SP-AMS with a $PM_{2.5}$ inlet was operated in the dual vaporizer mode to simultaneously measure non-refractory $PM_{2.5}$ (NR-$PM_{2.5}$) and rBC. The dual vaporizer SP-AMS utilizes both a laser vaporizer and a resistively heated tungsten thermal vaporizer (600°C) to convert particles into the gas phase for ionization (Avery et al., 2020). The dual vaporizer SP-AMS was programmed to cycle between "laser-on" mode and "laser off" mode. During laser-off mode it functions equivalently to a conventional high-resolution time-of-flight aerosol mass spectrometer (HR-AMS) and only material that vaporizes at 600°C, including most organics and the ammonium salts of nitrate, sulfate and chloride, is measured. (DeCarlo et al., 2006; Onasch et al., 2012).

The BC number and mass concentrations were measured with a single particle soot photometer (SP2). Dry (<50% RH) and humidified (85% RH) aerosol absorption, scattering, and extinction were measured at 405 and 532 nm using a two-wavelength cavity ringdown-photoacoustic spectrometer (CRD-PAS) (Langridge et al., 2011).

Meteorological data, including temperature, relative humidity, precipitation rate and wind speed, were measured on site. Ozone concentration was measured using an Ozone Analyzer (Thermo-Fisher Scientific). Trace gas measurements were performed at the Texas Commission of Environmental Quality (TCEQ) Deer Park site, located 6 km from the La Porte sampling location (Figure D1). Hourly NO, NO_2

and SO_2 concentrations were retrieved from the TCEQ website (https://www.tceq.texas.gov/cgi-bin/compliance/monops/daily_summary.pl?cams=35, last access 8/25/2023).

D1.2 Soot-Particle Aerosol Mass Spectrometer Operation

The laser-only SP-AMS was programmed to automatically switch between mass spectrum (MS) only mode, combined MS/ePToF mode, and event trigger single particle (ETSP) mode. Each mode lasted 5 minutes, with two runs of MS/ePToF resulting in a total cycle time of 20 minutes. The *m/z* range for MS/ePToF and ETSP was 10 - 317 amu, however for the MS-only runs, the *m/z* range was increased to 900 amu to investigate the presence of fullerene soot clusters.

Calibration of the SP-AMS ionization efficiency (IE) was performed using dried monodisperse ammonium nitrate (NH_4NO_3) aerosol (Canagaratna et al., 2007; Jayne et al., 2000). The relative ionization efficiencies (RIE) of ammonium, sulfate and chloride were determined using ammonium nitrate, ammonium sulfate and ammonium chloride respectively, and found to be 3.14, 1.15 and 1.43. The RIE for nitrate was corrected for ions other than NO^+ and NO_2^+ and was found to be 1.05. Particle size calibration was conducted using polystyrene latex spheres (PSLs) ranging from 97 nm to 800 nm prior to and following deployment. Because vaporization of pure ammonium salts and PSLs requires the tungsten vaporizer, the above-mentioned calibrations were performed both before and after the instrument deployment. The RIE of rBC was determined using size selected regal black (Cabot Corp) following the removal of the thermal vaporizer. Two independent calibrations were performed prior to the start of sampling and following the end of sampling, and an RIE of 0.28 was determined for rBC.

The organic CO_2^+ signal was corrected for the influence from $CO_{2(g)}$ by subtracting the time dependent gas-phase measurements from a collocated AERIS CO_2 monitor. The ammonium signal was constrained to the NH_2^+ peak, as the NH_3^+ had an elevated background due to interference from the OH^+ peak and NH^+ was influenced by the $^{15}N^+$ peak. The ratio of NH^+/NH_2^+ (0.07) and NH_3^+/NH_2^+ (1.18) measured during the ammonium nitrate calibration were used.

A coating thickness dependent collection efficiency (CE) was applied as was done previously (Collier et al., 2018; Willis et al., 2014). The following sigmoidal relation from Collier et al. (2018) was used

$$E = 0.34 + \left[\frac{0.16}{1+\exp\left(\frac{2.5-R_{\frac{coat}{BC}}}{0.19}\right)}\right] \quad \text{(D1)}$$

where $R_{coat/BC}$ is the mass ratio of coating material to rBC. As can be seen from this equation, the CE ranged from 0.34 for the most thinly coated particles, to 0.5 for more thickly coated particles. This correction is needed because thickly coated particles produce a narrower particle beam, resulting in better particle beam – laser beam overlap.

D1.3 Positive Matrix Factorization Analysis

Positive Matrix Factorization (PMF) was conducted with both organic and inorganic ions included in the mass spectral matrix. The inorganic ions used were C_{1-4}^+ for rBC, SO^+, SO_2^+, HSO_2^+, SO_3^+, HSO_3^+, $H_2SO_4^+$ for sulfate, NO^+ and NO_2^+ for nitrate, and K^+. Ammonium ions were not included due to uncertainty from interference with water signal and chloride was not included due to low signal to noise. The matrix was prepared using previously established guidelines (Ulbrich et al., 2009; Zhang et al., 2011). Noisy ions with S/N < 0.2 were removed while ions with S/N < 2 and those scaled to CO_2^+ (i.e., O^+, OH^+, H_2O^+, CO^+) were downweighted.

The four-factor solution was chosen as the best solution based on analysis of the temporal and spectral features. Progressing from three factors to four factors resulted in the separation of a factor dominated by potassium and a decrease in the total residual. However, the five-factor solution shows non-meaningful splitting of the sulfate factor. The rotational ambiguity was explored by varying the fPeak between -1 and 1, however these solutions showed negligible change in Q/Q_{exp} and splitting of the sulfate factor therefore an fpeak equal to zero was selected.

D1.4 Estimating Organic Elemental Ratios from ETSP results

The average atomic oxygen/carbon (O/C) and hydrogen/carbon (H/C) ratios for single particle spectra were estimated by linear decomposition. The improved ambient (IA) ratios were first calculated for the ensemble measurements using the high resolution mass spectra (Canagaratna et al., 2015b). The elemental ratios were decomposed to the organic fraction at *m/z* 43 (f_{43}), 44 (f_{44}), 55 (f_{55}) and 57 (f_{57}). Time points with OA concentrations < 0.5 μg m^{-3} were removed to avoid noisy data points. The results of decomposition are as follows

$$O/C = (1.899 * f_{43}) + (3.968 * f_{44}) + (4.173 * f_{55}) + (2.178 * f_{57}) \quad (D2)$$

$$H/C = (7.571 * f_{43}) + (2.078 * f_{44}) + (14.39 * f_{55}) + (8.602 * f_{57}) \quad (D3)$$

These equations were then used to reconstruct the elemental ratios for each single particle spectra. The reconstructed values capture the variation in O/C well (slope = 0.97, r^2 = 0.74) but show more scatter for H/C (slope = 1.0, r^2 = 0.21). The variation of these ratios for each particle class is shown in figure D11.

D1.5 Predicting Single Particle Aerosol Hygroscopicity

Hygroscopicity of single particles was predicted using Zdanovskii-Stokes-Robinson (ZSR) mixing rule and the hygroscopicity paramter (κ) introduced in Petters and Kreidenweis (2007). This method assumes that the overall hygroscopicity of an aerosol is proportional to the κ value of each component, weighted by the respective volume faction. For any particle *i*, κ_i can be calculated as

$$\kappa_i = \sum_1^j \kappa_j V_{i,j} \quad (D4)$$

where κ_j is the hygroscopicity parameter for pure compound *j*, and $V_{i,j}$ is the volume fraction of compound j in particle *i*. The density and κ for all compounds used are shown in table D2. The volume fraction for individual particles was calculated by dividing the measured mass concentration for particle events measured by ETSP mode by the assumed density of each species. Nitrate and chloride were assumed to be in the form of their ammonium salts. Sulfate was first apportioned to potassium sulfate

using the measured K^+ signal, and all remaining sulfate was assumed to be in the form of ammonium sulfate. The organic density was parameterized based on the method described in Kuwata et al. (2012).

$$\rho = 12 + (H/C) + 16 * (O/C) / [7 + 5 * (H/C) + 4.15 * (O/C)] \quad \text{(D5)}$$

The organic hygroscopicity was estimated from the paramaterization introduced in Duplissy et al. (2011).

$$\kappa = 2.2 * f_{44} - 0.13 \quad \text{(D6)}$$

The choice of species has important implications on the results, as this will alter both the volume fraction and the hygroscopicity and a brief explanation of the assumptions is given here. In addition to ammonium salts, atmospheric anions can also be found as sodium salts (i.e. $NaNO_3$, NaCl, Na_2SO_4). However, low concentrations of Na^+ was measured by the SP-AMS and these compounds were assumed to be negligible. Atmospheric potassium can be found in a variety of forms. In addition to K_2SO_4, this commonly includes KNO_3 and KCl (Cao et al., 2019; Pratt et al., 2011; Zauscher et al., 2013). However, during periods of elevated K^+, there was a molar excess K^+ relative to NO_3^- or Cl^- suggesting that these were not the major species present. As mentioned above, ammonium was not included in the ETSP processing, therefore it was not possible to estimate the aerosol acidity or separate sulfate signal between $(NH_4)_2SO_4$, NH_4HSO_4 and H_2SO_4. Here, we make the assumption that the aerosol is neutralized and all sulfate not attributed to K_2SO_4 is in the form of ammonium sulfate.

The critical supersaturation value for individual particles was estimated by solving the following equation for S_c

$$\kappa = \frac{4A^3}{27D_d^3 \ln^2 S_c} \quad \text{(D7)}$$

$$A = \frac{4\sigma_{s/a} M_w}{RT\rho_w} \quad \text{(D8)}$$

where D_d is the dry aerosol diameter measured by SP-AMS, $\sigma_{s/a}$ is the surface tension of the solution/air interface, ρ_w is the density of water, M_w is the molecular weight of water, R is the universal gas constant and T is temperature. Here we assume values of $\sigma_{s/a}$ = 0.072 J m^{-2} and T = 298.15K (Petters and Kreidenweis, 2007).

D1.6 Back Trajectory Analysis

Backtrajectories were calculated using the Hybrid Single Particle Integrated Trajectory (HYSPLIT) model (Draxler and Hess, 1998). 240 hour back trajectories were initiated every 3 hours using the 1 degree Global Data Assimilation System (GDAS) meterology. Each trajectory was initiated at the sampling location at a height of 100 m above ground level. Concentration Weighted Trajectories (CWT) were calculated in the ZeFir program within Igor Pro to investiate potential geographical source regions (Petit et al., 2017).

D2. Figures

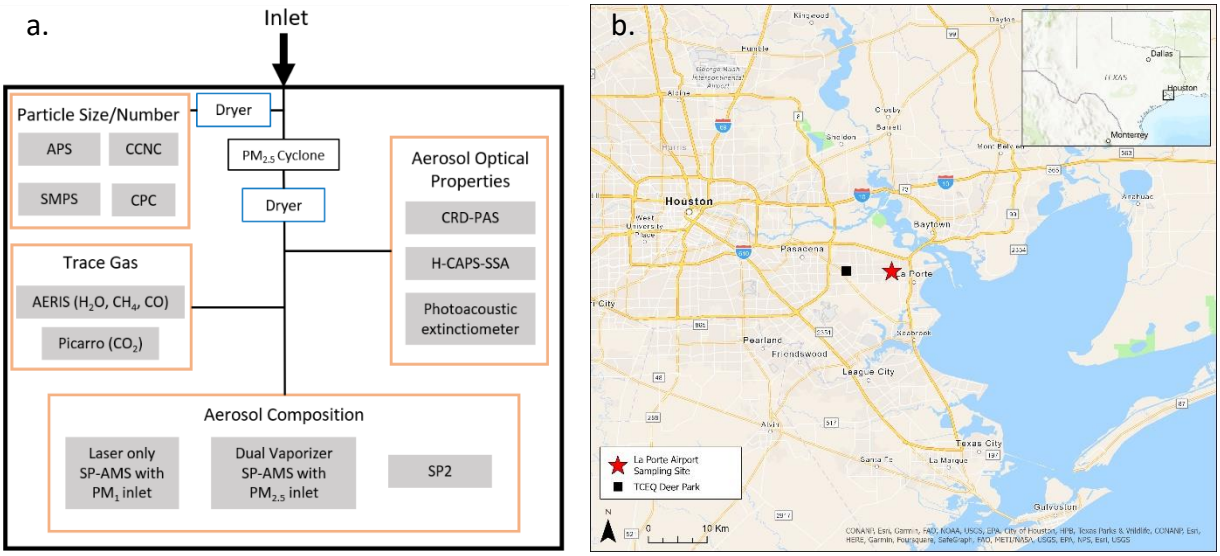

Figure D1: (a) Schematic of the experimental layout during the TRACER field campaign. Acronyms: APS: Aerodynamic Particle Sizer, CCNC: Cloud Condensation Nuclei Counter, SMPS: Scanning Mobility Particle Sizer, CPC: Condensation Particle Counter, CRD-PAS: Cavity Ring Down- Photoacoustic Spectrometer, H-CAPS-SSA: Humidified cavity-attenuated phase shift-single scattering albedo monitor, SP2: Single Particle Soot Photometer. (b) Map depicting the location of the La Porte sampling site (red star) in the greater Houston region.

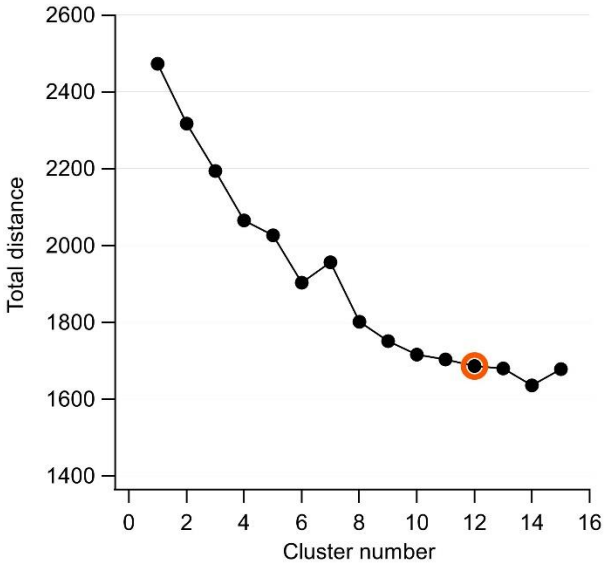

Figure D2: Total Euclidian distance between individual particles and the cluster average as a function of cluster number. The final 12-cluster solution is marked with the orange circle.

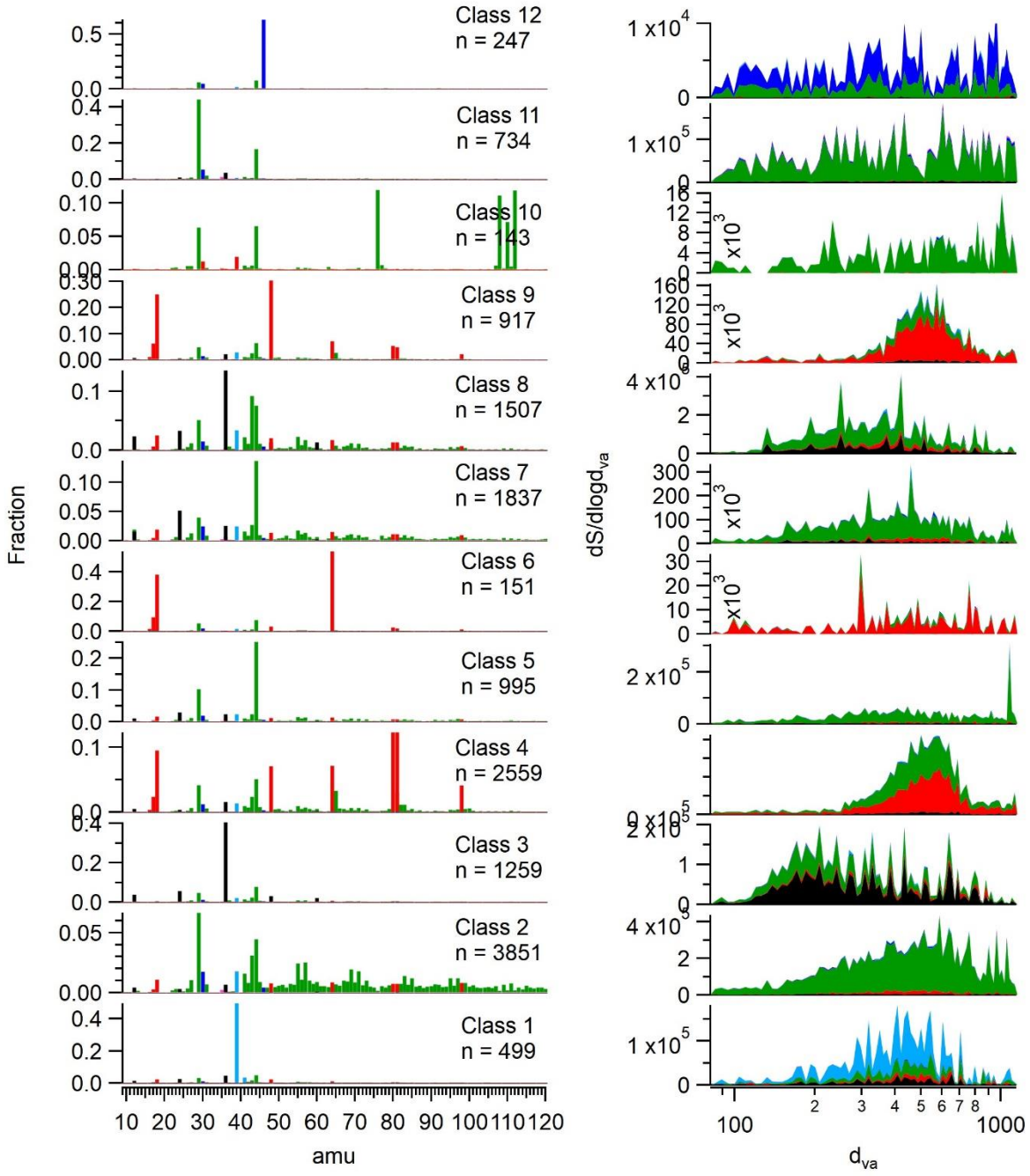

Figure D3: Average mass spectra and size distributions of particle clusters prior to merging similar clusters. Clusters 4, 6 and 9 were merged into a single sulfate cluster. Clusters 5 and 7 were merged into a single OOA cluster. Class 10 was discarded as a noise artifact.

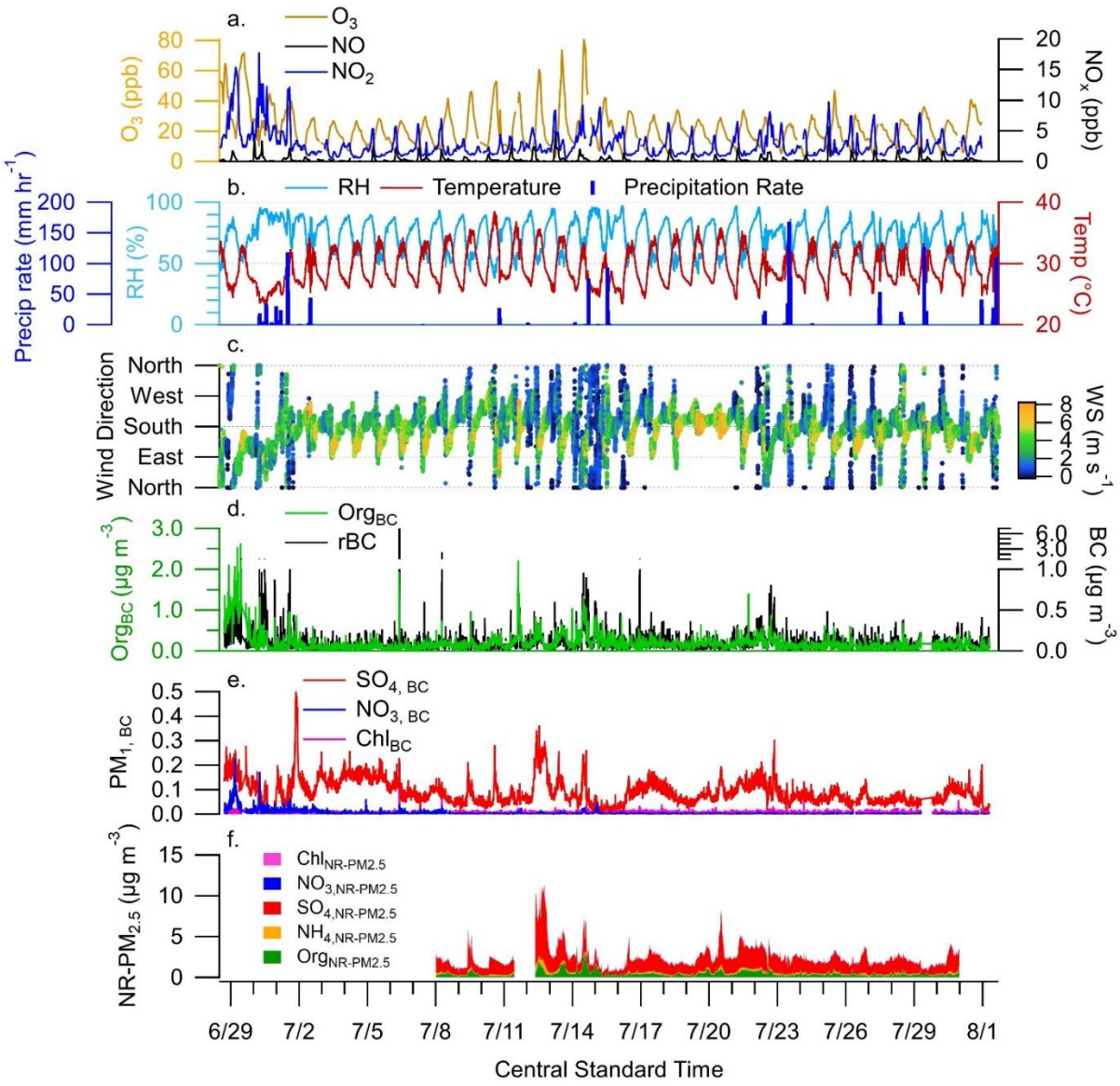

Figure D4: Time series of (a) trace gases, (b) meterological parameters, (c) wind speed and direction (d,e) rBC and associated coating material, (f) NR-$PM_{2.5}$ measured by co-located dual vaporizer SP-AMS in laser-off mode.

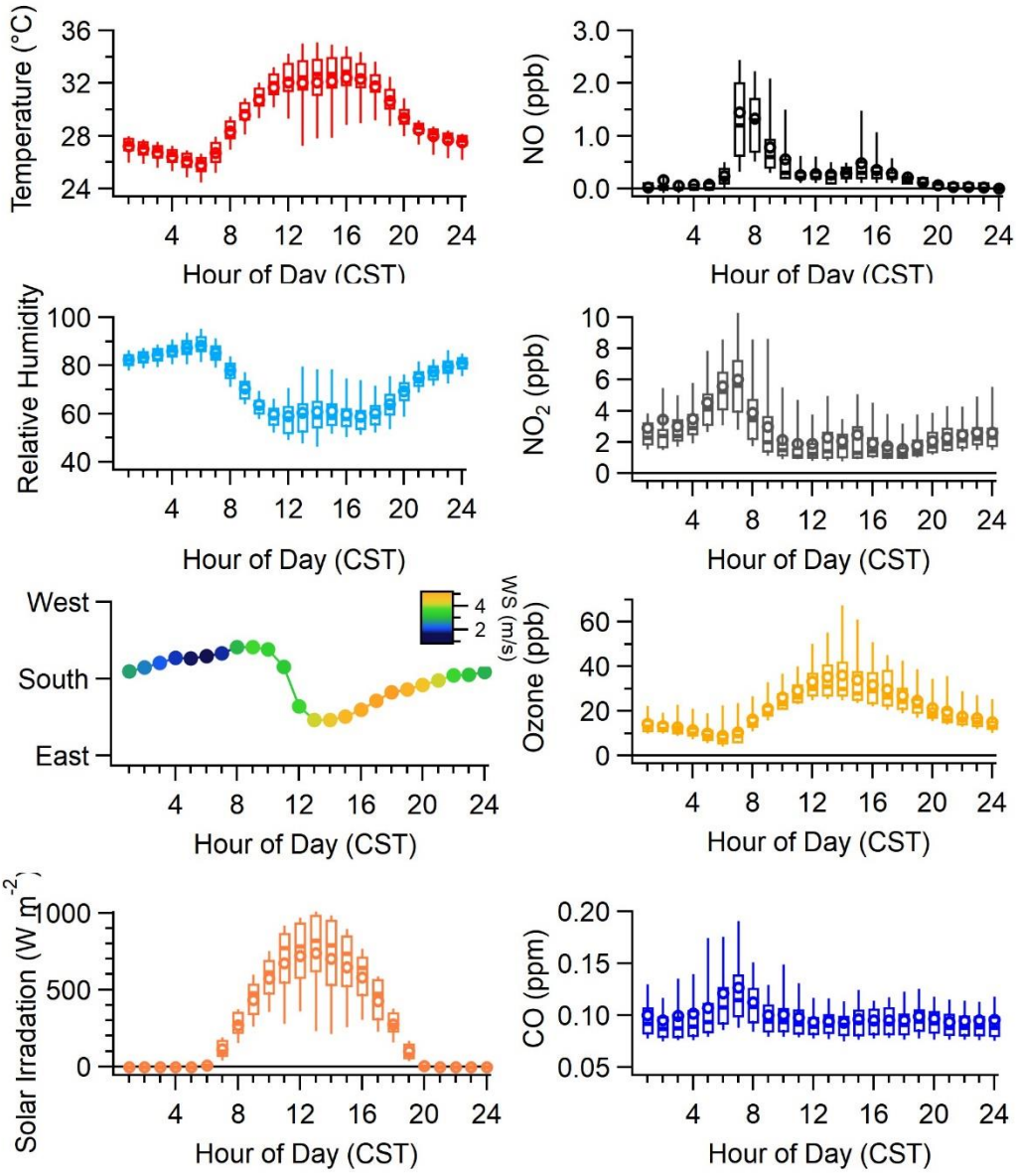

Figure D5: Diurnal variation in meteorological parameters and trace gas species. Solid and open symbols represent the median and mean respectively. Boxes indicate 25-75th percentile and whiskers indicate 10-90th percentiles.

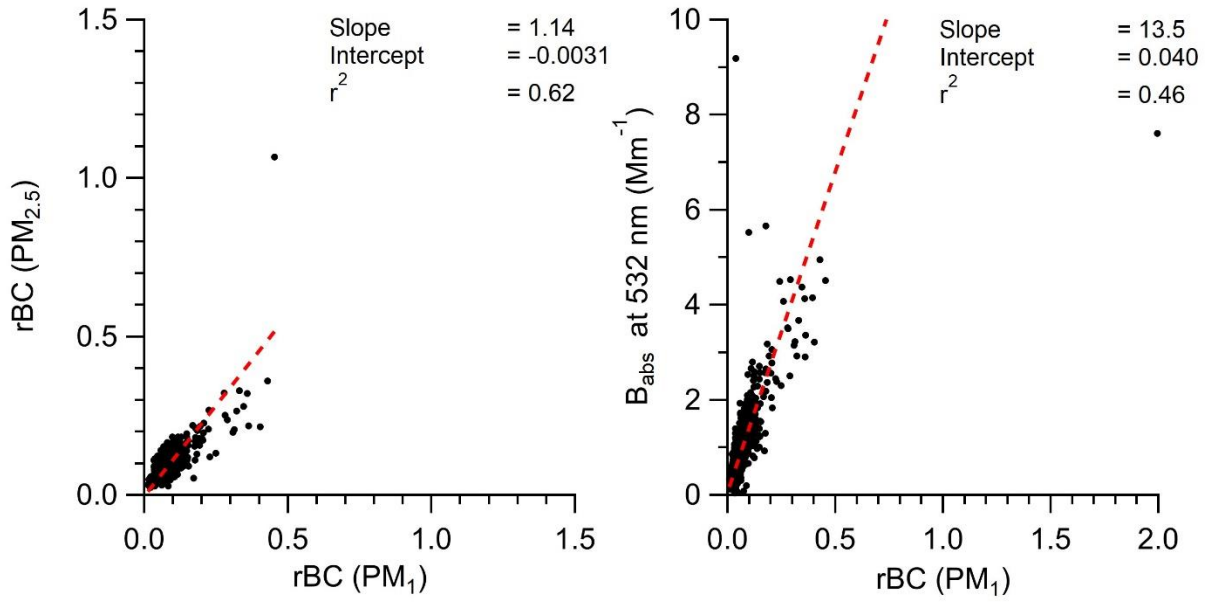

Figure D6: (a) Correlation between rBC measured by dual vaporizer SP-AMS equipped with $PM_{2.5}$ lens and laser-only SP-AMS. (b) Correlation between aerosol absorption at 532nm measured by photoacoustic spectroscopy and rBC measured by laser-only SP-AMS. Fit lines are orthogonal distance regressions.

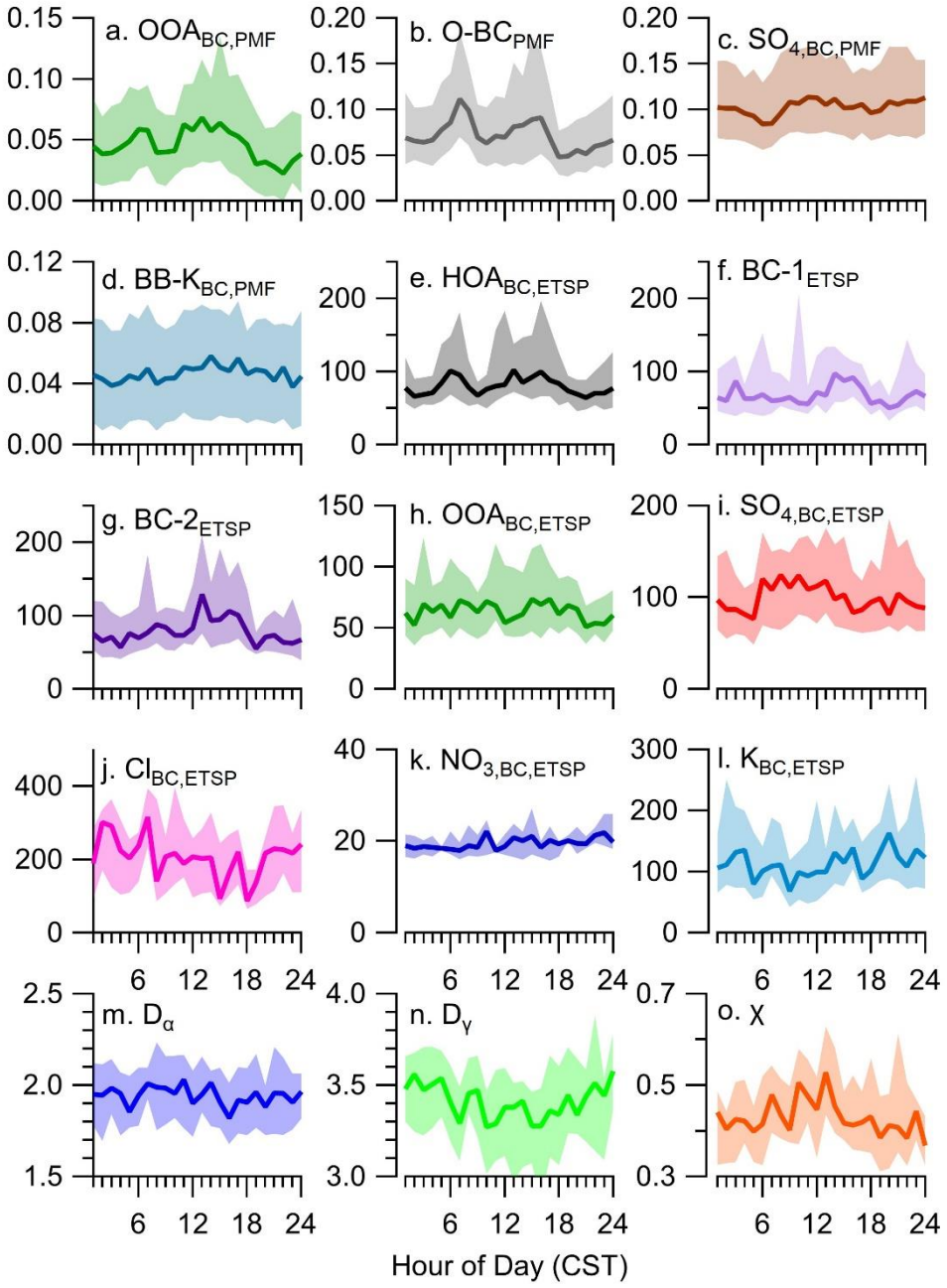

Figure D7: diurnal profiles of (a-d) PMF factors, (e-l) ETSP particle clusters, (m-o) mixing state metrics. Solid line is hourly median value and shaded area represents the interquartile range. Units for a-d are μg m^{-3} and e-l are ions.

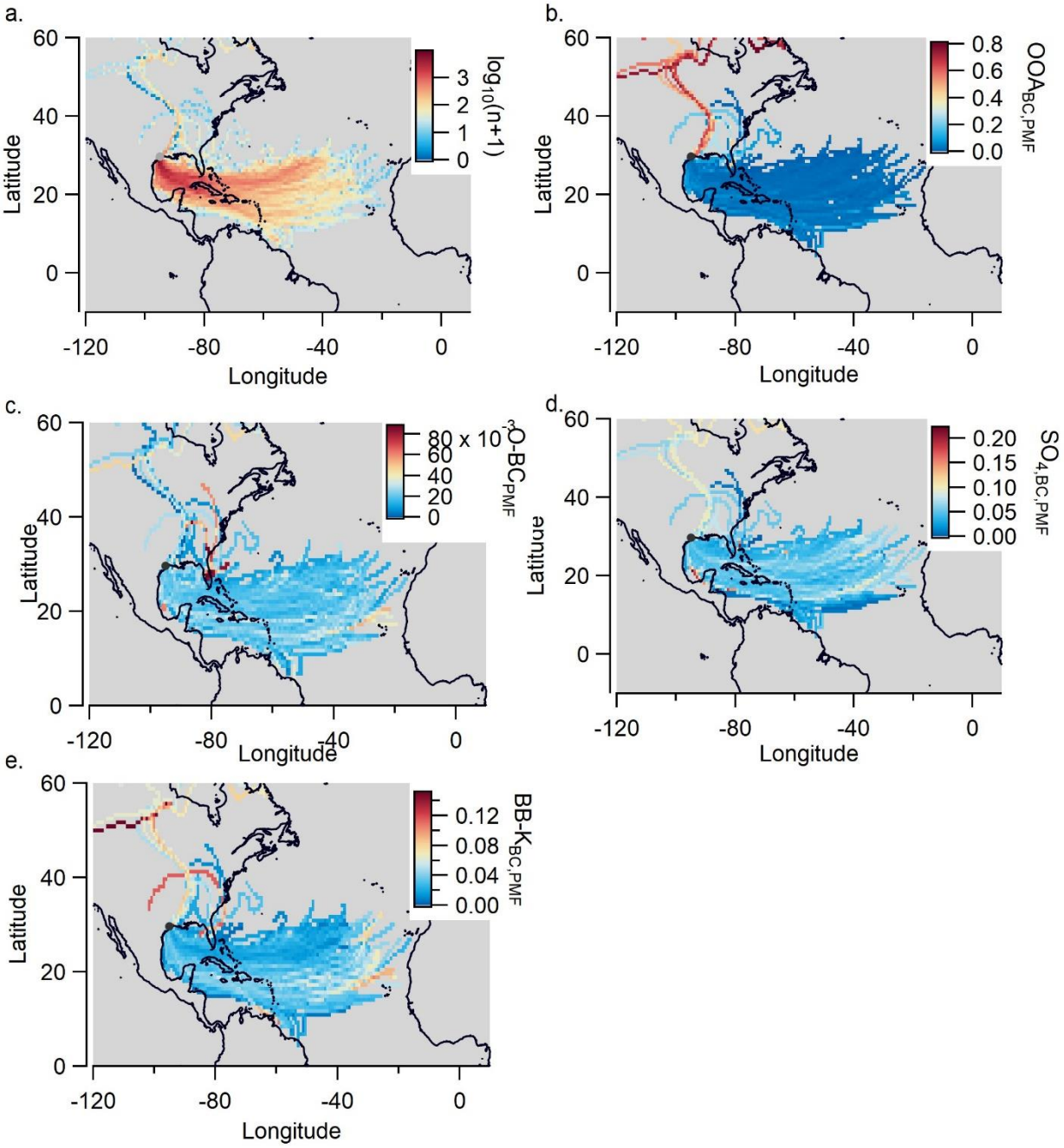

Figure D8: 14-day back trajectories from the La Porte sampling site originating every hour for the duration of the sampling period. (a) Back-trajectory density (b-e) concentration weighted back trajectories for each PMF factor.

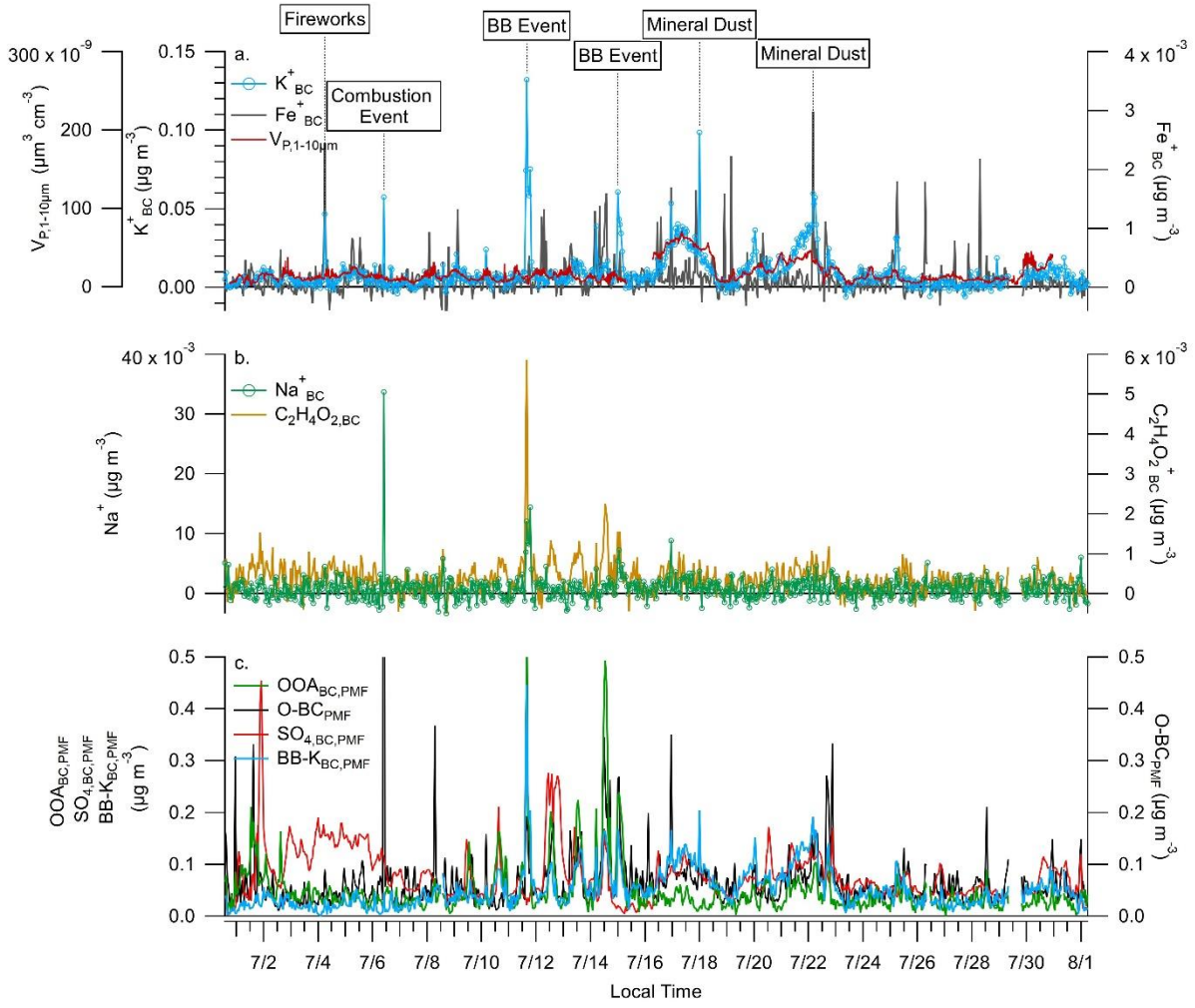

Figure D9: Time series comparison of (a) K^+ and Fe^+ measured by laser-only SP-AMS and aerosol volume between 1-10µm ($V_{1\text{-}10\mu m}$) measured by aerodynamic particle sizer. (b) Na^+ and $C_2H_4O_2^+$ measured by laser-only SP-AMS. (c) soot particle PMF factors. All species are averaged to one hour time resolution.

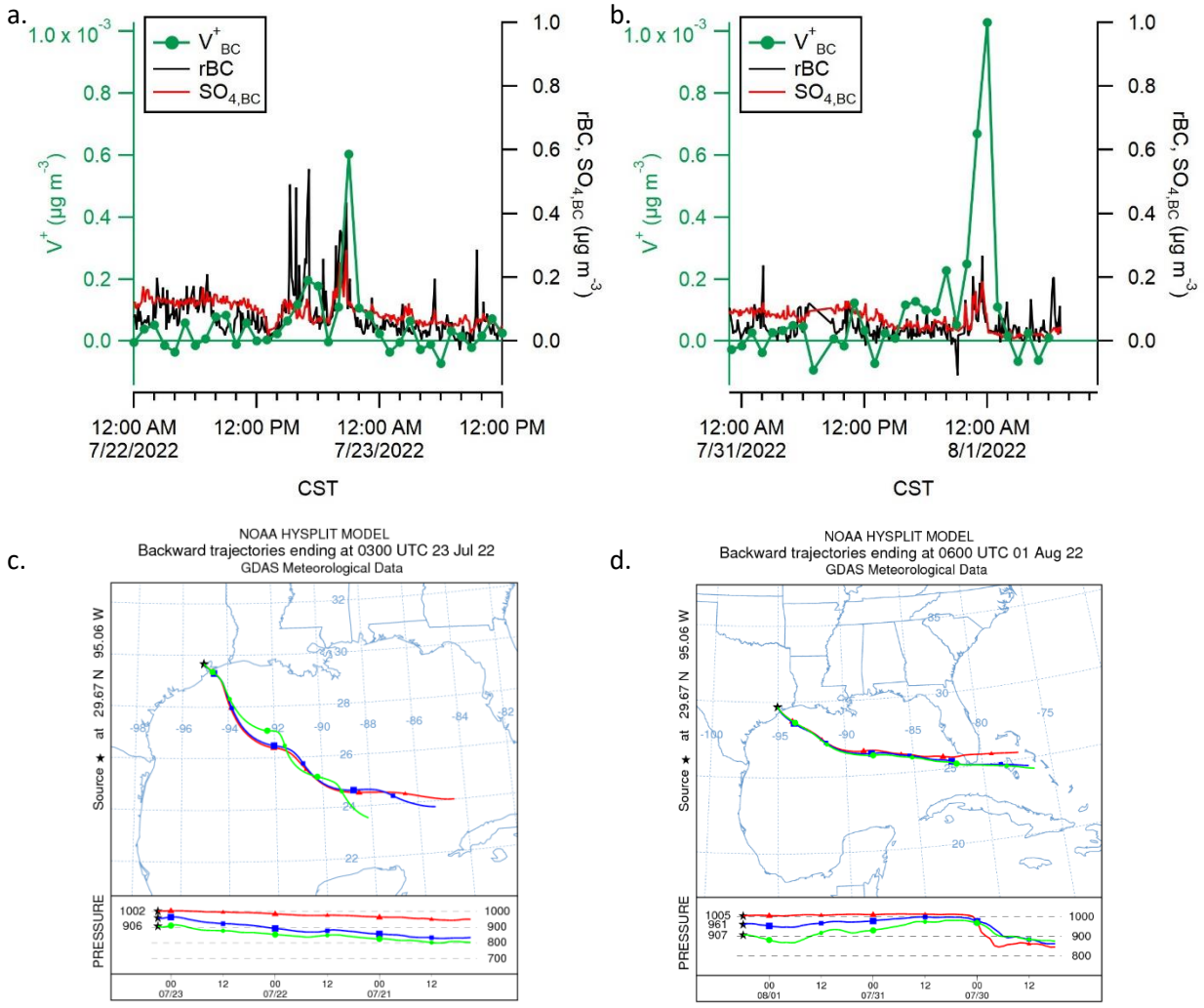

Figure D10: (a, b) Time series of vanadium events on Jul 22 and Jul 31-Aug 1. Vanadium is presented in nitrate equivalent concentration and is averaged to one hour. (c, d) Hysplit back trajectory originating at the sampling site at the time of peak V^+ concentration.

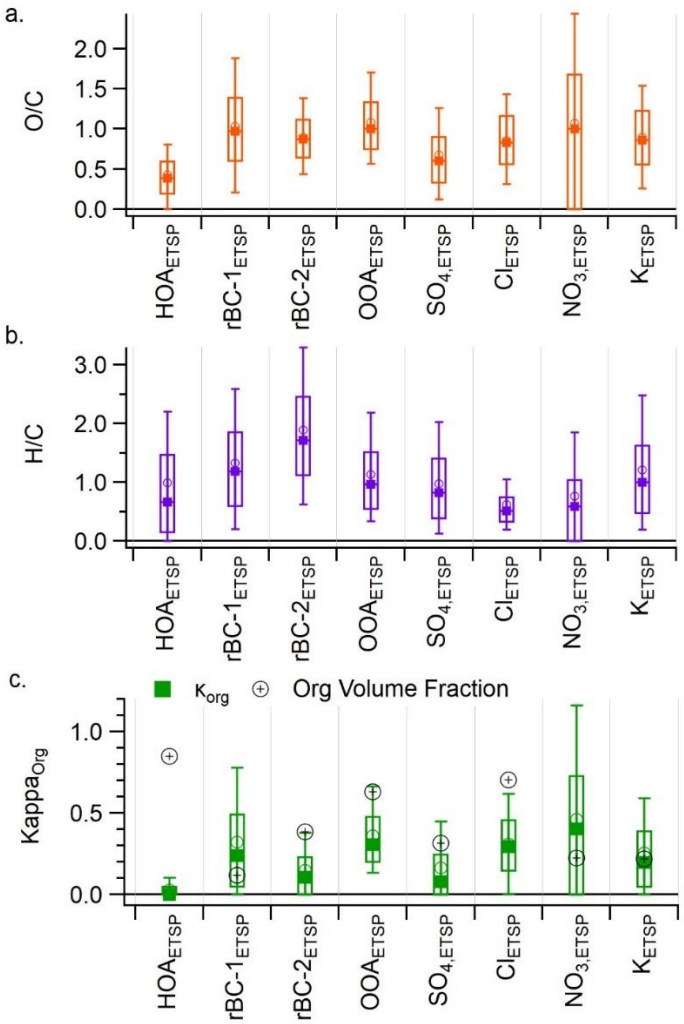

Figure D11: (a) OA O/C and (b) OA H/C ratio for single particle spectra, separated by particle class. (c) Kappa values calculated for the organic fraction of the single particle spectra, separated by particle class. Solid and open marker are the median and mean, box represents 25-75th percentile, whiskers represent 10-90th percentile. Cross symbols in (c) represent the average organic volume fraction of single particles.

Table D1: Single-particle signal threshold settings used during event trigger single particle (ETSP) measurements.

	Jun 30th – Jul 6th		Jul 6th – Aug 1st	
ROI	*m/z*	Trigger Level (ions)	*m/z*	Trigger Level (ions)
1	36	5	36	4
2	24	3	43	6
3	48	7.5	46-150	5.5

Table D2. Density and hygroscopicity parameters of pure compounds used in the calculation of κ.

Species	Density (g cm^{-3})	Hygroscopicity parameter (κ)
NH_4NO_3	1.72	0.67[1]
NH_4Cl	1.53	0.93[2]
$(NH_4)_2SO_4$	1.77	0.61[1]
K_2SO_4	2.66	0.69[2]
rBC	0.9	0
Organic	Variable[3]	Variable[4]

1. (Petters and Kreidenweis, 2007)
2. (Almeida et al., 2019)
3. (Kuwata et al., 2012)
4. (Duplissy et al., 2011)

Table D3: Number and percentage of particles in each ETSP class with no detectable rBC signal.

Class	Number of particles with no detectable rBC	Percent of particles with no detectable rBC
$HOA_{BC,ETSP}$	2949	77%
$BC\text{-}1_{ETSP}$	0	0%
$BC\text{-}2_{ETSP}$	157	10%
$OOA_{BC,ETSP}$	1351	48%
$SO_{4,BC,ETSP}$	2380	66%
$Cl_{BC,ETSP}$	279	38%
$NO_{3,BC,ETSP}$	236	96%
$K_{BC,ETSP}$	144	29%

References

Almeida, G. P., Bittencourt, A. T., Evangelista, M. S., Vieira-filho, M. S. and Estadual, U.: Characterization of aerosol chemical composition from urban pollution in Brazil and its possible impacts on the aerosol hygroscopicity and size distribution, Atmos. Environ., 202(March 2018), 149–159, doi:10.1016/j.atmosenv.2019.01.024, 2019.

Avery, A. M., Williams, L. R., Fortner, E. C., Robinson, W. A. and Onasch, T. B.: Particle detection using the dual-vaporizer configuration of the soot particle Aerosol Mass Spectrometer (SP-AMS), Aerosol Sci. Technol., 55(3), 254–267, doi:10.1080/02786826.2020.1844132, 2020.

Canagaratna, M. R., Jayne, J. T., Jimenez, J. L., Allan, J. D., Alfarra, M. R., Zhang, Q., Onasch, T. B., Drewnick, F., Coe, H., Middlebrook, A., Delia, A., Williams, L. R., Trimborn, A. M., Northway, M. J., DeCarlo, P. F., Kolb, C. E., Davidovits, P. and Worsnop, D. R.: Chemical and microphysical characterization of ambient aerosols with the aerodyne aerosol mass spectrometer, Mass Spectrom. Rev., 19(2), 173–181, doi:10.1002/mas.20115, 2007.

Canagaratna, M. R., Jimenez, J. L., Kroll, J. H., Chen, Q., Kessler, S. H., Massoli, P., Hildebrandt Ruiz, L., Fortner, E., Williams, L. R., Wilson, K. R., Surratt, J. D., Donahue, N. M., Jayne, J. T. and Worsnop, D. R.: Elemental ratio measurements of organic compounds using aerosol mass spectrometry: Characterization, improved calibration, and implications, Atmos. Chem. Phys., 15(1), doi:10.5194/acp-15-253-2015, 2015.

Cao, W., Martí-Rosselló, T., Li, J. and Lue, L.: Prediction of potassium compounds released from biomass during combustion, Appl. Energy, 250(May), 1696–1705, doi:10.1016/j.apenergy.2019.05.106, 2019.

Collier, S., Williams, L. R., Onasch, T. B., Cappa, C. D., Zhang, X., Russell, L. M., Chen, C. L., Sanchez, K. J., Worsnop, D. R. and Zhang, Q.: Influence of Emissions and Aqueous Processing on Particles Containing Black Carbon in a Polluted Urban Environment: Insights From a Soot Particle-Aerosol Mass Spectrometer, J. Geophys. Res. Atmos., 123(12), 6648–6666, doi:10.1002/2017JD027851, 2018.

DeCarlo, P. F., Kimmel, J. R., Trimborn, A., Northway, M. J., Jayne, J. T., Aiken, A. C., Gonin, M., Fuhrer, K., Horvath, T., Docherty, K. S., Worsnop, D. R. and Jimenez, J. L.: Field-deployable, high-resolution, time-of-flight aerosol mass spectrometer, Anal. Chem., doi:10.1021/ac061249n, 2006.

Draxler, R. R. and Hess, G. D.: An overview of the HYSPLIT_4 modelling system for trajectories, dispersion and deposition, Aust. Meteorol. Mag., 1998.

Duplissy, J., Decarlo, P. F., Dommen, J., Alfarra, M. R., Metzger, A., Barmpadimos, I. and Prevot, A. S. H.: Relating hygroscopicity and composition of organic aerosol particulate matter, Atmos. Chem. Phys., 1155–1165, doi:10.5194/acp-11-1155-2011, 2011.

Jayne, J. T., Leard, D. C., Zhang, X., Davidovits, P., Smith, K. A., Kolb, C. E. and Worsnop, D. R.: Development of an aerosol mass spectrometer for size and composition analysis of submicron particles, Aerosol Sci. Technol., doi:10.1080/027868200410840, 2000.

Kuwata, M., Zorn, S. R. and Martin, S. T.: Using elemental ratios to predict the density of organic material composed of carbon, hydrogen, and oxygen, Environ. Sci. Technol., 46(2), 787–794, doi:10.1021/es202525q, 2012.

Langridge, J. M., Richardson, M. S., Lack, D., Law, D. and Murphy, D. M.: Aircraft instrument for comprehensive characterization of aerosol optical properties, part i: Wavelength-dependent optical extinction and its relative humidity dependence measured using cavity ringdown spectroscopy, Aerosol

Sci. Technol., 45(11), 1305–1318, doi:10.1080/02786826.2011.592745, 2011.

Onasch, T. B., Trimborn, A., Fortner, E. C., Jayne, J. T., Kok, G. L., Williams, L. R., Davidovits, P. and Worsnop, D. R.: Soot particle aerosol mass spectrometer: Development, validation, and initial application, Aerosol Sci. Technol., doi:10.1080/02786826.2012.663948, 2012.

Petit, J. E., Favez, O., Albinet, A. and Canonaco, F.: A user-friendly tool for comprehensive evaluation of the geographical origins of atmospheric pollution: Wind and trajectory analyses, Environ. Model. Softw., doi:10.1016/j.envsoft.2016.11.022, 2017.

Petters, M. D. and Kreidenweis, S. M.: A single parameter representation of hygroscopic growth and cloud condensation nucleus activity, Atmos. Chem. Phys., 13(2), 1081–1091, doi:10.5194/acp-13-1081-2013, 2007.

Pratt, K. A., Murphy, S. M., Subramanian, R., Demott, P. J., Kok, G. L., Campos, T., Rogers, D. C., Prenni, A. J., Heymsfield, A. J., Seinfeld, J. H. and Prather, K. A.: Flight-based chemical characterization of biomass burning aerosols within two prescribed burn smoke plumes, Atmos. Chem. Phys., 11(24), 12549–12565, doi:10.5194/acp-11-12549-2011, 2011.

Ulbrich, I. M., Canagaratna, M. R., Zhang, Q., Worsnop, D. R. and Jimenez, J. L.: Interpretation of organic components from Positive Matrix Factorization of aerosol mass spectrometric data, Atmos. Chem. Phys., doi:10.5194/acp-9-2891-2009, 2009.

Willis, M. D., Lee, A. K. Y., Onasch, T. B., Fortner, E. C., Williams, L. R., Lambe, A. T., Worsnop, D. R. and Abbatt, J. P. D.: Collection efficiency of the soot-particle aerosol mass spectrometer (SP-AMS) for internally mixed particulate black carbon, Atmos. Meas. Tech., doi:10.5194/amt-7-4507-2014, 2014.

Zauscher, M. D., Wang, Y., Moore, M. J. K., Gaston, C. J. and Prather, K. A.: Air quality impact and physicochemical aging of biomass burning aerosols during the 2007 San Diego wildfires, Environ. Sci. Technol., 47(14), 7633–7643, doi:10.1021/es4004137, 2013.

Zhang, Q., Jimenez, J. L., Canagaratna, M. R., Ulbrich, I. M., Ng, N. L., Worsnop, D. R. and Sun, Y.: Understanding atmospheric organic aerosols via factor analysis of aerosol mass spectrometry: A review, Anal. Bioanal. Chem., doi:10.1007/s00216-011-5355-y, 2011.